



**HAL**  
open science

# Algorithms and applications of the Monte Carlo method : Two-dimensional melting and perfect sampling

Etienne Bernard

► **To cite this version:**

Etienne Bernard. Algorithms and applications of the Monte Carlo method : Two-dimensional melting and perfect sampling. Data Analysis, Statistics and Probability [physics.data-an]. Université Pierre et Marie Curie - Paris VI, 2011. English. NNT: . tel-00637330

**HAL Id: tel-00637330**

**<https://theses.hal.science/tel-00637330>**

Submitted on 1 Nov 2011

**HAL** is a multi-disciplinary open access archive for the deposit and dissemination of scientific research documents, whether they are published or not. The documents may come from teaching and research institutions in France or abroad, or from public or private research centers.

L'archive ouverte pluridisciplinaire **HAL**, est destinée au dépôt et à la diffusion de documents scientifiques de niveau recherche, publiés ou non, émanant des établissements d'enseignement et de recherche français ou étrangers, des laboratoires publics ou privés.

ÉCOLE NORMALE SUPÉRIEURE  
Département de Physique  
Laboratoire de Physique Statistique



THÈSE DE DOCTORAT DE L'UNIVERSITÉ PIERRE ET MARIE CURIE

Présentée par

**Etienne Bernard**

pour obtenir le titre de Docteur de l'Université Pierre et Marie Curie

**Algorithms and applications of the Monte Carlo method:  
Two-dimensional melting and perfect sampling**

Soutenue le 21 septembre 2011 devant le jury composé de :

<b>Jean-Louis Barrat</b>	Rapporteur
<b>Walter Kob</b>	Examineur
<b>Werner Krauth</b>	Directeur de thèse
<b>Michael Moore</b>	Rapporteur
<b>Pascal Viot</b>	Examineur



## General introduction

Statistical physics aims to understand the behavior of systems composed of many interacting elements. These systems display interesting collective phenomena, even if interactions are local. The solid state of matter is an example of such a phenomenon: the particles are correlated up to infinite distances, and the system moves as a single block. Sometimes, this behavior can be understood analytically. For example, some phase transitions are well described by mean-field theories [1], or by renormalization-group theory [2]. However, for other systems, the analytic methods fail to give correct results. In these cases, the system can be studied by the means of numerical approaches, and among them, the Monte Carlo method [3, 4].

The Monte Carlo method was developed in the late 1940s in order to study nuclear reactions. This method, and especially the Markov-chain Monte Carlo method, allows efficient computation of high-dimensional integrals. It is now used in several domains, including mathematics, economy, biology, and physics. In the context of statistical physics, the Monte Carlo method aims to reproduce the statistical behavior of a system at the thermodynamic equilibrium. To that purpose, an algorithm randomly samples configurations of the system with the appropriate probability distribution. These configurations are then used to compute the statistical properties of the system, that is, its thermodynamic properties. The Monte Carlo method is an important tool of statistical physics.

This PhD thesis concerns the conception and the study of Monte Carlo algorithms, as well as their applications to fundamental problems. It reviews the work achieved between September 2008 and September 2011 at the Ecole Normale Supérieure under the direction of Werner Krauth. During these three years, I collaborated with Werner Krauth, David B. Wilson, Cédric Chanal and Manon Michel. The thesis is divided in two parts. The work of Part I is the object of two publications [5, 6] (see Section 7.1 and Section 7.3), and the work of Part II is the object of one publication [7] (see Section 7.2) (another one is in preparation [8]).

Part I concerns the solid-liquid (that is, the melting) transitions in two dimensions, and is the main work of this thesis. These phase transitions have been heavily studied by the Monte Carlo method but they are still poorly understood. This part focuses on the simplest particle system: the hard-disk model. The nature of the melting transition in this model has been debated since 1962 [9]. With Werner Krauth and David B. Wilson,

I designed the “event-chain” algorithm [5] which outperforms previous methods for dense hard-disk systems. I then used this algorithm with Werner Krauth to perform large-scale simulations of the hard-disk system in order to study the melting transition. The results provide a clear answer about the nature of the transition [6].

The study of the hard-disk melting transition in Part I exposes to the thermalization problems of Markov chains. In systems such as hard disks or spin glasses, it is difficult to ensure that the Markov-chain Monte Carlo simulations have reached the thermodynamic equilibrium. Part II concerns this fundamental problem of the Monte Carlo method. A possible solution is studied: the coupling-from-the-past (CFTP) method. This method, developed by Propp and Wilson [10], is a “perfect-sampling” Monte Carlo method. The configurations (samples) which are generated from the algorithm are distributed according to the exact desired distribution. The CFTP method is hard to apply to most interesting physical systems. In Part II of this thesis, I analyze the applications of the CFTP method in systems such as hard disks or spin glasses. With Werner Krauth and Cédric Chanal, I showed that the limitation of this method is related to the chaotic properties of the Markov chains, the so-called “damage spreading” [7]. The CFTP method might lead to important progress in statistical physics, as it would provide rigorous statistical results in fundamental problems.

# Contents

<b>General introduction</b>	<b>3</b>
<b>I Two-dimensional melting</b>	<b>7</b>
<b>Introduction</b>	<b>9</b>
<b>1 Transitions in two dimensions</b>	<b>11</b>
1.1 Two-dimensional solids . . . . .	11
1.2 Transitions in 2D XY models . . . . .	18
1.3 Scenarios for two-dimensional melting . . . . .	29
<b>2 Event-chain Monte Carlo algorithms for hard spheres</b>	<b>41</b>
2.1 Hard-sphere simulations . . . . .	41
2.2 The event-chain algorithm . . . . .	48
2.3 Implementation of the algorithm . . . . .	57
<b>3 Simulation method</b>	<b>63</b>
3.1 Choice of ensemble . . . . .	63
3.2 Statistical errors . . . . .	66
3.3 Computation of observables . . . . .	68
<b>4 Hard-disk melting transition</b>	<b>77</b>
4.1 Phase coexistence . . . . .	77
4.2 Nature of the phases . . . . .	86
4.3 Thermalization and finite-size effects . . . . .	91
4.4 Other simulations . . . . .	96
<b>Conclusion</b>	<b>101</b>

<b>II</b>	<b>Perfect sampling</b>	<b>103</b>
	<b>Introduction</b>	<b>105</b>
<b>5</b>	<b>The coupling-from-the-past method</b>	<b>107</b>
5.1	The Monte Carlo method . . . . .	107
5.2	Coupling from the past . . . . .	111
5.3	Survey problem . . . . .	114
<b>6</b>	<b>Damage spreading and coupling in Markov chains</b>	<b>119</b>
6.1	Chaos in Markov chains . . . . .	119
6.2	Spin glass . . . . .	123
6.3	Hard spheres . . . . .	124
6.4	Griffeath's coupling . . . . .	128
	<b>Conclusion</b>	<b>131</b>
<b>7</b>	<b>Publications</b>	<b>141</b>
7.1	Publication I . . . . .	141
7.2	Publication II . . . . .	147
7.3	Publication III . . . . .	154

# Part I

## Two-dimensional melting





## Introduction

Although nature is composed of three spatial dimensions, two-dimensional (2D) systems are frequently observed. Surfaces, interfaces or membranes are examples of such systems. Physics in 2D unveils fascinating behavior, which strongly differ from three-dimensional (3D) ones. For example, in a particle system, the diffusion coefficient of a particle is infinite [11]. Another example is given by the properties of 2D solids: These solids are oriented like crystals, however, the position of their particles show infinite fluctuations with respect to the crystal lattice [12]. In a general way, 2D systems show larger fluctuations than in 3D. This can lead to phases where correlations extend over infinite distances but without a global ordering of the system. These phases are similar to critical phases in second-order phase transitions: they are characterized by power-law (also called algebraic) correlation functions, and are thus scale free. Along with these phases, 2D systems display a specific phase transition: the Kosterlitz-Thouless (KT) transition [13, 14]. This transition has found many applications in superfluids and superconducting films, or in 2D melting for example [15, 16]. 2D physics is an extremely active field of research in Soft matter [17, 18], hard condensed matter [19, 20], quantum gases [21], or even fluid mechanics [22] for example.

An interesting topic of 2D physics concerns the properties of phase transitions in these systems. A phase transition occurs when, under the change of an external parameter (pressure or temperature for example), a system is transformed into a qualitatively different phase. For example, we consider water (in three dimensions) at a pressure  $P = 100\text{kPa}$  and at a temperature  $T = 20^\circ\text{C}$ . Under these conditions, the molecules of water are little correlated to each other, and they can easily move. Therefore, the state of the system is disordered: it is liquid. As the temperature is decreased, molecules become correlated to each other on larger scales. At  $T = 0^\circ\text{C}$ , the correlations extend over the whole system, the system is ordered: it is a crystal and thus a solid. The scenario of this transition is well understood: at  $T = 0^\circ\text{C}$ , a block of ice appears. Then, the block grows as the system is cooled, until all the water is turned into ice. During the transformation, the temperature is constant at  $T = 0^\circ\text{C}$ . This phase transition is of the first-order type. A transition is said to be first order when the transformation is discontinuous. Here, the ice and the water at  $T = 0^\circ\text{C}$  are the limiting phases. In other systems (such as the ferromagnetic Ising model), the transition is continuous. In three dimensions, the

liquid-solid transition is generally of the first-order type.

We now consider molecules of water in 2D, that is, molecules lying in a planar box. At high temperature, the system is disordered: it is liquid. At low temperature, the system gets ordered: it is solid. An important question is to know how these two phases connect. For example, this transition could be discontinuous as in the 3D case. But it could also be continuous, or it could even follow a scenario in several steps. This unanswered question is investigated in this thesis for the fundamental model of hard disks.

The nature of the hard-disk melting transition is hardly studied by analytic analysis, but it can be studied by numerical methods such as the Monte Carlo method. In Chapter 1, I introduce to the problem of 2D melting, and summarize principal theories. In Chapter 2, I describe the event-chain Monte Carlo algorithm [5] (see Section 7.1). I show the particularities of the algorithm and compare its efficiency to previous algorithms. Chapter 3 and Chapter 4 concern the application of the event-chain algorithm to the hard-disk melting transition. In Chapter 3, I describe the methods used to study the transition. Finally, in Chapter 4, I present the results obtained. The transition is found to follow an unexpected scenario [6] (see Section 7.3).

## Transitions in two dimensions

In this chapter, I discuss the paradoxical properties of 2D particle systems, which cannot crystallize yet may form solids. I then introduce the KT transition through the example of the 2D XY model, and show that transitions in 2D are not universal. Finally, I address the question of the nature of the melting transition of 2D solids.

### 1.1 Two-dimensional solids

2D solids were first thought to be thermodynamically unstable [23, 1]. It is now known that these solids exist, yet with a weaker ordering than 3D solids. The nature of their melting transition has been controversial and was still recently debated [24, 25] (see [17, 18] for reviews). I will present a solution in Chapter 4.

#### 1.1.1 Existence of the two-dimensional solid

A solid is defined as a material possessing a non-zero shear modulus [26]. For many systems, the solid state is also defined by the long-range order of their structure, and is called a crystal [27]. A crystal is a periodic structure whose particles are located at the nodes of a lattice. In a 3D crystal, the mean square of the thermal displacement  $\vec{u}_i$  of an atom  $i$  from its lattice position is finite, and the solid is said to show long-range “positional order”. This property is experimentally observed by the diffraction pattern of elastic scattering experiments (a Fourier analysis of the periodicity of the system). For an atomic density

$$\rho(\vec{r}) = \sum_{i=1}^N \delta(\vec{r} - \vec{r}_i), \quad (1.1)$$

the intensity of the diffraction pattern is given by the structure factor

$$S(\vec{k}) = \frac{1}{N} \left| \int \rho(\vec{r}) \exp i\vec{k} \cdot \vec{r} \, d^d r \right|^2 \quad (1.2)$$

where  $\vec{k}$  is the momentum transfer,  $N$  is the number of particles, and  $d$  is the dimension of the system. Due to the atoms’ finite displacement from their respective lattice positions, the structure factor of a 3D solid is a lattice of  $\delta$ -functions, called Bragg peaks.

In 3D, the crystalline state is possible because the system is highly connected. Indeed, the number of paths connecting two distant particles is large enough to prevent fluctuations from disrupting the order. In one dimension (1D), the system is less connected. This leads to strong fluctuations, and to the absence of a long-range order. A simple example is given by the 1D elastic chain, where atoms of mass  $m$  are connected to their nearest neighbors by elastic springs. The thermal fluctuations of each spring contribute independently, and lead to strong displacements of the atoms from their lattice position,  $\langle (u_i - u_j)^2 \rangle \propto |r_i - r_j|$ . The order is thus short ranged (see Fig. 1.0). In 2D, the possibility of an order has been an important question.

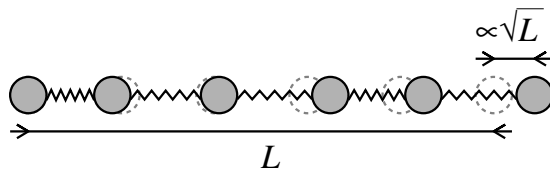


**Figure 1.1:** 1D elastic chain. The undeformed positions are shown in dashed lines. The positional order is short ranged.

Peierls, in 1934 [23, 28], studied the ordering of the harmonic solid (a solid with linear elasticity and fixed connectivity, see Section 1.1.2) in various dimensions. Peierls showed that in 2D, the mean square atoms' displacement from their lattice position fluctuates as  $\langle (\vec{u}_i - \vec{u}_j)^2 \rangle \propto \log |\vec{r}_i - \vec{r}_j|$ . Therefore, this system possesses no long-range positional order. This result was assumed to extend to non-harmonic solids, and was interpreted as proving that 2D solids cannot exist. Thirty years later, Alder and Wainwright [9] found, by numerical simulations, that the hard-disk system undergoes a phase transition. These results indicated that a 2D solid exists and initially put doubt on the generalization of Peierls' result to non-harmonic solids. Following the landmark work on 2D ordering by Mermin and Wagner [29], Mermin [12] analytically proved that atoms interacting with any finite-ranged continuous potential cannot show long-range positional order in 2D. This result, known as the Mermin-Wagner theorem, extended Peierls' result and ended the debate on the existence of a solid with a classic crystalline order. Nevertheless, the theorem does not exclude the possibility for another kind of 2D solid: Mermin [12] noted that the harmonic solid shows an "orientational" long-range order, and that this could provide an interpretation for the solid seen in hard disks.

It is now understood that 2D solids do exist, although they do not show the same crystalline order as 3D solids. Studies of electrons [30] or colloids [31] confined to a surface are experimental proof of their existence.

### 1.1.2 The harmonic solid

Solids under stress exhibit deformations which, in the limit of small deformations, are proportional to the applied stress. In this limit, the harmonic approximation can be made. The solid can then be seen as atoms connected together by classic springs having a quadratic potential: the discrete equivalent of the elasticity theory [26]. At large scales, the thermal deformations are small, and therefore a solid (under no stress) can always be

considered as harmonic. The harmonic-solid model, which can be solved analytically, is a key model for the ordering of solids.

At zero deformation, the atoms are located on their respective lattice positions  $\vec{R}$ . The thermal energy displaces the atoms, and their new position is  $\vec{r}(t) = \vec{R} + \vec{u}(\vec{R}, t)$ . The displacement field  $\vec{u}(\vec{R}, t)$  can be expanded in planar waves (phonons)

$$\vec{u}(\vec{R}, t) = \int \vec{u}_k(t) \exp i\vec{k} \cdot \vec{R} \, d^d k, \quad (1.3)$$

$$\text{with } \vec{u}_k(t) = \vec{a}_k \exp i\omega_k t + \vec{b}_k \exp -i\omega_k t.$$

In Eq. (1.3),  $\omega_k$  is the angular frequency associated to the wave vector  $\vec{k}$ . The sum on  $\vec{k}$  extends over the first Brillouin zone and  $\vec{u}_{-\vec{k}} = \vec{u}_k^*$  as  $\vec{u}$  is real. In the harmonic solid, the linear elasticity approximation is exact. Phonons are independent and the solid can be seen as a gas of thermally excited non-interacting phonons. The equipartition of energy in this gas gives

$$\langle |u_k|^2 \rangle \propto k_B T \frac{1}{\omega_k^2}, \quad (1.4)$$

also the density of state depends upon the dimension  $d$  of the system by  $D(k) \propto k^{d-1}$ , and for small  $k$  phonons  $\omega_k \propto k$  (constant sound velocity). The weight of all phonons with small  $|\vec{k}| = k$  is therefore  $\propto k^{d-3}$ ; for  $d \leq 2$  the weight diverges at  $k = 0$ . Consequently, long-wavelength phonons destroy long-range order. Indeed, using Eq. (1.3) and Eq. (1.4), the quadratic displacement of the atoms  $\vec{\Delta r}^2 = [\vec{u}(\vec{R}) - \vec{u}(\vec{0})]^2$  satisfies

$$\langle \vec{\Delta r}^2 \rangle \propto k_B T \int \frac{1 - \cos \vec{k} \cdot \vec{R}}{\omega_k^2} \, d^d k, \quad (1.5)$$

which gives, for  $R$  larger than the microscopic cut-off  $a$ ,

$$\langle \vec{\Delta r}^2 \rangle_{R \gg a} \propto k_B T \int_{k > 1/R}^{k < 1/a} \frac{1}{k^2} \, d^d k, \quad (1.6)$$

and thus at large distances

$$\langle \vec{\Delta r}^2 \rangle \propto k_B T \cdot \begin{cases} R & \text{for } d = 1 \\ \ln R & \text{for } d = 2 \\ \text{const.} & \text{for } d \geq 3 \end{cases}. \quad (1.7)$$

As predicted by the weight of long-wavelength phonons, fluctuations of positions are finite only for  $d \geq 3$ . This rules out the possibility of a stable 1D or 2D crystal. However, in 2D the fluctuations scale only logarithmically with the distance (see Eq. (1.7) and Fig. 1.1). As shown below, this shows that the positions are correlated over the whole system. As a consequence, it is not possible to apply a shear strain without stressing the system [32]. Therefore the system shows a non-zero shear modulus, and is a solid. Furthermore, the harmonic solid shows a different kind of long-range order as pointed by Mermin [12]. The field  $\vec{r}(\vec{R} + \vec{a}) - \vec{r}(\vec{R})$  corresponds to the relative position of two

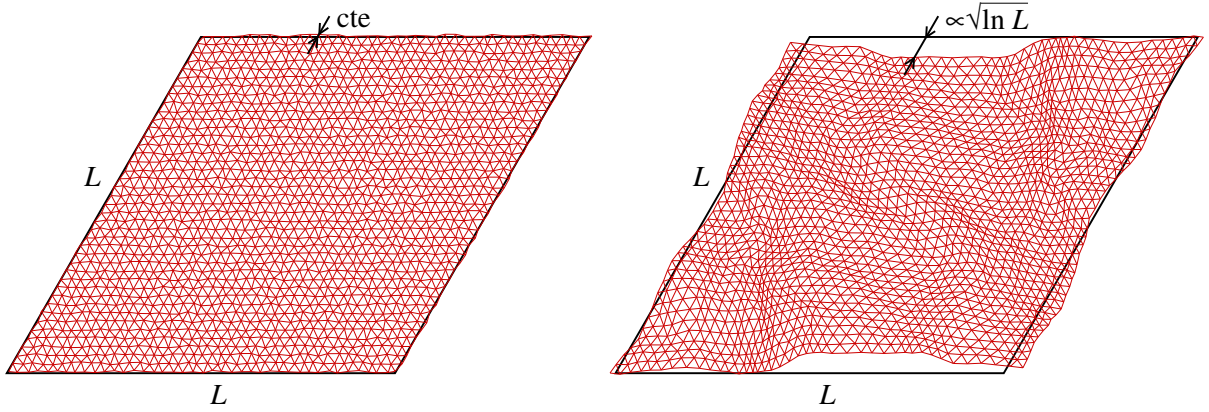


**Figure 1.2:** Crystals with a triangular lattice under thermal fluctuations. The black lines represent the positions of the undeformed borders. *Left:* Crystal with long-range positional order: the fluctuations about the lattice are finite. *Right:* 2D harmonic lattice: the fluctuations about the lattice are logarithmic with the distance, yet the orientation is conserved.

neighboring atoms, and can define a local orientation of the system. Its spatial correlation can be computed using Eq. (1.3) and Eq. (1.4),

$$\begin{aligned}
 & \left\langle [\vec{r}(\vec{R} + \vec{a}) - \vec{r}(\vec{R})] \cdot [\vec{r}(\vec{a}) - \vec{r}(\vec{0})] \right\rangle \\
 &= a^2 + \left\langle [\vec{u}(\vec{R} + \vec{a}) - \vec{u}(\vec{R})] \cdot [\vec{u}(\vec{a}) - \vec{u}(\vec{0})] \right\rangle \\
 &\xrightarrow{r \rightarrow \infty} a^2.
 \end{aligned} \tag{1.8}$$

The orientation of the solid is then correlated across infinite distances, that is, the 2D harmonic solid shows long-range orientational order.

The harmonic solid lacks positional order, as shown. It is possible to quantify the decay of the correlations by

$$C_{\vec{K}}(r) = \left\langle \exp \left( i\vec{K} \cdot \vec{\Delta r} \right) \right\rangle_{|\vec{\Delta r}|=r} \tag{1.9}$$

where  $\vec{K}$  is the first Bragg peak of the lattice. In the harmonic approximation

$$C_{\vec{K}}(r) = \left\langle \exp \left( i\vec{K} \cdot \vec{\Delta r} \right) \right\rangle = \exp \left[ -1/2 \left\langle (\vec{K} \cdot \vec{\Delta r})^2 \right\rangle \right], \tag{1.10}$$

and as  $\left\langle (\vec{K} \cdot \vec{\Delta r})^2 \right\rangle \propto k_B T \ln R$  (Eq. (1.7)), the correlation function at large distance satisfies <sup>1</sup>

$$C_{\vec{K}}(r) \sim r^{-\nu_K} \quad \text{with} \quad \nu_K \propto k_B T. \tag{1.11}$$

The positional order decays algebraically, rather than exponentially (as in 1D). This scale-free behavior is typical of low-dimensional systems. The positional order of this system is said to be quasi-long ranged. As a consequence, the peaks of the structure factor are infinite [33, 34], although not  $\delta$ -functions as for the 3D case. For long-range positional

<sup>1</sup>Logarithmic corrections are ignored.

order, the first Bragg peak in a system of size  $L$  behaves as  $S(\vec{K}) \propto L^2$  and has a width  $\propto 1/L$ . For the 2D harmonic solid, Eq. (1.11) and Eq. (1.2) yield

$$S(\vec{K}) \sim L^{2-\nu_K}, \quad (1.12)$$

and the peak has a specific shape [35]

$$S(\vec{k}) \sim 1/|\vec{k} - \vec{K}|^{2-\nu_K}. \quad (1.13)$$

For  $\nu_K \geq 2$ , the Bragg peaks remain finite. However, this should not be interpreted as a transition (contrary to what was suggested in [33]). Indeed, the correlation function is still algebraic and no qualitative changes occur in the thermodynamic properties of the system.

Algebraic correlation functions are usually associated with critical phases at continuous transitions [36]. These phases are affected by critical slowing down. Indeed, as the correlation length is infinite, the dynamics of the system is slow and the thermalization is time large. For local dynamics this phenomenon can also occur in the solid phase as the correlations are algebraic. This has important consequences for simulations (see Section 1.3.3).

The harmonic solid is thus characterized by its long-range orientational order and quasi-long-range positional order. As the relative deformations at large scale are small, the qualitative results obtained in the elastic description are also valid for generic 2D systems in their ordered phase.

### 1.1.3 Graphene and buckling

Graphene, discovered in 2004 [37], is a flat monolayer of carbon packed in a honeycomb pattern. This material was first obtained by exfoliating a single layer of graphite. Because of its unique electric properties, graphene is now an intensely explored topic of research.

The above results for the ordering of 2D solids are valid for solids strictly confined in 2D. For 2D solids which are allowed to bend into the third dimension, the results hold if the atomic bonds cannot break. If atomic bonds are allowed to break, the system reduces its free energy by the formation of defects (dislocations and disclinations, see Section 1.3.2) whose energies are lowered by the possibility of buckling the system into the third dimension [38, 39, 40]. This causes the solid to melt. For this reason, free-standing solids, such as graphene, should not exist. However, as the covalent bonds of graphene are strong, the melting process is very slow. Graphene is thus metastable, with an extremely long life time.

The apparent long-range positional order (shown by the fact that the charge carriers travel long distances without being scattered) has been said to contradict the Mermin-Wagner theorem. One solution to this contradiction was that this 2D material was standing on a 3D substrate. However, free-standing graphene [41] exists and exhibits the same properties. In fact, as 2D solids exhibit quasi-long-range positional order, it can be difficult to distinguish a true long-range order from a quasi-long-range order in a finite-size system.

The decay of positional order in graphene can be estimated as follows. In the harmonic approximation, graphene is a triangular lattice with two atoms per cell, forming



a hexagonal pattern. In the linear elasticity approximation, graphene can be considered isotropic [42] and the values of its elastic coefficients agree in simulations [42] and experiments [43]. The Young modulus is  $\mathcal{E} \simeq 300\text{N.m}^{-1}$  while the Poisson ratio is  $\sigma \simeq 0.3$ . The strong covalent bonds of carbon make this material stiff. If graphene layers are added with an inter-layer spacing of  $h = 0.335\text{nm}$  (as for graphite), the Young modulus would be  $\mathcal{E} \simeq 1000\text{ GPa}$  while  $\mathcal{E} \simeq 200\text{ GPa}$  for steel. The positional correlation function for an elastic triangular lattice is given by (see Section 1.3.2)

$$C_{\vec{K}}(r) \sim r^{-\nu_K} \quad \text{with} \quad \nu_K = \frac{k_B T 4\pi (1 + \sigma)(3 - \sigma)}{3a_0^2 \mathcal{E}}, \quad (1.14)$$

for a temperature of  $T = 293\text{K}$  and a lattice spacing of  $a_0 = 0.246\text{nm}$  the exponent is found to be  $\nu_K \simeq 0.003$ . The correlation function decays then very slowly,  $(r/a_0)^{-\nu_K} = 0.1$  giving  $r \sim 10^{300}a_0$ . It is therefore impossible to distinguish this quasi-long-range order from a long-range order in experimental samples.

The example of graphene illustrates the slow decay of algebraic functions arising in low dimensional physics, and the importance of finite-size effects.

### 1.1.4 The hard-disk solid

Hard-sphere systems are simple models of short-range interacting particles. Particles are spheres of radius  $\sigma$  which do not interact but cannot overlap. Hard spheres, in 3D and in 2D (hard disks), occupy a special place in statistical mechanics. Indeed, many fundamental concepts, from the virial expansion (by van der Waals [44] and Boltzmann [45]), to long-time tails [11], to 2D melting [9], were first discussed in these extraordinarily rich physical systems. These models have also played a crucial role in the history of computation: both the Metropolis algorithm [46] and molecular dynamics [47] were first implemented for monodisperse hard disks in a box.

Because of the absence of energy, the phase diagram of hard-sphere systems is identical at all temperatures  $T = 1/k_b\beta$  (only the velocities vary). Therefore the phase diagram depends upon only one parameter. For  $N$  hard disks in a box of volume  $V$  (constant-density ensemble), this parameter is the packing fraction  $\eta = N\pi\sigma^2/V$  (also called the density). For hard disks in a constant-pressure ensemble, this parameter is the rescaled pressure  $\beta P\sigma^2$ . In these models, the absence of attractive part does not allow for a liquid-gas transition, the generic term of liquid is thus given to the disordered phase. At low density, the hard-sphere liquid is well described by effective theories [48], and easily simulated because of its essentially local nature.

The purely repulsive interaction does not prevent the system from being ordered. Correlations increase with density, both for the positions and the orientations. In 3D, the system shows an ordered phase at high densities [49]. This transition results from an “order from disorder” phenomenon: At high density, ordered configurations can allow for larger fluctuations, and thus higher entropy, than the disordered liquid. The hard-sphere systems are examples showing that collective behavior also arises from purely entropic systems.

Alder and Wainwright [9] performed molecular-dynamics simulations of hard disks, in the constant-density ensemble. They found that for a density  $\eta \simeq 0.7$ , much lower than the close packing density  $\eta_{\text{cp}} = \pi/(2\sqrt{3}) \simeq 0.907$ , the equation of state (pressure

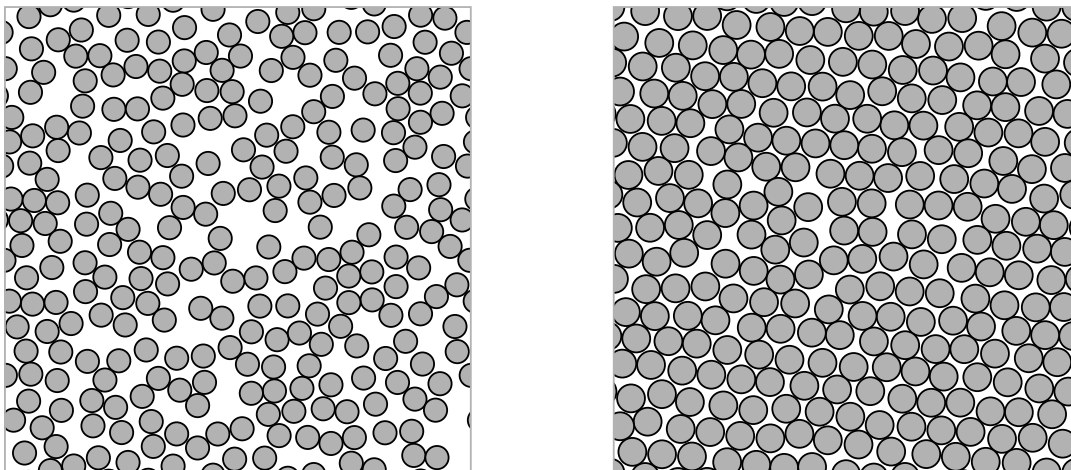


**Figure 1.3:** Configurations of  $16^2$  hard disks in a square box with periodic boundary conditions. *Left:* At the packing fraction  $\eta = 0.5$ , the system is not ordered, it is thus liquid. *Right:* At  $\eta = 0.72$ , the system is packed in an approximately triangular lattice whose orientation is correlated up to infinite distances, it is thus solid.

over volume) showed two distinct branches connected by a loop. This behavior, though obtained from small system sizes, hints at the existence of a phase transition, and therefore of a hard-disk solid (see Fig. 1.2). This discovery helped to realize that Peierls' argument [23, 28] does not rule out the existence of 2D solids, and motivated the work of Mermin and Wagner [29, 12].

It is interesting to note that the Mermin-Wagner theorem has only been proved for continuous potentials; it does not apply to hard disks and this system could therefore show a long-range positional order in principle. Although not rigorously proved, it is clear that the hard-disk system cannot show a long-range order, as for the other 2D solids. Indeed, as noted in Section 1.1.2, the harmonic approximation is valid at low temperature and large scale. Therefore, the hard-disk solid satisfies the same qualitative properties as the harmonic solid: long-range orientational order and quasi-long-range positional order.

It can be surprising that hard disks, which have no attractive parts, can be seen as an elastic medium. A way to understand this is to look at how the system reacts to a perturbation. If two neighboring disks are displaced apart from a small quantity, the others disks would hit harder on the outer faces of the two disks, which would cause them to get closer. The two disks actually see an effective continuous and attractive potential created by the rest of the system. This interaction can also be interpreted as a depletion interaction [50]: when two disks are close, the available space for the other disks increases, and so does the total entropy. One should note that the absence of potential energy does not prohibit an elastic behavior. Indeed, elasticity is caused by a change of free energy (and thus both energy and entropy) toward deformation. Therefore the hard-disk system can show an elastic behavior, the origin of elasticity being only entropic.

## 1.2 Transitions in 2D XY models

Before analyzing the melting of particle systems, we examine simpler lattice models: the 2D XY models. As for the melting transition now, the nature of transitions in these models has been debated, and especially for the principal one, the 2D rotor XY model [51, 52]. The debate ended with the progress of Monte Carlo algorithms in these systems [53, 54]. The transition in the 2D rotor XY model follows a KT transition [13]. The study of this simple model helps understand 2D melting.

### 1.2.1 2D XY models

2D XY models are systems of bi-dimensional spins interacting on a 2D lattice, and are invariant under a global rotation. A spin  $i$  is defined through its angle  $\theta_i$  by  $\vec{S}_i = (\cos \theta_i, \sin \theta_i)$ , and the interaction is a function of differences  $\theta_j - \theta_i$  of the spins.

The principal 2D XY model with short-range interactions is the rotor model, which is defined by the Hamiltonian

$$H = -J \sum_{\langle i,j \rangle} \vec{S}_i \cdot \vec{S}_j. \quad (1.15)$$

$J$  is the spin stiffness, and the sum extends over the nearest neighbors. Let  $\theta(\vec{r})$  be the continuous field given by the coarse-grained spins. At low temperature and large scale, the small variation of  $\theta(\vec{r})$  allows the expansion of the Hamiltonian to be done at the first non-zero order. This corresponds to the harmonic approximation. The renormalized Hamiltonian becomes

$$H_R = \frac{1}{2} J_R \int [\vec{\nabla} \theta(\vec{r})]^2 d^2 r, \quad (1.16)$$

$J_R$  is the renormalized spin stiffness. As for the harmonic solid, the field is Gaussian, therefore analytically solvable. The fluctuations of  $\theta(\vec{r}) - \theta(\vec{0})$  satisfy

$$\langle (\theta(\vec{r}) - \theta(\vec{0}))^2 \rangle = \frac{2}{\beta J_R} \int \frac{d^2 k}{(2\pi)^2} \frac{1 - \cos \vec{k} \cdot \vec{r}}{k^2} \quad (1.17)$$

$$\sim -\frac{1}{\pi \beta J_R} \ln \frac{r}{a}, \quad (1.18)$$

where  $a$  is the microscopic cut-off, and the correlation function

$$C(r) = \langle \vec{S}(\vec{0}) \cdot \vec{S}(\vec{r}) \rangle = \exp \left[ -1/2 \langle (\theta(\vec{r}) - \theta(\vec{0}))^2 \rangle \right]. \quad (1.19)$$

Again, the fluctuations are logarithmic, and the correlation function tends to decay algebraically at large distances <sup>2</sup>,

$$C(r) \sim r^{-\nu} \quad \text{with} \quad \nu = \frac{1}{2\pi\beta J_R}. \quad (1.20)$$

In agreement with the Mermin-Wagner theorem, the system lacks long-range order, but shows quasi-long-range order. No length scale is present in this system, and the correlation

---

<sup>2</sup>Logarithmic terms are ignored.

length is infinite; the system can be seen as a critical phase of a second-order phase transition. As the fluctuations occur even at large scale, this phase shows critical slowing down.

As for the 2D solid, the harmonic approximation holds for the 2D XY model at low temperatures and large length scales. The aforementioned results are thus valid for any 2D XY models, thus the low-temperature phase is always algebraic. At high temperatures, the system is disordered. The nature of the transition between the two phases is not easily obtained through renormalization, and actually depends on the microscopic model. We discuss the KT transition, which is seen in the 2D rotor XY model and is also seen in the melting of 2D particle systems.

## 1.2.2 The Kosterlitz-Thouless transition

Kosterlitz and Thouless [13, 14], as well as Berezinsky independently [55, 56], showed that an original phase transition could occur in 2D systems. This continuous transition, referred to as the KT transition, connects a phase whose order is quasi-long ranged (the correlation function is algebraic) to a phase whose order is short ranged. The transition is ruled by the formation of topological defects, such as dislocations for a solid, or vortices in spin systems with continuous symmetry. This theory successfully describes many 2D transitions, such as the transition in XY models, or the transition toward superfluidity in bi-dimensional quantum systems for example [57]. This transition is also at the basis of the Kosterlitz-Thouless-Halperin-Nelson-Young (KTHNY) theory for the melting of 2D solids (see Section 1.3.2). In a heuristic approach, the mechanism and important results of this transition are given in the formalism of the rotor XY model.

The solution of the Hamiltonian of Eq. (1.16) in the low temperature phase (Eq. (1.20)) does not exhibit any phase transition. This result is due to the harmonic approximation which does not account for the invariance under the local transformation  $\theta_i \rightarrow \theta_i \pm 2\pi$ . This assumption is correct at low temperatures, and at a scale large enough, the topology of the field for any closed path  $\mathcal{C}$  satisfies

$$\oint_{\mathcal{C}} \vec{\nabla}\theta(\vec{r}) \cdot d\vec{l} = 0. \quad (1.21)$$

This assumption is however not satisfied at higher temperatures. This can be interpreted by the presence of defects, called vortices. A vortex is a topological defect in which the orientation winds by  $\pm 2\pi$  (see Fig. 1.3). For a closed path  $\mathcal{C}$  surrounding a vortex

$$\oint_{\mathcal{C}} \vec{\nabla}\theta(\vec{r}) \cdot d\vec{l} = 2\pi q, \quad (1.22)$$

where  $q$  is called the winding number of the vortex, and  $q = \pm 1$  for simple vortices. The appearance of vortices at low temperature can be shown by the famous free-energy argument of Kosterlitz and Thouless [13, 14]. At a large distance  $r$  from the center of the vortex

$$\left| \vec{\nabla}\theta(\vec{r}) \right| = \frac{1}{r}, \quad (1.23)$$

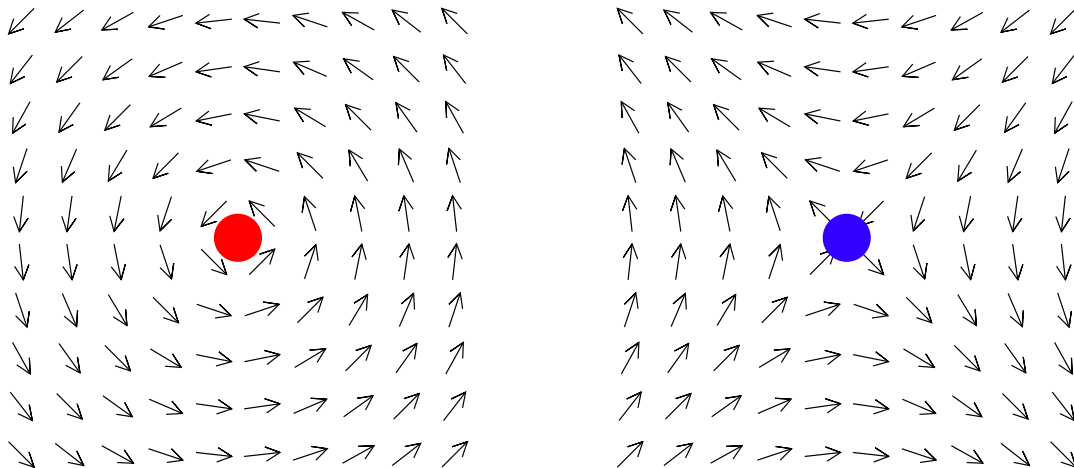


**Figure 1.4:** Vortices in the XY model, the orientation winds by  $2\pi$  for a path around the vortex. *Left:* Positive vortex, the winding number is  $q = 1$  (see Eq. (1.22)). *Right:* Negative vortex, the winding number is  $q = -1$  (see Eq. (1.22) again).

The winding number is zero for a superposition of a  $q=1$  and a  $q=-1$  vortex.

in a system of size  $L$ , the total energy of a single vortex is then

$$E_v = \frac{1}{2}J_R \int_a^L 2\pi r \frac{1}{r^2} dr + E_c \quad (1.24)$$

$$= \pi J_R \ln \frac{L}{a} + E_c \quad (1.25)$$

where  $E_c$  is the core energy of the vortex. The vortex can be placed at any position, and therefore the entropy added by the presence of a single vortex is

$$S_v \sim k_B \ln \frac{L^2}{a^2}, \quad (1.26)$$

which scales in the same way as the energy. The free energy cost due to the presence of a single vortex is therefore

$$F_v = E_v - TS_v \\ \sim \left( \pi J_R - \frac{2}{\beta} \right) \ln \frac{L}{a}. \quad (1.27)$$

For  $\beta J_R > 2/\pi$ ,  $F_v \rightarrow \infty$  as the system size is increased, the presence of a single vortex is therefore not possible (confirming the hypothesis of Eq. (1.21)). The phase thus shows an algebraic correlation function, as expected. For  $\beta J_R < 2/\pi$ ,  $F_v \rightarrow -\infty$  as the system size is increased, therefore the vortices are present and disrupt the orientation. As a consequence, the phase shows short-range order. Therefore, a phase transition takes place at<sup>3</sup>

$$\beta_{\text{KT}} J_R = \frac{2}{\pi}. \quad (1.28)$$

---

<sup>3</sup>This relation explains the universal jump of the superfluid density ( $\rho(T_{\text{KT}})/T_{\text{KT}} = 2m^2/\pi\hbar^2$ ) at the transition seen in 2D superfluids [58].

This result does not give the exact value of the transition temperature, as the renormalized spin stiffness  $J_R$  is not known. However, it yields the exponent  $\nu$  of the correlation function: Eq. (1.20) and Eq. (1.28) show that for  $T = T_{KT}$ ,

$$C(r) \sim r^{-\nu}, \quad \text{with } \nu = 1/4. \quad (1.29)$$

As this value does not depend on  $J_R$ , and therefore not on the microscopic model, it is universal. This value is important as it can, in principle, be measured in simulations [52] or experiments [57]. However, it should be stressed that this behavior is only exact at large distances. At shorter distances, logarithmic corrections should be included [59].

The behavior of the system near the transition is understood by the analysis of the system of interacting vortices. Two vortices of winding number  $q_i$  and  $q_j$  interact through a logarithmic potential

$$U_{ij}(r_{ij}) = -\pi J_R q_i q_j \ln\left(\frac{r_{ij}}{a}\right) + 2E_c \quad (1.30)$$

where  $r_{ij}$  is the distance between the vortices. Vortices with opposite winding numbers are attracted while those with the same repel each other. This potential is identical to the electrostatic interaction in 2D. The interacting vortices thus behave as a 2D Coulomb gas. The Hamiltonian of the system has two parts. The first is due to the harmonic fluctuations of the orientation (spin waves), and the second is due to the interaction between the vortices,

$$H = \frac{1}{2} J_R \int [\vec{\nabla}\theta(\vec{r})]^2 d^2r + \sum_{ij} U_{ij}(r_{ij}). \quad (1.31)$$

Kosterlitz and Thouless [13, 14] analyzed this Hamiltonian near the transition with a renormalization method, which compute the evolution of  $J_R$  as the scale is increased. The main results are presented below.

### Low-temperature phase

For  $T < T_{KT}$ , the presence of a single vortex is prohibited as shown by the free-energy argument of Eq. (1.27). However, two vortices with opposite charge do not disrupt the orientation (see Fig. 1.3), the presence of vortices bound in pairs is therefore possible. A pair of vortices disrupts the orientation on a scale of the order of their distance of separation, the interaction between two vortices is therefore logarithmic with this distance and satisfies Eq. (1.30). The pairs of vortices are thermally created with a typical distance of separation given by a Boltzmann factor  $\exp -\beta E_{\text{pair}}$ . At scales above the typical distance of separation, the field is defect free, and the pairs only renormalize  $J_R$ . A renormalization treatment [13, 14] gives that in the vicinity of the transition, the spin stiffness at the largest scales shows a cusp: for  $T \lesssim T_{KT}$ ,

$$J_R(T) = J_R(T_{KT}^-) [1 + \text{const.}(T_{KT} - T)^{1/2}]. \quad (1.32)$$

This yields for the correlation function at large distances

$$C(r) \sim r^{-\nu} \quad \text{with } \nu = \frac{1}{4} [1 - \text{const.}(T_{KT} - T)^{1/2}]. \quad (1.33)$$

As for the exponent  $\nu = 1/4$ , the behavior of the correlation function near the transition, for example the value of the exponent  $1/2$  of  $(T_{\text{KT}} - T)^{1/2}$ , can be studied in simulations [52]. However, the temperature range and length scales in which Eq. (1.32) and Eq. (1.33) hold are not clear.

### High-temperature phase

For  $T > T_{\text{KT}}$ , free vortices are present, their density  $n_f$  increases from zero at the transition to a finite value at a higher temperature. As vortices destroy the orientational order, the correlation function decays exponentially with a correlation length corresponding to the typical distance between the free vortices:

$$C(r) \simeq \exp -r/\xi \quad \text{with} \quad \xi = \frac{1}{\sqrt{n_f}}. \quad (1.34)$$

The phase is thus disordered. The renormalization treatment [13, 14] shows that for  $T \gtrsim T_{\text{KT}}$ ,

$$\xi \propto \exp \left( \text{const.} |T - T_{\text{KT}}|^{-1/2} \right). \quad (1.35)$$

The correlation length in the disordered phase increases exponentially as the transition temperature is approached, which is faster than for any second order transition [36]. The behavior of the correlation length near the transition can be used in simulations [52, 24] or experiments [60]. However, the temperature range in which this behavior is valid is not clear.

As the system is short ranged, subsystems separated from a distance larger than the correlation length can be considered independent of each other. Therefore, the renormalized spin stiffness  $J_{\text{R}}$  goes to zero at large scales. Thus,  $J_{\text{R}}$  changes discontinuously at the transition from  $J_{\text{R}}(T_{\text{KT}}^-) = 2k_{\text{B}}T_{\text{KT}}/\pi$  to  $J_{\text{R}}(T_{\text{KT}}^+) = 0$ . This should not be interpreted as a first order transition since the correlation lengths at the transition are infinite.

The KT transition is a continuous transition which occurs in 2D systems. This theory relies on the assumption that the low-temperature phase stays ordered up to the unbinding of vortices. The transition temperature  $T_{\text{KT}}$  therefore constitutes an upper bound for the transition. This point is explained in Section 1.2.4 and is important to understand when studying the melting of hard disks in Chapter 4.

The assumption of vortex unbinding is correct for the 2D rotor XY model, and a KT transition occurs in this system [61]. The correlation length at the transition (and at lower temperatures) is infinite. Therefore, the system is prone to critical slowing down and finite-size effects. Moreover, the theoretical predictions give asymptotic behavior. In order to study the KT transition in a real finite-size system, we perform simulations on the 2D rotor XY model. This work intends to understand the typical phenomena that could be observed in the melting of hard disks (see Chapter 4).

### 1.2.3 Simulations of the 2D rotor XY model

As shown later in Section 1.3.2, the melting of 2D particle systems is possibly related to KT transitions. The 2D rotor XY model constitutes a toy model in order to study the properties of this transition in a real system.



As for the melting of 2D solids, the nature of the transition of the 2D rotor XY model has long been debated [51, 52]. The transition was expected to be either first order or of the KT type. Monte Carlo simulations allow one to numerically study the thermodynamics of a system by sampling configurations with the appropriate Boltzmann distribution (see Section 2.1.2). However, this sampling can be slow to achieve for systems with large correlation lengths, as is often the case in 2D. The debate ended with the discovery of a set of new algorithms [53, 54], referred to as spin-cluster algorithms, which are able to flip large clusters of spins in the same time, reaching thermodynamic equilibrium much faster than with previous algorithms. It is now agreed that the transition follows a KT scenario. The inverse transition temperature of  $\beta_{\text{KT}}J = 1.1199(1)$  is known precisely [62].

To illustrate the finite-size effects in this model, we performed simulations in a system of  $N$  spins on a square lattice of size  $L = \sqrt{N}$  with periodic boundary conditions at a constant temperature. We used the Wolff algorithm [54] as it is the fastest algorithm for this system. Fig. 1.4 shows a method to visualize a snapshot of the system, inspired by what is done in Ising systems. The direction of the total orientation (magnetization) was computed through

$$\vec{M} = \sum_{i=1}^N \vec{S}_i. \quad (1.36)$$

The spins were then colored depending on their orientation toward the total orientation, which was computed by  $\cos \alpha$ ,  $\alpha = \text{angle}(\vec{S}_i, \vec{M})$ . Spins pointing toward the main orientation are colored in white, whereas spins pointing in the opposite direction are colored in black. By using this visualizing method, the output is easy to interpret, despite not being able to differentiate between two directions which are symmetric toward the main direction. The vortices were then localized by computing the winding number around each inter-space of the lattice. The negative vortices are shown in blue while the positive ones are shown in red.

In the low-temperature phase, the system is oriented (see Fig. 1.4). Given an infinite system, this orientation would tend to zero. In practice however, the system is oriented in a finite sample. This is shown by the slow algebraic decay of the correlation function (see Fig. 1.5). As predicted, the vortices are tightly bound in pairs (see Fig. 1.4). The system is scale free, therefore the size of the largest clusters scale in the same way as the system size. The value of the exponent  $\nu$  can be fitted from the correlation function.

In the high-temperature phase, the total orientation is  $M = 0$  for a system larger than the size of the largest clusters (see Fig. 1.4). The short-range order is confirmed by the correlation function, which decays exponentially. The correlation length can be extracted from a fit in the pure exponential part seen at large distances (see Fig. 1.5). The size of the largest clusters is related to the correlation length. At  $\beta J = 0.9$ , the largest clusters of the same orientation have a size  $\simeq 10a$ , which agrees with the correlation length measured on the correlation function (see Fig. 1.4 and Fig. 1.6). Because of the periodic boundary conditions, the total winding number is always zero. However, at  $\beta J = 0.9$  for example, vortices are not bound in close pairs. One way to show that vortices are free is to compute the vorticity (winding number) on a path of increasing size  $l$ . In the case of bound pairs, the path breaks  $\propto l$  pairs, therefore, the total vorticity behaves as  $w \propto \sqrt{l}$ . On the other



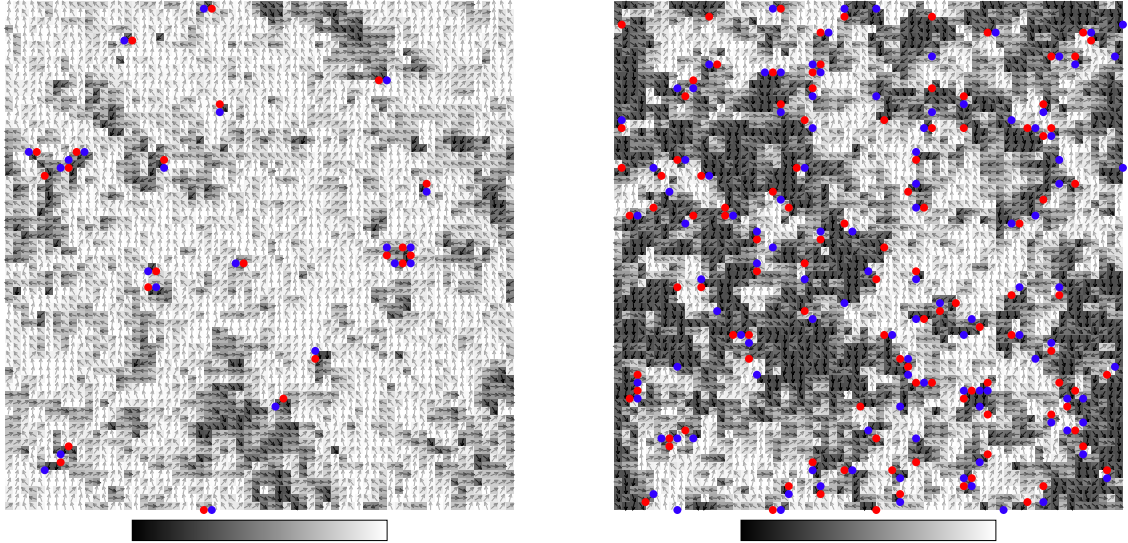


**Figure 1.5:** Two 2D rotor XY-model configurations of  $64^2$  spins near the transition. Spins pointing in the main direction are printed in white, while spins in the opposite direction are printed in black. Positive vortices are shown by a red dot, and negative vortices by a blue dot. *Left:*  $\beta_{\text{KT}} = 1.12$  ( $T \simeq T_{\text{KT}}$ ), the system is oriented. Pairs of vortices are all closely bound. *Right:*  $\beta_{\text{KT}} = 0.9$  ( $T > T_{\text{KT}}$ ), the total orientation is zero. Some vortices are free, and the largest clusters have a typical size  $\xi \simeq 10a$  which corresponds to the correlation length.

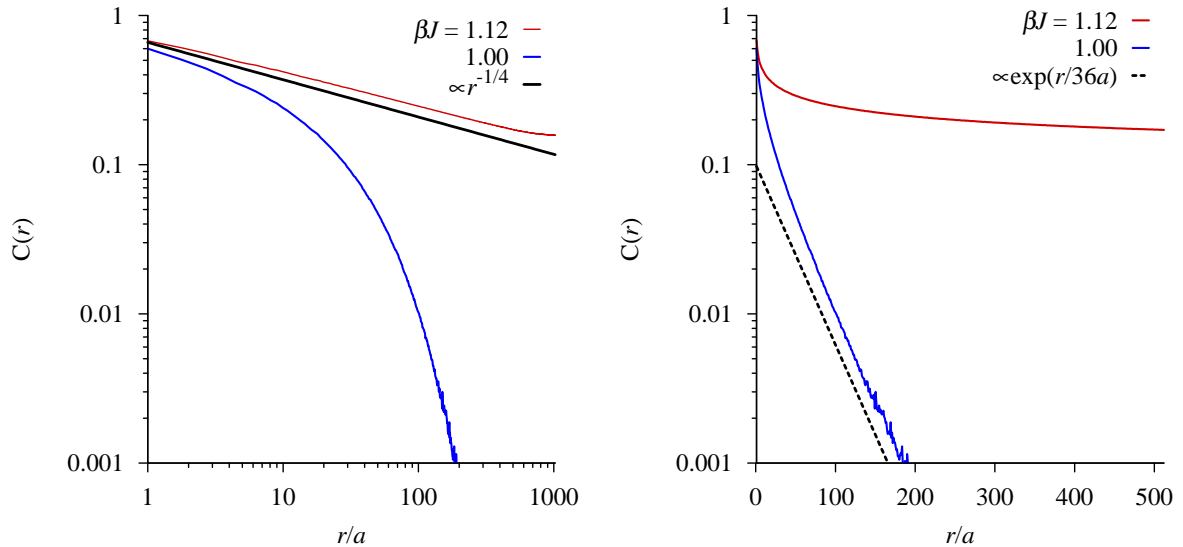


**Figure 1.6:** Correlation functions of the 2D rotor XY model for  $T > T_{\text{KT}}$  and  $T \simeq T_{\text{KT}}$  in the planar rotor XY model. *Left:* Log-log view. At  $\beta J = 1.12$ , the system shows a quasi-long-range order with a coefficient close to  $1/4$ , although different. This is due to neglected logarithmic corrections as well as finite-size effects. *Right:* Semi-log view. At  $\beta J = 1.00$  the system shows a short-range order with a correlation length  $\xi/a \simeq 36$

hand, in the case of free vortices, the number of vortices inside the closed path is  $\propto l^2$ , giving a vorticity  $w \propto l$ .

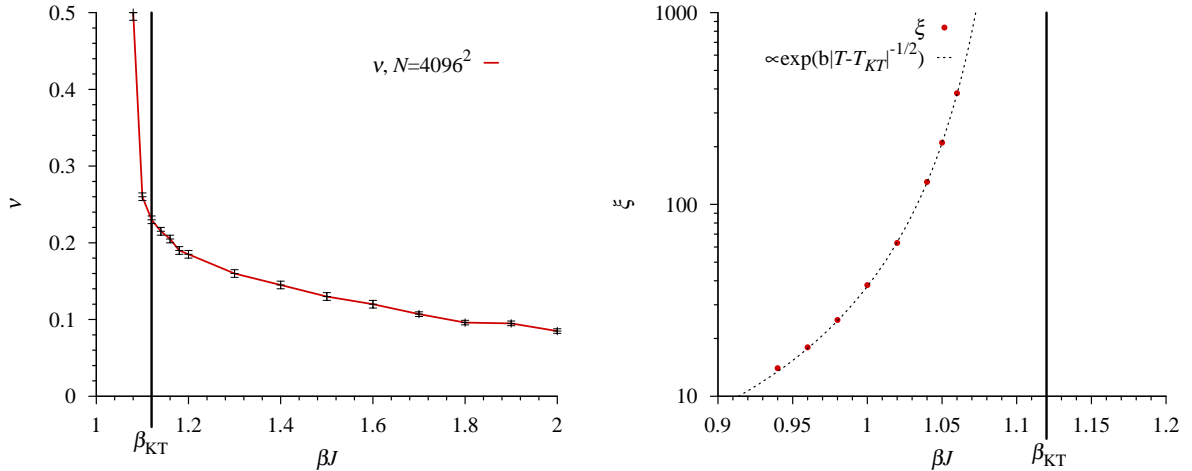


**Figure 1.7:** Behavior near the transition for the 2D rotor XY model computed in a system of  $4096^2$  spins. *Left:* Temperature dependence of the coefficient of the algebraic correlation function. A cusp can be seen. The transition exponent is  $\nu_{KT} \simeq 0.23$ , which is close to  $1/4$ , although different. The difference is due to neglected logarithmic corrections. *Right:* Temperature dependence of the correlation length. The behavior predicted by the KT theory is seen.

## Determination of the temperature transition

The temperature transition of the 2D rotor XY model is precisely known. Hasenbusch [62] showed, by mapping the XY model on the body-centered-solid-on-solid (BCSOS) model, which is analytically solvable, and using a Monte Carlo renormalization group method, that  $\beta_{KT} = 1.1199(1)$ . Although this result was obtained with small lattice sizes ( $L < 256$ ), this method avoided the problem of the logarithmic corrections [59]. The extremely precise results obtained with this method have been confirmed by standard finite-size scaling analysis [61].

The method used to precisely determine the value of  $\beta_{KT}J = 1.12$  is not easily transportable to 2D melting. The behavior of the correlation length near the transition is surprisingly close to what is predicted by the theory (see Fig. 1.6). However, other values of  $\beta_{KT}$  and of the constant  $b$  also give good fit. Therefore, the behavior of the correlation length is hardly useful to determine the transition value.

Near the transition, the exponent  $\nu$  of the algebraic correlation function seems to show a cusp, as predicted by the theory. However, the finite size of the system smooths the cusp, and a fit is therefore not relevant. At the transition, the exponent is found to be  $\nu_{KT} = 0.23$ , which is close to the expected value  $1/4$ , although different. This difference is due to neglected logarithmic corrections [59] and to finite-size effects. The  $1/4$  exponent can therefore only be used to approximately locate the transition.

## Finite-size effects

Most numerical simulations are performed in finite systems. In order to obtain the property of the system at the thermodynamic limit ( $N \rightarrow \infty$ ), one must account for the finite-size effects. In the perspective of studying the melting transition (see Chapter 4),

it is interesting to observe the behavior of finite-size effects in this model, and especially for a temperature below the transition where the correlation length is infinite.

In the high-temperature phase, the correlation length  $\xi$  corresponds to the maximum length scale of the system. For a system whose size  $L$  is larger than  $\xi$ , an observable  $\mathcal{O}$  typically reaches its thermodynamic-limit value  $\mathcal{O}_\infty$  exponentially with  $L$ :

$$\mathcal{O}_L - \mathcal{O}_\infty \underset{L \gg \xi}{\sim} \text{const. exp} -L/\xi. \quad (1.37)$$

Fig. 1.7 shows the correlation function at a temperature above  $T_{\text{KT}}$  for different system sizes. The finite-size effects can be seen at the end of the function in a region of length  $\sim 40a$  which corresponds to the correlation length. Also, the finite-size effects are small as the size is increased. In this phase, the thermodynamic-limit behavior is reached, for all practical purpose, in systems a few times larger than the correlation length.

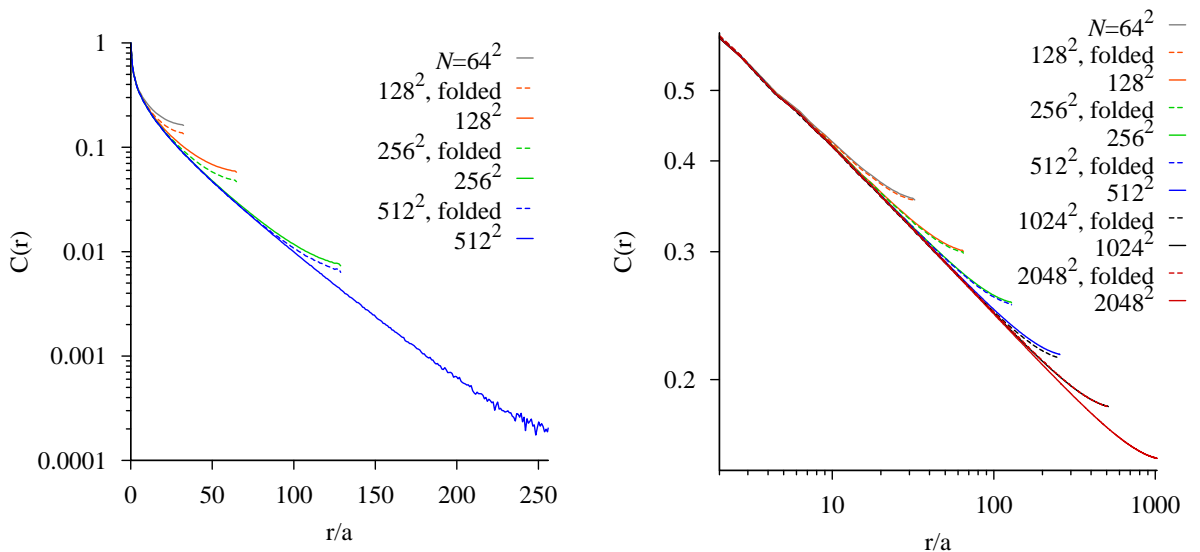


**Figure 1.8:** Finite-size effect on the correlation function of the 2D rotor XY model for  $T > T_{\text{KT}}$  and  $T \simeq T_{\text{KT}}$ . *Left:* At  $\beta J = 1.00$ , the effect is localized on a scale of  $\sim 40a \simeq \xi$ , and decreases exponentially with system size. Simulations must be larger than the correlation length. *Right:* At  $\beta J = 1.12$ , the finite-size effect is scale free. It is seen on region for  $r > L/4$  and is well understood by the selection of modes.

In the low-temperature phase, the correlation length is infinite. Therefore, it is essential to understand finite-size effects. As shown in Fig. 1.7, the finite size in the low temperature region affects the correlation function for  $r > L/4$  (that is, half of the function computed), and the effect is independent of the system size. This shows that little information is lost by reducing the system size. A naive finite-size model for the correlation function confirms this assumption. Let  $C_L(\vec{r})$  be the correlation function in a square box of size  $L$  under periodic boundary conditions.  $C_L$  can be expanded in Fourier components

$$C_L(\vec{r}) = \frac{1}{L^2} \sum_{\vec{k}} \tilde{C}_L(\vec{k}) \exp(i\vec{k} \cdot \vec{r}) \quad \text{with} \quad k_i = n_i \frac{2\pi}{L}, \quad n_i \in \mathbb{Z}, \quad (1.38)$$

which gives, in the infinite limit, the Fourier transform

$$C_\infty(\vec{r}) = \frac{1}{(2\pi)^2} \int \tilde{C}_\infty(\vec{k}) \exp(i\vec{k} \cdot \vec{r}) d^2k. \quad (1.39)$$

We assume that the finite box selects the allowed modes without changing their weights, that is  $\tilde{C}_L = \tilde{C}_\infty$  (except for the  $\vec{k} = \vec{0}$  mode which is determined by  $C_L(\vec{0}) = 1$ ). This assumption is strictly equivalent to assuming that  $C_L$  is the sum of all images of  $C_\infty$  in the periodic space:

$$C_L(\vec{r}) = \sum_{\vec{N}} C_\infty(\vec{r} - \vec{N}) + \text{const.} \quad \text{with} \quad N_i = n_i L, n_i \in \mathbb{Z}. \quad (1.40)$$

This gives a relation between the correlation function in a system of size  $L$  and a system of size  $L/2$ :

$$C_{L/2}(\vec{r}) = \sum_{\vec{N}} C_L(\vec{r} - \vec{N}) + \text{const.} \quad \text{with} \quad N_i = \{0, L\}. \quad (1.41)$$

A way to test the naive finite-size model is therefore, as in Eq. (1.41), to “fold”  $C_L$  on itself and compare it to  $C_{L/2}$ . In the low-temperature region, the folded  $C_L$  almost matches  $C_{L/2}$ , whereas this is not the case in the high-temperature region (see Fig. 1.7). This assumption of mode selection is therefore a good approximation for finite-size effects in the XY model but only in the low-temperature (harmonic) phase. This result shows that properties of a phase whose correlation length is infinite can be obtained from a finite-size simulation. This is of interest for the study of the melting transition in Chapter 4.

## 1.2.4 Non-universality of the transition

In higher spatial dimensions, renormalization theory [2] suggests that the nature of the transition in spins systems does not depend upon the microscopic model. Rather, it depends solely upon the dimension and the degree of symmetry of the system. This property is called strong universality. In 2D systems, the strong universality is broken, as can be seen in the different XY models.

As discussed in Section 1.2, it was not expected that the transition in the 2D rotor XY model was necessarily of the KT type, the transition could have been first order [51]. A phase transition is said to be first order (see Section 1.3.1) when the system changes from one phase to the another discontinuously. This transition has the particularity that the phase in the disordered region has a finite correlation length at the transition point. In a continuous transition (as the KT transition or a second-order transition), the correlation length becomes infinite at the transition. A first-order transition is therefore referred to as “weak” when the correlation lengths (in unit of lattice spacing) are large, and “strong” when they are comparable to the atomic dimensions.

In order to understand the validity of the KT theory, we examine its assumptions. The KT theory predicts a transition mechanism between a phase whose correlation function is algebraic and a disordered phase. The existence of the algebraic phase is not debated as the harmonic approximation becomes exact for any microscopic model in the limit of low temperatures. Under the condition that the harmonic approximation is still valid up to the vortices unbinding, the renormalization treatment of the transition is correct

and does not introduce any other assumptions. The KT theory is thus built on the assumption that the low-temperature phase remains stable up to the vortex-unbinding transition. While the temperature  $T_{\text{KT}}$  yields an upper limit for the stability of the algebraic low-temperature phase, a transition at a lower temperature can preempt the KT transition.

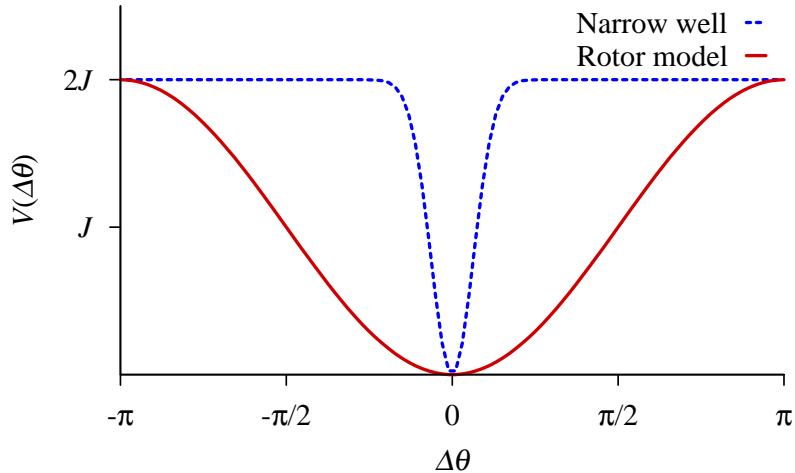


**Figure 1.9:** Interactions of neighboring spins  $i$  and  $j$  as a function of  $\Delta\theta = \theta_j - \theta_i$  for different 2D XY models. For the rotor model (red curve), the low-temperature phase is stable up to the vortex unbinding: the transition is of the KT type. For potentials with a narrow well around 0 (blue dashed curve), the stiffness at large scales is high enough for the KT transition to be preempted by a first-order transition.

Indeed, Domany et al. [63] showed that the KT theory breaks down in the XY model for specific interactions. In XY models, two neighboring spins  $i$  and  $j$ , whose angles are  $\theta_i$  and  $\theta_j$ , interact through a  $2\pi$ -periodic potential  $V(\Delta\theta)$ , where  $\Delta\theta = \theta_j - \theta_i$ . In the case of the 2D rotor model, the potential is  $V(\Delta\theta) = J(1 - \cos(\Delta\theta))$ , which shows a large well around  $\Delta\theta = 0$  (see Fig. 1.8). Domany et al. performed simulations on potentials with a narrow well around  $\Delta\theta = 0$  (see Fig. 1.8 again), and found that the transition was not of the KT type, rather it was first order.

This result can be understood as follows: The depth of the potentials in Fig. 1.8 fixes an energy scale  $\sim 2J$ . For a temperature  $k_B T \gg J$ , the phase is necessarily disordered as the thermal energy of a spin is higher than this energy scale. This ensures that if the phase is still ordered, a discontinuous transition toward disorder occurs around  $k_B T_{1st} \propto J$ . Moreover, in the KT theory the vortex-unbinding transition occurs at  $k_B T_{\text{KT}} = J_R \pi/2$ . Therefore, there is competition between

$$T_{\text{KT}} \propto J_R \quad \text{and} \quad T_{1st} \propto J. \quad (1.42)$$

In the “narrow-well” potential of Fig. 1.8, neighboring spins are strongly attracted for short fluctuations of  $\theta$ , the rigidity of the system at low temperature is thus increased. As the width of the well goes to zero, one has  $J_R \gg J$ , and therefore  $T_{\text{KT}} \gg T_{1st}$ . This behavior is similar to the crossover from second-order to first-order transition in the  $q$ -state Potts model as the number of state  $q$  is increased, this can be interpreted as a vacancy condensation [64].

Following this argument, it is even possible that two successive transitions occur in this system. First, a KT transition where the quasi-long-range ordered phase continuously changes into a short-range ordered phase. Second, a first-order transition where the short-range ordered phase discontinuously turns into another short-range ordered phase (as in liquid-gas transition). A similar first-order transition between two short-ranged ordered phases has been observed in the 2D Heisenberg model (0(3) symmetry) [65] and confirmed [66]. The absence of strong universality is thus observed in 2D systems, and in 2002, van Enter and Shlosman [66] proved it for the 2D Heisenberg model. This result for lattice systems suggests that the melting transition in 2D particle systems is also not universal, and that KT transitions can be preempted by first-order transitions. This is the case in the melting of hard disks in Chapter 4 (see Section 4.1).

## 1.3 Scenarios for two-dimensional melting

We now examine the case of 2D particle systems. The melting transition in these systems is more complex than for lattice systems, and it is the subject of a long-standing debate [17, 18]. In this section, the principal theories are presented. One is a classic first-order transition, and the other one follows the ideas of Kosterlitz and Thouless. This section exposes elements needed to understand the results of the hard-disk model in Chapter 4.

### 1.3.1 First-order transition

A transition is said to be first order when the system changes from one phase to another discontinuously. In 3D and higher, solids generally melt through a first-order transition. In two dimensions, the question is open. In hard disks, the loop seen in the equation of state of Alder and Wainwright was first interpreted as a classic first-order transition. In Chapter 4, we will see that a first-order transition indeed occurs in the melting of hard disk, between a liquid and a “hexatic” phase (see Section 4.1).

A first-order transition has the particularity to show a phase coexistence given an appropriate thermodynamic ensemble. For example, a first-order transition in a  $XY$  model shows a phase separation in the microcanonical  $(N, E)$  ensemble. This is a result of the energy per particle of both phases being different. For 3D hard spheres [49], the system is phase-separated at the transition in the constant-density ensemble  $(N, V, T)$ . Indeed, the densities of both phases are different. This phenomenon is understood by the concavity of the free energy  $F_{\text{pure}}(V)$  that a scenario without phase separation would have (see Fig. 1.9).

For a specific volume  $v = V/N$  between two limiting values  $v_1$  and  $v_2$  (as in Fig. 1.9), the free energy per particle  $f = F/N$  is lowered through a phase coexistence:

$$f_{\infty}(v) = f(v_1) + n_2[f(v_2) - f(v_1)] < f_{\text{pure}}(v), \quad n_2 = \frac{v - v_1}{v_2 - v_1} \in [0, 1] \quad (1.43)$$

where  $n_2 = N_2/N$  is the proportion of phase 2, and  $n_1 = N_1/N = 1 - n_2$  is the proportion of phase 1.

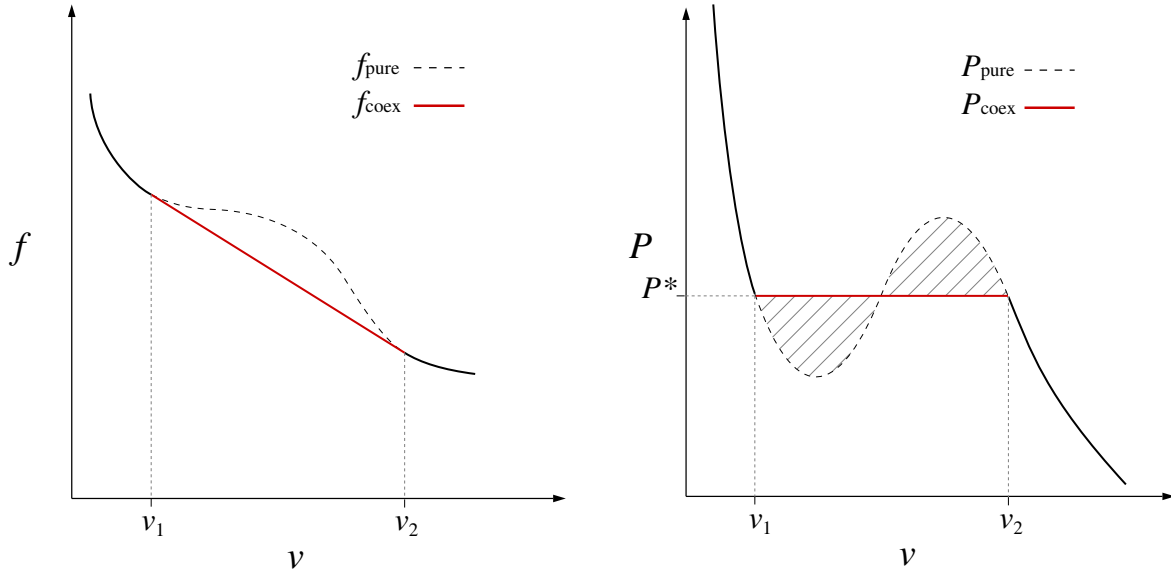


**Figure 1.10:** *Left:* Schematic free energy as a function of the specific volume for a particle system underlying a first-order transition. The concavity of the energy induces a phase separation. *Right:* Pressure *vs.* specific volume obtained by integration of  $f(v)$ . For  $v_1 < v < v_2$  two phases coexist. The dashed loop is thermodynamically unstable.

The pressure, defined as  $P = -\partial f / \partial v$ , would show a loop only if the system was kept pure<sup>4</sup>. This is known as a “van der Waals loop”. This loop is thermodynamically unstable as shown by minimization of the free energy. The pressure takes instead a constant value  $P^*$  in the coexistence region.  $P^*$  can be determined directly from the  $P(v)$  curve by equalizing the areas of the loop below and above  $P^*$  (dashed areas in Fig. 1.9) as  $P(v)$  must satisfy

$$\int_{v_1}^{v_2} P(v) dv = f(v_1) - f(v_2) = \text{const.} \quad (1.44)$$

This is known as the “Maxwell construction”. This construction allows computation of the value of the pressure at the transition  $P^*$  as well as the densities of the coexisting phases. This method has been used in Chapter 4 to study a first-order transition (see Section 4.1.2).

In a constant-pressure ensemble  $(N, P, T)$ , the system shows no phase coexistence in equilibrium, it jumps directly from a phase to the other at  $P = P^*$ . However, if  $P \simeq P^*$ , the time needed to switch from one phase to the other can be large because of the free energy needed to form an interface during the switch. As a consequence, the pure-phase branches are metastable: a constant-pressure simulation would explore them, and an hysteresis around  $P^*$  would be found as the pressure is increased or decreased.

The above results for a first-order transition (finite correlation length, phase coexistence, and hysteresis) can be obtained in computer simulations and are specific to a first-order transition. The finite-size effects can however make discriminating between a weak first-order transition (large correlation length) and a continuous transition difficult in practice. Alder and Wainwright [9], and many authors since them, observed a pres-

<sup>4</sup>The loop is not necessarily continuous as the two phase can show different symmetries for example.



sure loop in constant-density simulations. This has been interpreted as the existence of a first-order transition. This loop, which does not correspond to a van der Waals loop, has been theoretically explained by Mayer and Wood [67] as the effect of the interface tension (see Section 4.1.2). The transition in 2D systems was considered as a classic first order up until Kosterlitz and Thouless presented their continuous scenario.

### 1.3.2 The KTHNY theory

The KT theory of Kosterlitz and Thouless described for the XY model in Section 1.2.2 has also been originally developed for the melting of 2D solids [13]. In this case, the solid-liquid transition is ruled by unbinding of the topological defect of the positional order: the dislocations. This theory was completed by Nelson and Halperin [32, 68], as well as Young [69]. They noticed that the unbinding of dislocations did not lead to the disordered liquid phase but to a new phase, called hexatic. In the hexatic phase the positional order is short ranged and the orientational order is quasi-long ranged. The transition from the hexatic to the liquid is again a KT transition, ruled by the unbinding of the topological defects of the orientation: the disclinations. This two-stage melting theory is referred to as the Kosterlitz-Thouless-Halperin-Nelson-Young (KTHNY) theory. Later, various first-order scenarios, based on unbinding of grain boundary, vacancies condensation, or simultaneous unbinding of dislocation and disclination, were considered [70, 71, 72, 73].

In Chapter 4, we show that the melting transition for hard disks follows a two-stage scenario with a hexatic phase. The solid-hexatic transition is of the KT type, and the liquid-hexatic transition is first order. The following reviews the principal results of the KTHNY theory, which are similar to the results of the KT transition developed in the XY model.

	Solid	Hexatic	Liquid
Position	Quasi-long	Short	Short
Orientation	Long	Quasi-long	Short

**Table 1.1:** Positional and orientational ordering in the KTHNY theory.

#### The solid phase

In the low-temperature phase of the 2D solid, the harmonic approximation can be made. The solid phase has then the same property as the harmonic solid: long-range orientational order and quasi-long-range orientational order. The qualitative argument given for the harmonic solid is quantitatively developed with the theory of elasticity [26] for an isotropic medium, whose lattice is triangular (the most common lattice of 2D solids).

Let  $\vec{u}(\vec{r})$  be the displacement field of the solid. The strain tensor is given by

$$u_{ij}(\vec{r}) = \frac{1}{2}(\partial_i u_j + \partial_j u_i) \quad i, j \in \{1, 2\}, \quad (1.45)$$

which is linearly related to the stress tensor. In an isotropic medium, the stress and strain tensors are related by two elastic coefficients  $\lambda$  and  $\mu$ :

$$\sigma_{ij} = 2\mu u_{ij} + \lambda \delta_{ij}(u_{11} + u_{22}). \quad (1.46)$$



$\lambda$  and  $\mu$  are the Lamé elastic coefficients, and  $\mu$  is the shear modulus. The Hamiltonian is then

$$H_{\text{sol}} = \frac{1}{2} \int \sum_{i,j} (2\mu u_{ij}^2 + \lambda u_{ii}^2) d^2r. \quad (1.47)$$

The positional correlation function of Eq. (1.9) can be computed for a triangular lattice in the limit of large distances [32],

$$C_{\vec{K}}(r) \propto r^{-\nu_K} \quad \text{with} \quad \nu_K = \frac{k_B T |K|^2}{4\pi} \frac{3\mu + \lambda}{\mu(2\mu + \lambda)}, \quad (1.48)$$

where  $\vec{K}$  is a vector of the reciprocal lattice. The correlation function is again algebraic, its coefficient is principally determined by the shear modulus. The first Bragg peak of a triangular lattice satisfies  $|K| = \frac{4\pi}{a_0\sqrt{3}}$ ,  $a_0$  being the lattice spacing. The coefficient  $\nu_K$  is then

$$\nu_K = \frac{k_B T 4\pi (1 + \sigma)(3 - \sigma)}{3a_0^2 \mathcal{E}}, \quad (1.49)$$

where  $\mathcal{E}$  and  $\sigma$  are the 2D Young's modulus and Poisson's ratio, respectively.<sup>5</sup>

As for the harmonic solid, the orientation is long-range ordered. The structure factor at a Bragg peak shows

$$S(\vec{K}) \propto L^{2-\nu_K} \quad \text{and} \quad S(\vec{k}) \propto 1/|\vec{k} - \vec{K}|^{2-\nu_K}, \quad (1.50)$$

the diffraction pattern is then a lattice of Bragg peaks whose shape is a power law instead of  $\delta$ -functions for long-range-ordered solids.

### Solid hexatic transition

This solution of Eq. (1.48) does not exhibit a phase transition, as the bonds between the atoms are supposed not to break. A lower temperature, this assumption is not valid and defects such as dislocations appear. The scenario of vortex unbinding in the XY model or 2D-superfluid can be transferred directly to the melting of the solid phase with the dislocations playing the role of the vortices. A dislocation is a topological defect of the lattice. It can be interpreted as a missing or an extra row of disks starting from the defect. This defect is defined by its Burgers vector. Let us consider a path around the defect which would be closed in a perfect lattice. The Burgers vector is defined as the vector by which this path fails to close (see Fig. 1.10).

The same free-energy argument of Section 1.2.2 is developed with the dislocations instead of the vortices. A dislocation deforms the system; it requires elastic energy. At a distance  $r$ , the deformation is  $u_{ij} \propto 1/r$ , a similar calculus to the vortex energy gives the energy of a single dislocation (with a Burgers vector  $|\vec{b}| = a_0$ ) in a system of size  $L$  [74],

$$E_{\text{disloc}} = \frac{a_0^2}{16\pi} \mathcal{E} \ln \frac{L^2}{a_0^2} + E_c. \quad (1.51)$$

---

<sup>5</sup>In an isotropic 2D system, these moduli can be expressed through the elastic constants as  $\mathcal{E} = 4\mu \frac{\lambda + \mu}{\lambda + 2\mu}$  and  $\sigma = \frac{\lambda}{\lambda + 2\mu}$ .

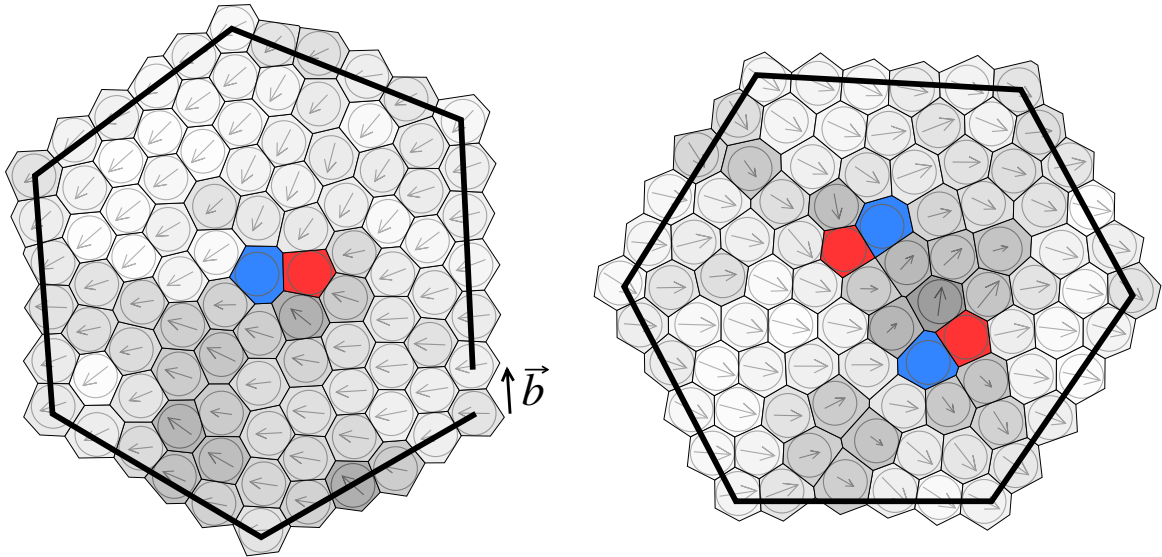


**Figure 1.11:** Dislocations in hard disks. Disks with five and seven neighbors are in red and blue respectively (neighbors are defined by the Voronoi construction (see Section 3.3.1) the local orientation is shown by vectors which represents  $\Psi$  (see Eq. (1.65) and Section 3.3.1 again) *Left:* A free dislocation. A path around the defect, which would be closed in a perfect lattice, fails to close by  $\vec{b}$ . The deformation field spreads over the entire system, and an infinite elastic energy is necessary to create a single dislocation. The orientation is not disrupted. *Right:* A bound pair of dislocations, the lattice is only locally stressed, the elastic energy is finite.

where  $E_c$  is the core energy. As for the vortices again, the dislocation can be placed at any position, the entropy added by its presence is then

$$S_{\text{disloc}} \simeq k_B \ln \frac{L^2}{a_0^2}, \quad (1.52)$$

which scales in the same way as the energy. The free energy cost due to the presence of a single dislocation for a large system is therefore

$$F_{\text{disloc}} \simeq \left( \frac{a_0^2}{16\pi} \mathcal{E} - k_B T \right) \ln \frac{L^2}{a_0^2}. \quad (1.53)$$

The solid then melts at

$$k_B T_m = \frac{a_0^2}{16\pi} \mathcal{E}. \quad (1.54)$$

Below this temperature, the dislocations are bound in pairs (or other structures with a zero Burgers vector) which does not disrupt the positional order (see Fig. 1.10). Above  $T_m$ , the dislocations are free, and thus disrupt the positional order.

The argument developed here can be extended to hard disks, even though temperature plays no role in this system. Indeed, Young's modulus  $\mathcal{E}$  depends upon temperature and density (or pressure). As there is no energy in the hard disk system, the two competing terms are both entropic,

$$F_{\text{disloc}}^{\text{hd}} \simeq k_B T \left( \frac{a_0^2}{16\pi} \mathcal{E}'(\eta) - 1 \right) \ln \frac{L^2}{a_0^2}, \quad (1.55)$$

and the density plays the role of the temperature.

As for the universal jump of the spin stiffness, the above melting temperature gives a universal value for the dimensionless Young's modulus at the transition:

$$\frac{a_0^2}{k_B T_m} \mathcal{E} = 16\pi. \quad (1.56)$$

This universal value can be used in Monte Carlo simulations to localize the transition by measuring the elastic coefficients [75, 76, 77]. As there are two elastic coefficients, the exponent  $\nu_{K_m}$  of the correlation function at the transition is therefore not universal. However, Eq. (1.49) and Eq. (1.56) show that  $\nu_{K_m}$  is only function of the Poisson's ratio

$$\nu_{K_m} = \frac{1}{3} - \frac{(\sigma - 1)^2}{12}, \quad (1.57)$$

and as  $\sigma \in [0, 1]$ , the exponent at the transition satisfies the inequality

$$\frac{1}{4} \leq \nu_{K_m} \leq \frac{1}{3}. \quad (1.58)$$

As for the 1/4 exponent in the XY model (see Section 1.2.2), this inequality can be tested in simulations [78] and experiments [79].

In the solid, the bound dislocations interact logarithmically through the elastic media <sup>6</sup>, the analysis by renormalization theory of this gas of dislocations gives the behavior of the elastic modulus near the transition, which shows a similar cusp to the spin stiffness of the XY model. The shear modulus for  $T \lesssim T_m$  satisfies

$$\mu(T) = \mu(T_m)[1 + \text{const.}(T_m - T)^{0.36963..}] , \quad (1.60)$$

and as the positional order is short ranged above the melting temperature,  $\mu(T_m^+) = 0$ . Free dislocations destroy the positional order, the correlation length of the system thus corresponds to the typical distance between the dislocations. If the free-dislocation density is  $n_{\text{disloc}}$ , the positional correlation function is

$$C_{\vec{K}}(r) \simeq \exp(r/\xi_p) \quad \text{with} \quad \xi_p = \frac{1}{\sqrt{n_{\text{disloc}}}}, \quad (1.61)$$

and for  $T \gtrsim T_m$ ,

$$\xi_p \propto \exp\left(\text{const.}|T - T_m|^{-0.36963..}\right). \quad (1.62)$$

As for the XY model, this transition is realized if the solid phase remains stable up to the dislocation-unbinding temperature (or density). The melting temperature obtained is therefore an upper limit for the stability of the solid phase. This KT transition could be preempted by a first-order transition. In Chapter 4, we show by numerical simulations that this phase transition is indeed of the KT type for hard disks.

---

<sup>6</sup>Plus a term of orientation which has no qualitative consequences in the solid, the Hamiltonian is

$$H_{\text{disloc}} = \frac{-\mathcal{E}}{8\pi} \int \vec{b}(\vec{r}) \cdot \vec{b}(\vec{r}') \ln \frac{|\vec{r} - \vec{r}'|}{a_0} - \frac{\vec{b}(\vec{r}) \cdot (\vec{r} - \vec{r}') \vec{b}(\vec{r}') \cdot (\vec{r} - \vec{r}')}{|\vec{r} - \vec{r}'|^2} d^2r d^2r' + E_c \int |\vec{b}(\vec{r})|^2 d^2r \quad (1.59)$$

## The hexatic phase

Nelson and Halperin [32, 68] showed that the unbinding of dislocations, which destroys positional order, results in a thermodynamic phase which does not completely disrupt the orientation of the system. Indeed, the system passes from long-range ordered to quasi-long-range ordered. This phase is called hexatic.

The free dislocations destroy positional order, and as a consequence the shear modulus is zero [68], the system is thus not solid anymore. However, the dislocations do not disrupt the orientation (as is seen in Fig. 1.10). We define the orientation field

$$\theta(\vec{r}) = \frac{1}{2}(\partial_i u_j - \partial_j u_i) \quad (1.63)$$

which on large length scales is described by the Hamiltonian

$$H_{\text{hex}} = \frac{1}{2}K_A \int |\vec{\nabla}\theta(\vec{r})|^2 d^2r, \quad (1.64)$$

$K_A$  being the Frank constant (as in liquid crystals) and satisfies  $K_A \propto \zeta_p^2$ . This Hamiltonian is similar to the one of the low-temperature phase of the XY model with  $K_A$  playing the role of the renormalized spin stiffness. As the lattice is triangular, the angles  $\theta_i$  and  $\theta_i \pm \pi/3$  represent the same orientation of the system, and one may define the local orientation with the complex valued order parameter

$$\psi(\vec{r}) = \exp i6\theta(\vec{r}) . \quad (1.65)$$

This order parameter is easily computed in a simulation (see Section 3.3.1). The analogy with the XY model is then complete with  $\vec{S}(\vec{r}) = (\text{Re}(\psi), \text{Im}(\psi))$  and  $K_A = J_R/36$ . The orientational correlation function, defined by

$$C_o(r) = \frac{\langle \psi^*(\vec{r})\psi(\vec{0}) \rangle}{\langle |\psi|^2 \rangle}, \quad (1.66)$$

shows therefore an algebraic decay at large distances:

$$C_o(r) \underset{\infty}{\sim} r^{-\nu_o} \quad \text{with} \quad \nu_o = \frac{18}{\pi\beta K_A}. \quad (1.67)$$

As the correlation of the orientation goes to zero, an infinite sample shows no orientation. Its diffraction pattern (structure factor) should thus be constituted of isotropic rings, as for a liquid. However, as the loss of orientation is algebraic, there is always an orientation in a finite sample. This can be seen by computing the “total” orientation

$$\Psi = \frac{1}{V} \int \psi(\vec{r}) d^2r, \quad (1.68)$$

which is directly related to the correlation function and scales with the system size  $L$  as

$$\langle |\Psi| \rangle \underset{\infty}{\sim} r^{-\nu_o/2}. \quad (1.69)$$

The rings are therefore always modulated and show six brighter spots (for a triangular lattice). The angular width of the spots is determined by the angular fluctuations and increases with system size. The radial part is determined by the positional correlation length  $\xi_p$ . The structure factor at the first ring (or spot) takes a finite value and the radial part is expected to be a Lorentzian shape

$$S(k) \propto \frac{\xi_p^2}{1 + [(k - K)\xi_p]^2} \quad (1.70)$$

where  $K$  is the radius of the ring (as in a liquid). However, the correlation between density fluctuation and order parameter in the hexatic can turn this shape into more of the square-root Lorentzian shape [80]. In any case, the width of the ring is  $\propto 1/\xi_p$ , which gives a simple way to measure the positional correlation length.

While dislocations are free in an infinite system, a finite system with periodic boundary conditions will set the total Burgers vector to zero. The freedom of dislocations can still be tested on closed paths of increasing size below the system size as is explained in Section 1.2.3.

### Hexatic-liquid transition

In the KTHNY theory, another KT transition occurs between the hexatic and the liquid by unbinding of the topological defect of the orientation: the disclinations. A disclination corresponds to a particle having five or seven neighbors (instead of six in a regular triangular lattice, see Fig. 1.11). As a consequence, the orientation defined by  $\psi$  winds by  $\pm 2\pi$  for a closed path around the defect. This defect is similar to a vortex in the XY model<sup>7</sup>. Disclinations are bound in the hexatic phase, which forms dislocations (see Fig. 1.10), and do not disrupt the orientation, they unbind at a given temperature (or density) to form the liquid.

The results of the KT transition in the XY model are then directly transferable using  $K_A = J_R/36$ . The transition thus occurs at

$$k_B T_i = \frac{72K_A}{\pi}, \quad (1.71)$$

and the correlation function at the transition is

$$C_o(r) \underset{\infty}{\sim} r^{-\nu_o} \quad \text{with} \quad \nu_o = 1/4. \quad (1.72)$$

$K_A$  jumps to zero above the transition temperature, and for  $T \lesssim T_i$ ,

$$K_A(T) = K_A(T_i^-)[1 + \text{const.}(T_i - T)^{1/2}]. \quad (1.73)$$

This gives for the correlation function

$$C_o(r) \underset{\infty}{\sim} r^{-\nu_o} \quad \text{with} \quad \nu_o = \frac{1}{4}[1 - \text{const.}(T_i - T)^{1/2}]. \quad (1.74)$$

---

<sup>7</sup>The only difference is the asymmetry in the core energy between a positive and negative disclination [40] (as a vacancy has a lower energy than an interstitial, a positive disclination has a lower core energy than a negative one).

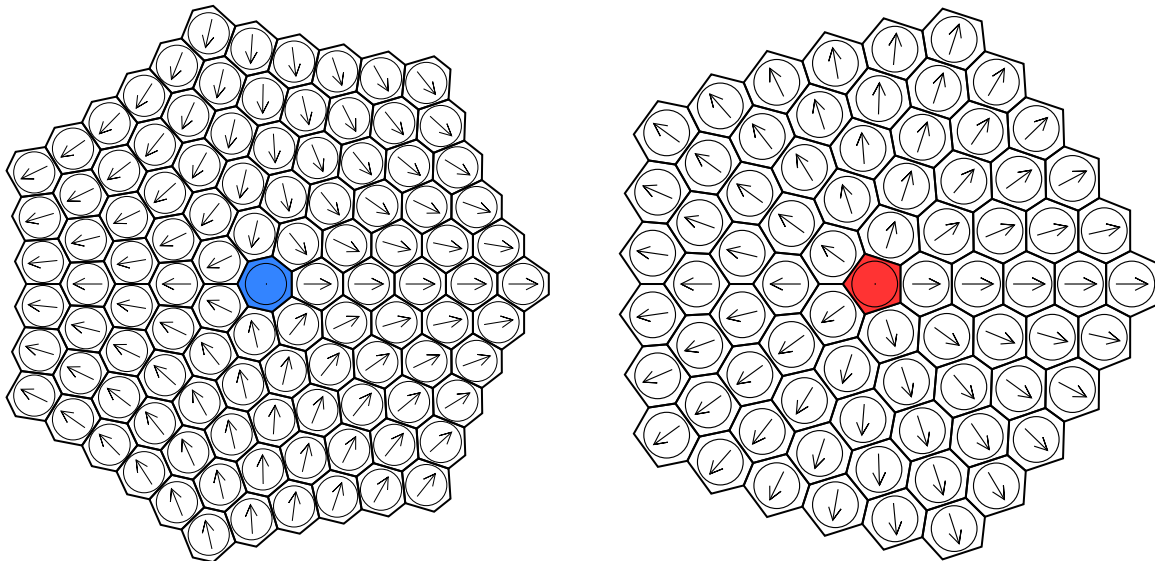


**Figure 1.12:** Schematic disclinations in hard disks. The local orientation is shown by the arrows (see Eq. (1.65) and Section 3.3.1), disks with five and seven neighbors are in red and blue, respectively. *Left:* A “negative” disclination, the core disk has seven neighbors, the orientation winds by  $-2\pi$  as for an anti-vortex. *Right:* A “positive” disclination, the core disk has five neighbors, the orientation winds by  $2\pi$  as for a vortex. Two bound opposite disclinations do not disrupt the orientation, their unbinding leads to the liquid phase.

In the liquid phase, the orientational correlation function is short ranged with a correlation length  $\xi_o$  given by the typical distance between disclinations,

$$C_o(r) \underset{\infty}{\approx} \exp -r/\xi_o \quad \text{with} \quad \xi_o = \frac{1}{\sqrt{n_{\text{disclin}}}}, \quad (1.75)$$

and shows for  $T \gtrsim T_i$ ,

$$\xi_o \propto \exp \left( \text{const.} |T - T_i|^{-1/2} \right). \quad (1.76)$$

In the liquid, the structure factor shows isotropic rings, whose radial shape are Lorentzians of width  $1/\xi_p$ .

### Other defects

The two successive KT transitions of the KTHNY theory are ruled by the behavior of topological defects of the system. Other defects also exist but do not change the topology of the system. The simplest ones are vacancies and interstices which correspond to a missing or an extra particle in the lattice. These defects require a finite elastic energy, and thus they will always be present at a given density (especially the vacancies), but do not change the qualitative behavior of the system. They can also be understood as closely bound dislocations.

### 1.3.3 Experiments and simulations

Many experiments and simulations have been performed in order to understand the 2D melting transition (see [17, 18] for a complete review), here is a short summary.

A way to form a 2D solid, and study its melting, is to create monolayers of an element adsorbed on a crystalline substrate [81]. The substrate is generally graphite, which shows large planar surfaces. The adsorbed gas can be of different type: helium, xenon, ethylene for example. This system does not show any thermalization problem, or finite-size effect. Also, its structure can be studied by X-ray diffraction. In order for the substrate to have little influence, the phase studied has to be incommensurable with it. However, the crystalline substrate always interacts directionally, and this departs this system from an ideal 2D system. No clear conclusions can be obtained from these experiments [17].

Another 2D system is constituted of electrons confined at the surface of liquid helium by an electric field. This is an ideal 2D system as there is no substrate. However, it is difficult to analyze the structure of this system by a diffraction experiment; only dynamic and elastic measurements can be done. The results are compatible with the KTHNY theory but no definitive conclusion can be drawn without knowing the structure of the system [30].

Experiments have also been performed on thin liquid-crystal films [82, 83]. Liquid-crystals are composed of large non-isotropic molecules whose shape leads to a rich phase diagram. The smectic phase of liquid-crystal is composed of layers that weakly interact together, and is therefore close to a 2D system. By reducing the number of layers, it is possible to create thin suspended films of few layers which approach ideal 2D systems. These systems do not suffer from thermalization problems or finite-size effects. Moreover, their elastic property can be determined (with a torsion oscillator), as well as their internal structure with X-ray diffraction. The KTHNY scenario has been observed in these systems [83]. This constitutes the only experimental evidence of the existence of the hexatic phase, and of the validity of the KTHNY theory.

Other experiments have studied the behavior of colloidal suspensions [31, 79, 84]. Colloids are constituted of large spherical molecules of size  $\sim \mu\text{m}$  dispersed in a liquid. In order for the system to be bi-dimensional, the colloid particles are confined at an interface or between two plates. The particles can interact electrically if they are charged, or just as hard spheres. Due to the large size of the particles, it is relatively easy to observe the system and compute observables using video-microscopy for example. In that sense, colloids are the crossover between experiments and simulations. These systems can be set up almost perfectly bi-dimensional. However, even if the particles are light enough to be displaced by thermal motion, the thermalization time is much higher than for atomistic systems, and especially in highly correlated 2D phases. Another problem is to reach systems of size large enough. Therefore, colloids experiments share the same problem as simulations: large thermalization time and limited-size system.

An important body of simulations has been performed to study the 2D melting transition since the first one by Alder and Wainwright [9]. Most simulations have been performed in the constant-density or constant-pressure ensemble (see Section 3.1), using either the Markov-chain Monte Carlo method, or the molecular dynamics<sup>8</sup> (see Chapter 2). Different systems have been studied, such as soft spheres [85, 78, 86], Lennard-

---

<sup>8</sup>A mix of both methods, referred to as hybrid Monte Carlo, is also used.



Jones gas [87, 88], Coulomb repulsion [89, 90], but most of the studies focused on the simplest of the model: the hard-disk model [9, 91, 92, 93, 24, 25]. The algorithms used are local and prone to critical slowing down. Therefore, the simulations, as for the colloids experiments, require long thermalization time, and this prevents reaching the system size needed to properly study the transition. In this thesis, we study the phase transition for hard disks (see Chapter 4) with the use of a new Monte Carlo algorithm (see Chapter 2).

## Conclusion

2D systems display rich and interesting behavior, as for example, the KT transition [13, 14]. The way 2D solids melt is still not completely understood. The KTHNY theory predicts that these solids melt through two successive KT transitions. However, these transitions could be preempted by first-order transitions as shown in XY models. The XY models also show that the nature of 2D transitions can be obtained through Monte Carlo simulations in finite-size systems. Therefore, as for the study of the XY models, an efficient Monte Carlo algorithm could be a solution to access the nature of the melting transitions. Chapter 2 focuses on Monte Carlo algorithm for hard disks with in the objective to efficiently study the melting transition in this model.





## Event-chain Monte Carlo algorithms for hard spheres

In this chapter, I introduce numerical methods which can be used to compute the thermodynamic properties of hard-sphere systems, that is, the molecular dynamics and the Monte Carlo methods. I then expose the event-chain algorithm, a simple yet powerful Monte Carlo algorithm for hard-core systems. The event-chain algorithm has been presented in the first publication [5] (see Section 7.1), and we used it to perform the large-scale simulations needed to access the nature of the hard-disk melting transition (see Chapter 4).

### 2.1 Hard-sphere simulations

#### 2.1.1 Molecular dynamics

Molecular-dynamics simulation is the direct integration of Newton’s laws of motion, which describe the time evolution of particle systems. Usually, the equations are solved by discretizing the time in time step  $\delta t$ . For each time step, interactions between particles are computed and velocities updated. This discretization induces an error that is negligible if  $\delta t$  is small enough.

The hard-disk system is composed of elastic disks of mass  $m$ , and the state of the system is fully determined by the disks positions and velocities (see Fig. 2.0). In this system, molecular dynamics can be achieved without discretization. The time of the next collision (the next “event”) is computed, and the velocities after a collision are updated by momentum and energy conservation:

$$\vec{v}'_1 + \vec{v}'_2 = \vec{v}_1 + \vec{v}_2 \quad \text{and} \quad v'^2_1 + v'^2_2 = v^2_1 + v^2_2, \quad (2.1)$$

where  $(\vec{v}_1, \vec{v}_2)$  and  $(\vec{v}'_1, \vec{v}'_2)$  are the velocities of the disks involve in the collisions before and after the collision, respectively.<sup>1</sup>

The molecular-dynamics method was first implemented for hard spheres [47], and was the first method used to show the existence of the hard-disk solid [9]. In order to estimate the efficiency of this method, we simply analyze the behavior of particles’ motion. The

---

<sup>1</sup>The same “event-driven” algorithms can be used on “stepped” approximation of continuous potentials [94].

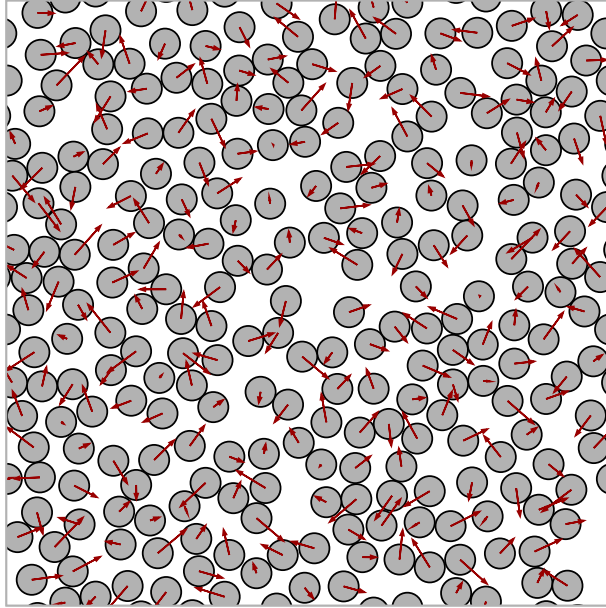


**Figure 2.1:** Snapshot of a molecular-dynamics simulation of hard disks. The arrows represent disks' velocities.

same analysis is done for the Monte Carlo methods in Section 2.2 and Section 2.1.3. In 3D and higher, the particles under molecular dynamics perform a Brownian motion. If  $\vec{r}(t)$  is the position of a particle, the displacement of the particle from  $t = 0$  to a time  $t$  satisfies

$$\langle [\vec{r}(t) - \vec{r}(0)]^2 \rangle = Dt, \quad (2.2)$$

where  $D$  is the diffusion coefficient<sup>2</sup>. In 1D and 2D, the particles do not satisfy a Brownian motion, they are superdiffusive. This property, showed by the “long-time tail” of the velocity auto-correlation function [11], is due to the conservation of momentum. Indeed, let us consider that at  $t = 0$ , a particle has a momentum  $m\vec{v}(0)$ . This particle exchanges momentum with neighboring particles by interacting with them. The initial momentum is then (statistically) spread by diffusion in a sphere of radius  $R \propto \sqrt{t}$ . The knowledge of the initial velocity  $\vec{v}(0)$  gives then information about the scaling of the velocity: for a large time  $t$ ,

$$\langle \vec{v}(t) \rangle \propto \frac{\vec{v}(0)}{R^d}. \quad (2.3)$$

Therefore, the velocity auto-correlation function satisfies for large  $t$

$$\langle \vec{v}(0) \cdot \vec{v}(t) \rangle \propto t^{-d/2}, \quad (2.4)$$

and the quadratic displacement can then be computed

$$\langle [\vec{r}(t) - \vec{r}(0)]^2 \rangle = \int_0^t \int_0^t \langle \vec{v}(t') \cdot \vec{v}(t'') \rangle dt' dt'' \quad (2.5)$$

$$\approx 2t \int_0^t \langle \vec{v}(0) \cdot \vec{v}(t') \rangle dt'. \quad (2.6)$$

---

<sup>2</sup>Other definitions of  $D$  can be used.  $D$  is then multiplied by a constant factor.

Eq. (2.6) and Eq. (2.4) give for large  $t$ :

$$\langle [\vec{r}(t) - \vec{r}(0)]^2 \rangle \propto \begin{cases} t\sqrt{t} & \text{for } d = 1 \\ t \ln t & \text{for } d = 2 \\ t & \text{for } d \geq 3 \end{cases} . \quad (2.7)$$

The motion of particles is therefore diffusive for  $d \geq 3$  and superdiffusive for  $d = 1$  or  $d = 2$ . However, in finite-size system, the radius  $R$  of the sphere in which the initial momentum is spread cannot exceed the length  $L$  of the system. Therefore,  $t_{\max} \propto L^2$  in the integral of Eq. (2.6). For  $d = 2$ , the diffusion coefficient thus satisfies<sup>3</sup>  $D_L \propto \ln L$  for large systems. As a consequence, the thermalization time (in number of collisions) for the molecular dynamics is expected to be faster than for diffusive processes (such as reversible Markov chains) by a factor  $O(\ln N)$ . As molecular dynamics in 2D is superdiffusive, this method seems a good choice for simulations. However, the factor  $O(\ln N)$  increases slowly with system size. A good implementation is needed in order to outperform Markov-chain Monte Carlo methods.

The naive implementation has a complexity of  $O(N^2)$  per collision as there are  $\propto N^2$  collisions to compute for each event. The implementation of a cell scheme to store particle positions reduces this complexity to  $O(N)$  per collision. Another improvement consists in avoiding to compute the same collision many times. To do so, a list of collisions to come is stored, chronologically sorted, and updated during the simulation. This corresponds to a classic problem of priority queues [95]. The implementation of priority queues can be achieved with various types of binary trees in order to reach a complexity of  $O(\ln N)$  per collision [96]. Finally, additional information about molecular dynamics of hard spheres enables a priority queue of  $O(1)$  per collision to be reached [97]. The fastest current implementations are still with a priority queue  $O(\ln N)$ , which for  $32^2$  disks at  $\eta \sim 0.7$  reaches about  $1.7 \times 10^9$  collisions per hour on a 2.6GHz workstation [98]<sup>4</sup>. The parallelization is also an important feature of an algorithm. A speed-up factor of  $\propto \sqrt{N_p}$  is obtained for molecular dynamics, where  $N_p$  is the number of CPU [100, 101].

Molecular dynamics integrate the equation of motion. Therefore, this method gives both thermodynamic and dynamic information about the system. The thermodynamics properties of the system can be obtained by other methods. Statistical physics shows that, as positions and velocities are independent in the Hamiltonian of the system, the distribution of velocities is independent of the distribution of positions. The distribution  $\pi_v$  for the velocity  $\vec{v} = (v_x, v_y)$  of a particle (identical for each particle) follows a Maxwell distribution

$$\pi_v(v_x, v_y) \propto \exp -\beta \frac{1}{2} m (v_x^2 + v_y^2), \quad (2.8)$$

which can be directly sampled. This is not the case of the distribution of positions. Each valid configuration of the hard-disk system has the same energy. Therefore, the distribution of positions is uniform, that is, each valid configuration has the same probability. This property comes from the very nature of the molecular dynamics which conserves

---

<sup>3</sup>With periodic boundary conditions, the positions of particles have to be computed with respect of the mass center to find this result, as the total system has a non-zero momentum.

<sup>4</sup>The fastest implementation with a priority queue  $O(1)$  is  $2.5 \times 10^8$  collisions per hour for 3D hard spheres on a similar CPU [99].

phase-space volume<sup>5</sup> and is time reversible<sup>6</sup>. This ensures that for hard spheres, the uniform distribution is stationary through molecular dynamics. Moreover, ergodicity has been rigorously proved for hard spheres [102, 103], which show that the hard-sphere system indeed converges toward this stationary distribution.

It is possible to reproduce the same statistical properties with other methods than molecular dynamics, such as stochastic processes. A large freedom is given in the choice of these “unphysical” processes, and this can lead to an increase of the efficiency. The following concerns these algorithms.

## 2.1.2 The Monte Carlo method

The statistical properties of hard spheres can be obtained by randomly sampling configurations. The samples are then used to compute distributions as well as mean values of observables, and therefore access the thermodynamics of the system. This is known as the Monte Carlo method [3, 4]. In Part II of this thesis, I describe the Monte Carlo method in further detail, and discuss a method to solve the problem of thermalization.

A computer is able to generate independent random numbers  $\gamma \in [0, 1]$  with a uniform distribution. The generation of hard-disk configurations is however not straightforward. A naive method is to place disks at random positions sampled uniformly in the box, and to reject the configurations which show overlaps. This direct sampling gives the appropriate distribution for the configurations, but the rejection rate is prohibitive at high density.

One possibility to overcome this difficulty is to start from an initial valid configuration, then to “mix” the system. The mixing process is achieved by performing small changes while ensuring that the configuration stays valid during the process (see Fig. 2.1). When the process has been run for a time long enough, that is, when the system is decorrelated from the initial configuration, a sample can be extracted. This process is then performed again in order to extract other samples. The time needed to decorrelate from the initial configuration (that is, when the system reached the thermodynamic equilibrium) is called the thermalization time, or the correlation time. This method is known as the Markov-chain Monte Carlo method [46]. A Markov chain is a random walk without memory (each step is independent) in the configuration space.

Let  $\Omega$  be the configuration space. The stochastic process performed by a Markov chain is fully determined by the probability of  $P(i \rightarrow j)$  to move from a configuration  $i \in \Omega$  to another configuration  $j \in \Omega$ , called the transition probabilities. In a discrete configuration space  $(P(i \rightarrow j))_{i,j}$  is called the transfer matrix. In a continuous configuration space (as for hard disks) this transfer matrix is a continuous operator. In this thesis, the discrete notation is adopted for simplicity, and it is valid because most algorithms conserve the configuration-phase volume. In the general case, a continuous analysis is however needed (see Section 2.2.2).

The transition probabilities are chosen in order for the stationary distribution (that is, the steady state of the transfer matrix) to be the required distribution  $\pi \propto \exp -\beta E$ . For hard disks this distribution is uniform, restricted to the valid configurations.

The distribution  $\pi$  is stationary under the application of the transfer matrix, that is,  $\pi$  is a fixed point of the Markov chain. This property is expressed by the balance

---

<sup>5</sup>Louville’s theorem.

<sup>6</sup>This property is closely related to the detailed-balance condition in Markov-chain processes.

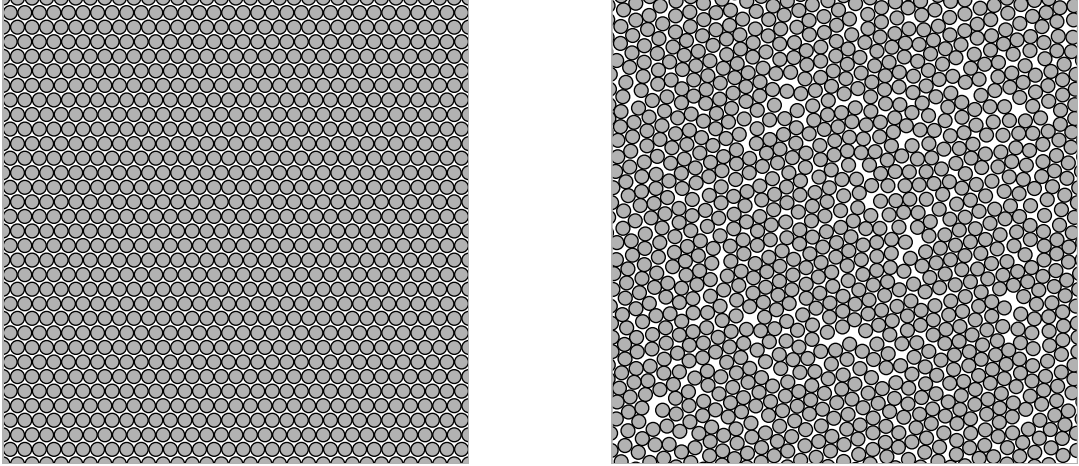


**Figure 2.2:** Initial and thermalized configurations with the Markov-chain Monte Carlo method for  $32^2$  disks at  $\eta = 0.710$ . *Left:* The initial configuration is a triangular lattice. *Right:* Configuration after thermalization, each disk has been displaced  $5 \times 10^9$  times.

condition. Let  $\phi(A \rightarrow B)$  be the probability flux from  $A$  toward  $B$ , two subsets of the configuration space. For the stationary distribution  $\pi$ , the flux  $\phi$  satisfies

$$\forall A \subset \Omega \quad \phi(A \rightarrow \Omega) = \phi(\Omega \rightarrow A) , \quad (2.9)$$

which expresses the balance of the probability fluxes in and out of each subset of the configuration space at the stationary distribution. In a discrete configuration space, this equality can be written as

$$\forall i \in \Omega \quad \pi(i) \sum_{j \in \Omega} P(i \rightarrow j) = \sum_{j \in \Omega} \pi(j) P(j \rightarrow i) . \quad (2.10)$$

For simplicity, most Markov chains satisfy a stronger condition, the detailed-balance condition, which itself implies the balance condition. The detailed-balance condition is given by

$$\forall A, B \subset \Omega \quad \phi(A \rightarrow B) = \phi(B \rightarrow A) , \quad (2.11)$$

and it expresses the equality of probability fluxes between each pair of subsets at the stationary distribution. This condition is related to the time reversibility of molecular dynamics, and is sometimes known as micro-reversibility. In a discrete configuration space, the above equality becomes

$$\forall i, j \in \Omega \quad \pi(i) P(i \rightarrow j) = \pi(j) P(j \rightarrow i) . \quad (2.12)$$

This condition implies that the Markov chain and its probability distribution are diffusive. For hard disks, as the distribution is uniform, the detailed-balance condition is expressed by  $P(i \rightarrow j) = P(j \rightarrow i)$  (between valid configurations) which is referred to as the reversibility of the algorithm.

In Section 2.2, we will see that the event-chain algorithm allows the detailed-balance condition to be broken, that is, only the balance condition of Eq. (2.9) is satisfied. This property is not common for Monte Carlo algorithms, and it allows speeding-up of the equilibration.

The second condition in order for the Markov chain to reach the stationary distribution  $\pi$  is that the dynamic indeed converges toward this fixed point. This convergence is ensured by the stochastic nature of the dynamics and by the ergodicity of the Markov chain. Here, the ergodicity is defined by the possibility for the chain to eventually reach any part of the configuration space.

### 2.1.3 The local Metropolis algorithm

The Metropolis algorithm [46] is the historically first proposal for satisfying the detailed-balance condition of Eq. (2.12). In this algorithm, moves are attempted with the transition probabilities  $A(i \rightarrow j)$ . The moves are then accepted with a suitable probability  $p_{\text{acc}}(i \rightarrow j)$  given by

$$p_{\text{acc}}(i \rightarrow j) = \min \left( 1, \frac{\pi_j}{\pi_i} \times \frac{A(j \rightarrow i)}{A(i \rightarrow j)} \right). \quad (2.13)$$

The transition probabilities  $P(i \rightarrow j) = A(i \rightarrow j) \times p_{\text{acc}}(i \rightarrow j)$  then satisfy the detailed-balance condition. In the canonical ensemble, the distribution satisfies  $\pi(i) \propto \exp -\beta E_i$ , where  $E_i$  is the energy of the configuration  $i$ . If the trial probability is reversible ( $A(i \rightarrow j) = A(j \rightarrow i)$ ), the Metropolis algorithm becomes

$$\forall i, j \in \Omega \quad p_{\text{acc}}(i \rightarrow j) = \min(1, \exp -\beta(E_j - E_i)), \quad (2.14)$$

and for hard disks

$$\forall i, j \in \Omega \quad p_{\text{acc}}(i \rightarrow j) = \begin{cases} 1 & \text{if } j \text{ is a valid configuration} \\ 0 & \text{if } j \text{ shows overlaps} \end{cases}. \quad (2.15)$$

The first simulations with the local Metropolis algorithm were performed on the hard-disk system in the 1950s [46]. At each step of this algorithm, a disk  $k$  at position  $\vec{r}_k$  is randomly sampled among the  $N$  disks of the system. A displacement vector  $\vec{\delta}_k$  is then sampled with a distribution satisfying  $\pi_d(\vec{\delta}_k) = \pi_d(-\vec{\delta}_k)$ . The disk  $k$  is displaced toward  $\vec{r}'_k = \vec{r}_k + \vec{\delta}_k$  if it does not induce an overlap, and is kept at its initial position otherwise (the move is then said to be rejected, see Fig. 2.2). Each step of the algorithm, whether it is an accepted or a rejected move, constitutes one move. The discrete time  $t$  of the chain is the number of move.

The efficiency of the local Metropolis algorithm depends only on the distribution  $\pi_d(\vec{\delta}_k)$ . The detailed-balance condition requires  $\pi_d(\vec{\delta}_k) = \pi_d(-\vec{\delta}_k)$ . The most important parameter of the distribution  $\pi_d$  is its range, and we consider an isotropic and constant choice for  $\vec{\delta}_k$ :  $|\vec{\delta}_k| = \delta$ . Other choices for  $\pi_d(\vec{\delta}_k)$  do not influence the efficiency of the algorithm.

In order to understand the performance of the local Metropolis algorithm, we analyze the behavior of single particle displacements. Because of the detailed-balance condition, each disk moves diffusively, characterized by a diffusion coefficient  $D$  (Eq. (2.2)). The diffusion of a disk at a high density is the result of a  $N$ -body interaction and has several time scales. At short times, the disk is trapped into a ‘‘cage’’ formed by its neighbors.



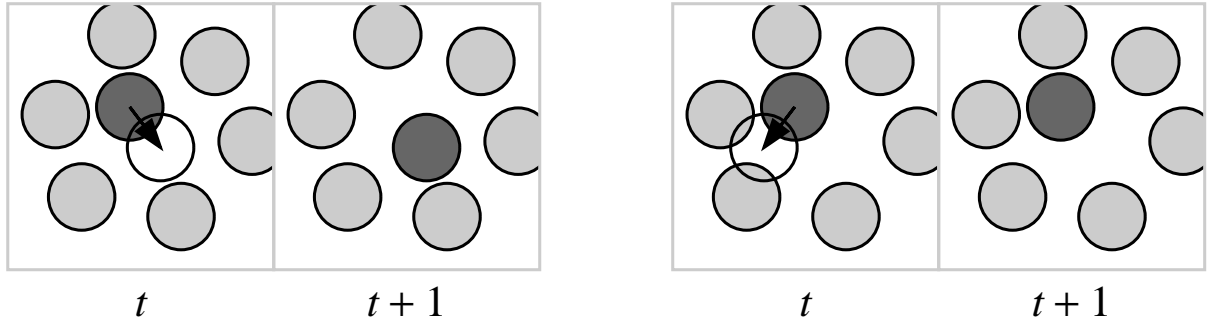


**Figure 2.3:** Moves of the local Metropolis algorithm. *Left:* Accepted move. *Right:* Rejected move. (Ref [5], cf. Section 7.1).

The diffusion coefficient is therefore higher at short times than at large times. Only the long-time behavior is interesting for thermalization, the diffusion coefficient is defined as

$$D = \lim_{t \rightarrow \infty} \frac{\langle [\vec{r}(t) - \vec{r}(0)]^2 \rangle}{t}. \quad (2.16)$$

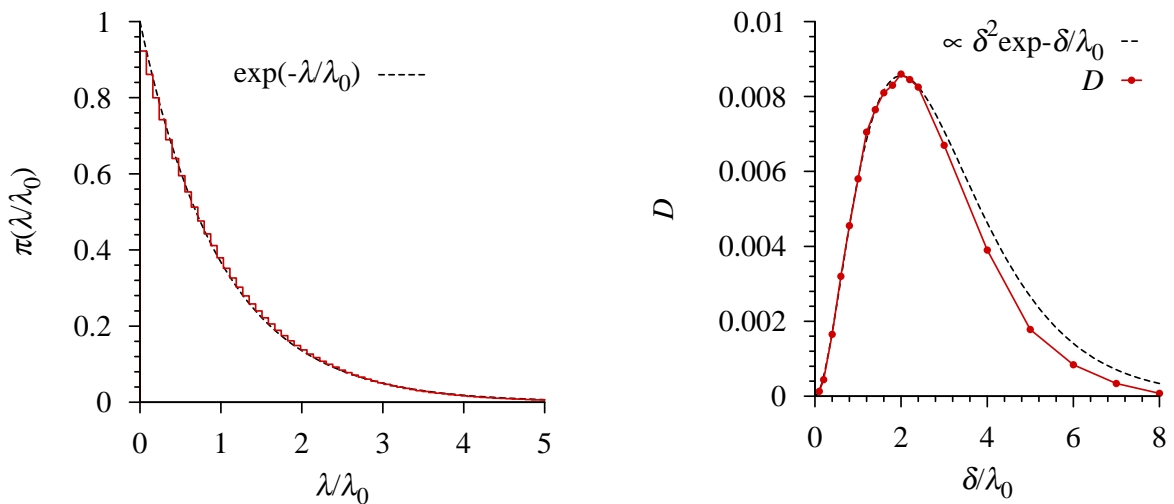


**Figure 2.4:** *Left:* Histogram  $\pi_f(\lambda/\lambda_0)$  of the free path  $\lambda$  for  $32^2$  disks at density  $\eta = 0.71$ . The distribution is close to an exponential even in the solid phase. (Ref [5], cf. Section 7.1). *Right:*  $\delta$ -dependence of the diffusion coefficient of a disk in the local Metropolis algorithm for  $32^2$  disks at density  $\eta = 0.71$ . The length unit is  $\lambda_0$  and the time is counted in attempted move per disks. The optimal value of the step length is  $\delta_{\text{opt}} \simeq 2\lambda_0$  as expected by the short-time diffusion argument.

One might expect that the diffusion coefficient at large times is related to the diffusion coefficient at short times. The disks are displaced by a distance  $\delta$ , and accepted with a probability  $p_{\text{acc}}$ . The short-time diffusion coefficient is therefore given by  $D_{\text{loc}} = \delta^2 p_{\text{acc}}(\delta)$ . In order to determine  $p_{\text{acc}}(\delta)$ , we define the “free path”  $\lambda$  of a disk as the distance it must move in a given direction to strike another disk. The ensemble average of  $\lambda$  yields the mean-free path  $\lambda_0$ . The distribution of the free path  $\pi_f(\lambda/\lambda_0)$  is an



exponential in the low-density limit, but even at high density it is well approximated by an exponential

$$\pi_f(\lambda/\lambda_0) \simeq \exp(-\lambda/\lambda_0) \quad (2.17)$$

(see Fig. 2.3). This ansatz gives that  $p_{\text{acc}}(\delta) = \exp(-\delta/\lambda_0)$ , and that the short-time diffusion coefficient is

$$D_{\text{loc}}(\delta) = \delta^2 \exp(-\delta/\lambda_0). \quad (2.18)$$

The result of the competition between the step length and the acceptance rate gives thus an optimal value of  $\delta_{\text{opt}} = 2\lambda_0$  for the step length. The short-time diffusion coefficient is then  $D_{\text{loc}}(\delta_{\text{opt}}) = 4\lambda_0^2/e^2$  and the acceptance rate is only  $p_{\text{acc}} \simeq 14\%$ .

The long-time diffusion coefficient is related to the behavior of the short-time diffusion coefficient. For small values of  $\delta$ , and up to a few unities,  $D \simeq 0.015 \times D_{\text{loc}}$  (see Fig. 2.3). The optimal value is then  $\delta_{\text{opt}} \simeq 2\lambda_0$  as predicted by the short-time analysis. The proportionality between both coefficient breaks down for higher values of  $\delta$  (see Fig. 2.3). The proportionality between  $D_{\text{loc}}$  and  $D$  for small  $\delta$  is explained by a simple argument: During the Markov process, the configuration diffuses in the  $2N$ -dimensional configuration space. The valid subset of the configuration space is complex and can be seen as a  $2N$ -dimensional porous media, with a typical length of  $\lambda_0$ . For  $\delta \ll \lambda_0$ , the diffusion is not influenced by the “walls” of the configuration space; the increase of  $\delta$  can be seen as an increase in temperature for this diffusion process. It is therefore expected that  $D \propto \delta^2$ . This proportionality stays valid up to a few  $\lambda_0$  by adding the acceptance rate. For larger values of  $\delta$  this simple picture is however not valid.

The local Metropolis algorithm converges toward the appropriate distribution and is easy to implement. One can expect more than  $\sim 10^{10}$  displacements per hour for a well optimized implementation on a single 3Ghz CPU. This algorithm can also be easily parallelized with a speed-up factor  $\propto N_p$ , the number of CPU. However, a move with this algorithm is not equivalent to a molecular-dynamics collision for the thermalization. In CPU time, the fastest implementation of molecular dynamics is faster to thermalize than a well optimized local Metropolis algorithm, but by only by a small factor (about  $\sim 10$ , see Section 2.2.3). Because of its simplicity, the hard-disk melting transition has been mostly studied with this algorithm. The thermalization time is however important at high densities, preventing simulations to reach system sizes large enough to conclude on the nature of the hard-disk melting transition.

The local Metropolis algorithm can be also implemented in spin systems. For these systems, the cluster (non-local) algorithms are much more efficient [53, 54]. It is with these algorithms that the nature of the transition in the 2D XY model has been understood. For hard disks, the local Metropolis algorithm has been the most efficient Monte Carlo algorithm at high densities for 50 years.

## 2.2 The event-chain algorithm

The following introduces a Markov-chain Monte Carlo algorithm developed in collaboration with Werner Krauth and David B. Wilson: the event-chain algorithm [5] (see Section 7.1). The event-chain algorithm is a rejection-free Markov-chain Monte Carlo algorithm designed for hard-core interactions. In a single move, it displaces an arbitrary

long chain of particle in a long-range coherent motion. This algorithm has the particularity that it can be set up “irreversible”, (that is, without the detailed-balance condition). This property, which is usually seen in simple Markov chains [104], increases the efficiency of the thermalization. This algorithm is the first algorithm that clearly outperforms the local Metropolis algorithm.

### 2.2.1 Straight event-chain algorithm

The simplest version of the event-chain algorithm is the “straight event-chain” (SEC) algorithm. A move of this algorithm starts by the sampling of an initial disk  $k$  and an angle  $\theta$ . The disk  $k$  is displaced straight in the direction  $\theta$  until it collides with another disk  $k'$ . The latter is then displaced in the same direction until it collides with yet another disk and so on (see Fig. 2.4). The move stops when all displacements add up to a total length parameter  $\ell$ .

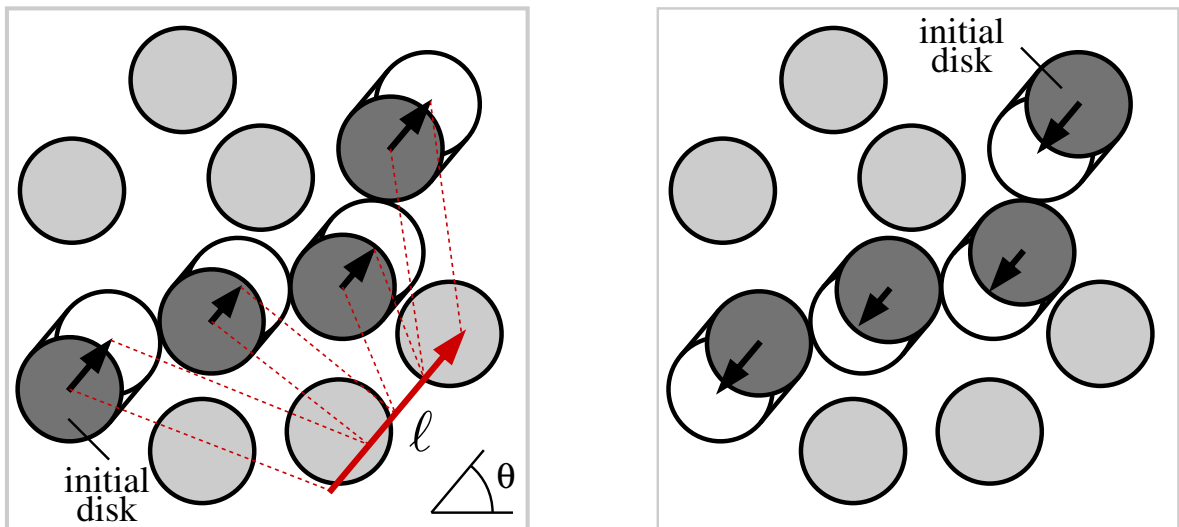


**Figure 2.5:** *Left:* A move of the event-chain algorithm from a configuration  $a$  (left panel) to a configuration  $b$  (right panel). Disks are displaced individually in the same direction until they collide with another disk or the total length  $\ell$  is used up (red arrow). *Right:* Event-chain move from the configuration  $b$  with the angle  $\theta + \pi$  starting with the last displaced disk of the move shown in the left panel. The algorithm is reversible. (Ref [6], cf. Section 7.3)

The move is reversible and thus the algorithm can be set up to satisfy the detailed-balance condition for the uniform distribution. Indeed, let us consider a move in the direction given by  $\theta$  which changes the system from a configuration  $a$  to a configuration  $b$ . In the configuration  $b$ , the move starting with the last displaced disk of the  $a \rightarrow b$  move, and with the angle  $\theta + \pi$ , gives the configuration  $a$  (see Fig. 2.4). Therefore, if the distribution of the angle satisfies  $\pi_d(\theta) = \pi_d(\theta + \pi)$ , the transition probabilities satisfy  $P(a \rightarrow b) = P(b \rightarrow a) \forall a, b$ . Moreover, the volume of the configuration space is conserved through this dynamics (see Section 2.2.2). The detailed-balance condition in this continuous space is therefore satisfied and the stationary distribution of this Markov chain is uniform.

For each move, the total length  $\ell$  can be sampled from a distribution. If the distribution allows infinitely small values of  $\ell$ , the ergodicity is rigorously proved. Indeed, the whole configuration space can be accessed through infinitely small displacements of single disks.

This algorithm improves the local Metropolis in three respects: First, this algorithm is rejection-free, which naturally increases its efficiency. Second, it displaces long chains of particles in the same direction (see Section 2.2.3). Third, it allows the detailed balance condition to be broken, while preserving the balance condition of Eq. (2.9). Indeed, with periodic boundary conditions, the distribution of angles can be set up such as  $\pi_d(\theta) \neq \pi_d(\theta + \pi)$ , the chain then breaks the detailed-balance condition but preserves the balance condition of Eq. (2.9).

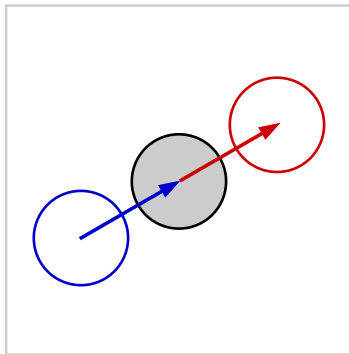


**Figure 2.6:** Balance of probability flux for one disk in a box with periodic boundary conditions. For each angle  $\theta$ , the configuration  $a$  (gray disk) reaches only one configuration (red disk), and is reached by only one configuration (blue disk). The balance condition is satisfied for the movements restricted to the angle  $\theta$ . This argument can be generalized to an  $N$ -particle system.

To illustrate this property, we compute the balance of the probability fluxes in and out of a given configuration  $a$ . In the case of a single disk in a box with periodic boundary conditions, this is easily done. For any given angle  $\theta$ , one move is possible for the configuration  $a$ . Moreover, the incoming probability flux comes from only one configuration: the configuration obtained by applying a  $\theta + \pi$  move to the configuration  $a$ . For any angle  $\theta$ , the probability fluxes in and out of the configuration  $a$  are then balanced (see Fig. 2.5). This argument can be generalized to  $N$  disks. For any given angle  $\theta$ , there are  $N$  possible moves, corresponding to the  $N$  possible initial disks. Moreover, there are  $N$  configurations which “fill” the configuration  $a$ , each of them obtained by performing a  $\theta + \pi$  move with one of the  $N$  disks as initial disk. The balance condition is then satisfied for the movements restricted to any angle  $\theta$ . The stationary distribution is therefore uniform for any distribution  $\pi_d(\theta)$  (as long as the ergodicity is not broken).

The angle can be chosen, say  $\theta \in [0, \pi]$ . The Markov chain is then irreversible as moves have no “return” moves. The hard-disk system shows a global translation, however the distribution of positions is uniform. Other choices for  $\pi_d$  are possible, but at least two independent directions are needed in order to preserve ergodicity. The fastest implementation alternates moves in the  $+x$  and  $+y$  directions ( $\theta = 0, \pi/2$ ), and is called the “ $xy$  version” (see Section 2.3).

The irreversible Markov chains, known as “lifted” Markov chains, have been studied

in mathematics [104] but only for simple discrete systems. The lifting of Markov chain can be adapted to generic reversible Metropolis algorithm by splitting the system in two irreversible replicas, and computing the appropriate probability to switch between replicas [105, 106]. These Markov chains mix generally faster than the classic reversible chains as they induce probability flows in the configuration space.

## 2.2.2 Other versions

The SEC algorithm is the simplest version of the event-chain algorithm, and is the fastest to thermalize (in CPU time). Other versions of the algorithm, where disks are not displaced along straight trajectories, can also be considered.

A simple modification of the SEC algorithm is done by changing the direction of displacement of the disks after each collision. This process must however preserve the configuration-space volume. This constraint leaves only two possibilities: the collided disk (see Fig. 2.7) may be displaced either in the original direction (SEC algorithm) or in the direction reflected with respect to the collision axis. The latter choice is called the “reflected event-chain” (REC) algorithm (see Fig. 2.6).

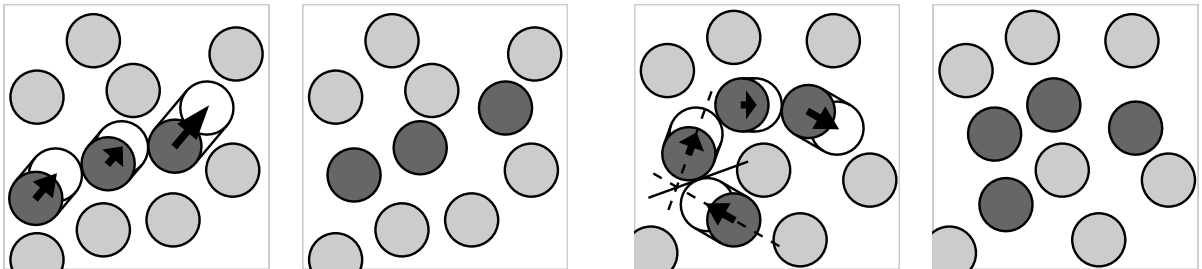


**Figure 2.7:** *Left two panels:* A move of the straight event-chain (SEC) algorithm. *Right two panels:* A move of the reflected event-chain (REC) algorithm. (Ref [5], cf. Section 7.1).

Let  $a$  be a configuration, and  $\epsilon_a$  a small subset of the configuration space centered around  $a$ . Let  $b$  be the configuration obtained by a move starting with the disk  $k$  and the angle  $\theta$ , and  $\epsilon_b$  the resulting subset obtained by application of this move  $(k, \theta)$  to  $\epsilon_a$ . The configuration-space volume is conserved if the volumes of  $\epsilon_a$  and of  $\epsilon_b$  are equal.

Between two collisions, the displacements are straight, the configuration-space volume is conserved. During a collision, the change in configuration-space volume is limited to the two disks involved in the collision, referred to as the “incoming” and the “collided” disk (see Fig. 2.7). We compute this volume variation in the frame of the collided disk. In the limit of an infinitely small subset  $\epsilon_a$ , the circular collision surface is flat. The computation of the change of volume is therefore reduced to the variation of configuration-space volume for a collision against a wall (the collision line). Let  $\alpha_1$  and  $\alpha_2$  be the angles between the initial direction and the collision line before and after the collision. The ratio  $\mu$  of the volumes before and after the collision is given by

$$\mu = \frac{\sin \alpha_2}{\sin \alpha_1}, \quad (2.19)$$

which differs from one unless  $\alpha_1 = \alpha_2$  or  $\alpha_1 = \pi - \alpha_2$  (see Fig. 2.7). In general, for a move consisting of  $n$  collisions, the volume ratio is  $\mu_{\text{tot}} = \mu_1 \times \dots \times \mu_n$ . An acceptance

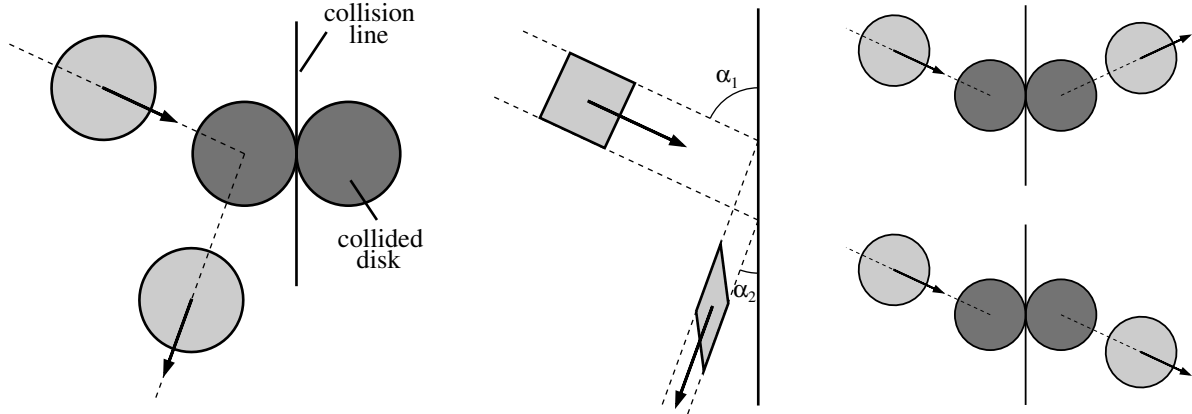


**Figure 2.8:** *Left:* An event-chain collision in the reference frame of the collided disk. In the limit of an infinitely small  $\epsilon_a$ , the circular collision surface is flat (the collision line). *Center:* Transformation of a small subset of the configuration space during the collision: its volume is not conserved. *Right:* The volume is conserved only for the values  $\alpha_1 = \alpha_2$  (upper panel) or  $\alpha_1 = \pi - \alpha_2$  (lower panel).

probability of  $p_{\text{acc}} = \min(1, \mu_{\text{tot}})$  is therefore necessary to preserve the balance condition<sup>7</sup> The choice  $\alpha_1 = \pi - \alpha_2$  for each collision corresponds to the SEC algorithm, and the choice  $\alpha_1 = \alpha_2$  corresponds to the REC algorithm (see Fig. 2.7 and Fig. 2.6). A combination of the two types of collision is also possible. It is interesting to note that  $\alpha_1 = \alpha_2$  corresponds to the angles of molecular dynamics. As shown in Section 2.2.3, the REC algorithm is less efficient than the SEC algorithm.

Versions of the algorithm where disks do not move straight are also possible. For example the disks can be displaced with a constant-curvature trajectory (circular trajectory) between collision, and collide as in Fig. 2.7. More exotic versions can be designed, for example with disks that rotate toward a given fixed point. These version were found not to outperform the irreversible version of the SEC algorithm. In the following, the performance of the SEC algorithm is analyzed and compared to those of the local Metropolis and of the REC algorithms.

### 2.2.3 Efficiency analysis

The analysis of the convergence of Markov chains efficiency, related to the time needed to decorrelate from the initial configuration, is a vast topic [107]. As a first indication, one may again compute (cf. Section 2.1.3) the short-time diffusion coefficient  $D_{\text{loc}}$  of the event-chain dynamics. To that purpose, let us suppose that the lengths of subsequent displacements in the chain are independent. In that case, the expected number of particles in the chain is  $\langle M(\ell) \rangle = \ell/\lambda_0 + 1$ . We index the displacement during one event-chain move through a time-like variable  $t$  with  $0 \leq t \leq \ell$ . The mean-square displacement of an event-chain move (the expected sum of the squares of the individual displacements) can be expressed through the probability  $\pi(t, t')$  that both times  $t$  and  $t'$  belong to the same

<sup>7</sup>This acceptance rate was tested on simple algorithms which do not preserve the configuration-space volume (as  $\theta_{t+1} = \theta_t + \text{const.}$ ). The stationary distribution is uniform only with the use of this acceptance probability.

particle displacement:

$$\langle \Delta \mathbf{x}^2(\ell) \rangle = \int_0^\ell \int_0^\ell \pi(t, t') dt dt'. \quad (2.20)$$

The ansatz of Eq. (2.17) gives  $\pi(t, t') = \exp(-|t - t'|/\lambda_0)$ . This yields the short-time diffusion coefficient of the event-chain dynamics in an infinite system:

$$D_{\text{loc}}^\infty(\ell) = \frac{\langle \Delta \mathbf{x}^2(\ell) \rangle}{\langle M(\ell) \rangle} = 2\lambda_0^2 \frac{\exp(-\ell/\lambda_0) + \ell/\lambda_0 - 1}{\ell/\lambda_0 + 1}. \quad (2.21)$$

For small  $\ell/\lambda_0$ ,  $D_{\text{loc}}^\infty(\ell) \sim_0 \ell^2$ , as for the local Metropolis algorithm. For large  $\ell/\lambda_0$ ,  $D_{\text{loc}}^\infty(\ell) \xrightarrow{\infty} 2\lambda_0^2$ , which is  $e^2/2 \sim 4$  times larger than in Eq. (2.18) for the local Metropolis algorithm. This factor corresponds to the efficiency gain expected for a generic event-chain algorithm with large  $\ell/\lambda_0$ , even though it is significantly larger for the SEC algorithm.

In a finite system, Eq. (2.21) must be corrected for the center-of-mass displacement. For the SEC algorithm, the corrected short-time diffusion coefficient  $D_{\text{loc}}(\ell)$  drops to zero for  $\ell/\lambda_0 \rightarrow \infty$  because in a finite box, all disks then participate in the chain, and the system moves as a solid block. The REC algorithm, in contrast, saturates to a constant short-time diffusion coefficient for large chains as the center of mass is not linearly displaced during a move.

In order to compute the efficiency of the event-chain algorithm, one could, as for the Metropolis algorithm, compute the long-time diffusion coefficient of a disk. However, this value might not be relevant as it is related to the behavior of single particle, and does not necessarily capture  $N$ -body effects. In order to compute the thermalization time of an observable, it is better to study the auto-correlation of a thermodynamic observable.

Empirically, one can compute the auto-correlation function of a given observable  $\mathcal{O}$  defined by

$$C(\Delta t) \propto \langle [\mathcal{O}(t + \Delta t) - \langle \mathcal{O} \rangle][\mathcal{O}(t) - \langle \mathcal{O} \rangle] \rangle \quad (2.22)$$

and normalized so that  $C(0) = 1$ . The auto-correlation function has many time scales ( $\tau > \tau_1 \geq \dots$ ) which are given by the eigenvalues of the transfer operator of the Markov chain (see Part II, Section 5.1.2)

$$C(t) = a_0 \exp(-t/\tau) + a_1 \exp(-t/\tau_1) + \dots \quad (2.23)$$

The objective is to compute the largest of these time scales  $\tau$  referred to as the ‘‘correlation time’’. All observables are in principle equivalent as the time scales of the transfer operator are the same, however the weights ( $a_0, a_1, \dots$ ) associated with these time scales are different according to the observable. It is difficult to compute  $\tau$  with an observable whose value of  $a_0$  is small as it is difficult to be sure that the largest time is reached (see Section 4.3.1). A global observable, which is slow to decorrelate, should be used.

We define the orientational order parameter  $\Psi$  by

$$\Psi = \frac{1}{N} \sum_{j=1}^N \psi_j \quad (2.24)$$

with

$$\psi_j = \frac{1}{n_j} \sum_{\langle k,j \rangle} \exp(i6\theta_{j,k}). \quad (2.25)$$

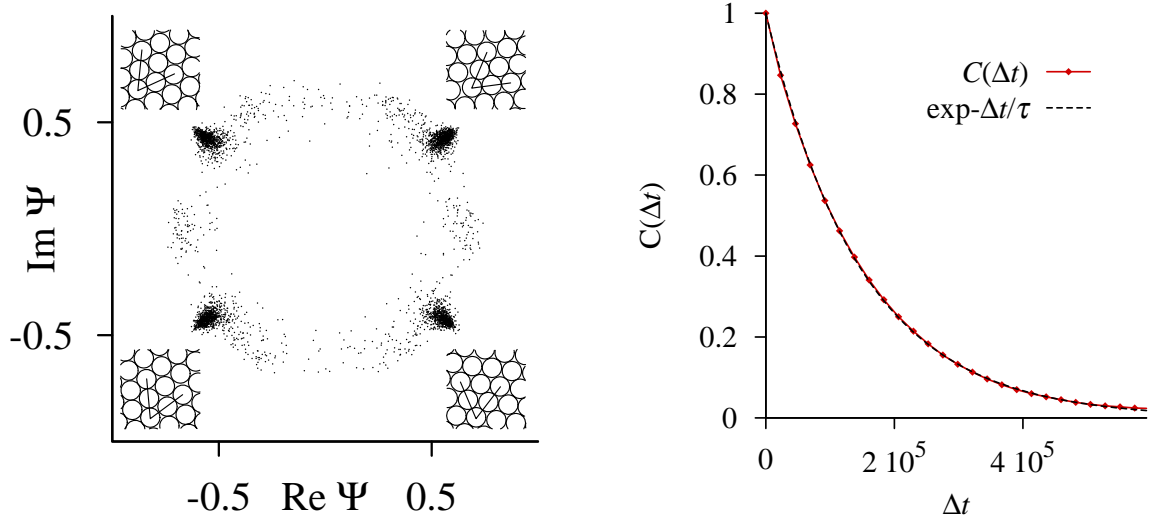


**Figure 2.9:** *Left:* Distribution of  $\Psi$  for  $16^2$  disks in a periodic square box at density  $\eta = 0.71$ . The distribution is anisotropic but symmetric towards both axes. The diagonal squares show the orientation of the system for different values of the order parameter. *Right:* Auto-correlation function of  $\Psi$  for this system. The correlation time is obtained from an exponential fit. (Ref [5], cf. Section 7.1).

The sum extends over the  $n_j$  neighbors of the disk  $j$ , and  $\theta_{j,k}$  is the angle of the bond between the disk  $j$  and its neighbor  $k$  (see Section 3.3.1). This observable has also been chosen in order to compute the validity of the implementations in Section 2.3.3, and in view of applications in Chapter 4.  $\Psi$  is the slowest observable that we found in this system. Indeed, the argument of this complex-valued observable defines the global orientation of the system. The correlation time associated to this observable is therefore related to the time needed for the system to perform a complete rotation in the box. This is a slow process at high densities (see Fig. 2.9). Probable values of  $\Psi$  form an irregular ring around the origin. The square box implies that  $\pi(\Psi)$ , the probability distribution of  $\Psi$ , is symmetric by reflection over the real and imaginary axes, and therefore that  $\langle \Psi \rangle = 0$  (see the scatter plot in Fig. 2.8). The knowledge of the full distribution  $\pi(\Psi)$  would be needed to ensure that the system is thermalized. This is not the case, but the fact that  $\langle \Psi \rangle = 0$  partly prevents to miss a high time scale. The correlation function is then simply computed by the ensemble average

$$C(\Delta t) = \langle \Psi(t) \Psi^*(t + \Delta t) \rangle / \langle \Psi \Psi^* \rangle. \quad (2.26)$$

This function decays to zero exponentially for large  $\Delta t$  (see Fig. 2.8). The decay constant  $\tau$  and the “speed” of the algorithm  $1/\tau$  are obtained by a fit, from one single long simulation with  $t \gg \tau$ .

The correlation times are long in the transition region (see Fig. 2.9), the efficiency tests are therefore performed on small systems with up to  $32^2$  disks. The global rotation of the system has no physical sense, and one can be tempted to use the observable  $|\Psi|$  instead. However, as shown in Section 4.3.1, one can miss the largest time scale with this choice. For the purpose of this study, it is safer to use the observable which decorrelates the slowest, that is,  $\Psi$ .



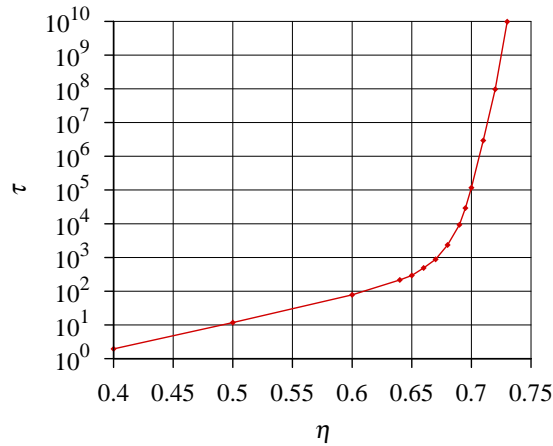


**Figure 2.10:** Density dependence of the correlation time for the local Metropolis algorithm (in displacement per disks) for  $32^2$  disks. The correlation time increases strongly (but remains finite) for densities  $\eta \gtrsim 0.7$  as the system hardly rotates inside the square box.

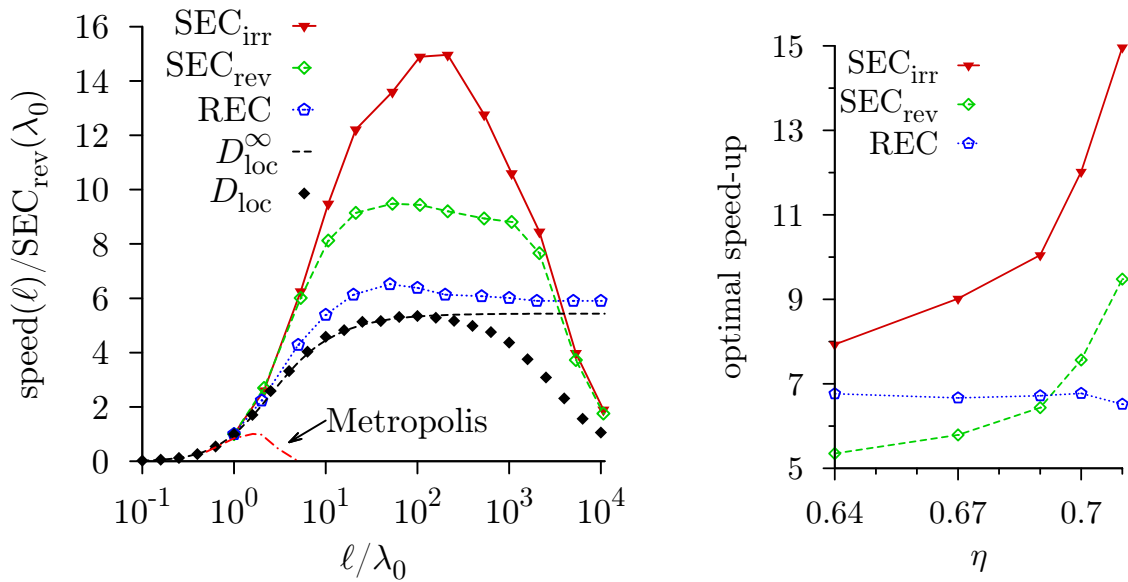


**Figure 2.11:** *Left:* Efficiency of the SEC and the REC algorithms for  $32^2$  disks at  $\eta = 0.71$ . The speeds are normalized by the speed of the reversible SEC algorithm at  $\ell/\lambda_0 = 1$ . The speed of the local Metropolis algorithm (with  $\delta = \ell$ ) and the mean-square displacement per particle from Eq. (2.21) are also shown. *Right:* Density dependence of the optimal speed-up factor. The efficiency of the SEC algorithms increases at the transition. The same behavior is observed for molecular dynamics. (Ref [5], cf. Section 7.1).

The event-chain algorithms with  $\ell/\lambda_0 = 1$  is as fast as the local Metropolis algorithm for its optimal step size  $\delta = 2\lambda_0$ . This well-defined value is chosen as a reference for the different algorithms. The time is measured in number of displaced disks for the event-chain algorithm and in number of attempted moves for the local Metropolis algorithm. In implementation, the time needed for a disk displacement in the event-chain algorithm



is however found to be smaller than the time needed for a move attempt in the local Metropolis algorithm.

For small total displacements  $\ell/\lambda_0 \ll 1$ , the speeds of all the algorithms (reversible and irreversible SEC, REC, and local Metropolis algorithm) are equal and, as expected, proportional to the short-time diffusion coefficient  $D_{\text{loc}}^\infty(\ell) \sim \ell^2$  (see Fig. 2.10). For larger  $\ell/\lambda_0$ , the event-chain algorithm realizes a considerable speed-up compared to the local Metropolis algorithm (also in Fig. 2.10). The speed of the REC algorithm globally follows the behavior of  $D_{\text{loc}}^\infty(\ell)$  and reaches a speed-up factor of  $\sim 6$  toward the local Metropolis algorithm. This behavior can be understood as the dynamics increases  $D_{\text{loc}}^\infty(\ell)$  but the move is not correlated over large distance. Both versions of the SEC algorithm (reversible and irreversible) outperform the REC algorithm, illustrating the usefulness of straight trajectories. The speeds of both algorithms follow the behavior of  $D_{\text{loc}}$ , and they go to zero for large  $\ell$ .

For large  $\ell/\lambda_0$ , the irreversible SEC algorithm is faster than the reversible version. This speed-up is however limited (up to  $\sim 2$  times for  $64^2$  disks at  $\eta = 0.710$ ). A similar speed-up is obtained by an irreversible Monte Carlo algorithm in a Ising model [106]. Unlike the REC algorithm, the SEC algorithm becomes more efficient (as compared to the local Metropolis algorithm) as one approaches the transition from the liquid phase (at density  $\eta \sim 0.710$ ). This property is shared with molecular dynamics (see Fig. 2.10).

The speed-up of the SEC algorithm over the local Metropolis algorithm can be understood by a simple argument. First, as explained before, the short-time diffusion coefficient is larger, which gives a factor  $\sim 4$ . However, this simple picture should be corrected by  $N$ -body effects (the reaction of the system), which are different in both dynamics. In the local Metropolis algorithm, when a disk is displaced, it increases the density at the new position, and reduces the density at the old position. As a consequence, the system suppresses this density fluctuation by diffusion; the disk tends to go back in its original position. This effect, which can also be seen as an elastic reaction of the system to the stress imposed by the move, gives a negative long-time tail to the velocity (displacement here) auto-correlation function  $C_v(t)$  [108, 109]

$$C_v(t) \sim -t^{-d/2-1}. \quad (2.27)$$

In the SEC algorithm, any disk that undergoes a collision is in turn displaced in the same direction. Consequently, the move only creates a density fluctuation at the extremity of the chain of particles. The system is not stressed by this more “physical” move, therefore, the disks do not tend to go back in their original position. This property is confirmed by the analysis of the displacement auto-correlation function.

For  $64^2$  disks at  $\eta = 0.710$ , the optimal speed-up obtained is  $\sim 6$  for the REC algorithm,  $\sim 10$  for the reversible version of the SEC algorithm, and  $\sim 20$  for its irreversible version (see Table 2.0). Analysis on larger systems show that the speed-up is not much further increased<sup>8</sup>. The optimal speeds up are reached for  $\ell$  larger than a constant value, about  $\ell > 100\lambda_0$ .

In term of displaced disks, the maximal speed-up factor is equal to  $\sim 20$  for the best algorithm, and does not increase much with the system size. In term of CPU time, a

---

<sup>8</sup>However, the simulations performed in Fig. 4.18 of Section 4.3.1 show that the event-chain algorithm can reach speed-ups of  $\sim 100$  in an non-equilibrium dynamics.

$N$	Optimal speed-up	
	Reversible	Irreversible
64	$\sim 6$	$\sim 8$
256	$\sim 8$	$\sim 11$
1024	$\sim 9$	$\sim 15$
4096	$\sim 10$	$\sim 20$

**Table 2.1:** Optimal speed-up reached by the SEC algorithm (with respect to the local Metropolis algorithm) at density  $\eta = 0.71$  as a function of particle number.

move attempt with the local Metropolis algorithm is more time-consuming than a disk displacement with the event-chain algorithm (as it requires only a few random numbers for example), which gives another factor  $\sim 2$ . The effective speed-up brought by the irreversible SEC algorithm is therefore  $\sim 40$  in CPU time. In number of collision, molecular dynamics has been found to be  $\sim 60$  times more efficient than the local Metropolis algorithm, a collision is however time consuming. The effective speed-up brought by the molecular dynamics for the fastest implementation (see Section 2.1.1) is therefore  $\sim 10$  compared to the local Metropolis algorithm. The event-chain algorithm is thus more efficient than the molecular dynamics but by a small factor only ( $\sim 4$ ). The event-chain algorithm is however easy to implement and safe from rounding errors (see Section 2.3).

## 2.2.4 Extensions of the algorithm

The number of CPUs per computer system is increasing. It is therefore interesting to analyze the possibilities of parallelization for the event-chain algorithm. The algorithm does not increase its performance for  $\ell > 100\lambda_0$ , it can then be used with  $\ell = 100\lambda_0$ . The algorithm is then local for systems of size  $N \gg 100^2$  disks, and thus easily parallelizable. A way to achieve such a parallelization is to split the system in subsystems of size  $N_{\text{sub}} \gtrsim 100^2$  disks, each subsystem being controlled by a single CPU. This basic parallelization would give a speed-up  $\propto N_p$  where  $N_p$  is the number of CPU.

As for molecular dynamics [94], the event-chain algorithm can be extended to stepped potentials which mimic continuous potentials. For example, the interaction potential can be discretized by constant energy steps  $\delta E$ . The energy landscape seen by a particle is then discrete with an energy step  $\delta E$ . Let  $E$  be the energy of a configuration, a movement similar to the event-chain algorithm can be performed: A particle is displaced straightly until it collides with a “wall” at the energy level  $E$ . The “wall” corresponds to a collision with another particle, and the collision is reversible.  $\ell$  can then be chosen as the sum of the displacements in the energy level  $E$ . This constitutes an algorithm sampling configurations whose potential energy is  $E$ . One can sample the canonical ensemble by coupling this algorithm with a local Metropolis algorithm for example. This algorithm represents an efficient, simple, and parallelizable algorithm for generic particle systems.

## 2.3 Implementation of the algorithm

In order to perform the large-scale simulation needed in this thesis, the event-chain algorithm must be carefully implemented and optimized. The algorithm used is the ir-

reversible “ $xy$ ” version of the event-chain algorithm, which is the fastest version (see Section 2.2.3).

### 2.3.1 Optimization of the algorithm

The total displacement  $\ell$  is the only tunable parameter of the event-chain algorithm. As shown in Section 2.2.3, the efficiency saturates for  $\ell$  larger than a value which does not increase with the system size (a few hundreds of displaced disks). The efficiency decays only for  $\ell \sim N$ . The value of  $\ell$  is therefore not crucial as long as  $1 \ll \ell \ll N$ . We chose  $\ell \propto \sqrt{N}$ .

A number of algorithmic techniques allow us to optimize the algorithm. Let  $L_{\text{coll}}$  be the collision length of two disks, that is, the distance that a disk can be displaced in a given direction before it collides with the other disk (see Fig. 2.11).  $L_{\text{coll}}$  should only be computed for neighboring disks. To that purpose, the disks positions are stored in a cell scheme. The CPU time needed to perform a displacement is therefore  $O(1)$ . The computation of the collision length  $L_{\text{coll}}$ , as well as the update of positions and of the cell scheme, are the most time consuming part of the program. In the  $xy$  version, disks only move horizontally to the right ( $+x$  direction) or vertically to the top ( $+y$  direction) (see Fig. 2.11). These restrictions have several advantages which reduce the computation time. First, positions are updated along one coordinate only, and if a particle crosses a cell boundary, the new cell to which the particle belongs is known. Second, the direction of the movement allows to only explore 6 cells for possible collisions (see Fig. 2.11 again). Third, the collision length  $L_{\text{coll}}$  is computed without using time-consuming trigonometric functions: For a  $+x$  movement, the collision length between a disk  $i$  at position  $\vec{r}_i$  and a disk  $j$  at position  $\vec{r}_j$  is given by

$$L_{\text{coll}} = \Delta x - \sqrt{(2\sigma)^2 - \Delta y^2} \quad (2.28)$$

where  $(\Delta x, \Delta y) = \vec{r}_j - \vec{r}_i$ .

As the precise value of  $\ell$  is not crucial, the only parameter to optimize for the implementation of the algorithm is the size of the cells in which particle positions are stored. Too large cells increase the number of collision tests, while too small cells suppress long displacements. The optimal size of cells corresponds to about one disk per cell (as in Fig. 2.11).

### 2.3.2 Optimization of the code

The CPU time per collision can be used through judicious choice of programming language, compiler, and optimization of programming. The algorithm was coded in Fortran90, which is well adapted to the scientific computation. Fortran90 allows perfect control of the computation such as the random number generation or the precision of the variables for example. The compiler used was Gfortran, the computer used is a cluster of 128 CPUs which are 64bytes Intel Xeon E5540 running at 2.53GHz with 8MB of cache memory.

As individual simulations in this project were running for several months, an important effort to optimize the code was profitable. Memory requirements can be reduced through

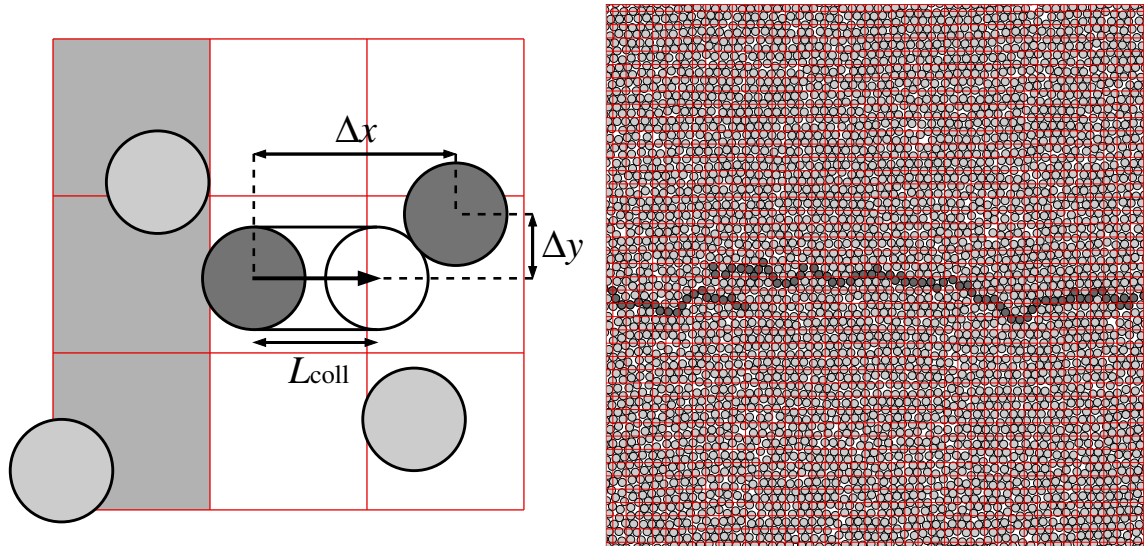


**Figure 2.12:** Event-chain move in the  $+x$  direction. The cell scheme is shown in red. *Left:* A single displacement, only 6 cells are explored for a possible collision.  $L_{\text{coll}}$  can be computed in a simple way without trigonometric functions. If the displaced particle is crossing its cell boundary, the new cell is necessarily the one on the right. *Right:* A complete move during the thermalization of  $64^2$  disks at  $\eta = 0.706$ . The displaced disks are colored in dark gray. The length of the move is chosen to be  $\ell \propto \sqrt{N}$ . The only parameter to optimize is the size of the cells.

a lower precision of the numbers. In a 64 bytes processor, the CPU time needed to perform a computation with simple (32 bytes) or double-precision (64 bytes) is identical. However the allocation of the memory is important in the optimization. Indeed, it takes roughly  $\sim 1$  CPU cycle to access the registers memory,  $\sim 10$  cycles to access cache memory,  $\sim 100$  cycles to access RAM memory, and  $\sim 1000$  cycles to access hard-drive memory. The goal is to store the maximum amount of data in the fastest, but smallest, memory level. In that sense, the precision of numbers is reduced to single precision.

Other improvements were achieved by optimizing each computation. This was done by exploring the program with a profiler which computes the exact time spent in each part of the program. This “fine-tuning” proved efficient. The last step was to find the best optimization option for the compiler, the simplest one “-O2” for Gfortran being already very efficient.

The optimized code performs more than  $3.10^{10}$  displaced disks for systems up to  $N = 256^2$ . For larger systems, this speed drops to  $10^{10}$  displaced disks per hour for a  $N = 2048^2$  system. This speed roughly corresponds to one displacement per 100 CPU cycles, a value that could be still improved by coding the time-consuming subroutines in assembly language, the code would then be CPU specific. This would allow one to allocate memory in a precise way; the disks which are likely to be part of the move could, for example, be already stored in registers or cache memory.

### 2.3.3 Stability and verifications

For long runs (up to  $10^{14}$  displacements), rare events, such as rounding errors due to finite precision, can occur and disrupt the simulations. In order to prevent such an event, a simple addition was made to the algorithm: the collision length was taken as  $\max(L_{\text{coll}}, 0)$ . In that way, if the collision length is  $L_{\text{coll}} < 0$  (meaning that the moving disk and collided disk are overlapping), the (backward) displacement is not accepted. The result is that the incoming disk does not move, and the collided overlapping disk is displaced forward: this reduces the overlapped region. As a global consequence, a starting configuration with many overlapping disks quickly “heals” by itself and becomes a valid configuration: the algorithm is stable and runs with more than  $10^{14}$  displacements can be performed without trouble.

The implementation was carefully tested by comparing the distribution of a given observable obtained with the event-chain algorithm and with an independent algorithm such as the local Metropolis algorithm. To that purpose the orientational order parameter  $\Psi$  of Eq. (2.24) is used. In order to increase the efficiency of this test, the simulations are performed in the transition region ( $\eta \sim 0.7$ ), where a small violation of the balance condition has large consequences on the stationary distribution. The distribution for all the algorithms were found to be identical, confirming the validity of their stationary distribution (see Fig. 2.12).

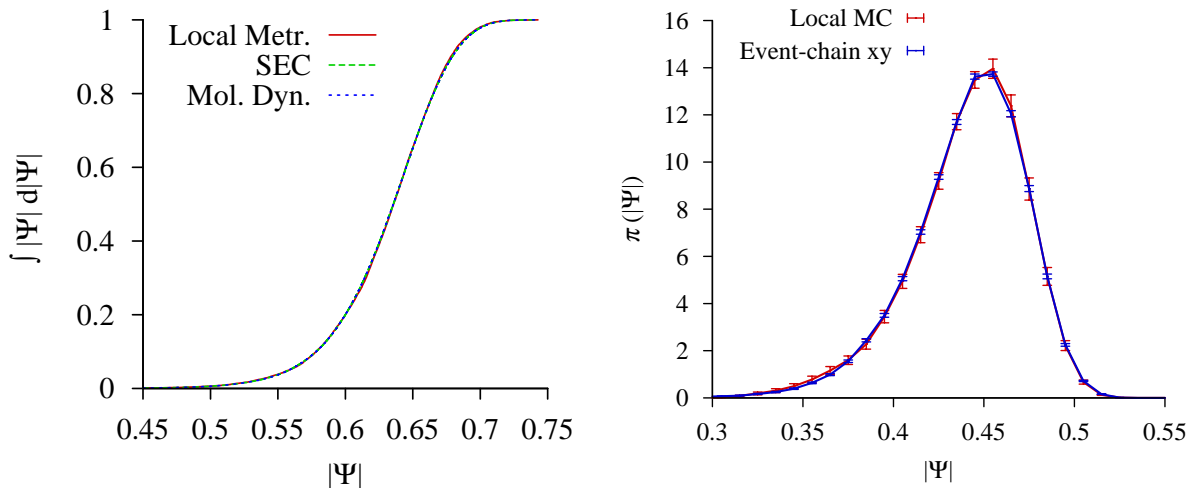


**Figure 2.13:** Comparison of the distribution of  $|\Psi|$  (see Eq. (2.24)). *Left:* Integrated distribution of  $|\Psi|$  for  $32^2$  disks at  $\eta = 0.71$ . The irreversible SEC algorithm, the molecular dynamics, and the local Metropolis algorithm are compared. The distributions are identical. (Ref [5], cf. Section 7.1). *Right:* Distribution of  $|\Psi|$  plotted for  $256^2$  disks at  $\eta = 0.706$  with both the local Metropolis algorithm and the event-chain  $xy$  optimized algorithm. The distributions agree well for  $64 \cdot 10^6$  displacement per particles. (Ref [6], cf. Section 7.3).

## Conclusion

The event-chain Monte Carlo algorithm provides an efficient method in order to simulate hard-core systems. For hard disks, the algorithm was found to be up to  $\sim 40$  times faster

than the local Metropolis algorithm (in CPU time), and up to  $\sim 4$  times faster than the molecular dynamics (in CPU time again). This speed-up is in part explained by the fact that the movement does not induce local compression in the system. In the SEC version, the constant direction also increases the efficiency. Finally, the irreversible SEC version further increases the speed-up. This provides an example of the benefits of breaking the detailed-balance condition in Monte Carlo algorithms going beyond the lifted Markov chains [104].

The event-chain algorithm is easy to implement, parallelizable, safe from rounding errors, and it can be extended to stepped potentials. This algorithm is thus an interesting alternative to the local Metropolis algorithm or to molecular dynamics. The event-chain algorithm has been chosen in this thesis to perform the large-scale simulations of hard disks in order to study the melting transition (see Chapter 3 and Chapter 4).



In this chapter, I detail the methods used to study the hard-disk melting transition (see Chapter 4 and Section 7.3). I discuss the choice of the thermodynamic ensemble, and discuss the statistical error of observables. I then describe the different observables computed during the simulations.

## 3.1 Choice of ensemble

Away from a phase transition, thermodynamic ensembles are equivalent in the limit of large systems. A transition can however break this equivalence. For example, the first-order transition of hard spheres shows a phase coexistence only in a constant-density ensemble. Moreover, in finite-size systems, the fluctuations and finite-size effects depend on the ensemble. These physical effects are complemented by the non-equivalence of the thermalization time of algorithms, and by technical difficulties of implementation. The choice of the thermodynamic ensemble is therefore important. The use of different ensembles would allow one to get complementary information. Nevertheless, the constant-density ensemble will prove sufficient in Chapter 4 to draw conclusions on the nature of the hard-disk melting transition.

### 3.1.1 Constant-density ensemble

In the canonical constant-density (or  $NVT$ ) ensemble, the volume  $V$  and the number of particles  $N$  of radius  $\sigma$  are kept constant. For hard spheres, the temperature  $T$  has no influence on the statistics of the positions; it only affects the velocity distribution. The system is then fully determined by  $N$  and the packing fraction (or density)

$$\eta = \frac{N\pi\sigma^2}{V}, \quad (3.1)$$

the ratio of the occupied volume over the total volume. The partition function for the hard-disk system is defined as

$$Q_{N,V} = \frac{1}{N!} \int \pi(\vec{r}_1, \dots, \vec{r}_N) dr^{2N} \quad (3.2)$$



where  $\pi(\vec{r}_1, \dots, \vec{r}_N) = \exp(-\beta E)$  equals 1 if there is no overlap and 0 otherwise.

Near a first-order transition, this ensemble shows neither metastability nor hysteresis, but rather allows for the phenomenon of thermodynamic phase coexistence which, itself, is absent in the constant-pressure ensemble. The phase coexistence shows large thermalization time. Indeed, the coarsening process to separate the phases is slow, about  $O(N\sqrt{N})$  per particle in  $2D$  for a local dynamic [110] (see Section 4.3.1). Another problem of this ensemble arises in the solid phase. As the length of the box is constant, the box tends to impose a lattice spacing which commensurate with the box. This can induce large finite-size effects.

This ensemble is the simplest to implement, as it requires only particle moves. Moreover, algorithms in this ensemble are fast: with the use of a cell scheme, they require a time  $O(1)$  to move one particle. Because of its simplicity and speed, the main simulations presented in Chapter 4 are performed in this ensemble.

### 3.1.2 Constant-pressure ensemble

In the constant-pressure (or  $NPT$ ) ensemble, the pressure  $P$  as well as  $N$  and  $T$  are kept constant. The volume is then free to fluctuate. For hard spheres,  $P \propto T$ , the system is therefore totally determined by  $N$  and the reduced pressure  $\beta P$  (in order for the pressure to be dimensionless we use  $\beta P(2\sigma)^2$  as pressure parameter in the following). The partition function for hard disks becomes

$$Z_{N,\beta P} = \int Q_{N,V} \exp(-\beta PV) dV. \quad (3.3)$$

The behavior in this ensemble is similar to the constant-density ensemble near a continuous transition. At a first-order transition however (see Section 1.3.1), the  $NPT$  ensemble does not show a phase coexistence, the system directly jumps from one phase to the other.

This ensemble requires particle moves and volume changes. Volume changes are generally done by the classic Wood algorithm [111], which performs homothetic transformations in order to change the volume. An efficient method has been developed to discriminate between a continuous and a first-order transition in this ensemble [112], and is used for hard disks [91]: The volume distribution in a finite system shows two overlapping peaks around the transition, corresponding to the two phases which are alternatively explored (see Fig. 3.0). In the thermodynamic limit, the peaks become infinite and do not overlap as the creation of an interface would cost free energy. The scaling of the free-energy barrier with system size can be extracted from the double-peak structure and is predicted to scales as  $\Delta F \propto \sqrt{N}$  at a first-order transition.

This method has two main problems. First, the free-energy barrier increases with system size. Therefore, the time needed to switch from a phase to another, and thus the thermalization time, becomes large<sup>1</sup>. Second, the classic constant-pressure algorithm for hard disks [111] is slow (see Section 4.4.1), a CPU time of  $O(N)$  per particle is needed to thermalize, and this problem has not yet been overcome.

---

<sup>1</sup>This issue can be overcome by an external field allowing regions which have a low probability to be crossed. The samples have then to be re-weighted [113, 114]

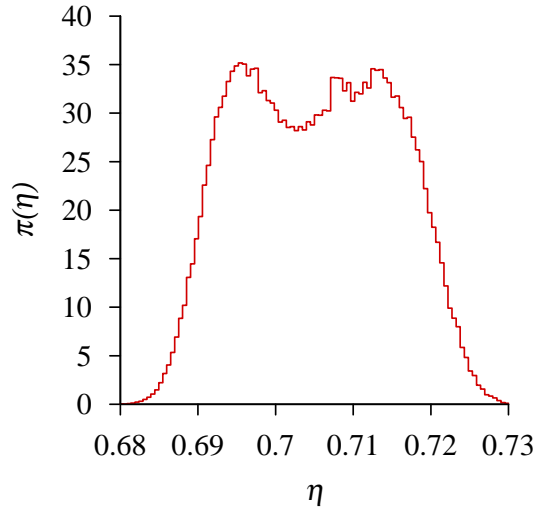


**Figure 3.1:** Density distribution in a constant-pressure simulation for a system of  $32^2$  particles at  $\beta P(2\sigma)^2 = 9.13$ . The interface free energy can be computed from the ratio between the heights of the two peaks and of the height of the minimum between them. Wood’s classic algorithm was run for a few days, but the data are still noisy.

The main simulations presented here have not been performed in this ensemble, however a few simulations in the Gibbs ensemble (which requires volume changes, see Section 4.4.1) were performed to obtain qualitative results.

### 3.1.3 Grand-canonical ensemble

The last main ensemble is the grand-canonical (or  $\mu VT$ ) ensemble, where the chemical potential  $\mu$ , as well as  $V$  and  $T$  are kept constant. The number of particles then fluctuates around its mean value. As for the pressure,  $\mu \propto T$  for hard spheres, the system is therefore totally determined by  $V$  and the parameter  $\beta\mu$ . The partition function for hard disk can be defined as

$$Z_{\beta\mu,V} = \sum_N Q_{N,V} \exp(-\beta\mu N). \quad (3.4)$$

This ensemble is similar to the constant-pressure ensemble and shows a similar behavior at a first-order transition.

This ensemble requires moves as well as insertions and removals of particles. The removal of a particle is straightforward, however the insertion of particle requires free space in the system. Particles can be inserted randomly in the whole system and rejected when they overlap. This sampling can be slow at high densities, however it has the same complexity of  $O(1)$  per inserted particle (see Section 4.4.1).

The little CPU time needed to sample the number of particles renders the grand-canonical ensemble a better choice than the constant-pressure ensemble. This ensemble is however not used in the main simulations of this thesis.

## 3.2 Statistical errors

The samples generated by the Markov chain allow one to compute averages of observables. These samples are correlated and therefore two main questions arise. The first concerns the sampling rate in the chain, and the second concerns the estimation of the statistical error.

### 3.2.1 Sampling rate

Let  $t_{\text{sim}}$  be the total simulation time of a Markov-chain Monte Carlo simulation.  $t_{\text{sim}}$  is the total number of step of the Markov chain, and is taken continuous for simplicity. An observable  $\mathcal{O}$  with finite variance is extracted from the Markov chain after  $\Delta t$  time steps. For a large number  $n = t_{\text{sim}}/\Delta t$  of uncorrelated samples, the statistical error on the mean value of  $\mathcal{O}$  whose standard deviation is  $\sigma = \sqrt{\langle(\mathcal{O} - \langle\mathcal{O}\rangle)^2\rangle}$  is given by

$$\text{Err}(n) = \frac{\sigma}{\sqrt{n}}. \quad (3.5)$$

Let  $\tau$  be the correlation time, that is, the typical time needed for the chain to reach the thermodynamic equilibrium. For  $\Delta t \ll \tau$ , the samples are correlated and Eq. (3.5) underestimates the error. Also, the large number  $n$  of data requires memory and CPU time. In contrast, for  $\Delta t \gg \tau$ , data are uncorrelated (and Eq. (3.5) is correct), but the number  $n$  of data is small. The objective is to increase  $\Delta t$  to an optimal value.

In the limit of  $\Delta t \rightarrow 0$ , and for an initial condition already thermalized, the error can be computed through the auto-correlation function  $C(t)$ . With  $x = \mathcal{O} - \langle\mathcal{O}\rangle$  and  $\sigma^2 = \langle x^2 \rangle$ ,  $C(t)$  is given by

$$C(t) = \frac{\langle x(0)x(t) \rangle}{\sigma^2}. \quad (3.6)$$

The mean value of  $x$  is then

$$M(t_{\text{sim}}) = \frac{1}{t_{\text{sim}}} \int_0^{t_{\text{sim}}} x(t) dt. \quad (3.7)$$

The error, defined as the standard deviation of the mean value, satisfies then

$$\text{Err}(t_{\text{sim}})^2 = \langle M(t_{\text{sim}})^2 \rangle = \frac{1}{t_{\text{sim}}^2} \int_0^{t_{\text{sim}}} \int_0^{t_{\text{sim}}} \langle x(t)x(t') \rangle dt dt' \quad (3.8)$$

$$= \frac{2\sigma^2}{t_{\text{sim}}^2} \int_0^{t_{\text{sim}}} \int_0^t C(t' - t) dt dt', \quad (3.9)$$

which for  $t_{\text{sim}}$  larger than the largest time scale  $\tau$  of  $C(t)$  becomes

$$\text{Err}(t) \underset{\infty}{\approx} \sqrt{\frac{2\sigma^2 D_e}{t_{\text{sim}}}} \quad \text{with} \quad D_e = \int_0^{\infty} C(t) dt. \quad (3.10)$$

The statistical error is then  $\propto 1/\sqrt{t_{\text{sim}}}$ , which was expected as for a chain where  $t_{\text{sim}} \gg \tau$ , the chain can be cut into independent parts of size  $\sim \tau$ . The error thus behaves as a

diffusion process and the diffusion constant  $D_e$  is given by the integrated correlation function.

The error in Eq. (3.10) is the minimal error given by a simulation time  $t_{\text{sim}}$ . For a finite time step  $\Delta t$ , the discretization of the integral in Eq. (3.10) leads to the expression

$$\text{Err}(t) \underset{\infty}{\sim} \sqrt{\frac{2\sigma^2 D'_e}{t_{\text{sim}}}} \quad \text{with} \quad D'_e = \sum_{i=0}^{\infty} C(i\Delta t)\Delta t. \quad (3.11)$$

For a simple exponentially decaying function  $C(t) = \exp(-t/\tau)$ , the discretization error satisfies

$$\frac{D'_e - D_e}{D_e} \leq \exp(\Delta t/\tau) - 1, \quad (3.12)$$

it is therefore sufficient to choose  $\Delta t$  only a few times smaller than  $\tau$ . The case is more complex when the auto-correlation function has many time scales. If  $C(t)$  is a sum of exponentials

$$C(t) = \frac{1}{\sigma^2} \sum_i \sigma_i^2 \exp -t/\tau_i \quad \text{with} \quad \sum_i \sigma_i^2 = \sigma^2, \quad (3.13)$$

the diffusion coefficient satisfies  $\sigma^2 D_e = \sum \sigma_i^2 \tau_i$ , and one has then

$$\frac{D'_e - D_e}{D_e} \leq \frac{\sum \sigma_i^2 \tau_i (\exp \Delta t/\tau_i - 1)}{\sum \sigma_i^2 \tau_i}. \quad (3.14)$$

We see in Eq. (3.14) that even a small  $\tau_i$  can lead to a large discretization error if  $\sigma_i$  is large. In that case, it would be necessary to sample with  $\Delta t \ll \tau_i$ . In practice, the method consists of sampling with the shortest time step in the limit of memory and computer time. In the simulations of this thesis, the extraction time steps are different for each observable, in order to lose little information.

### 3.2.2 Error estimation

The discussion above explained how to obtain the smallest error possible. Here, we describe how to compute this error. The estimation of the error on a given observable is an important topic of the Markov-chain Monte Carlo method. There are two problems related to the error estimation in a Markov chain. First, the chain has to be longer than the largest time scale of the system (the thermalization or correlation time). Second, the chain has to be long enough in order to estimate the standard deviation of the computed observable. If both conditions are satisfied, the auto-correlation function can then be computed, and the error is obtained through Eq. (3.11).

However, there are no rigorous arguments to validate if the chain has been run longer than the thermalization time. This problem is a major aspect of the Markov-chain Monte Carlo method and is the subject of Part II. In practice, long simulations are performed on small systems, then the system size is increased while the thermalization time behavior is computed. In a general way, the simulations give information about the physics of the system, which in return gives information about the thermalization time. This method is not rigorous and has to be used carefully.

In this thesis, we estimated the error by a more simple and robust method than computing the auto-correlation function. A Markov chain was run for a long time (one year of computation), its only purpose being to compute the thermalization time of the system and extract a few independent configurations. These configurations are the initial conditions of independent short runs used to compute the observables. The number of initial configurations have to be large enough in order to estimate the standard deviation  $\sigma$  of the observable. In this thesis,  $n = 64$  configuration were always used.

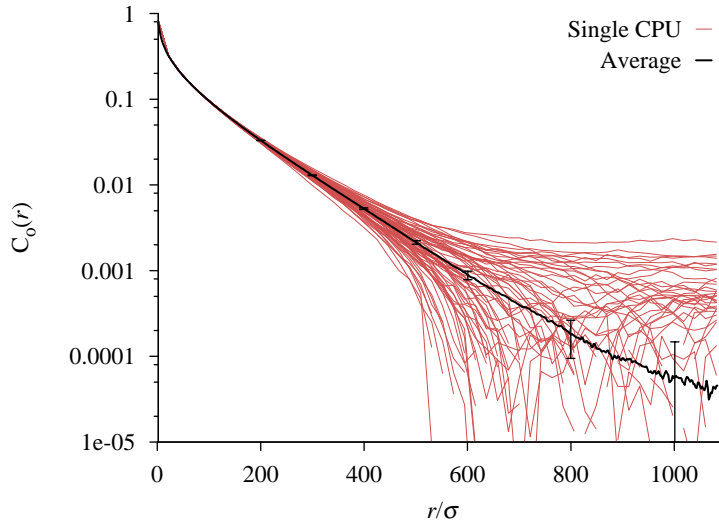


**Figure 3.2:** Example of error estimation for the orientational correlation function of  $1024^2$  particles at  $\eta = 0.700$ . Each of the 64 simulations are independents, allowing a safe computation of the standard deviation. (Ref [6], cf. Section 7.3).

The value of an observable  $\mathcal{O}$  is then directly computed by averaging over the  $n$  runs (see Fig. 3.1),

$$\langle \mathcal{O} \rangle = \frac{1}{n} \sum_{\text{runs}} \langle \mathcal{O} \rangle_{\text{single run}}. \quad (3.15)$$

The standard deviation is given by

$$\sigma = \sqrt{\langle (\mathcal{O} - \langle \mathcal{O} \rangle)^2 \rangle}, \quad (3.16)$$

and the statistical error by

$$\text{Err} = \sigma / \sqrt{n}. \quad (3.17)$$

This method is simpler, safer, and more adapted to parallel computing than the computation of the integrated auto-correlation function of Eq. (3.11) only.

### 3.3 Computation of observables

Monte Carlo simulations give access to any observable. Here we discuss the order parameter and control variables relevant for the melting transition in hard disks.

### 3.3.1 Orientational order parameter

The orientation defined in Section 1.3.2 with the displacement field  $\vec{u}(\vec{r})$  can be defined in a particle system as the angle  $\theta_{j,k}$  of a bond  $\vec{r}_k - \vec{r}_j$  connecting two neighboring disks  $j$  and  $k$  with respect to a given axis (see Fig. 3.2). As the lattice in the hard-disk solid is triangular, the angles  $\theta_{j,k}$  and  $\theta_{j,k} \pm \pi/3$  represent the same orientation of the system. An appropriate orientation of the system in order to have only one value of the orientation per disk is then  $6\theta_{j,k}$ . Therefore, the local orientational order parameter  $\psi_j$  of the disk  $j$  is defined by

$$\psi_j = \frac{1}{n_j} \sum_{\langle k,j \rangle} \exp(i6\theta_{j,k}) , \quad (3.18)$$

where the sum goes over the  $n_j$  neighbors of disk  $j$  (see Fig. 3.2 again). For a perfect

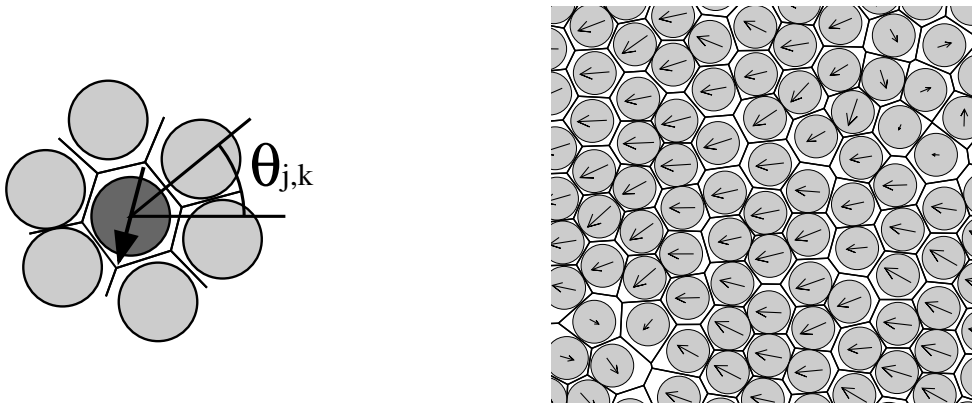


**Figure 3.3:** *Left:* Local orientational bond-order parameter  $\psi_j$  of the disk  $j$ . The argument of the parameter corresponds to 6 times the angle of a bond, and it defines the orientation of the local hexagonal neighborhood. *Right:* Orientation field of a hard-disk configuration at a density  $\eta = 0.7$ . (Ref [6], cf. Section 7.3).

hexagonal neighborhood around the disk  $j$ , the angle of this complex-valued order parameter corresponds to 6 times the angle of a bond. Moreover, the magnitude of  $\psi_j$  measured the degree of local order:  $|\psi_j| = 1$  for a perfect hexagon while  $|\psi_j| \sim 0$  for a disordered neighborhood. The vector  $(\text{Re}(\psi_j), \text{Im}(\psi_j))$  is the analogue of a spin in the XY model. This order parameter requires a definition of neighboring disks, which is done in this thesis through the Voronoi tessellation (Delaunay triangulation [115]): the disk  $j$  and  $k$  are neighbors if the midpoint of the line connecting their centers is closer to  $j$  and  $k$  than to any other disk.

It has proved helpful to directly visualize the field. This can be done in the same way as for XY spins (see Section 1.2.3). The local orientations are colored depending on the argument of the local orientational parameter. The color follows a red-green-blue colorbar going from blue for orientations pointing in the projection axis, to red for the opposite direction. This visualizing method does not differentiate two orientations symmetric toward the projection axis, it is however easy to interpret (see Section 4.1).

The global orientational order parameter of a configuration can then be computed by

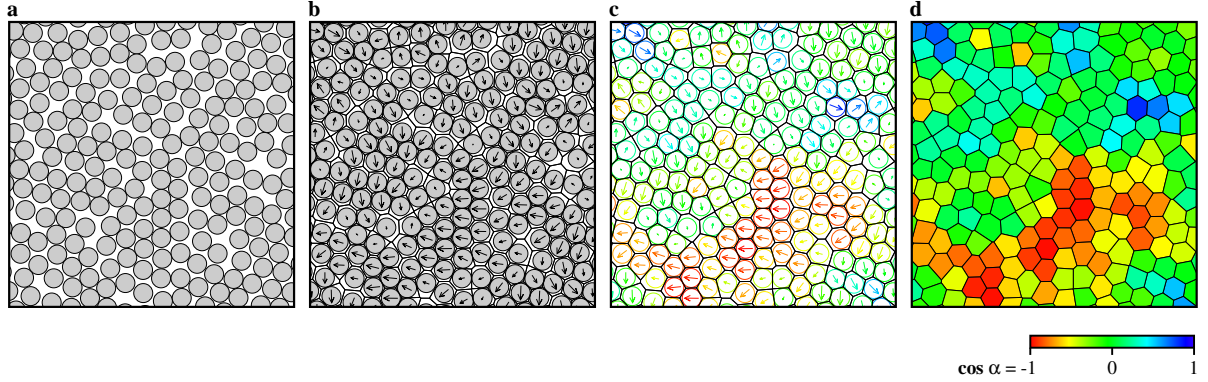


**Figure 3.4:** Close view of the construction for the visualization of the orientational field. **a:** Hard disks **b:** Voronoi construction, the arrows represent the local orientations. **c:** Coloration of the orientation depending on their projection toward a given axis. **d:** The Voronoi cells are colored. (Ref [6], cf. Section 7.3).

averaging the local orientation on the  $N$  disks

$$\Psi = \frac{1}{N} \sum_{j=1}^N \psi_j. \quad (3.19)$$

In an infinite system,  $\Psi$  is finite in the solid phase and zero otherwise. However,  $\Psi$  is also finite in a hexatic (or in a liquid) because of the finite size of the sample. A finite-size analysis is then required. Information of further interest is given by the spatial orientational correlation function. The orientational correlation between two disks  $i$  and  $j$  is given by  $\psi_i^* \psi_j / \langle |\psi|^2 \rangle$ . The orientational correlation function  $C_o(r)$  at a distance  $r$  is obtained by averaging the correlations of pairs whose distance satisfies  $r - \delta r/2 < |\vec{r}_j - \vec{r}_i| < r + \delta r/2$ . The discretization step  $\delta r$  of  $C_o(r)$  is chosen to be  $\delta r \sim \sigma$ . In a sample it is not necessary to chose the  $N(N-1)/2$  pairs, a number of pairs  $\propto N$  leads to little loss of information. The extraction rate is chosen to be  $10 \times N$  pairs each  $10^3 \times N$  displacements.

### 3.3.2 Defects and density

The KTHNY theory is based on defect unbinding. A disk with five neighbors is identified as a positive disclination, while a disk with seven neighbors as a negative disclination. The dislocation are seen as a pair of five and seven disclinations (see Section 1.3.2). A view of these defects is seen on Fig. 3.4.

The number of defects can give insights about the nature of the phase. A more relevant observation is to determine whether the defects are bound or not. In a system with periodic boundary conditions, the number of opposite defects are always equal (the total Burgers vector is zero as well as the total winding number). The strategy to distinguish between bound pairs and free defects is then (as for vortices, see Section 1.2.3) to compute the Burgers vector (or winding-number) on a subsystem of increasing size  $l$ . In the case of bound pairs, the total Burgers vector (or winding number) behaves as  $\propto \sqrt{l}$ , while in the case of free defects, the Burgers vector (or winding number) is  $\propto l$ . This procedure is hard to apply in practice (and is not applied in this thesis) as the density of free defects is much



lower than the density of bound defects; it requires large subsystems to get significant results.

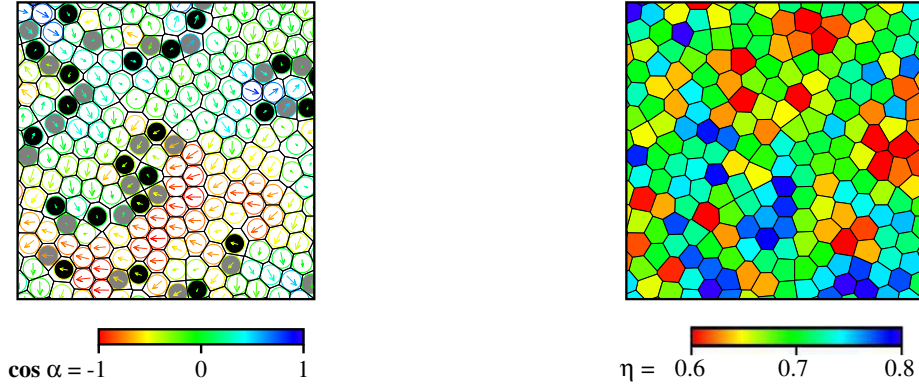


**Figure 3.5:** Close view of the defect and local density visualization *Left:* Disks with seven neighbors (negative disclinations) are colored in black while disks with five neighbors (positive disclination) are colored in gray. *Right:* To visualize the local density, the Voronoi cells are colored depending on their area. The large local fluctuations impose a coarse-graining in order to visualize large-scale density fluctuations (see Section 4.1 and Section 7.3).

The local density of the system is directly computed with the area of the Voronoi cell of each disk (see Fig. 3.4), and colored as for the orientation field. However, the local fluctuations of density are large, and this prevents distinguishing between two phases of slightly different densities. The density of a cell is thus replaced by the averaged density  $\eta_{cg}$  of the neighboring cells up to a distance of  $50\sigma$ . This coarse-graining allows visualization of large-scale density fluctuations (see Fig. 4.1).

### 3.3.3 Positional order

The positional order is defined by the structure factor  $S(\vec{K})$  at the first Bragg peak  $\vec{K}$ . For  $N \rightarrow \infty$ ,

$$S(\vec{K}) = \frac{1}{N} \left| \sum_n \exp i\vec{K} \cdot \vec{r}_n \right|^2 \quad (3.20)$$

$$= \frac{1}{N} \sum_{n,m} \exp i\vec{K} \cdot (\vec{r}_m - \vec{r}_n). \quad (3.21)$$

As the computing time is  $O(N)$  for the evaluation of Eq. (3.20) and  $O(N^2)$  for Eq. (3.21), the former choice has been widely used [78, 25]. However, Eq. (3.21) should be used. Indeed, the relevant quantity is  $\exp i\vec{K} \cdot (\vec{r}_m - \vec{r}_n)$ , and in a finite system with periodic boundary conditions, the vector  $\vec{r}_m - \vec{r}_n$  should be the shortest one. In the first definition (Eq. (3.20)), this choice is not possible, and nearby disks  $(n, m)$  separated by a boundary count as being distant and thus enhance the positional order. Moreover, Eq. (3.21) can be computed in  $O(N)$  by random sampling without loss of information.

The behavior of the structure factor with system size reveals the positional ordering of the system. One can also compute the positional correlation function defined as

$$C_{\vec{K}}(r) = \left\langle \exp i\vec{K} \cdot (\vec{r}_m - \vec{r}_n) \right\rangle_{d(i,j)=r}. \quad (3.22)$$



The above observables can be computed by extracting the value  $\vec{r}_m - \vec{r}_n$  of pairs of disks  $(n, m)$ , and computing  $\vec{K} \cdot (\vec{r}_m - \vec{r}_n)$ . However, this method requires knowledge of the position of the first Bragg peak  $\vec{K}$  before the simulation. This problem could be solved under the approximation that the peak's position is at the same position as the peak given by the perfect triangular lattice  $\vec{k}_{\text{perf}}$  [78, 25]. The absolute value  $|\vec{k}_{\text{perf}}| = k_{\text{perf}}$  could then be computed with the density of the system only,

$$k_{\text{perf}} = \frac{2\pi}{a_0\sqrt{3}/2} \quad \text{with} \quad a_0 = \sqrt{\frac{V}{N\sqrt{3}/2}}, \quad (3.23)$$

the only varying parameter being the orientation which can be computed through the global orientational order parameter  $\Psi$ . However, this approximation is incorrect in the hard-disk system, as the value of  $k_{\text{perf}}$  differs from the value of  $k_{\text{peak}}$ , even at high densities (see Fig. 3.5). This difference is explained by the defects in the system, and especially by the vacancies: their density is always finite as their elastic energy is finite. This difference in the value of  $\vec{K}$  leads to incorrect positional order for a distance  $L \gg 1/|k_{\text{peak}} - k_{\text{perf}}|$ . For  $\eta = 0.720$ ,  $|k_{\text{peak}} - k_{\text{perf}}| \simeq 0.005/\sigma$ . The correlation function computed with  $k_{\text{perf}}$  is therefore not valid at a distance larger than  $r \sim 1/(0.005/\sigma) = 200\sigma$ . It is thus crucial to use the appropriate value of  $\vec{K}$  in order to access the long-distance behavior of the positional order.

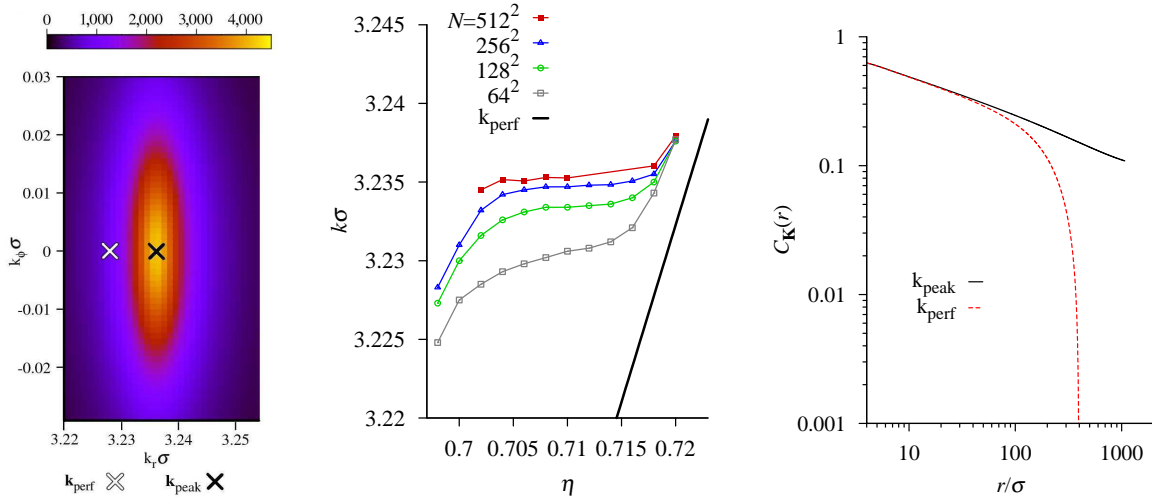


**Figure 3.6:** *Left:* First Bragg peak for  $1024^2$  disks at  $\eta = 0.718$ , the position  $k_{\text{peak}}$  of the maximum of the peak is not the perfect triangular lattice position  $k_{\text{perf}}$ . *Center:* Bragg peak  $k_{\text{peak}}$  vs. density for different system sizes. Even at high density,  $k_{\text{peak}} - k_{\text{perf}} \simeq 0.005/\sigma$  because of the finite concentration of defects. *Right:* Positional correlation function at  $\eta = 0.720$  with the two values of  $|\vec{K}|$ : the correlation computed with  $k_{\text{perf}}$  is underestimated for distances  $r > 200\sigma$ . (Ref [6], cf. Section 7.3).

In order to avoid the problem of knowing  $|\vec{K}|$ , the values of  $\vec{r}_m - \vec{r}_n$  are stored in a 2D histogram. This corresponds to computing the 2D pair-correlation function  $g(\vec{r})$ . Let  $\rho_d(\vec{r})$  be the average density seen by a disk. The pair-correlation function is defined by  $g(\vec{r}) = \rho_d(\vec{r})/\rho_0$  where  $\rho_0$  is the density of the system. By definition,  $g(\vec{r})$  corresponds to the above histogram normalized in order to have  $\langle g(\vec{r}) \rangle = 1$ .

As the system performs global rotations, the vectors  $\vec{r}_m - \vec{r}_n$  are rotated by the total orientation of the system  $\arg \Psi$ . This allows the averaging of  $g(\vec{r})$  on many samples. In order for the first Bragg peak to be properly computed, the resolution of the histogram has to be  $\delta r \ll \sigma$ .  $g(\vec{r})$  requires then a large amount of memory, which is however not prohibitive. First, the symmetry of the triangular lattice allows storage of the values of  $g(r, \theta)$  for only  $\theta \in [0, \pi/6]$  without information loss. Second, a resolution of  $\delta r = \sigma/5$  is enough. For the largest system of  $1024^2$  disks, there is therefore only  $\sim 10^7$  values to store for the histogram.

The structure factor is computed with a Fourier transform of  $g(\vec{r})$ <sup>2</sup>:

$$S(\vec{k}) = 1 + \rho_0 \int g(\vec{r}) \exp i\vec{k} \cdot \vec{r} \, d^2r, \quad (3.24)$$

which allows the value of  $\vec{k}_{\text{peak}}$  to be determined. The positional correlation function is then computed through  $g(r, \theta)$  in polar coordinates

$$C_{\vec{k}_{\text{peak}}}(r) = \frac{1}{2\pi g(r)} \int g(r, \theta) \exp i\vec{k}_{\text{peak}} \cdot \vec{r} \, d\theta. \quad (3.25)$$

$C_{\vec{k}_{\text{peak}}}(r)$  shows oscillations, and this can prevent the determination of the positional order. These oscillations are removed by using  $g(r, \theta) - 1$  instead of  $g(r, \theta)$ , or by averaging with a Gaussian window as

$$C_{\vec{k}}^{\text{av}}(r) = \text{const.} \int C_{\vec{k}}(r') g(r') \exp -[(r' - r)/(2\sigma)]^2 \, dr'. \quad (3.26)$$

When  $g(\vec{r})$  is known, there is however a simpler way to access the positional correlations which does not require any Fourier transform. Near the solid,  $g(\vec{r})$  is a lattice of peaks. The decay of these peaks with distance gives the positional correlation function. A cut along a given axis can be performed in order to look at the decay (see Fig. 3.6 and Fig. 4.13).

In the liquid or hexatic phase, the positional correlation function is not defined as these phases are not oriented in the thermodynamic limit. In practice,  $\xi_p$  is computed only in the hexatic phase, where the system is always oriented in a finite system. However, we note that the correlation length  $\xi_p$  is not rigorously defined. As for the orientation, the extraction rate is  $10 \times N$  pairs each  $10^3 \times N$  displacements.

### 3.3.4 Pressure and chemical potential

In the constant-density ensemble, where the volume  $V$  is a control parameter, the pressure is an observable which enters the equation of state. The canonical pressure is given by:

$$P = - \frac{\partial F(N, V, T)}{\partial V}, \quad (3.27)$$

where  $F(N, V, T) = -k_B T \ln Q_{N, V}$  and  $Q_{N, V}$  is given by Eq. (3.2). This value can be computed in a simulation using the virial theorem:

$$P = \frac{Nk_B T}{V} + \frac{1}{2} \left\langle \sum_{i,j} \vec{f}(\vec{r}_i - \vec{r}_j) \cdot (\vec{r}_i - \vec{r}_j) \right\rangle. \quad (3.28)$$

---

<sup>2</sup> $g(\vec{r}) - 1$  can also be used in order to remove the central peak.

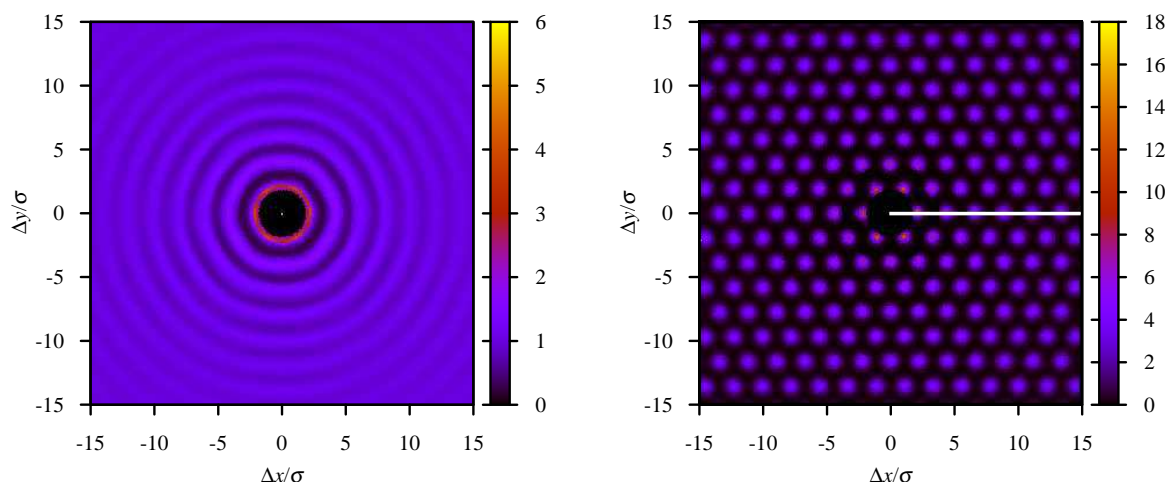


**Figure 3.7:** Pair-correlation function  $g(\vec{r})$  for different densities. *Left:*  $\eta = 0.696$ , the system is not oriented,  $g(\vec{r})$  is isotropic (a slight anisotropy is observed due to the residual orientation in a finite-size system). *Right:*  $\eta = 0.720$ , the system is oriented,  $g(\vec{r})$  is a lattice. The structure factor as well as the positional correlation function can be computed. The decay of the peaks along an axis (white line) is a direct way to access the positional order without a Fourier transform.

For hard disks, the potential is discontinuous, the virial pressure [116] can be computed through:

$$P = \frac{N}{V}k_B T + 2\pi\sigma^2 \left(\frac{N}{V}\right)^2 g(2\sigma^+)k_B T \quad (3.29)$$

where  $g(2\sigma^+)$  is the contact value of the isotropic pair correlation function. The dimensionless pressure  $\beta P(2\sigma)^2$  is then

$$\beta P(2\sigma)^2 = \frac{4}{\pi}\eta[1 + 2\eta g(2\sigma^+)]. \quad (3.30)$$

The isotropic pair-correlation function is computed with high precision near  $r = 2\sigma$ . The contact value  $g(2\sigma^+)$  is then obtained through a fit of this function with a polynomial (see Fig. 3.7). In order to compute the statistical error, the fits are performed on each of the 64 independent runs. The high-precision computation of  $g(r)$  is done by extracting each pair of neighboring disks ( $O(N)$ ) each  $50 \times N$  displacements.

The chemical potential  $\mu$  as a function of volume is also an equation of state of the canonical ensemble. If the equation of state  $P(v)$  is already known, the computation of the chemical potential is not needed as  $P$  and  $\mu$  are related through the Gibbs-Duhem relation

$$Nd\mu = VdP. \quad (3.31)$$

However,  $\mu(V)$  can be used to confirm the results obtained through the virial pressure. The chemical potential is defined in the constant-density ensemble by

$$\mu = \frac{\partial F(N, V, T)}{\partial N}. \quad (3.32)$$

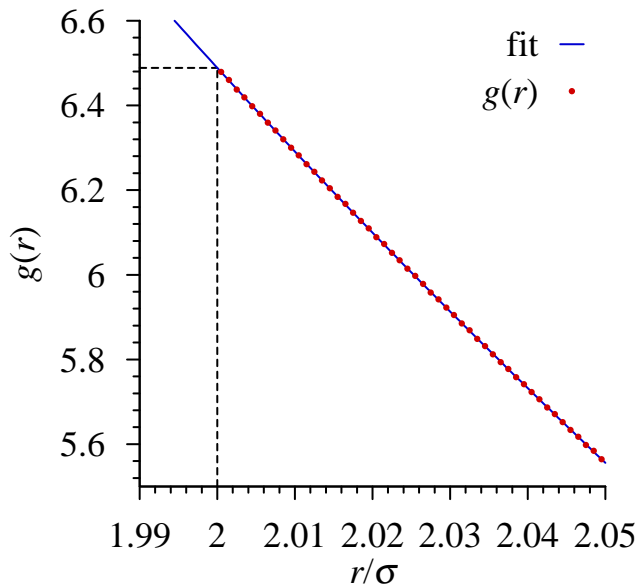


**Figure 3.8:** Isotropic pair-correlation function  $g(r)$  near the contact value  $2\sigma$  for one of the 64 runs at  $\eta = 0.708$ ,  $N = 1024^2$ . A polynomial fit is performed in order to extract the contact value  $g(2\sigma^+)$  which yields the pressure.

Other definitions of  $Q_{N,V}$  can be used to turn it dimensionless, with the single consequence of adding a constant to  $\mu$ , a non-issue as only differences in  $\mu$  are relevant.  $\mu$  can be computed by the Widom insertion method [117]: An extra disk is randomly inserted (with a uniform distribution) in the system. If the disk does not overlap other disks the attempt is successful, and failed otherwise. The probability for successful insertion  $p_i$  is computed. Direct computation of Eq. (3.32) gives

$$\beta\mu = \ln \frac{N}{V p_i}, \quad (3.33)$$

and as additive constants are irrelevant, the chemical potential is computed in this thesis through

$$\beta\mu = \ln \frac{\eta}{p_i}. \quad (3.34)$$

The probability of insertion is low at high densities ( $p_i \simeq 2.5 \times 10^{-6}$  for  $\eta \sim 0.7$ , see Section 4.1.2), and a large number of trials are performed, of the order of  $N$  each  $5 \times N$  displacements.

## Conclusion

The Monte Carlo method in the constant-density ensemble, with the use of the event-chain algorithm, provides a simple yet efficient method to study the hard-disk system. The tools

discussed in the present chapter will allow us to study the hard-disk melting transition in Chapter 4. The direct visualization will reveal to be as useful as the quantitative computation of observables.

## Hard-disk melting transition

In this chapter, I present the results obtained for the melting transition of the hard-disk system. The simulations were obtained with the event-chain algorithm (see Chapter 2). The system displays a phase-coexistence region, and thus undergoes a first-order transition. I then show that the coexisting phases are liquid and hexatic. The hexatic-solid transition is found to be of the KT type. I finally address the question of thermalization and finite-size effects. These results have been published in [6] (see Section 7.3).

### 4.1 Phase coexistence

As seen in Chapter 1 (see Section 1.3.1), a first-order transition in a constant-density ensemble (for a particle system) shows a region of phase coexistence. This property is not shared with continuous transitions. The hard-disk system displays such a coexistence, and therefore undergoes a first-order transition.

#### 4.1.1 Direct visualization

A simple and convincing way to evidence the phase coexistence is to visualize the orientation field of a large thermalized configuration. The projection of the orientation field on the main orientation (see Section 3.3.1) for a configuration at  $\eta = 0.708$  shows that the system is separated into two distinct phases. In the first phase, the orientation is maintained over the whole system, and few defects are present. In the second phase, the orientation is disordered, and many defects are present (see Fig. 4.0).

The coexistence of the two phases in the constant-density ensemble is due to their different densities at the transition. The distribution of the local density  $\eta_{cg}$  (coarse grained on a radius of  $50\sigma$ ) is bimodal (see Fig. 4.0 e), and the two peaks correspond to  $\eta_{cg} \sim 0.700$  and  $\eta_{cg} \sim 0.716$ . In principle, the system could still be composed of patches at these two densities. However, the orientation does not confirm this picture. The visualization of the density field (see Fig. 4.1) at different densities confirms the phase separation: the oriented phase matches the high-density region  $\eta \sim 0.716$ , and the disordered phase matches the low-density region  $\eta \sim 0.700$ .



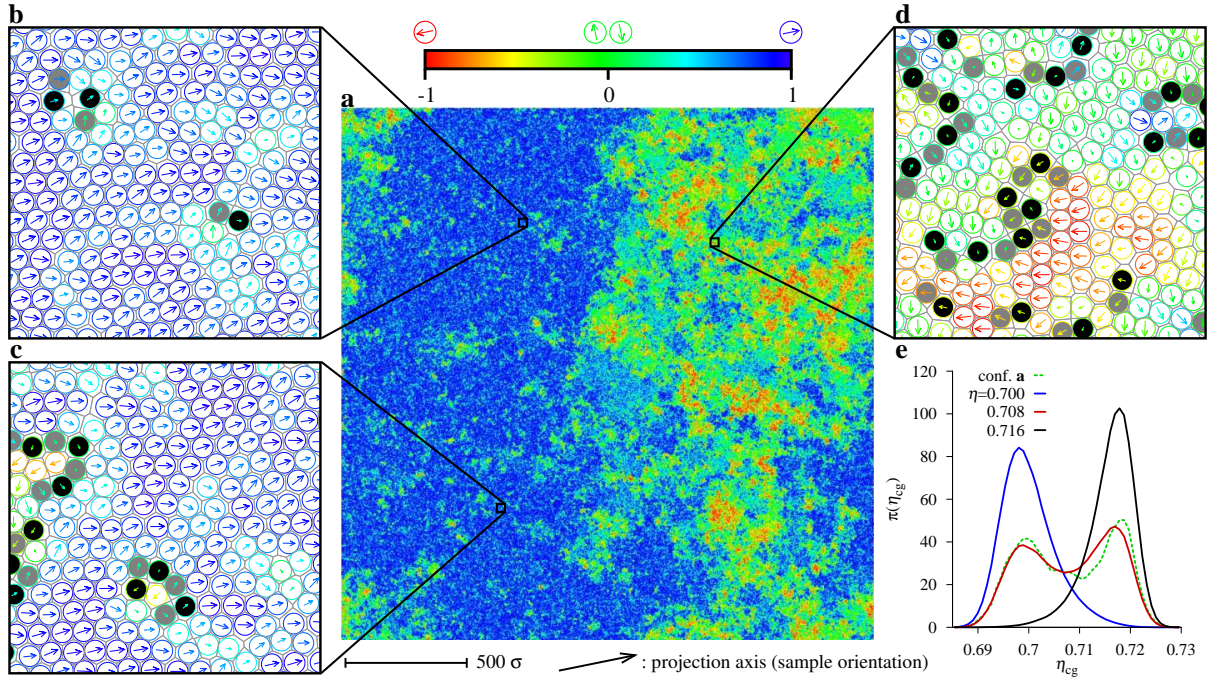


**Figure 4.1:** Visualization of the phase coexistence at  $\eta = 0.708$  for  $1024^2$  disks. **a:** Projection of the orientation on the main orientation. The system shows an oriented phase with a few defects (blue part, see detailed view **b** and **c**), which coexists with a disordered phase with many defects (multicolor part, see **d**). The two interfaces close onto themselves via the periodic boundary conditions. A free dislocation is seen in the ordered phase (**b**) which hints at the hexatic nature of the ordered phase. **e:** Distribution of the coarse-grained local density  $\eta_{cg}$ . The density is bimodal, with a peak at  $\eta_{cg} \sim 0.700$  and another one at  $\eta_{cg} \sim 0.716$ . (Ref [6], cf. Section 7.3).

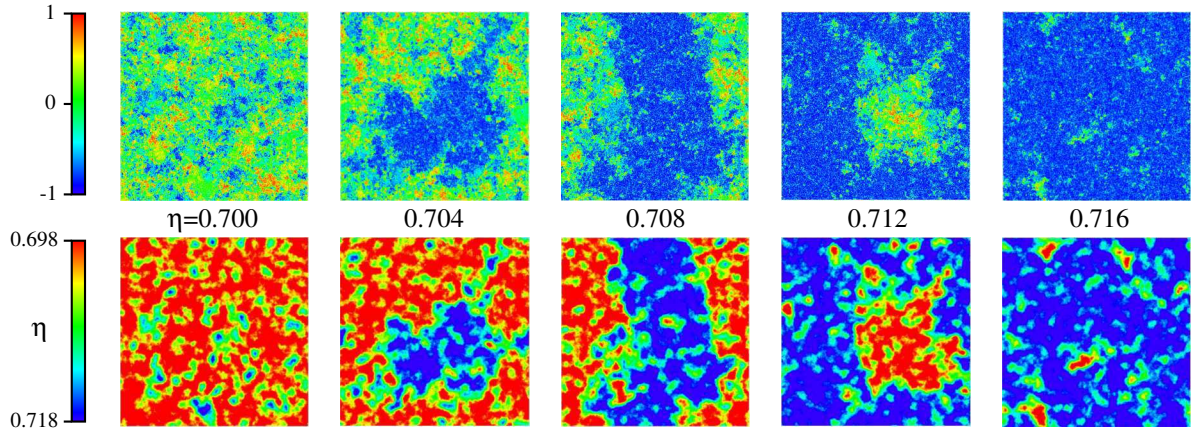


**Figure 4.2:** Synopsis of the orientation (upper panels) and coarse-grained local density  $\eta_{cg}$  (lower panels) of configurations of  $1024^2$  disks at different densities. The disordered phase has a low density ( $\eta \sim 0.700$ ), while the ordered phase has a high density ( $\eta \sim 0.716$ ). The interface minimizes its length in the periodic box: a (circular) bubble or a (flat) stripe depending of the density and system size. (Ref [6], cf. Section 7.3).

The evolution of the system with density follows what is expected for a first-order transition. At a density higher than  $\eta = 0.700$  ( $\eta \sim 0.704$ ), a “bubble” of the high-density phase appears in the system. The phase separation brings an extra free energy to the system  $\Delta F = \gamma\ell$  where  $\gamma$  is the interface tension and  $\ell$  is the length of the interface. The interface therefore minimizes its length, and this explains the bubble shape. The bubble would become asymptotically circular in the thermodynamic limit ( $N \rightarrow \infty$ ). At an intermediate density ( $\eta \sim 0.708$ ), the two phases have the same volume; each phase has a “stripe” shape. The two interfaces close onto themselves via the periodic boundary conditions, and would become flat in the thermodynamic limit. At a higher density ( $\eta \sim 0.712$ ), a bubble of the low-density phase is surrounded by the high-density phase. The bubble finally disappears at  $\eta \sim 0.716$  (see Fig. 4.1).

These direct observations indicate that for  $N = 1024^2$ , the hard-disk system displays a phase coexistence in the region  $\eta \in [0.700, 0.716]$ . This signals a first-order transition. The correlation lengths of these phases are smaller than the system size, therefore the first-order nature of the transition remains in the thermodynamic limit (see Section 4.3.2).

### 4.1.2 Equation of state

In order to quantitatively confirm the above observations, the equation of state (pressure or chemical potential over volume) is computed in the vicinity of the transition.

#### Pressure in a finite-size system

As seen in Chapter 1 (see Section 1.3.1), the first-order nature of the transition is the result of enforcing - for an infinite system - the convexity of the free energy (see Eq. (1.43)). The pressure takes a constant value  $P^*$  during the phase transformation. This result is valid for an infinite system as the interface free energy  $\Delta F = \gamma\ell$  between the two phases can be neglected. Indeed, the length of the interface scales as  $\ell \propto \sqrt{N}$  whereas the bulk free energy scales as  $F \propto N$ .

In a finite system, the interface free energy  $\Delta F$  cannot be neglected, and the total free energy of the system is not necessarily convex. As  $\Delta F \propto \ell$ ,  $P(v)$  shows a loop, which is thermodynamically stable (see Fig. 4.2). This loop, and the negative compressibility it implies, is in agreement with thermodynamics.

As for the van der Waals loop, the behavior of the system at the thermodynamic limit can be obtained through the Maxwell construction. The extra free energy per particle  $\Delta f = \Delta F/N$  for a system of size  $L = \sqrt{N}$  at a specific volume  $v$  can be computed by integrating  $P(v)$  with respect to  $P^*$ : as  $P = -\partial f/\partial v$ ,

$$\Delta f(v) = f_L - f_\infty = \int_{v_1}^v [P^* - P(v')] dv'. \quad (4.1)$$

For  $v$  such as  $P(v) = P^*$ , this corresponds to the hatched area of Fig. 4.2. This allows computation of the interface tension  $\gamma$  for this system. The fact that  $\Delta f \rightarrow 0$  for an infinite system confirms that the loop vanishes in the thermodynamic limit.

A continuous transition can also give a loop in a finite-size system [118], however the scaling of the interface free energy  $\Delta f$  would be different [112]. The finite-size scaling of  $\Delta f$  discriminates between a first-order and a continuous transition:  $\Delta f \propto 1/L$  in a



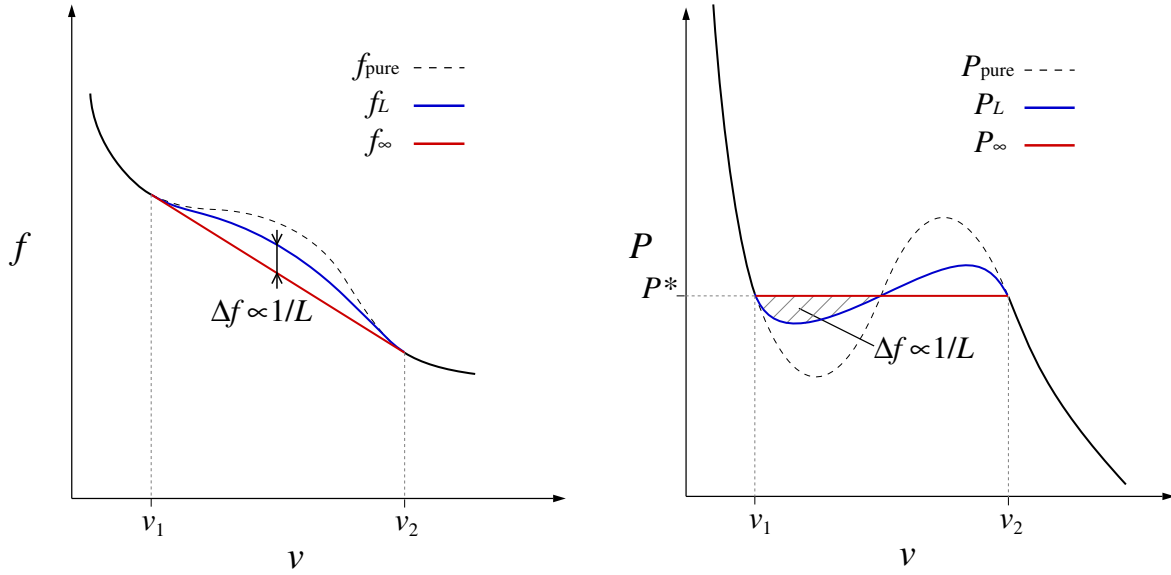


**Figure 4.3:** Qualitative behavior of the free energy and pressure in a constant-density ensemble for a first-order transition in the thermodynamic limit (red curve) and in a finite-size system (blue curve). *Left:* The interface tension brings an additional free energy  $\Delta F$  to the system which scales as  $\Delta F \propto \sqrt{N}$ . *Right:* The extra free energy induces a stable loop in the equation of state, the loop vanishes in the thermodynamic limit.

first-order transition while  $\Delta f$  decreases faster for a continuous transition. This method works for the  $q$ -state Potts model. It is known as the Lee-Kosterlitz method [112].

The behavior of an interface depends on its dimension [119]. A 1D interface with an interface tension  $\gamma \neq 0$  is “rough”, in the sense that its width scales as  $\sqrt{\ell}$  (see Fig. 4.3). However, the interface is “oriented”: the orientation is kept constant at large distances (see Fig. 4.3 again). This behavior justifies the assumption that  $\ell \propto \sqrt{N}$  for large systems.

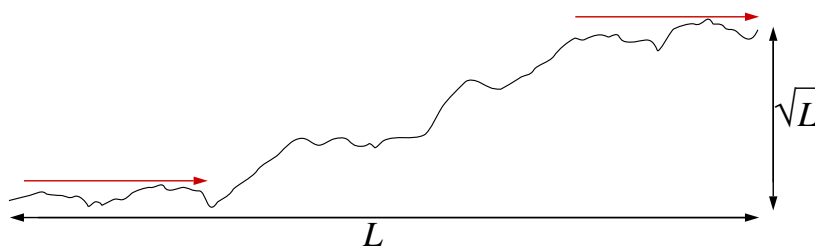


**Figure 4.4:** Schematic 1D interface with a tension  $\gamma \neq 0$ , the width is  $\propto \sqrt{L}$  but the orientation is kept constant. The total length of the interface for large distances is  $\ell \propto L$ .

### Hard-disk equation of state

The equation of state (computed through the virial pressure, see Section 3.3.4) for hard disks confirms the picture of a first-order transition (see Fig. 4.4). A loop in the transition region is observed, and reduces with system size. The Maxwell construction confirms the

limiting values of  $\eta \sim 0.700$  and  $\eta \sim 0.716$ .

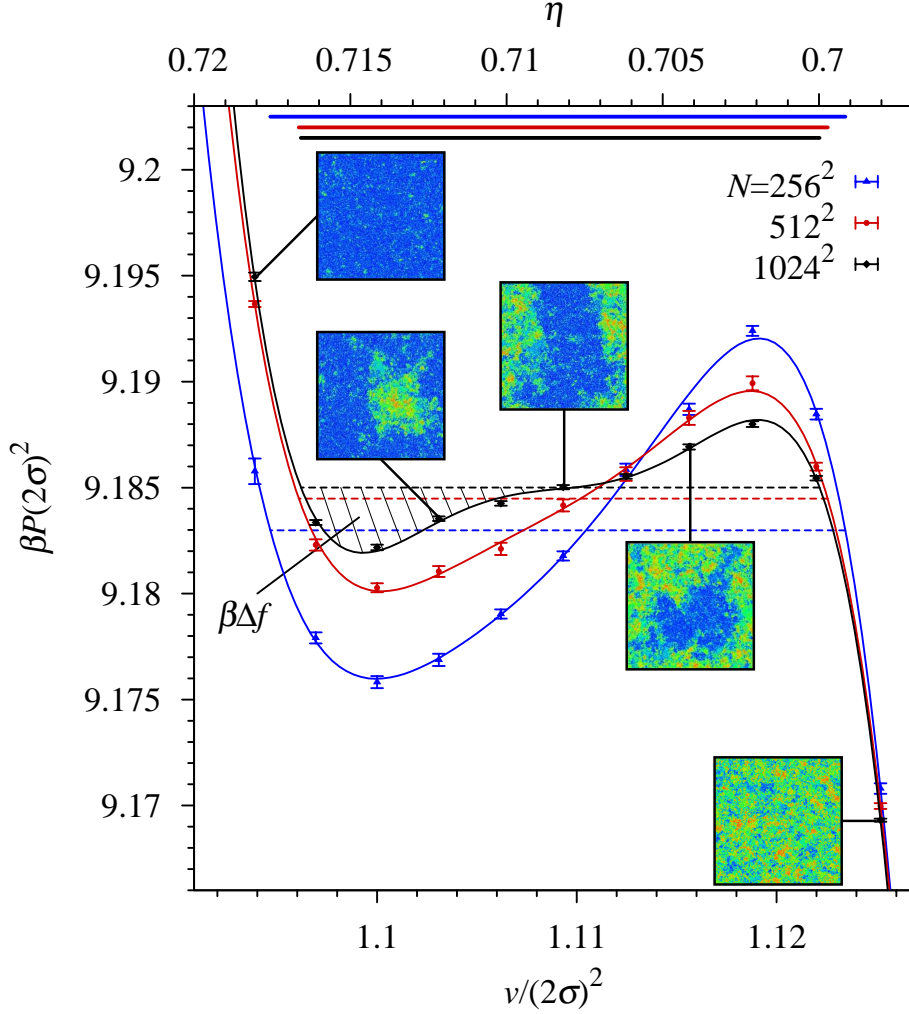


**Figure 4.5:** Equation of state  $P(v)$  (or  $P(\eta)$ , upper scale) for different system sizes. The results for each size are fitted by a 5<sup>th</sup> order polynomial. The observed vanishing loop is due to interface effects. The Maxwell construction confirms the value of the two coexisting densities  $\eta \sim 0.700$  and  $\eta \sim 0.716$ . The  $N = 1024^2$  and  $N = 512^2$  pure-phase branches are identical, the thermodynamic-limit behavior is reached for these densities. (Ref [6], cf. Section 7.3).

The hatched area of Fig. 4.4 corresponds to the dimensionless free energy per particle  $\beta\Delta f$  of the interface at  $\eta = 0.708$ . It is then possible to apply the Lee-Kosterlitz method [112] in this ensemble. Clearly,  $\beta\Delta f \propto 1/\sqrt{N}$ . This again confirms the first-order nature of the transition (see Fig. 4.5).

The interface tension  $\gamma$  is computed from the free energy difference  $\Delta f$  through

$$\Delta F = \gamma\ell. \quad (4.2)$$

The system at  $\eta = 0.708$  has two interfaces of length equal to the system size. This gives  $\ell = 2\sigma\sqrt{N\pi/\eta}$ , and therefore the dimensionless interface tension is

$$\gamma\beta 2\sigma = \beta\Delta f\sqrt{\eta/\pi}. \quad (4.3)$$

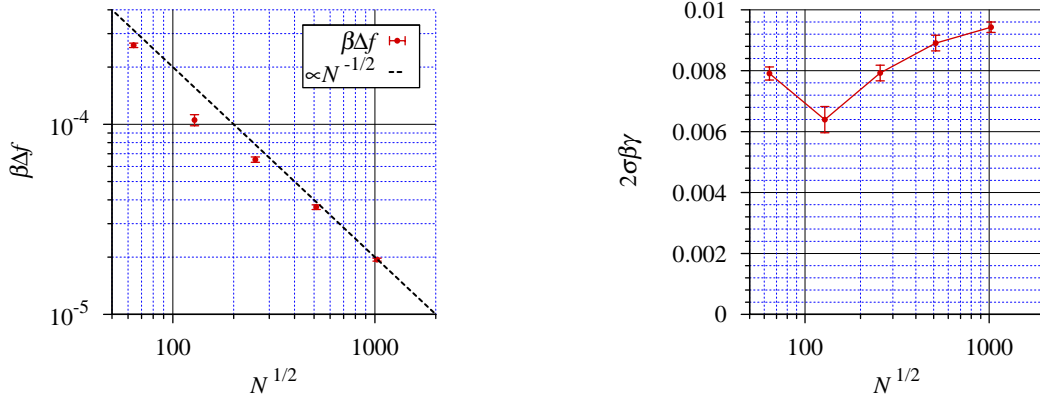


**Figure 4.6:** *Left:* Interface free energy per particle  $\beta\Delta f$  as function of system size. The scaling is consistent with the presence of an interface. *Right:* Interface tension measured with  $\beta\Delta f$ . For  $N = 1024^2$ ,  $\gamma\beta 2\sigma \simeq 0.0094$ .

For  $N = 1024^2$ , the interface tension is  $\gamma\beta 2\sigma \simeq 0.0094$ . The interface tension is sometimes seen as a consequence of energetic interactions between particles. This is actually a consequence of both entropy and energy. In the case of hard disks, its origin is only entropic: at the interface, the disks are neither from a phase nor from the other, the accessible space for both phases is therefore reduced.  $\gamma\beta 2\sigma$  roughly corresponds to the free energy needed to add an extra disk to the interface. This value can be compared to the typical kinetic energy of a disk  $\beta e_k = 1$ , which is two orders of magnitude higher. It can also be compared to a system with attractive interactions as water. The energy needed to add an extra atom to a liquid-gas water interface at  $T = 20^\circ\text{C}$  is roughly  $\beta\gamma_{\text{water}}a_0^2 \sim 0.2$ . The tension of the interface between the coexisting phase of hard disks is then twenty times smaller, and therefore, the interface exhibits large fluctuations in small systems. This makes the two-phase state difficult to observe and implies large thermalization times (see Section 4.3).

The finite-size effects outside of the coexistence phase are small for the largest systems. This is shown by the collapse of the pure-phase branches for  $512^2$  and  $1024^2$  disks (see Fig. 4.4). The pressure  $P^*$  computed by the Maxwell construction reaches a plateau for the largest systems. For  $1024^2$  disks, the pressure is  $\beta(2\sigma)^2P^* \simeq 9.185$  (see Fig. 4.6). The densities of the coexisting phases,  $\eta_L$  and  $\eta_H$ , also reach a plateau for the largest systems (see Fig. 4.6). For  $1024^2$  disks, their values are  $\eta_L \simeq 0.6999$  and  $\eta_H \simeq 0.7165$ .

These limiting densities and pressure allow computation of the latent heat of this transition. The specific latent heat in a first-order transition is defined as the energy needed to transform a particle of phase 1 in a particle of phase 2 in a  $(N, P, E)$  ensemble. This corresponds to the difference of specific enthalpy  $\Delta h = h_2 - h_1$  ( $h = H/N$  with  $H = E + PV$ ). As  $P$  is constant in this ensemble,

$$\Delta h = P\Delta v + \Delta e \quad (4.4)$$

where  $e$  is the specific internal energy of the system. Moreover,  $P/T = \text{const.}$  in the transition region, therefore  $T = \text{const.}$  and  $\Delta e = 0$  for hard disks (as the internal energy is only kinetic). The dimensionless specific latent heat thus becomes

$$\beta\Delta h = \beta P^* \times (v_2 - v_1). \quad (4.5)$$

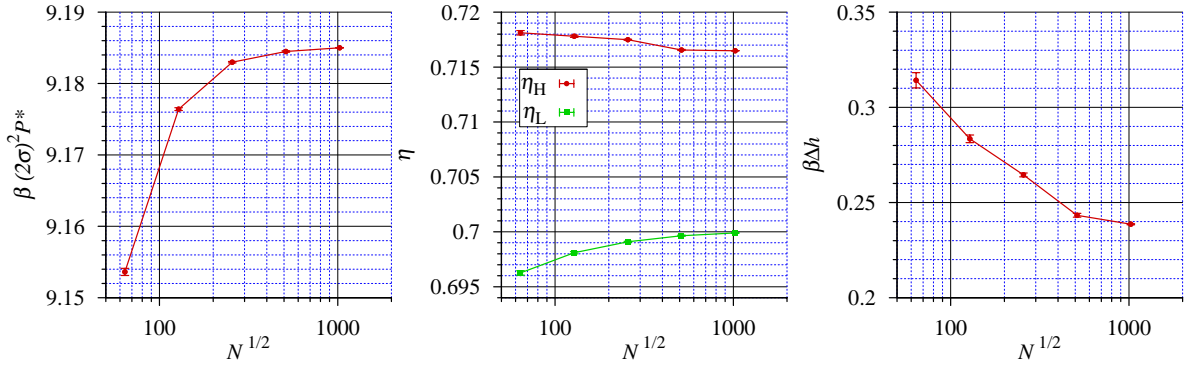


**Figure 4.7:** System-size dependence of observables at the transition *Left:* Pressure  $P^*$  obtained by the Maxwell construction.  $P^*$  reaches a plateau at  $\beta(2\sigma)^2 P^* = 9.185$ . *Center:* Low ( $\eta_L$ ) and high ( $\eta_H$ ) densities of the coexisting phases. The two quantities converge toward  $\eta_L = 0.7000$  and  $\eta_H = 0.7165$ . *Right:* Specific latent heat, the value of  $\beta\Delta h = 0.238$  is reached for the largest system.

For  $1024^2$  disks,  $\beta\Delta h \simeq 0.238$  (see Fig. 4.6) (the latent heat of the liquid-solid water transition, at  $T = 0^\circ\text{C}$  and  $P = 100\text{kPa}$ , is  $\beta\Delta h \sim 2.5$ ).

The plateau reached by the observables is a sign that the relevant correlation lengths are smaller than the system size, and thus that the results are valid in the thermodynamic limit. This is confirmed in Section 4.2.

### Shape of the loop

As seen in this section, the equation of state in a finite-size system shows a loop vanishing in the thermodynamic limit. This loop is indeed seen in Fig. 4.4. Another observation of the equation of state is that for  $1024^2$  disks, the shape of  $P(v)$  is qualitatively different from the one of the smaller systems. The equation-of-state loop in this very specific system was first studied by Mayer and Wood in 1965 [67], and also more generally for first-order transitions [120, 121]. In order to understand the shape of the loop, we solve the model of Mayer and Wood in the limit of large systems.

We consider the system of  $N$  particles in a volume  $V$  (specific volume  $v = V/N$ ) in a square box with periodic boundary conditions.  $P$  is the pressure of the system. In the system, two phase coexist. Their number of particles, volume, pressure, and chemical potential are  $N_1, V_1, P_1, \mu_1$  respectively for the phase 1, and  $N_2, V_2, P_2, \mu_2$  respectively for the phase 2. The specific volumes of this phases are noted  $v_1$  and  $v_2$ . The above quantities in the thermodynamic limit are labeled by a \*. The model assumes that the pressure in the pure-phase branches are proportional to the volume:  $P_1(v_1) = -K \times (v_1 - v_1^*)$ . This assumption is valid in the limit of large systems. For simplicity, it is assumed that the branches are symmetric. The equation for the chemical potential is directly obtained from Eq. (3.31).

The interface between the two phases has a free energy  $\Delta F = \gamma\ell$  and thus minimizes its length in the thermodynamic limit. For a square box with periodic boundary conditions, two types of interface are competing: a circular interface of size  $\ell_b$  (bubble

configuration), or two flat interfaces of size  $\ell_s$  (stripe configuration). As  $\ell_b = 2\sqrt{\pi V_1}$  and  $\ell_b = 2\sqrt{V}$ , a bubble configuration is expected for  $V_1 < V/\pi$  and  $V_2 < V/\pi$ , while a stripe configuration is expected for  $V/\pi < V_1 < V - V/\pi$ .

In the stripe configuration, the interface is flat. This gives  $P_1 = P_2 = P^*$ . A flat region in the equation of state is therefore expected (see Fig. 4.7).

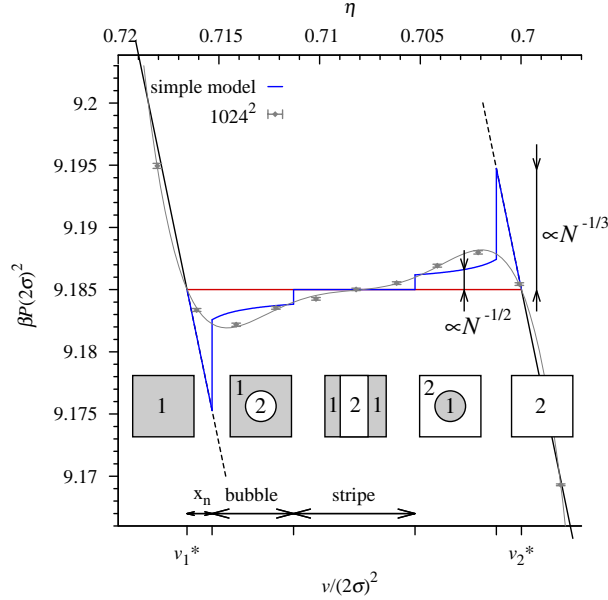


**Figure 4.8:** Asymptotic shape of the equation of state for the value of  $K$  and  $\gamma$  computed for  $1024^2$  disks. The flat part and the peak are qualitatively seen for  $1024^2$  disks. The large fluctuations of the interface, as well as the size dependence of the interface tension, prevent the system from showing an asymptotic shape. This shape would be seen for larger systems.

In the bubble configuration where  $V_1 < V_2$ , the equations are

$$\left\{ \begin{array}{l} P_1 = -K\delta v_1 + P^* \quad \text{with} \quad \delta v_1 = v_1 - v_1^* \\ P_2 = -K\delta v_2 + P^* \quad \text{with} \quad \delta v_2 = v_2 - v_2^* \\ P_2 - P_1 = \gamma/R \quad \text{with} \quad R = \sqrt{\pi V_1} \\ \mu_1 = \mu_2 \quad \text{which gives} \quad \delta v_1(v_1 + v_1^*) = \delta v_2(v_2 + v_2^*) \\ V_1 + V_2 = V \\ N_1 + N_2 = N \end{array} \right. \quad (4.6)$$

Mayer and Wood solved these equations by a Taylor expansion assuming that  $v_2 - v_1 \ll v$ . This does not converge to the exact result in the thermodynamic limit. In the limit of large systems  $\delta v_1 \ll v_1$  and  $\delta v_2 \ll v_2$ , it is thus preferable to perform an expansion over these small values. Let  $P_b$  be the total pressure in the bubble configuration. At the first order, the above equations give

$$P_b(x) = P^* - \frac{1}{\sqrt{N}} \frac{1}{\sqrt{x}} \gamma \sqrt{\frac{\pi v_2^*}{v_2^* - v_1^*}} + o(N^{-1/2}). \quad (4.7)$$

This result is not valid for  $x \rightarrow 0$  as the pressure in the bubble would be infinite. Near  $x \sim 0$ , there is a competition between a pure-phase state and a bubble state.

The free energy per particle for a bubble state  $f_b$  is from Eq. (4.7)

$$f_b(x) = \frac{1}{\sqrt{N}} \sqrt{\frac{x}{v_2^* - v_1^*}} 2\gamma \sqrt{\pi v_2^*} - P^* x + f(0) + o(N^{-1/2}). \quad (4.8)$$

This actually corresponds to the free energy given by the length of the interface for the phases in the thermodynamic-limit proportion. However, it does not mean that  $\delta v_1 = 0$  or  $\delta v_2 = 0$  in this approximation. Eq. (4.6) gives the free energy in the pure phase

$$f_p(x) = \frac{1}{2} K x^2 - P^* x + f(0). \quad (4.9)$$

The bubble appears for  $x = x_n$  when  $f_b(x_n) = f_p(x_n)$ . This gives

$$x_n = N^{-1/3} \left( \frac{\pi v_2^*}{v_2^* - v_1^*} \right)^{1/3} \left( \frac{4\gamma}{K} \right)^{2/3} + o(N^{-1/3}). \quad (4.10)$$

The nucleation point scales as  $N^{-1/3}$ , which induces peaks in the pressure curve near the boundaries of the coexistence region (see Fig. 4.7). However, the nucleation point does not change the  $\propto 1/\sqrt{N}$  scaling of the area of the loop ( $\beta \Delta f$ ). In  $d$ -dimensions, the same calculus for the nucleation point gives  $x_n \propto N^{-1/(d+1)}$ . The equation of state is then completely determined (the part where  $V_2 > V_1$  is completed by symmetry). The equation of state shows discontinuities due to the nucleation of a bubble (with a size  $\propto N^{2/3}$  at the nucleation point) or to the discontinuous change of the interface shape (bubble to stripe). This is allowed by thermodynamics, and the free energy is continuous.

This simple model yields the asymptotically correct equation of state for hard disks, given the input parameters  $\gamma$ ,  $v_1^*$ ,  $v_2^*$ ,  $K$ , and it interprets the data seen in Fig. 4.7. The system for  $1024^2$  disks satisfies  $\gamma \simeq 0.0094/(2\sigma\beta)$  and  $K \simeq 5/\beta(2\sigma)^4$ . The asymptotic shape (see Fig. 4.7) qualitatively explains the numerical results for  $1024^2$  disks: a flat part at the center and two peaks at the boundary of the coexistence region. However, there is still a difference between the model and the numerical results. This difference is in part due to the large fluctuations of the interface because the interface tension is low. Moreover, the interface tension at small scales is different from the one at large scales<sup>1</sup>, which explains the small size of the peaks.

## Chemical potential

The equation of state is also obtained from the chemical potential  $\mu$  computed with the Widom particle insertion method (see Section 3.3.4). The error on this observable is somewhat higher than for the pressure. Indeed, the low insertion probability of a disk around the transition ( $p_i \simeq 2.5 \times 10^{-6}$ , see Fig. 4.8) leads to large fluctuations for  $\langle p_i \rangle$ .

<sup>1</sup>As shown by the phenomenological behavior proposed by Tolmann [122] for small droplets

$$\gamma(R) = \frac{\gamma_\infty}{1 + 2\delta/R}. \quad (4.11)$$

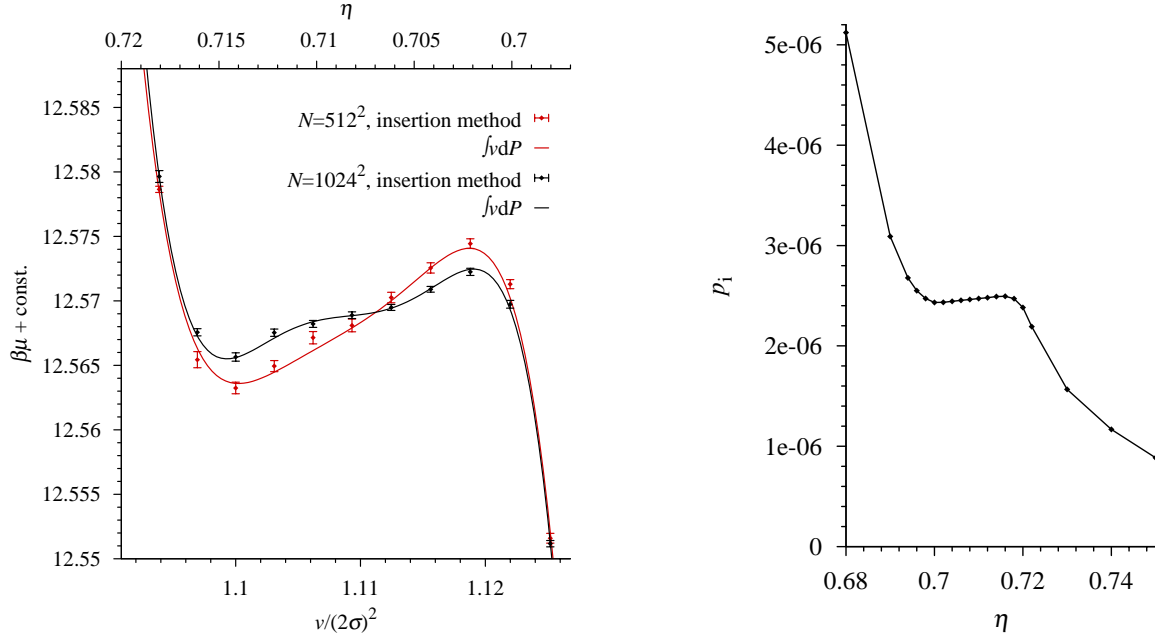


**Figure 4.9:** *Left:* Chemical-potential equation of state  $\mu(v)$ . The behavior is equivalent to the pressure equation of state.  $\mu$  is computed both by particle insertion and from  $P(v)$ . The two results are in good agreement, the Gibbs-Duhem relation is satisfied. *Right:* Density dependence of the insertion probability of a disk  $p_i$  for  $1024^2$  disks.

The equation of state  $\mu(v)$  shows the same behavior as  $P(v)$ <sup>2</sup> (see Fig. 4.8). A loop is observed at the same densities, and vanishes with increasing system size. The flat part at the center, as well as the two peaks, are also observed for  $1024^2$  disks. The computation of the coexisting densities and interface free energy (not performed by the Maxwell construction as  $V \neq \text{const.}$ ) give the same result as for  $P(v)$ .  $\mu$  is related to the pressure by the Gibbs-Duhem relation  $Nd\mu = VdP$ , which gives

$$\mu(v) = \int vP'(v) dv + \text{const.} \quad (4.12)$$

The chemical potential computed by the particle insertion method and from  $P(v)$  are in good agreement (see Fig. 4.8).

## 4.2 Nature of the phases

The phase coexistence is established by direct visualization and confirmed by the equation of state, the transition is thus first order. The following shows that the nature of the coexisting phases is liquid and hexatic. Moreover, the hexatic-solid transition is continuous.

<sup>2</sup>As  $\mu = \partial F/\partial N$ ,  $\mu(v)$  should have been plotted with  $V = \text{const.}$  instead of  $N = \text{const.}$  in order to have the analogy of  $P(v)$ . However, since the differences in density are small, this effect has not important consequences.



### 4.2.1 Low-density phase: liquid

The nature of the low-density phase is determined by analyzing the pure phase at  $\eta \simeq 0.700$ . The system is ordered in clusters of maximum size  $\sim 100\sigma - 200\sigma$  and disordered above this scale.

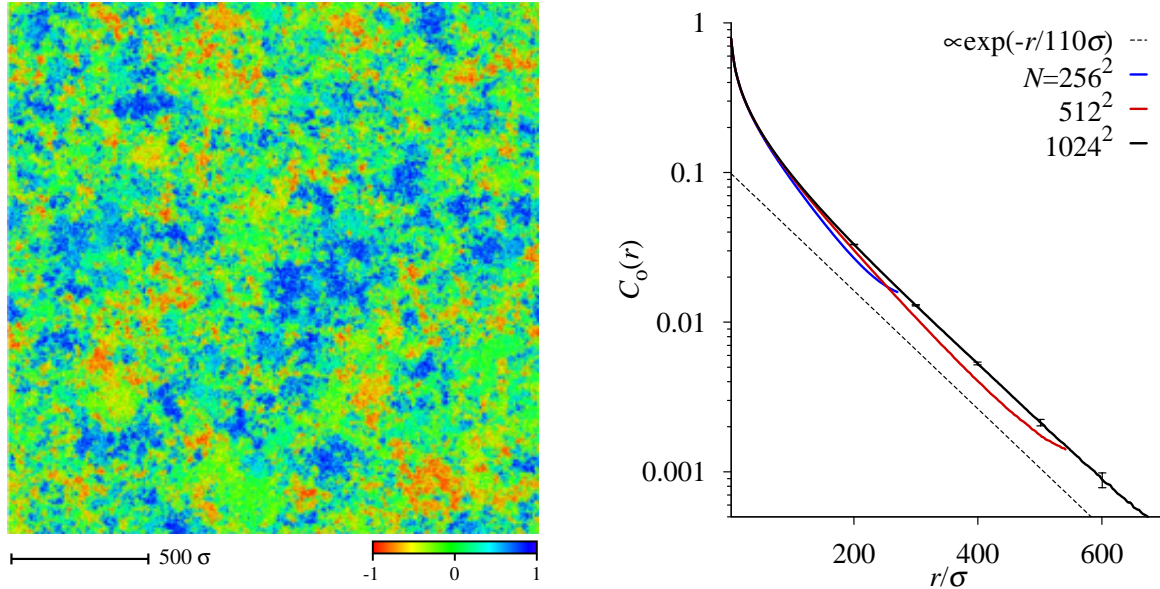


**Figure 4.10:** Identification of the low-density phase at  $\eta = 0.700$  *Left:* Projection of the local orientation on the main orientation for  $1024^2$  disks. The system is ordered in clusters of size  $\sim 100\sigma - 200\sigma$  and disordered above this scale. *Right:* Sample-averaged orientational correlation function at  $\eta = 0.700$ . The decay is exponential with a correlation length of  $\xi_o \sim 100\sigma$ .

above this scale; the phase is therefore liquid (see Fig. 4.9). The correlation length is more precisely computed through the orientational correlation function which behaves as  $C_o(r) \propto \exp(-r/\xi_o)$  at large distances. This gives a correlation length of  $\xi_o \sim 100\sigma$  (see Fig. 4.9 again). This large value partly explains the difficulty for small systems to discriminate between a first-order and a continuous transition. The correlation length is one order of magnitude larger than the disks, yet much shorter than the size of the system for  $512^2$  and  $1024^2$  disks. This point is crucial for the validity of the results, and explains the collapse of  $P(v)$  for  $512^2$  and  $1024^2$  disks in the pure-liquid branch (see Fig. 4.4). Therefore, the behavior of an infinite system is obtained with these system sizes.

The behavior of the correlation length at lower densities shows an important increase for  $\eta < 0.700$  (see Fig. 4.10). This behavior can be wrongly interpreted as evidence for a KT transition. This behavior is consistent with the view that a KT transition is preempted by a first-order transition, and that for other microscopic models the transition could be continuous, as is seen in XY models (see Section 1.2.4). For “small” systems, the decay of the correlation function in the coexistence region can be wrongly interpreted as algebraic (see Fig. 4.10). It is the result of a two-phase region where the interface shows large fluctuations. At  $\eta = 0.708$ , it is necessary to reach  $1024^2$  disk in order to see the two-phase behavior (see Fig. 4.10 again).



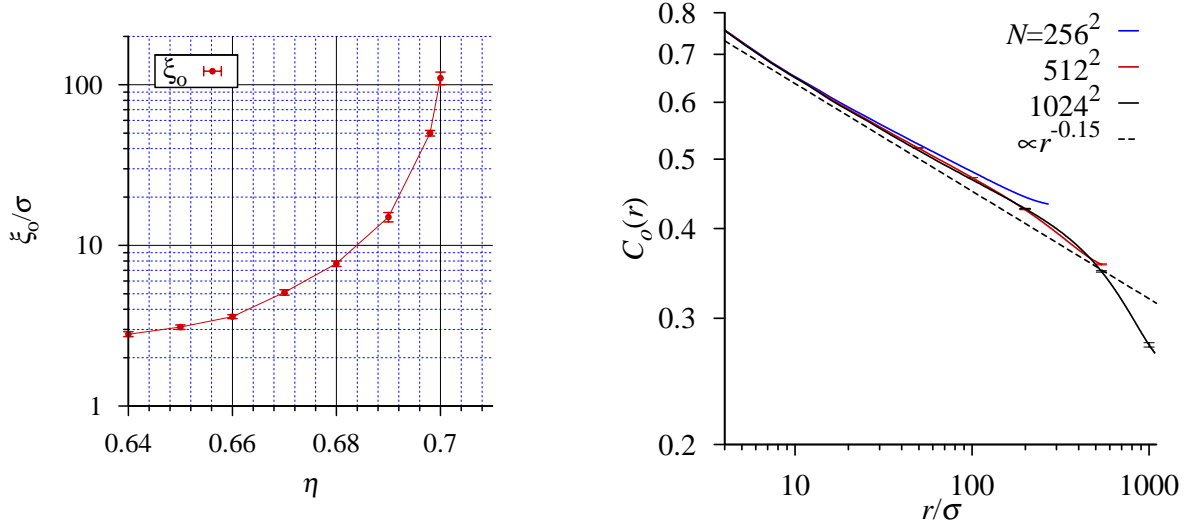


**Figure 4.11:** *Left:* Density dependence of the orientational correlation length  $\xi_0$ . *Right:* Orientational correlation function at  $\eta = 0.708$ . The decay seems algebraic for “small” systems ( $N = 256^2$  and  $N = 512^2$ ). For larger systems ( $N = 1024^2$ ), a change of behavior is seen at a distance of half the system size, due to the phase coexistence.

## 4.2.2 High-density phase: hexatic

The nature of the high-density phase is determined by analyzing the pure phase at  $\eta \sim 0.718$ , which is clearly out of the transition region (see Fig. 4.4). The orientation at this density is conserved along the whole system (see Fig. 4.11 and Fig. 4.12). This does not indicate that the phase is solid as a cut of  $g(\vec{r})$  along an axis shows that the positional order at this density is short ranged (see Fig. 4.11 again). The short-range positional order imposes that the shear modulus is zero [68], this phase can therefore not be a solid. Moreover, in the absence of a shear modulus, the next term in the small-deformation development of the Hamiltonian is [32, 68]

$$H_{\text{hex}} = \frac{1}{2}K_A \int |\vec{\nabla}\theta(\vec{r})|^2 d^2r, \quad (4.13)$$

$K_A$  being the Frank constant (see Chapter 1, Section 1.3.2). This shows that a phase with a short-range positional order cannot possess a long-range orientational order. The orientational order is therefore quasi-long ranged, and the phase at  $\eta = 0.718$  is hexatic. The high-density phase in the coexistence region ( $\eta \sim 0.716$ ) shows the same property as for  $\eta = 0.718$ , it is therefore also hexatic. The analysis of  $\eta = 0.718$  instead of  $\eta = 0.716$  is motivated by the fact that  $\eta = 0.718$  is clearly above the coexistence region.

The positional correlation length  $\zeta_p$  is extracted from the decay of the peaks of  $g(\vec{r}) - 1$ . This decay is exponential at large distances and the correlation length is found to be  $\zeta_p \sim 100\sigma$  (see Fig. 4.11 and Fig. 4.13). The correlation length at the coexisting hexatic  $\eta \sim 0.716$  is thus lower than this value. This result shows that the system size for  $512^2$  and  $1024^2$  disks are much larger than the correlation length. As the orientation is quasi-long ranged, it is not possible to reach a size larger than the orientational correlation length. However, the exponent  $\nu_o$  of  $C_o(r) \sim r^{-\nu_o}$  is small, and the finite-size effects are small (see Fig. 4.12). These results explain the collapse of  $P(v)$  for  $512^2$  and  $1024^2$  disks

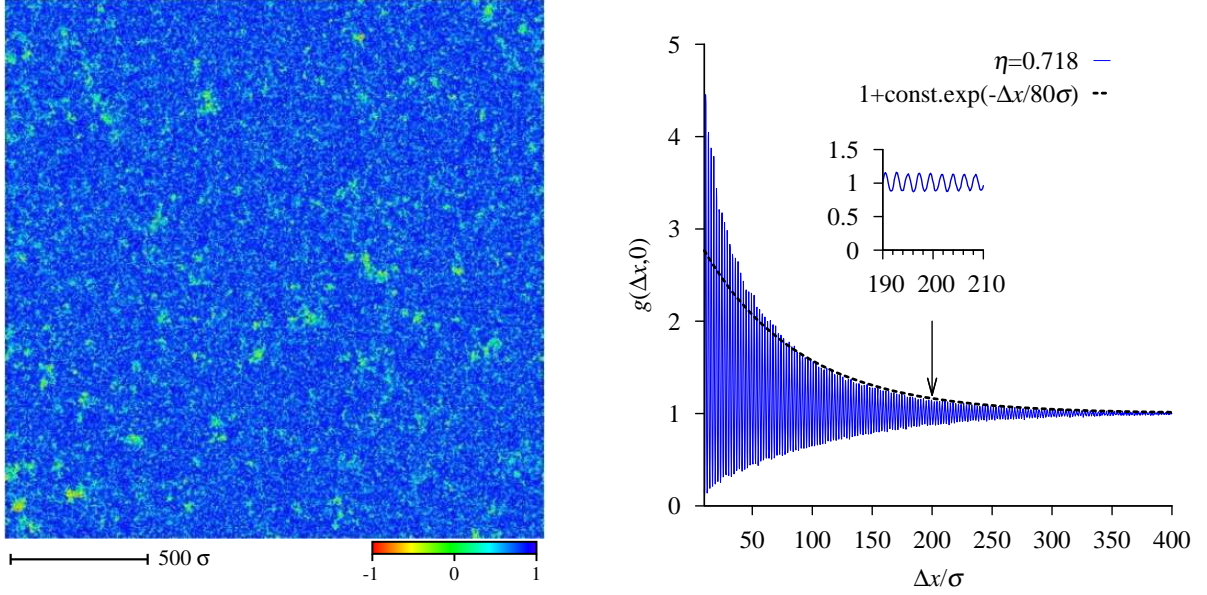


**Figure 4.12:** Nature of the phase at  $\eta = 0.718$ . *Left:* Projection of the local orientation on the main orientation for  $1024^2$  disks. The system is homogeneous and oriented. *Right:* Cut of the pair-correlation function  $g(\vec{r})$  along the  $(Ox)$  axis. The peaks decay exponentially, the positional order is short ranged with a correlation length  $\zeta_p \sim 100\sigma$ , indicating a hexatic phase.

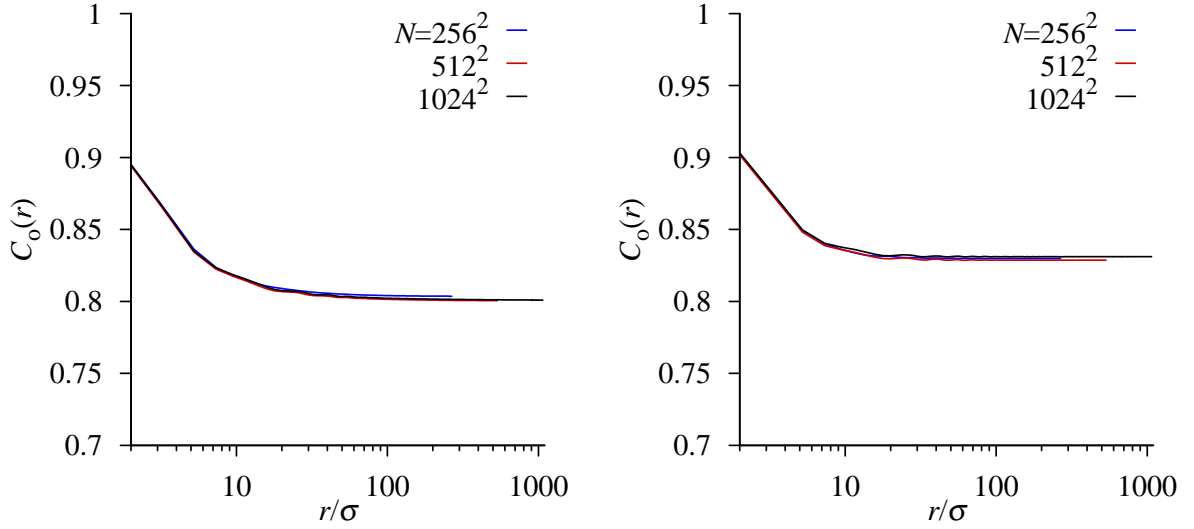


**Figure 4.13:** Size dependence of the orientational correlation functions at  $\eta = 0.718$  (left) and  $\eta = 0.720$  (right). The orientation seems to be long ranged for both densities. However, at  $\eta = 0.718$ , the short-range positional order implies that  $C_o(r)$  is quasi-long ranged. The small value of the exponent  $\nu_o$  near the transition explains this behavior. The orientation is not the appropriate observable to locate the hexatic-solid transition. (Ref [6], cf. Section 7.3).

in the pure-hexatic branch (see Fig. 4.4). The fact that  $\nu_o$  is small at  $\eta = 0.718$  (and as well at  $\eta = 0.716$ ) shows that the system is far from a KT instability (where the exponent is  $\nu_o = 1/4$ ). Also the orientational correlation length increases fast near  $\eta = 0.700$  (see Fig. 4.10). It is likely that a KT transition would occur for  $\eta \gtrsim 0.700$  if the system was

forced to be pure.

### 4.2.3 Hexatic-solid transition

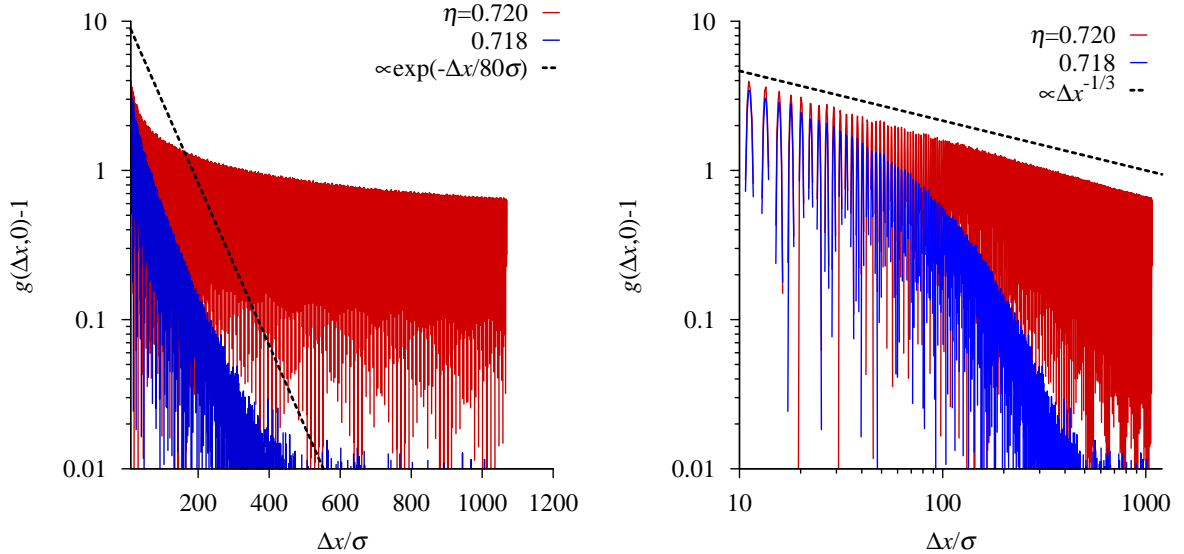


**Figure 4.14:** Positional correlations for  $\eta = 0.718$  and  $\eta = 0.720$  given by the decay of the peaks of  $g(r) - 1$ . *Left:* Semi-log view. The positional order for  $\eta = 0.718$  is short ranged with a correlation length  $\xi_p \sim 100\sigma$ . *Right:* Log-log view. The positional order for  $\eta = 0.720$  is algebraic with an exponent  $\nu_K \sim 1/3$ .  $\eta = 0.720$  is either in the solid phase or in the hexatic very close to the solid-hexatic transition. (Ref [6], cf. Section 7.3).

For  $\eta > 0.718$ , the positional correlation length increases with density, and shows an algebraic behavior at  $\eta = 0.720$  (see Fig. 4.13). At a solid-hexatic KT instability, the exponent of the positional correlation satisfies  $1/3 < \nu_K < 1/4$  (see Chapter 1, Section 1.3.2). The value of the exponent at  $\eta = 0.720$  is  $\nu_K \sim 1/3$ , which shows that the system is solid, or close to be. These results are confirmed by a finite-size behavior of the correlation functions (see Fig. 4.14) and by the finite-size behavior of the first Bragg peak of the structure factor (see Fig. 4.15): For  $\eta = 0.718$ , the maximum of the peak stops increasing for systems larger than  $128^2$  disks. The positional order is therefore short ranged (see Section 1.3.2). The width of the peak for  $N = 1024^2$  gives the positional correlation length,  $\xi_p \sim 100\sigma$ . For  $\eta = 0.720$ , the maximum of the peak increases with the system size up to the largest systems. Around  $\eta = 0.720$ , the system does not show any loop in the equation of state. Moreover, no coexistence region is observed. These observations show that the hexatic-solid transition is not first order, it is therefore a continuous transition, of the KT type.

The exact value of the transition density is difficult to determine because of finite-size effects, as well as thermalization artifacts (see Section 4.3). Nevertheless, the strong increase of the positional order, as well as the qualitative algebraic decay at  $\eta = 0.720$ , shows that the hexatic-solid transition takes place for  $\eta \gtrsim 0.720$ . This value corresponds to a pressure  $\beta P(2\sigma)^2 \gtrsim 9.233$  and a chemical potential  $\beta\mu = \ln \eta/p_i \gtrsim 12.62$ . The hexatic phase extends on a density region of  $\Delta\eta \gtrsim 0.004$ , which is narrow compared to the liquid-hexatic coexistence (see Fig. 4.16).

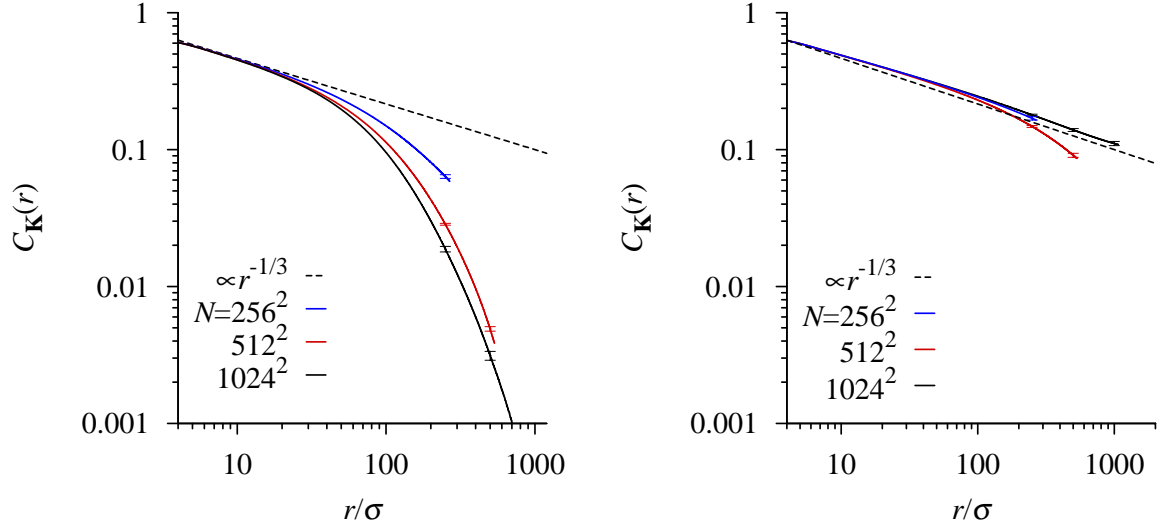


**Figure 4.15:** Size dependence of the positional correlation functions at  $\eta = 0.718$  and  $\eta = 0.720$ . *Left:*  $\eta = 0.718$ , the positional order gets shorter as the system size is increased. The system is thus short ranged in the thermodynamic limit. *Right:*  $\eta = 0.720$ , the positional order shows an algebraic behavior with an exponent close to  $1/3$ , the stability limit of the solid, for all system sizes. The results shows that the hexatic-solid phase transition occurs at  $\eta \gtrsim 0.720$ . (Ref [6], cf. Section 7.3).

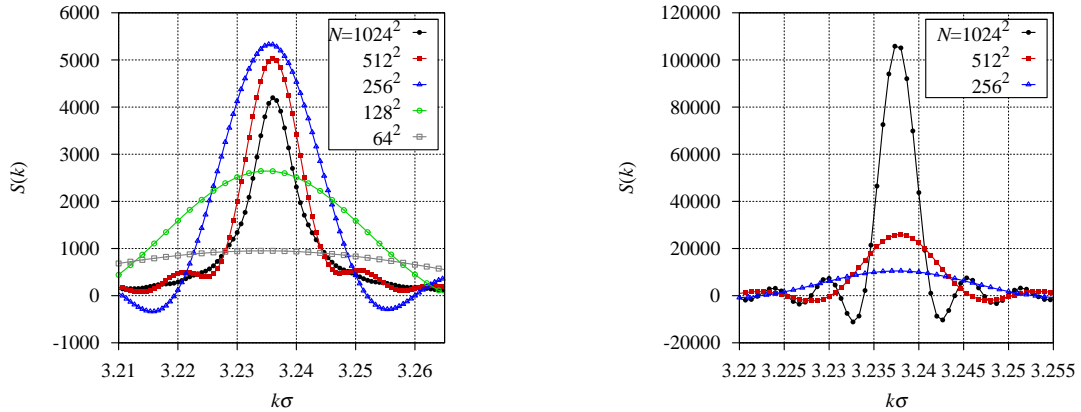


**Figure 4.16:** Size dependence of the first Bragg peak (radial view) of the structure factor at  $\eta = 0.718$  and  $\eta = 0.720$ . *Left:*  $\eta = 0.718$ , the maximum of the peak stops increasing for systems larger than  $128^2$  disks: the positional order is short ranged. The width of the peak for  $N = 1024^2$  gives  $\xi_p \sim 100\sigma$ . *Right:*  $\eta = 0.720$ , the maximum of the peak increases with system size up to the largest system.

### 4.3 Thermalization and finite-size effects

The hard disk system at high densities is strongly correlated. It is thus important to show that simulations have reached the thermodynamic equilibrium and that the systems are large enough to capture the thermodynamic-limit behavior.

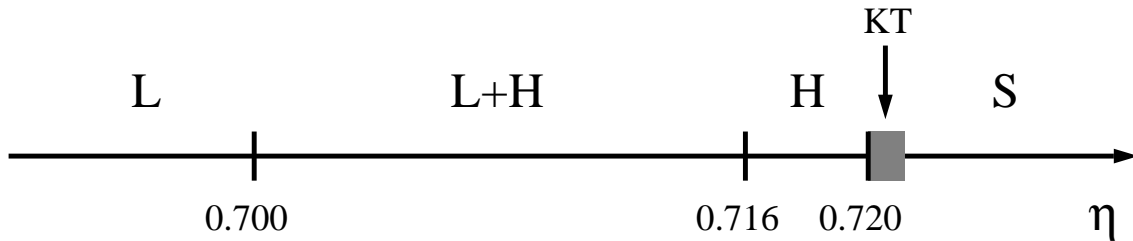


**Figure 4.17:** Phase diagram of the hard-disk system in the constant-density ensemble. The melting transition is in two steps with an intermediate hexatic phase. The liquid-hexatic transition is first order, with a coexistence region for  $\eta \in [0.700, 0.716]$ . The hexatic-solid transition is of the KT type, and occurs at a density  $\eta \gtrsim 0.720$ .

### 4.3.1 Thermalization time

One of the main issue of the Markov-chain Monte Carlo method is to ensure that thermalization is reached in the system studied. The rigorous methods developed in Part II for the hard-disk system are not practicable at these densities. However many strategies can be used.

As explained in Section 2.2.3, the naive method consists of running a simulation for a long time and computing the auto-correlation function  $C(t)$  of an observable  $\mathcal{O}$ . The auto-correlation function has many time scales ( $\tau > \tau_1 \geq \dots$ ) which are related to the eigenvalues of the transfer operator of the Markov chain (see Part II, Section 5.1.2). To compute the correlation time  $\tau$ , a global observable, which is slow to decorrelate, should be used. For that purpose, the absolute value of the total orientation  $|\Psi|$  is commonly used. However, this observable easily underestimates the value of the correlation time. For  $1024^2$  disks at  $\eta = 0.708$ , a simulation run for  $6.10^7$  displacement per disks gives a correlation time  $\tau \sim 4.10^4$  displacement per disks (see Fig. 4.17). This value does not correspond to the largest time scale, which is covered by the error on  $C(t)$  (see Fig. 4.17 and Fig. 4.18). In order not to miss the largest time scale, a better observable should be used. Another method is to perform long simulations on small systems, assuming that the largest time scale is reached there, and then to increase the system size by small steps while following the behavior of the correlation time. Again, this method is limited as the properties of a system can undergo important changes as the system size is increased, especially around a phase transition.

In this thesis, a simple yet efficient strategy is used in order to prove that at  $\eta = 0.708$ , the phase-separated state is thermalized. Two simulations were performed starting with very different initial configurations. In the first simulation, the initial configuration was ordered, obtained from a high-density solid. The system underwent a coarsening process, meaning that bubbles of liquid appear and grow with time. The system eventually reached a phase-separated state for  $\sim 10^6$  displaced disks (see Fig. 4.18). In the second simulation, the initial configuration was disordered, obtained by a quench from a low-density liquid (the radius of the disks were increased with only a few displacements). At short times, the system crystallized in random directions, leading to a poly-crystalline state. For

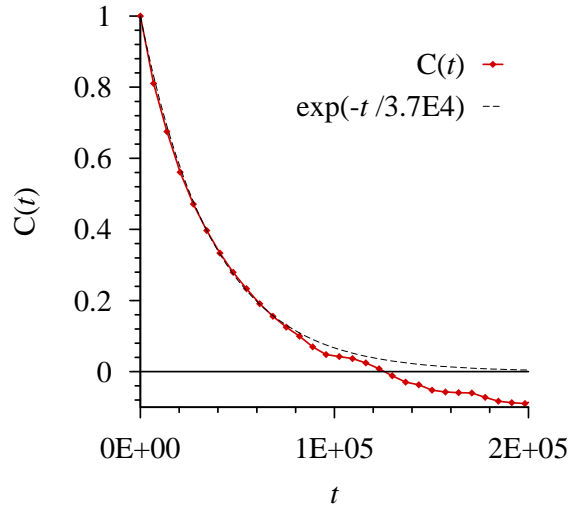


**Figure 4.18:** Auto-correlation function of  $|\Psi|$  for  $1024^2$  disks at  $\eta = 0.708$  computed for a long simulation ( $6.10^7$  displacement per disks). The apparent largest time scale is  $\sim 4.10^4$  displacement per disks. The error on the auto-correlation function is too large to capture the actual largest time scale of  $\sim 10^6$  displacement per disks.

larger times, the crystals rotated to agree on their orientation, then melted. The system eventually reached the phase-separated state again, at a time of  $\sim 10^6$  displacement per disks (see Fig. 4.18 again). The fact that these two very different initial configurations led to the same final state is strong evidence for the thermalization of the system. The thermalization time was found to be large, of the order of  $\sim 10^6$  displacement per disks for  $1024^2$  disks. This was achieved in a few days of simulation. The longest simulations, whose purpose was to extract the 64 initial configurations, were run for  $\sim 64 \times 10^6$  displacement per disks (almost one year of computation).

The large value of the thermalization time is not due to the correlations in the system, but to the slow coarsening process. For a local dynamic starting from the ordered state, the size of the bubbles is expected to follow a power-law behavior with time  $l(t) \propto t^{1/3}$  [110], which is compatible with the results obtained. The scaling of the thermalization time for this system is therefore  $\propto N^2\sqrt{N}$  (in total displaced disks) which means a simulation time of  $\sim 3$  month for  $2048^2$  disks (which was indeed observed, see Fig. 4.19) and  $\sim 10$  years for  $4096^2$  disks on a single CPU at 3Ghz. The correlation time in the phase-separated state is also expected to be large as the interface shows large fluctuations.

The same simulations were performed with the local Metropolis algorithm. These simulations were found to be  $\sim 20$  times slower for the disordered initial configuration, and  $\sim 100$  times slower for the ordered initial configuration. This shows that the event-chain algorithm is more efficient than the local Metropolis algorithm, and that simulation times much larger than what has been performed before [25, 123] are needed to see the phase separation at this size with the local Metropolis algorithm.

For densities lower than the coexistence region ( $\eta < 0.700$ ), the thermalization is easily reached as the system is liquid with a correlation length of  $\xi_o \sim 100\sigma$ . Just above the coexistence ( $\eta \gtrsim 0.716$ ), the thermalization is also easily reached. Indeed, the



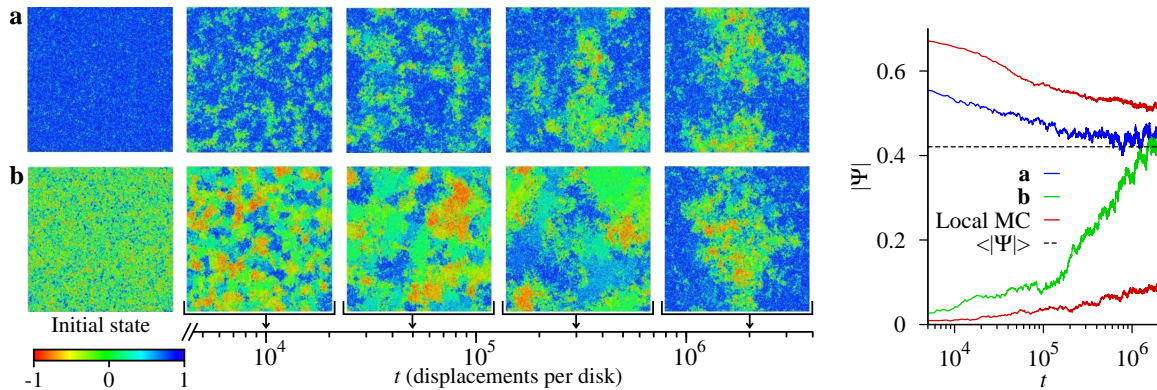


**Figure 4.19:** Thermalization test in the coexistence region by quenches from different initial configurations with  $1024^2$  disks at  $\eta = 0.708$ . *Left upper panel:* The initial configuration is ordered. The system undergoes a coarsening process up to the phase separation. *Left lower panel:* The initial configuration is disordered. A poly-crystalline state is first observed. Later, the system reaches the phase-separated state. *Right:* Time evolution of the total orientation  $|\Psi|$  for both quenches for the event-chain algorithm (blue and green curve) and for the local Metropolis algorithm (red curves). (Ref [6], cf. Section 7.3).

positional correlation length is  $\xi_p \sim 100\sigma$ , and the fluctuation of the orientational field are small because the orientation is almost long ranged.

For densities around the hexatic-solid transition, the positional correlation length  $\xi_p$  is higher than the size of the box. This induces both a problem of finite-size effect and of thermalization. Indeed, because of the anisotropy of the box, the properties of the system change with the orientation of the solid (or the hexatic). Rigorously, the system should perform a complete rotation in the box. This process is very slow and can only be achieved for small systems (up to  $256^2$  disks)<sup>3</sup>. As a consequence, the results obtained at these densities are only qualitative. It is not possible to determine with precision the density at the hexatic-solid transition. However, the absence of a loop in the pressure for each system size is sufficient to rule out a first-order hexatic-solid transition.

### 4.3.2 Finite-size effects

An other issue of simulation methods is to predict the behavior of the system in the thermodynamic limit  $N \rightarrow \infty$  with finite-size simulations. The arguments already mentioned before are reviewed and discussed in further detailed.

In the pure-liquid region ( $\eta < 0.700$ ), the orientational correlation length satisfies  $\xi_o < 100\sigma$ . The system behaves as independents subsystems of size  $\sim \xi_o \times \xi_o$ . For a system whose size  $L$  is larger than  $\xi_o$ , an observable typically reaches its thermodynamic-limit value exponentially with  $L$  (see Section 1.2.3 and Eq. (1.37)). A system only a few times larger than this length is thus enough to suppress finite-size effects. The system size of the largest system ( $1024^2$  disks) is 10 times larger than this length. The results obtained are therefore not concerned with finite-size effects. An experimental evidence of this statement is given by the collapse of the equation of state (see Fig. 4.4) in this

<sup>3</sup>However it is not very useful to perform the complete rotation as the finite size effects are not understood.

density region for  $512^2$  and  $1024^2$  disks.

In the pure-hexatic region, the orientational correlations are algebraic, the system is therefore concerned by finite-size effects (see Chapter 1, Section 1.2.3). However, the exponent  $\nu_o$  of  $C_o(r) \propto r^{-\nu_o}$  is small, this phase is close to the solid phase where the correlation length of the fluctuations of the orientation is  $\sim 10\sigma$ . The same observation as for the pure-liquid phase can then be made: as the positional correlation length  $\zeta_p \sim 100\sigma$  is smaller than the system size, the results are not concerned with finite-size effects. Again, the equation of state (see Fig. 4.4) collapses in this density region for  $512^2$  and  $1024^2$  disks.

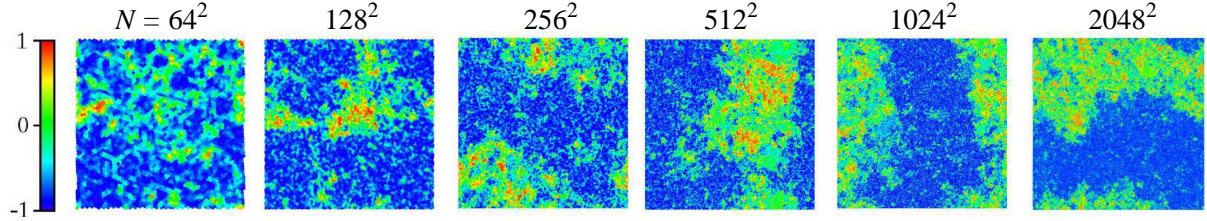


**Figure 4.20:** Snapshots of the orientation field at  $\eta = 0.708$  for different system sizes. The phase coexistence is clearly identified for  $N \geq 512^2$ . For  $N = 2048^2$ , a simulation time of  $\sim 10^7$  displacements per disk was required to reach the equilibrium.

The main finite-size effects in the coexistence region are due to the interface, and are well understood (see Section 4.1.2). The interface fluctuations vanish in the thermodynamic limit, but are large at small scales. The phase separation is therefore difficult to see in systems with  $N \leq 256^2$  (see Fig. 4.19). As the Maxwell construction removes interface effects, the observables  $P^*$ ,  $\eta_L$  and  $\eta_H$  reach a plateau (as for the observables in the pure-phase branches). Their values can be estimated at  $\beta(2\sigma)^2 P^* \simeq 9.185$ ,  $\eta_L \simeq 0.7000$  and  $\eta_H \simeq 0.7165$ .

As mentioned in Section 4.2.2, finite-size effects around the hexatic-solid transition are important because positional correlations are large. The shape of the box is a square, and the density is constant: this induces finite-size effects due to commensuration problems of the triangular lattice. The precise value of the transition density is therefore difficult to be determined from these results. Nevertheless, the strong increase of the positional order, as well as the qualitative algebraic decay at  $\eta = 0.720$ , shows that the hexatic-solid transition takes place for  $\eta \gtrsim 0.720$ .

Beyond the discussion about correlation lengths, a finite-size system shows fluctuations in its observables ( $P$  or  $\mu$  for example). The hexatic phase is narrow ( $\Delta\eta \gtrsim 4 \times 10^{-3}$ ), and a system with a size large enough is therefore needed to explore it. To estimate the fluctuations obtained in the constant-density ensemble, one can compute the pressure fluctuations. An equivalent method (for a pure phase) is to compute density fluctuations in a constant-pressure ensemble. These fluctuations are directly related to the compressibility of the system by the relation

$$\langle V^2 \rangle - \langle V \rangle^2 = -\frac{\partial V}{\partial \beta P}, \quad (4.14)$$

which can be computed through the equation of state. In the hexatic phase, the fluctuations are found to be  $\delta\eta \sim 0.2/\sqrt{N}$ . This gives for  $N = 1024^2$  a fluctuation of



$\delta\eta \sim 2 \times 10^{-4}$ . The fluctuations for the largest system are therefore one order of magnitude smaller than the density extension of the hexatic phase. The properties of the hexatic phase are thus well captured.

## 4.4 Other simulations

The choice of the method used to study the transition is influenced by the nature of the transition. We performed simulations in the ‘‘Gibbs ensemble’’. The different possibilities to study the transition in further details are then discussed.

### 4.4.1 Gibbs ensemble

The Gibbs ensemble [124] has been designed to study first-order transitions. As for the constant-density ensemble, the total number of particles  $N$  and the volume  $V$  of the system are constant. However, the system is composed of two separated subsystems which exchange volume and particles. Each subsystem, labeled 1 and 2, is chosen to be a square box with periodic boundary conditions. The number of particles and the volume of these boxes satisfy  $N_1 + N_2 = N$  and  $V_1 + V_2 = V$ . The exchanges of particles and volumes are set up in order for the pressure ( $P_1, P_2$ ) and the chemical-potential ( $\mu_1, \mu_2$ ) in the two boxes to equalize. In a coexistence region, each phase should be present in only one box, in order for the interface free energy to be removed. As a consequence, it is easy to analyze the properties of each phase.

The simulation involves three kinds of moves: displacements of particles, exchange of particles, and exchange of volume. The displacements of particles were performed with the event-chain algorithm. For the exchange of particles, one of the  $N$  particles of the system was picked with a uniform distribution, and was then inserted uniformly into the total volume. If the particle overlapped other disks, the move was rejected, otherwise the move was accepted. This process gives directly  $\langle \eta_1/p_{i1} \rangle = \langle \eta_2/p_{i2} \rangle$ , the chemical potential in both boxes are thus equalized. The speed of this process is limited by the rejection rate as in the vicinity of the transition  $p_i \simeq 2.5 \times 10^{-6}$  (see Fig. 4.8). In the pure-phase branches, the density fluctuations, computed through the equation of state, are  $\delta\eta \sim 0.2/\sqrt{N}$ . Assuming that positions are uniformly sampled between two insertion attempts, the density follows a random walk without memory with a step  $\delta\eta = 1/N$  each  $\delta t = 1/p_i$  attempts. The time needed to sample the total fluctuation of the system is then

$$\tau = \left( \frac{\Delta\eta}{\delta\eta} \right)^2 \delta t \sim 2 \times 10^4 N. \quad (4.15)$$

For  $1024^2$  disks, this requires only a few hours of computer time. The Gibbs ensemble is therefore not limited by the density fluctuations.

The sampling of volume fluctuations is however much slower to achieve. Indeed, the classic algorithms [111, 125] perform homothetic transformations in order to change the volume. These moves require a long simulation time. As there are  $N$  particles in the system, the maximal volume change by an homothetic transformation without overlaps is  $\delta V/V \propto 1/N$ . Moreover, the amount of time required to perform such a movement is  $\delta t \propto N$ . As the fluctuations are of the order  $\Delta V/V \propto 1/\sqrt{N}$ , the time needed to sample

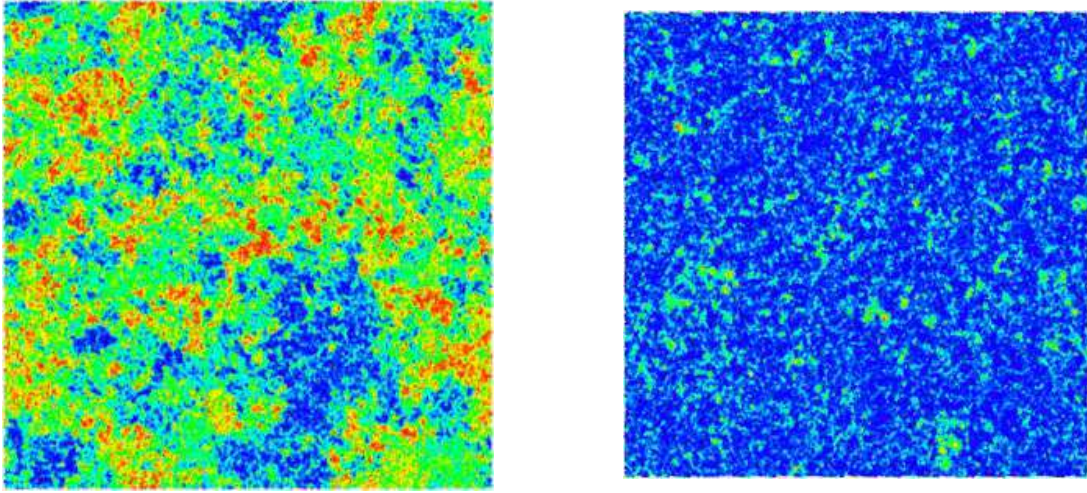


**Figure 4.21:** Snapshot of a simulation in the Gibbs ensemble for a system of  $N = 2 \times 256^2$  at  $\eta = 0.708$ . The system is phase-separated, each of the phase is located in a box. The low-density phase (left) is disordered while the high-density phase (right) is ordered. The volume of the low-density phase is higher than the volume of the high-density phase as the overall density is  $\eta < (\eta_2 - \eta_1)/2$ .

the total fluctuation of the system is

$$\tau = \left( \frac{\Delta V}{\delta v} \right)^2 \delta t \propto N^2. \quad (4.16)$$

This time is therefore extremely long for large systems. This argument holds for any continuous short-range potential. An algorithm [126] is claimed to achieve a complexity  $O(N)$  instead of  $O(N^2)$ . However, a simple scaling argument shows that this is not the case, the algorithm is still  $O(N^2)$ .

In order to reduce this sampling time, a new algorithm was used to perform volume changes. As for the constant-density algorithm (see Section 2.3), the particle positions in this algorithm are stored in cells. A volume change is performed by modifying the width of one of the lines or columns of this cell scheme. In order to keep the square shape, a line and a column are re-sized simultaneously. At each step of the algorithm a line and column are sampled with a uniform distribution for each box. A re-size parameter  $\delta V \in [-\delta_m, \delta_m]$  is sampled uniformly. The widths of the column-line pairs of the box 1 and 2 are changed in order for the volume to become  $V'_1 = V_1 + \delta V$  and  $V'_2 = V_2 - \delta V$ . The movement is rejected if there is an overlap and accepted otherwise. This algorithm satisfies the detailed balance and thus equalizes the pressure in the two boxes. The volume change  $\delta V$  satisfies, as for the homothetic transformation,  $\delta V \propto 1/N$ . However, the time needed to ensure the absence of overlaps is  $\delta t \propto \sqrt{N}$ . The algorithm is therefore  $O(N\sqrt{N})$  instead of  $O(N^2)$ . This algorithm is however not fast enough to reach system sizes larger than  $2 \times 256^2$  disks.

For  $2 \times 256^2$  disks at  $\eta = 0.708$ , the system shows two phases, each of them located in a single box (see Fig. 4.20). One of the phases has a disordered orientation and a density  $\eta \sim 0.700$ , while the other one is ordered and has a higher density  $\eta \sim 0.716$  (see Fig. 4.20 and Fig. 4.21). Moreover, the size of the low-density box is higher than the size

of the high-density box; this was expected as the overall density is  $\eta < (\eta_2 - \eta_1)/2$ . The pressure obtained is  $\beta(2\sigma)^2 P \simeq 9.18$ , and the chemical potential is  $\mu = \ln \eta / p_i \simeq 12.57$ . These results are consistent with the results obtained in the constant-density ensemble. However, the fluctuations of volume are slow to be sampled (see Fig. 4.21), and thus the total number of decorrelated configurations is not sufficient to give precise quantitative results with this ensemble.

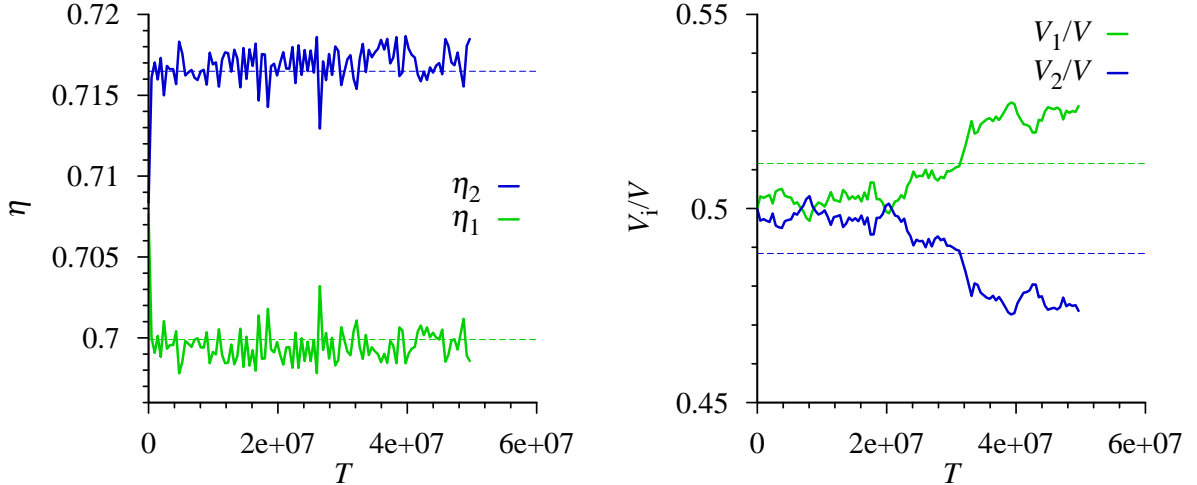


**Figure 4.22:** Gibbs simulation for a system of  $N = 2 \times 256^2$  at  $\eta = 0.708$ . The expected thermodynamic-limit value from the constant-density ensemble are shown in dashed line. *Left:* Time evolution of  $\eta_1$  and  $\eta_2$ . The result of the constant-density simulations are confirmed. *Right:* Time evolution of the volume  $V_1$  and  $V_2$ , the volume of the low-density box increases as expected. The fluctuations show a very long time scale.

#### 4.4.2 Future simulations for hard disks

The first-order nature of the liquid-hexatic transition is well established. Other ensembles can however explore this transition in further detail. In the constant-density ensemble, the coarsening leads to a long thermalization time of complexity  $O(N^2\sqrt{N})$  for large systems. Even when the phase separation is reached, the large interface fluctuations are slow to sample. Therefore, this ensemble should not be used on larger systems than  $1024^2$  disks. The constant-pressure ensemble has no interfaces, however the time needed to sample the volume fluctuations is also long, with a complexity  $O(N^2)$  (or  $O(N\sqrt{N})$  with the improved algorithm). This ensemble, as well as the Gibbs ensemble, should not be used either.

The next simulation in order to study the liquid-hexatic transition should be achieved in the grand-canonical ensemble. Simulations in this ensemble have a complexity  $O(N)$  and are simple to implement. The particle movement in this ensemble should either be performed with the event-chain algorithm or with a well-implemented molecular dynamics. An interesting work would be to explore the metastable branches, and show that they differ from the loop due to interface tension. In the picture of a KT transition

preempted by a first-order transition, it would be interesting to study the KT transition in the metastable low-density branch (for  $\eta \gtrsim 0.700$ ).

We now consider possible simulations to study the hexatic-solid transition. As shown before, the nature of this transition clearly seems to be continuous. Again the constant-pressure algorithm is slow to thermalize. A good way to study this transition should therefore be to perform simulations in the grand-canonical ensemble again. The shape of the box should fit a triangular lattice to avoid commensurability problems, as it is done with a rectangular box of size  $L \times L\sqrt{3}/2$ . The positional correlation function, as well as the elastic shear modulus, could then be computed and compared with the KTHNY theory.



## Conclusion

After 50 years of debate, it becomes clear that the hard-disk melting transition follows a two-step scenario with an intermediate hexatic phase. The solid-hexatic transition is continuous, as predicted by the KTHNY theory, while the hexatic-liquid transition is of the first-order type. The liquid phase appears (by formation of grain boundaries for example) at a density higher than the disclinations-unbinding density. The KT transition is thus preempted by this discontinuous transition. This result is specific to the hard-disk model and does not invalidate the KTHNY theory for other 2D systems.

The conclusion obtained regarding the nature of the hard-disk melting transition has been possible through the use of the event-chain algorithm (see Chapter 2), as well as a careful analysis (see Chapter 3). The solution of the melting problem presented in Part I of this thesis provides a starting point for the understanding of melting in films, suspensions, and other soft-condensed-matter systems. The solution developed here can help to study related problems such as the crossover from 2D to 3D melting as it is realized experimentally with spheres under different confinement conditions [84], or the influence of polydispersity for example [127]. Hard disks are a fundamental and simple model of particle systems. Theoretical, computational, and experimental research on more complex microscopic models should build on the hard-disk solution obtained here.



## Part II

# Perfect sampling





## Introduction

The Monte Carlo method in statistical physics allows the study of the thermodynamics of systems. This method can also be used to solve optimization problems, which are frequently observed in the industry or in computer sciences for example.

As seen in Part I of this thesis, the Markov-chain Monte Carlo method consists in randomly sampling a configuration of the system. To that purpose, a Markov chain explores the configuration space by random moves. For some complex configuration spaces, it can be difficult for the chain to explore them. The dynamics of the chain is then very slow, as in glassy systems for example, and it takes a long time for the system to reach the thermodynamic equilibrium. Moreover, the time needed to reach thermalization can be difficult to access. This is major problem. Indeed, it is crucial that the equilibrium is reached in order to study the statistical properties of the system. Therefore, without the knowledge of the thermalization time, it is impossible to obtain reliable results. This problem has been experienced in the study of the hard-disk melting transition (see Part I and Section 4.3.1), and is present in disordered systems such as spin glasses. This issue prevents important problems, such as the relationship between the glass transition and the thermodynamic transition in 3D Ising spin glasses, from being solved [128].

In 1996, Propp and Wilson developed a method to overcome the thermalization problem; a “perfect sampling” method. This method is called “Coupling from the past” (CFTP) [10]. The CFTP method is based on the coupling of Markov chains, and had an large impact in mathematics. However, this method has been found to only be applicable to specific systems, and it still fails to bring a major result in modern statistical physics. The limitation of the method was first thought to come from the “survey” problem. Indeed, this method requires to simultaneously follow a prohibitive number of Markov chains. However, Chanal and Krauth recently solved the survey problem for local Markov chains [129]. The true obstacle to the application of the CFTP method is actually due to the chaotic properties of the Markov chain, that is, the “damage-spreading” [7]. This is the principal result of this part.

For a  $N$ -element system, the classic Hamiltonian dynamics is generally chaotic. This means that two nearby initial conditions quickly separate with time. The same definition of chaos can be used for discrete random processes such as Markov chains. The chaoticity of a Markov chain is referred to as damage spreading [130]. As shown in this part,

the CFTP method cannot be applied to a chaotic dynamics. In order to apply the method, it is necessary to build a regular dynamics, that is, a dynamic where two different initial conditions get closer with time. These dynamics exist and examples are given in Chapter 6.

## The coupling-from-the-past method

In this chapter, I first introduce the Monte Carlo method. I then present the CFTP method and explain the survey problem. I finally present the patch algorithm of Chanal and Krauth [129], which solves the survey problem for local dynamics.

### 5.1 The Monte Carlo method

The Monte Carlo method is a powerful numerical method in order to compute the value of integrals in high dimensions. This method was originally developed in order to study nuclear reactions and is now used in various domains and particularly in statistical physics [3, 4].

#### 5.1.1 Direct sampling

Let  $\Omega$  be the state space of a physical system. In a heuristic approach, we first assume that  $\Omega$  is a hypercube of size  $L$  and dimension  $d$  (thus  $\Omega = [0, L]^d$ ). For a particle system,  $L$  would be the size of the cubic box, and  $d = ND$ , where  $N$  is the number of particles and  $D$  is the spatial dimension of the system<sup>1</sup>. Let  $x$  be a state (also called a configuration) of this space. At the thermodynamic equilibrium, the probability distribution of the configurations is noted  $\pi(x)$ . In order to access the thermodynamic properties of the system, one may compute the mean value of observables. Let  $\mathcal{O}$  be an observable of the system. The mean value of this observable is given by

$$\langle \mathcal{O} \rangle = \int_{[0, L]^d} \pi(x) \mathcal{O}(x) \, d^d x. \quad (5.1)$$

The Monte Carlo method aims at efficiently computing this integral.

We first compute  $\langle \mathcal{O} \rangle$  with the classic Riemann integration method. This method approximates  $\pi(x) \mathcal{O}(x)$  by a stepped function: the space is discretized in a regular way by steps of size  $\delta L$ . The value of the integral is then

$$\langle \mathcal{O} \rangle_{\text{R}} = \sum_x \pi(x) \mathcal{O}(x) \delta L^d \quad \text{with } x \in \{\delta L, 2\delta L, \dots, L\}^d. \quad (5.2)$$

---

<sup>1</sup>Only the positions are stored here.

Let  $n = (L/\delta L)^d$  be the total number of discrete value used to compute the integral. If  $\pi(x)\mathcal{O}(x)$  is smooth at the scale  $\delta L$  (which is generally the case for  $\delta L$  small enough), the numerical error induced by this method is  $\text{Err}_R \propto \delta L^2$  and therefore

$$\text{Err}_R \propto \frac{1}{n^{2/d}}. \quad (5.3)$$

For large values of  $d$  (corresponding to large  $N$  for particle systems), the number of discretization points required to compute the integral is large as it grows as  $L^d$ . Therefore, the Riemann integration method cannot be applied in high dimensions.

We now compute  $\langle \mathcal{O} \rangle$  by the direct Monte Carlo method. This method adopts a different sampling strategy: the space is randomly sampled instead of regularly. Let  $\{x_1, \dots, x_n\} \in [0, L]^d$  be  $n$  configurations randomly sampled. If the sampling distribution is uniform, the integral is computed by

$$\langle \mathcal{O} \rangle_{\text{DMC}} = \frac{L^d}{n} \sum_{i=1}^n \pi(x_i) \mathcal{O}(x_i). \quad (5.4)$$

As the samples are independent, the error on this integral satisfies

$$\text{Err}_{\text{DMC}} \propto \frac{1}{\sqrt{n}}. \quad (5.5)$$

The behavior of the error with the number of samples does not depend on the dimension of the space. For  $d \geq 5$ , in the limit of large  $n$ ,  $\text{Err}_R \gg \text{Err}_{\text{MC}}$ . This simple method is therefore much more efficient than the Riemann integration method in order to compute this integral.

For a uniform sampling distribution, the error is given by

$$\text{Err}_{\text{DMC}} = \frac{\sigma_{\text{DMC}}}{\sqrt{n}} \quad \text{with} \quad \sigma_{\text{DMC}} = \sqrt{L^d \int [\pi(x)\mathcal{O}(x)]^2 d^d x - \left[ \int \pi(x)\mathcal{O}(x) d^d x \right]^2}. \quad (5.6)$$

In practice, the distribution  $\pi(x)\mathcal{O}(x)$  shows strong variations. The choice of a uniform distribution in order to sample the system is then not adequate, as it leads to a very large standard deviation  $\sigma_{\text{DMC}}$ . For a  $N$ -element system, the time needed to sample a configuration of the system is  $\propto \exp(\text{const}.N)$ . A good example of this phenomenon is given by the direct sampling of hard spheres, which is impossible to achieve for large systems (see Part I, Section 2.1.2). An alternative is to sample the system with a distribution following the variation of  $\pi(x)\mathcal{O}(x)$ , such as  $\pi(x)$  for example. This choice of distribution gives an error  $\text{Err} = \sigma/\sqrt{n}$  with  $\sigma = \sqrt{\langle (\mathcal{O} - \langle \mathcal{O} \rangle)^2 \rangle}$ . However, even if the distribution  $\pi$  is properly defined, its structure can be complex; it is generally impossible to sample random configurations with this distribution. The Markov-chain Monte Carlo method is a solution to this problem.

### 5.1.2 The Markov-chain Monte Carlo Method

As describe in Section 2.1.2, a Markov chain is a memoryless stochastic process in the configuration space  $\Omega$ , that is, a random walk without memory. The chain starts at an initial

configuration  $x_0$ , then randomly explores the configurations of the system (see Fig. 5.0). The next configuration of the chain only depends upon the current configuration. The Markov-chain Monte Carlo method uses a Markov chain whose stationary distribution (that is, the probability distribution of configurations for  $t \rightarrow \infty$ ) is the distribution  $\pi$ . It is therefore an indirect way to sample configurations from the distribution  $\pi$ . This method is generally much more efficient than the direct approach.

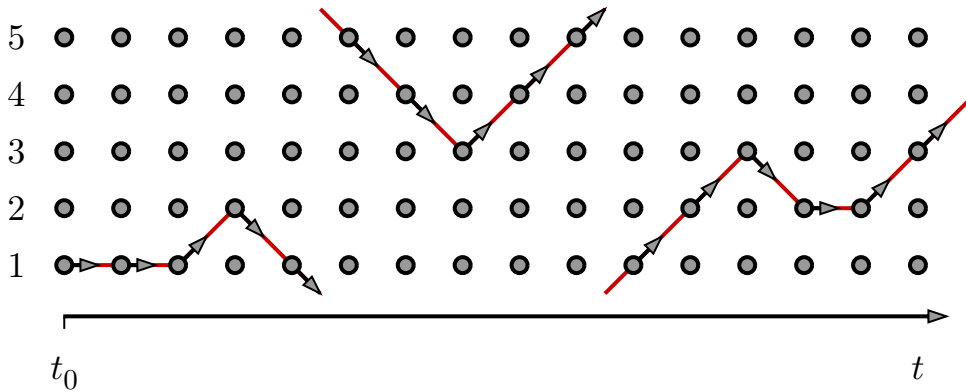


**Figure 5.1:** Random walk in 1D for a discrete system with periodic boundary conditions. The transition probabilities are 1/3 to go up, 1/3 to go down, and 1/3 to stay at the same configuration. (Ref [131]).

Let  $P(x \rightarrow y)$  be the transition probability of the Markov chain from a configuration  $x \in \Omega$  to another configuration  $y \in \Omega$ , and  $A = (P(x \rightarrow y))_{x,y}$  the transfer matrix. The chain starts from an initial configuration  $x_0$ , the initial probability distribution of the chain is therefore  $\pi_0 = \delta_{x,x_0}$ . If the distribution at a (discrete) time  $t$  is represented by the vector  $\pi_t \in [0, 1]^{\text{card}(\Omega)}$ , the distribution at a time  $t + 1$  is  $\pi_{t+1} = A\pi_t$ .  $\pi_t$  is therefore given by

$$\pi_t = A^t \pi_0. \quad (5.7)$$

In the case of a Markov chain satisfying the detailed balance condition, the operator  $A$  is symmetric and therefore diagonalizable in an orthogonal basis. Moreover, its eigenvalues satisfy  $|\lambda| < 1$  except for one of them  $\lambda_0 = 1$ . Let  $\{\Pi_0, \Pi_1, \Pi_2, \dots\}$  be the eigenvectors of  $A$  of respective eigenvalues  $\{\lambda_0 = 1 > |\lambda_1| \geq |\lambda_2| \geq \dots\}$ . The distribution  $\pi_t$  can be expanded on these eigenvectors and satisfies

$$\pi_t = \Pi_0 + a_1 \lambda_1^t \Pi_1 + a_2 \lambda_2^t \Pi_2 + \dots \quad (5.8)$$

Therefore, each eigenvector  $\Pi_i$  with  $i > 0$  displays a time scales  $\tau_i = -1/\ln |\lambda_i|$  and  $\tau_1 \geq \tau_2 \geq \dots$ .

Eq. (5.8) shows that the probability distribution of the chain converges toward the ground state  $\Pi_0$  of the transfer matrix. The transition probabilities must therefore be designed in order that  $\Pi_0 = \pi$ . This can be done by ensuring that the balance condition (see Section 2.1.2 Eq. (2.9)) or the more restrictive detailed-balance condition (see Section 2.1.2 Eq. (2.11)). A way to satisfy the detailed-balance condition is given by the Metropolis algorithm [46] (see Section 2.1.2).

For a time  $t \gg \tau_1$ , the distribution  $\pi_t$  is very close to the distribution  $\pi$ . A way to compute the mean value  $\langle \mathcal{O} \rangle$  is to extract the configuration of the chain each time step  $\Delta t$ . Let  $\{x_1, \dots, x_n\}$  be the  $n$  configurations extracted.  $\langle \mathcal{O} \rangle$  is computed by

$$\langle \mathcal{O} \rangle_{\text{MCMC}} = \frac{1}{n} \sum_{i=1}^n \mathcal{O}(x_i). \quad (5.9)$$

Under the condition that  $\Delta t \gg \tau_1$ , the error on  $\mathcal{O}$  is

$$\text{Err}_{\text{MCMC}} \simeq \frac{\sigma}{\sqrt{n}} \quad \text{with} \quad \sigma = \sqrt{\langle (\mathcal{O} - \langle \mathcal{O} \rangle)^2 \rangle}, \quad (5.10)$$

the equality would be strictly valid in the limit  $\Delta t \rightarrow \infty$ . This constitutes the Markov-chain Monte Carlo method.

### 5.1.3 Standard deviation and correlation time

The Markov-chain Monte Carlo method is powerful as it allows access to the distribution  $\pi$ . However, in order to estimate the error on an observable, the method faces two challenges.

First, the standard deviation  $\sigma$  of the observable has to be estimated. This problem is also present in the direct Monte Carlo method.  $\sigma$  would be perfectly known in the limit of an infinitely large number of sample. In most systems, only a small number of samples are required to obtain a good estimation. However, in other systems, this task can require a large - and unknown - number of samples. Such systems can be constructed by attributing a large value to  $\mathcal{O}$  in regions where  $\pi(x)$  is very small. A solution to this problem can be to sample the system with a distribution  $\propto \pi(x)\mathcal{O}(x)$  instead of  $\pi(x)$ . Therefore, even if there is no rigorous method to estimate the value of  $\sigma$ , the standard-deviation problem is not the main obstacle to the Markov-Chain Monte Carlo method.

The second problem is to know when the distribution has reached its steady state, that is, the amount of time needed for the system to lose the memory of its initial configuration  $x_0$  (the thermodynamic equilibrium). This constitutes the main issue of the method. The study of the convergence of Markov chains is an entire mathematical topic [132, 107]. Eq. (5.8) shows how the distribution converges toward its steady state. In a simple view, one can say that  $\tau = \tau_1$  is the typical time of convergence. This time corresponds to the asymptotic convergence of the chain, and is called the correlation time.

The correlation time can be computed by direct diagonalization of the transfer matrix  $A$ . However, it is in practice impossible as the size of  $A$  is very large.  $\tau$  is generally computed by the study of the asymptotic behavior of the auto-correlation function of an observable  $\mathcal{O}$  as shown in Section 2.2.3. The asymptotic behavior is however hard to access in interesting physical systems. An example of this difficulty is given by the hard-disk model; even for this simple model, it is difficult to ensure that the system is thermalized. As a consequence, many works on the hard-disk meting transition obtained doubtful and contradicting results as the systems studied were not decorrelated from their initial configuration (see Section 4.3.1). Another famous example is given by disordered systems such as spin glasses [133]. These systems show a complex energy landscape,



with many local minima. As a consequence, the Markov chain can be trapped in a local minimum, and the auto-correlation analysis would underestimate the correlation time. Many theoretical questions concern these systems, such as the relationship between the glass transition and the thermodynamic transition [128] in the 3D spin-glass model.

In order to solve these important problems, it would be useful to know the correlation time of the Markov chain. Algorithms have been developed which are able to sample configurations of the system with the exact desired distribution  $\pi$ . These sampling algorithms are referred to as perfect-sampling algorithms.

### 5.1.4 Perfect-sampling methods

The direct sampling of Section 5.1.1 constitutes the most simple perfect-sampling method. This method is however inefficient as the distributions which can be directly sampled are generally far from the desired distribution  $\pi$ . In specific problems, this problem can be overcome. For example, it is possible to obtain perfect sample of the 2D Ising spin-glass model efficiently [134, 135]. These methods use combinatorial techniques originally developed for the ferromagnetic case [136], and they cannot be extended to the 3D case. A more general scheme, the “Randomness recycler” [137], has been developed. This method applies to a variety of systems such as lattice hard spheres. This algorithm is however not yet applicable to hard disks or to the 3D Ising spin glass at low temperatures.

The following concerns a general perfect-sampling method which uses Markov chains: the CFTP method [10]. With the classic utilization of Markov chains, it seems impossible to obtain a perfect sample. Indeed, the system is always correlated (even slightly) to its initial configuration (see Eq. (5.8)). This fact can be changed under the condition that the run time is random. Simple examples of such processes are the card shuffling of Aldous and Diaconis [138] and the “dead-leaves” model [139]. In the more general CFTP method, the simulation time is also random.

## 5.2 Coupling from the past

The CFTP method [10] is a general scheme which turns a classic Markov chain into a perfect sampling process. This method uses the “coupling” phenomenon of Markov chains, where two Markov chains, starting from different initial configuration, eventually reach the same configuration.

### 5.2.1 Forward coupling

Let us consider two simultaneous Markov chains  $x_t$  and  $y_t$ , satisfying the same transition probabilities, but starting with different initial conditions, say  $x_0$  and  $y_0$ . We also assume that the transition probabilities do not depend upon the chain ( $x$  or  $y$ ) but only upon the configuration<sup>2</sup>. One can therefore build the “random maps”  $\{f_0, f_1, \dots\}$  where  $f_t : \Omega \rightarrow \Omega$  stores the transitions for each possible configuration of  $\Omega$  at a time  $t$  (see the arrows in Fig. 5.1 for example). The chains are then said to be coupled if at a time  $t$

---

<sup>2</sup>This is, for example, done by choosing the same random number sequence in both chains.

they occupy the same configuration. Once the chains are coupled, they follow the same path, that is,

$$x_t = y_t \quad \Rightarrow \quad x_{t'} = y_{t'} \quad \forall t' > t. \quad (5.11)$$

The coupling of Markov chains is commonly used in mathematics to prove various properties of the chains, such as ergodicity [140].

The coupling of Markov chains goes along with a loss of memory. Indeed, after the coupling, it is impossible to tell whether the initial configuration of the chain was  $x_0$  or  $y_0$ . This property can be used to design a perfect-sampling method. Let us start the coupling process with as many Markov chains as possible, that is, with chains starting from each possible initial configurations. The chains show several couplings until only one chain remains for  $t \geq \tau_{\text{coup}}$  (see Fig. 5.1). The time  $\tau_{\text{coup}}$  when the global coupling occurs is called the “coupling time”. This coupling process is called a “forward coupling”.

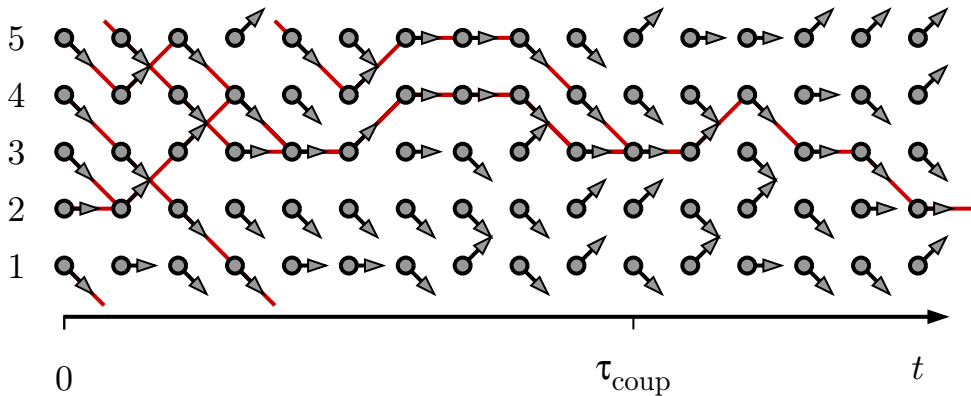


**Figure 5.2:** Example of forward coupling with the system in Fig. 5.0. The transition maps are represented by the gray arrows. After  $\tau_{\text{coup}} = 10$ , all Markov chains (red lines) follow the same path; the memory of the initial configuration is lost. (Ref [131]).

As the chains start from each possible configuration, the remaining chain after the time  $\tau_{\text{coup}}$  has no memory of any initial configuration. A “memoryless” algorithm can therefore be designed: the sample is extracted at  $t = \tau_{\text{coup}}$  after a forward coupling. This sampling is indeed memoryless, but its distribution differs from the stationary distribution  $\pi$  of the underlying Markov chain. This can be shown in a simple example. We consider a system constituted of two configurations, labeled 1 and 2, and a Markov chain whose transition probabilities are  $P(1 \rightarrow 2) = 0.5$  and  $P(2 \rightarrow 1) = 1$  (see Fig. 5.2). The stationary distribution of the chain is  $\pi(1) = 2/3$  and  $\pi(2) = 1/3$ . However, the coupling only occurs on the configuration 1. The stationary distribution of this process is thus  $\pi(1) = 1$  and  $\pi(2) = 0$ . A modification can turn the sampling both memoryless and satisfying the probability distribution  $\pi$ , that is, turning it perfect: the CFTP method.

## 5.2.2 Coupling from the past

We consider a forward coupling starting at an initial time  $t_{\text{init}} \rightarrow -\infty$ . The process generates the transition maps  $\{f_{\simeq -\infty}, \dots, f_{-2}, f_{-1}\}$ . At  $t = 0$ , the chains are necessarily

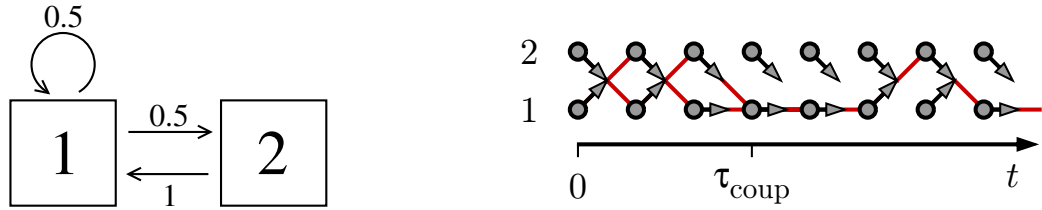


**Figure 5.3:** *Left:* A Markov chain for a two-state system. The arrows represent the transition probabilities. The stationary distribution is  $\pi(1) = 2/3$  and  $\pi(2) = 1/3$ . *Right:* The coupling can only occur on the configuration 1.

coupled. Moreover, as it corresponds to an infinite simulation time, the resulting unique configuration  $x_p$  at  $t = 0$  is distributed according to  $\pi$ . Because of the coupling, it is not necessary to run the process from  $t_{\text{init}} \rightarrow -\infty$ . Indeed, let us imagine that a forward coupling, starting from  $t < 0$ , couples before  $t = 0$ . Then, a forward coupling, starting from  $t' < t$  (with the same random maps), gives the same configuration  $x_p$  at  $t = 0$  (see Fig. 5.3). The configuration  $x_p$  is therefore the result of the infinite simulations; it forms a perfect sample distributed according to  $\pi$ . In order to find  $x_p$ , the transition maps can be explored backward ( $t = 0$ , then  $t = -1$ , etc.) until a forward coupling takes place before  $t = 0$ . This constitutes the CFTP method.

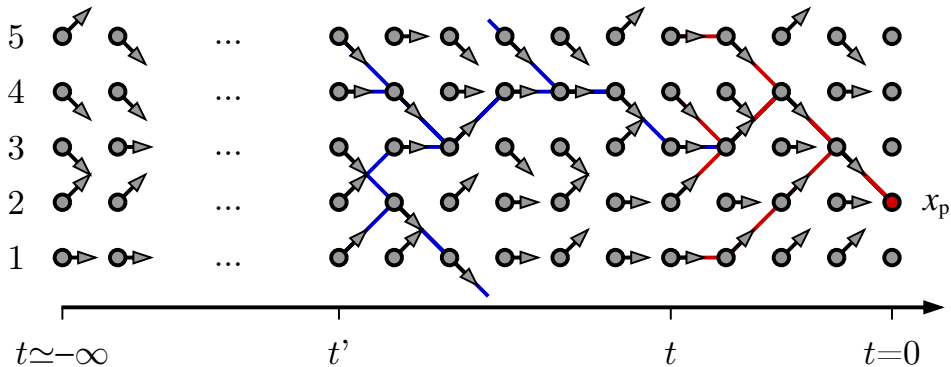


**Figure 5.4:** Example of a CFTP process with the system of Fig. 5.0. The configuration  $x_p$  at  $t = 0$  is determined by a coupling forward starting at  $t = -4$ . The same value for  $x_p$  is obtained from an earlier forward coupling (at  $t'$ ) and thus also from the infinite simulation ( $t \simeq \infty$ ).  $x_p$  is perfectly sampled. (Ref [131]).

In practice, the random maps  $\{f_{-T}, \dots, f_{-1}\}$  are generated, and  $T$  is a finite parameter of the algorithm. If the forward coupling, starting from  $t = -T$ , couples before  $t = 0$ , the sample  $x_p$  is then extracted. Otherwise, additional maps  $\{f_{-2T}, \dots, f_{-T-1}\}$  are generated and so on. The process stops when the unique state  $x_p$  is determined.

The CFTP method is not limited to discrete systems, and it can for example be applied to hard spheres (see Section 6.3). In systems with  $N$  elements (spins, hard spheres, etc), the configuration space generally grows exponentially with  $N$ . The CFTP thus faces two distinct challenges. First, it must survey the entire configuration space in order to prove

coupling. Second, it must ensure that the coupling time does not become much larger than the correlation time. The first problem has been solved for local Markov chains by the use of a patch algorithm [129, 131]. The second problem is related to the damage spreading of the Markov chain [7] (see Chapter 6).

## 5.3 Survey problem

The CFTP method requires to follow Markov chains starting from all possible initial configurations. The number of configurations in a system with  $N$  elements is very large. For example, a 2D Ising spin system with 64 spins has  $2^N \simeq 10^{1233}$  configurations. It is therefore impossible to track each Markov chain individually, because of limited computer time and memory.

### 5.3.1 Partial order

In specific systems, a “partial order” allows to track only two initial configurations. In these systems, the partial order “ $\preceq$ ” between configurations of the system is conserved by the random maps  $f$ :

$$x_t \preceq y_t \Rightarrow x_{t+1} \preceq y_{t+1}. \quad (5.12)$$

If two extrema for this order exists,  $x_{\min}$  and  $x_{\max}$ , the coupling of the chains starting from  $x_{\min}$  and  $x_{\max}$  implies the coupling of all chains. Therefore, only these two chains have to be followed in order to prove global coupling.

For example, a partial order is preserved in the Ising model with ferromagnetic interactions under heat-bath dynamics [10], or in a model of directed polymers under heat-bath dynamics again [131]. For these systems, the CFTP is thus easily applicable. The partial order also gives an indication about the coupling time  $\tau_{\text{coup}}$ . If  $\tau_{\text{corr}}$  is the correlation time, and  $N$  is the number of elements in the system, a theorem [10] states that the partial order implies

$$\tau_{\text{coup}}/\tau_{\text{corr}} \leq O(\ln N). \quad (5.13)$$

In the example of the ferromagnetic Ising model under heat-bath dynamics, the two extrema for the partial order are the configurations of magnetization  $M = N$  and  $M = -N$ . The partial order implies that the magnetization  $M^+(t)$  and  $M^-(t)$  of these initial configurations satisfy  $M^+(t) \geq M^-(t)$ . In the paramagnetic phase, these magnetizations converge toward zero with a typical time scale of  $\tau_{\text{corr}}$ :  $M^+(t) \sim N \exp(-t/\tau_{\text{corr}})$  and  $M^-(t) \sim -N \exp(-t/\tau_{\text{corr}})$ . This gives that the chains couple for approximately  $N \exp(-\tau_{\text{coup}}/\tau_{\text{corr}}) \sim 1$  and thus  $\tau_{\text{coup}} \sim \tau_{\text{corr}} \ln N$ . The partial order is however absent in most systems.

### 5.3.2 Patch algorithm

The patch algorithm [129, 131] is a general method which solves the survey problem for local Markov-chain dynamics. Instead of following the configurations individually, this algorithm follows the configurations from parts of them (the patches). The total set of configurations followed at a time  $t$  is larger than the actual set of remaining configurations. Therefore, this method gives an upper bound for the coupling time  $\tau_{\text{coup}}$ . The upper

bound is generally close to the real value of  $\tau_{\text{coup}}$ , and the extra computer time needed to perform this survey is not prohibitive. We describe this algorithm in the 2D Ising spin-glass model under heat-bath dynamics. The idea is however applicable to general systems (such as hard spheres) [131].

A configuration  $x$  of the 2D square-lattice Ising model is defined by the value of its  $N$  spins  $x = \{s_1, s_2, \dots, s_N\}$  where  $s_i \in \{-1, 1\}$ . The energy of this configuration is given by

$$E_x = - \sum_{\langle i,j \rangle} J_{ij} s_i s_j. \quad (5.14)$$

The sum extends over the nearest neighbors (with periodic boundary conditions). For the spin-glass version, the interactions are  $J_{ij} = \pm 1$  with equal probability. In the canonical ensemble, the distribution of the configurations satisfies  $\pi(x) \propto \exp(-\beta E_x)$  where  $\beta = 1/k_B T$  is the inverse temperature. Heat-bath dynamics consists in choosing at each step one spin  $s_k$ , and updating it with probabilities

$$\pi(s_k = \pm 1) = \frac{1}{1 + \exp(\mp 2h_k \beta)}. \quad (5.15)$$

The field on site  $k$  is given by  $h_k = \sum_l J_{kl} s_l$ . As a coupling process, the same random numbers are used for each configuration. The same spin is therefore selected for each configuration, and updated with the same random number  $\gamma$ .  $\gamma \in [0, 1]$  is uniformly sampled, and the update is done by

$$s_k = \begin{cases} 1 & \text{if } \gamma < \pi(s_k = 1) \\ -1 & \text{if } \gamma > \pi(s_k = 1) \end{cases}. \quad (5.16)$$

In this system, it is impossible to individually store the  $2^N$  initial configurations. We first consider a simple way to follow the set of configurations by the use of patches  $1 \times 1$ , that is, single spins. Each configuration can be constructed by the assembly of single spins. Therefore, the spins constitute the standard basis of the initial set  $\Omega_0 = \{-1, 1\}^N$ . During the simulation, configurations couple, and the set  $\Omega_t$  of remaining configurations at a time  $t$  reduces. As already mentioned, the exact tracking of  $\Omega_t$  is impossible. However, let us suppose that for a given spin update, the random number is  $\gamma \simeq 0$ . As a consequence, the field  $h_k$  does not influence the update (see Eq. (5.15) and Eq. (5.16)), and the resulting spin will be  $s_k = 1 \forall x \in \Omega_t$ . The element  $s_k = 1$  can then be removed out of the basis. The new basis generates a superset  $\tilde{\Omega}_t \supset \Omega_t$ , which is smaller than the initial set. For other updates, one might have to add a new element to the basis. Therefore, a method to ensure coupling can be to follow this superset by removing (or adding) elements to the basis when possible (or necessary). If the superset  $\tilde{\Omega}_t$  reduces to a single configuration, the coupling is ensured. This is the ‘‘summary states’’ method [141, 142, 143]. This method is only applicable at high temperatures. Indeed, if the temperature is too low, the amount of removed and added element of the basis equalizes and the superset takes an infinite time to reduce to a single configuration (while the actual set of remaining configurations  $\Omega_t$  does).

In order to ensure the coupling at lower temperature, the summary state strategy is used but with a different basis. Instead of storing configurations in a basis of single spins, the patch algorithm stores the configurations on a pseudo-basis made of rectangular

patches. We consider for example patches of size  $3 \times 3$ . The pseudo-basis is constituted of  $N$  sets  $\{S_1, S_2, \dots, S_N\}$ ,  $S_k$  being a set of patches  $3 \times 3$  centered around the spin  $k$ . At the initial state, each set  $S_k$  is composed of  $2^{3 \times 3} = 512$  patches. A superset of the configuration can be recovered by an assembly of these patches

$$\tilde{\Omega}_t = S_1 \otimes S_2 \otimes \dots \otimes S_N \quad (5.17)$$

(see Fig. 5.4). The patch algorithm uses three subroutines: the “update” of the patches, the “pruning” of the patches, and the “merging” of the patches.

Let  $s_k$  be the spin to update through heat-bath dynamics. The patches containing the spin  $s_k$  have to be updated. There are two different updates: If  $s_k$  is not at the border of the patch, the update is direct as the local field  $h_k$  can be computed within the patch. In this process, two patches of the same set  $S_k$  can become identical, one of them is thus removed out of the set. If  $s_k$  is at the border of the patch, the update has to assume each possible field  $h_k$  for each possible combination of the unknown spins. As a consequence, new patches might have to be included in the set.

The pruning process ensures the compatibility between patches. Indeed, as the patches are overlapping (see Fig. 5.4), a given patch of the set  $S_k$  can be incompatible with all patches of the neighboring set  $S_{k'}$ . The incompatible patches are then removed.

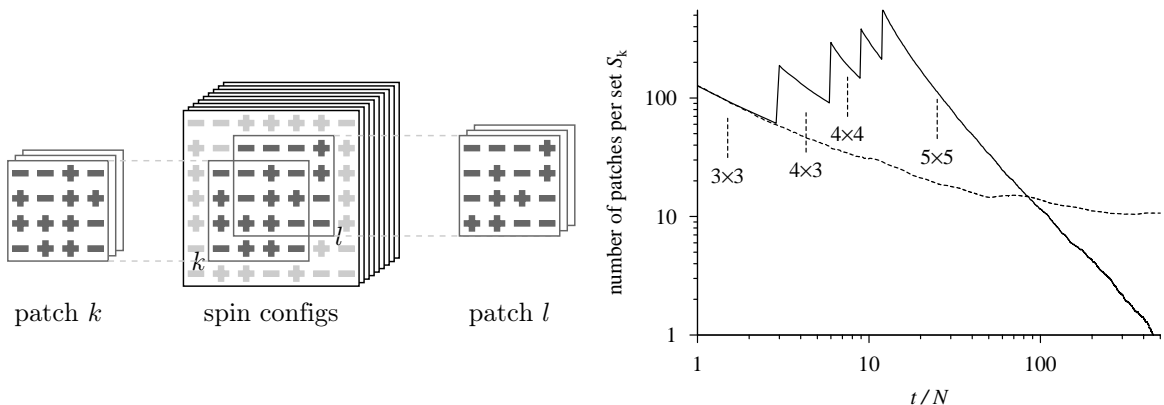


**Figure 5.5:** *Left:* The set of configurations is stored in patches. Each configuration can be made by an assembly of patches. *Right:* Number of patches per set  $S_k$  as function of time for the  $32 \times 32$  spin glass at  $\beta = 0.5$ . A simulation with  $3 \times 3$  patches is compared to a simulation with patches of increasing size. (Ref [7], see Section 7.2).

In this method, the number of patches per set decreases (see Fig. 5.4). If the temperature is high enough, the superset  $\tilde{\Omega}_t$  eventually reduces to a single configuration. At a lower temperature (as for the  $1 \times 1$  patches), the number of configuration in  $\tilde{\Omega}_t$  reaches a stationary value higher than 1. In order to avoid that, the patches are merged during the simulation in larger patches  $4 \times 4$ ,  $5 \times 5$ , and so on. This allows the superset  $\tilde{\Omega}_t$  to be reduced even further, eventually reaching a single-configuration state. Moreover, this merging process reduces the time needed to reach the single-configuration state (see Fig. 5.4).

As  $\tilde{\Omega}_t$  is a superset of  $\Omega_t$ , the time when  $\tilde{\Omega}_t$  is singular is an upper bound of the real coupling time  $\tau_{\text{coup}}$ . This upper bound is what is needed in order to apply the CFTP

method. This method applies to most local algorithms, such as the heat-bath algorithm in 3D Ising models, or the birth-and-death algorithm in hard spheres (see Section 6.3).

With this method, Chanal and Krauth [129] obtained perfect samples of the 2D Ising spin glass for a system of  $64 \times 64$  spins at a temperature  $\beta = 0.5$ . For 3D spin glass, they obtained perfect samples down to the temperature of  $\beta = 0.3$ . They also obtained [131] perfect sample of  $\sim 60$  hard disks at a density  $\eta = 0.28$ . These temperatures (and densities) are lower (higher) than what was reached previously. These values are however still far from the phase transitions ( $\beta_c \simeq 0.9$  [128] for 3D spin glass, and  $\eta \simeq 0.7$  for hard disks). At lower temperatures (or higher densities), the method fails to reach a single configuration.

## Conclusion

The CFTP method overcomes the problem of the initialization bias. This method could be helpful in physical systems where the correlation time is hard to access. However, the CFTP method encounters difficulties in these systems. Even the patch algorithm fails to sample 2D spin glasses at a temperature lower than  $\beta \simeq 0.5$ , or hard disks at a density higher than  $\eta \simeq 0.3$ . It is interesting to know if these difficulties are due to a failure of the tracking method, or merely the coupling time has a value much larger than the correlation time. This question is answered by the analysis of the coupling time as function of temperature (or density) and system size for spin glasses and hard disks. The results show that the tracking system is not responsible for these difficulties.





## Damage spreading and coupling in Markov chains

In this chapter, I show that the limitation of the CFTP method is due to the damage-spreading transitions of Markov chains, already studied in the literature [130, 144, 145]. I then discuss the behavior of these dynamical transitions in spin glasses and hard disks for various algorithms and coupling schemes. The transition temperatures and densities are found to depend on the coupling scheme. These results have been published in [7] (see Section 7.2).

### 6.1 Chaos in Markov chains

Chaos manifests itself in Hamiltonian dynamical systems when nearby initial configurations drift apart with time. Chaos can also be defined for cellular automata and for Markov chain algorithms. In these systems, following Kauffman [130], the drifting-apart of configurations is termed “damage spreading”. In contrast, for “regular” dynamics, two nearby initial configurations become identical after a finite time, and remain indistinguishable from then on. This behavior is closely related to the coupling of Markov chains. In systems with  $N$  elements (spins, hard spheres, etc), the configuration space generally grows exponentially with  $N$ . A chaotic dynamics would cause the coupling time to explode: it would become much larger than the correlation time as any two configurations have a very small probability for finding each other in a large space. Damage spreading has been studied in many physical systems, in particular spin glasses [144]. In several spin glass models with heat-bath dynamics, it is now well established that a dynamical damage-spreading transition occurs at a critical temperature,  $\beta_{\text{ds}}$ , located in the paramagnetic phase [145]. The dynamic is regular at temperatures higher than  $1/\beta_{\text{ds}}$  and chaotic at lower temperatures. Even for the 2D  $\pm J$  Ising spin glass, whose thermodynamic phase transition is at  $T = 0$  [146, 147], the transition to chaos takes place at finite temperature [145]. In the following, the behavior of the coupling time  $\tau_{\text{coup}}$  is studied for different algorithms, temperature (or density), and system size. To that purpose forward couplings are realized and averaged.

### 6.1.1 Partial survey

The patch algorithm of Section 5.3.2 gives an upper bound for the coupling time  $\tau_{\text{coup}}$ . A simple method allows a lower bound to be reached: the “partial survey”. In the partial survey, only a few initial configurations are individually followed until they couple. The knowledge of both bounds allows one to study the behavior of the coupling time at different temperatures (or densities) as function of system size.

In practice, only a small number of initial configurations  $N_{\text{init}}$  is needed to obtain a good lower bound of  $\tau_{\text{coup}}$ . Indeed, with increasing  $N_{\text{init}}$ , the coupling time is found to quickly saturate at its final value. This is called the “saturation” phenomenon (see Fig. 6.0). Moreover, this lower bound for  $\tau_{\text{coup}}$  is generally found to be equal to the upper bound found by the patch algorithm. This can be understood with a simple argument: Just before the coupling (of all initial configurations) only two Markov chains,  $x$  and  $y$ , remain. Under the assumption that about half of the initial chains are merged into  $x$ , and that the other half are merged into  $y$ , the probability that the partial-survey coupling time is lower than the actual coupling time  $\tau_{\text{coup}}$  is  $p = 1/2^{N_{\text{init}}}$ . This probability becomes very low for large values of  $N_{\text{init}}$ . Of course, the assumption of equal weight for the two last-remaining Markov chains can be broken in specifically designed systems. However, in the systems studied (Ising spin glass, hard spheres), the saturation property is always observed. In this thesis, the partial surveys are performed with a number of  $N_{\text{init}} = 10$

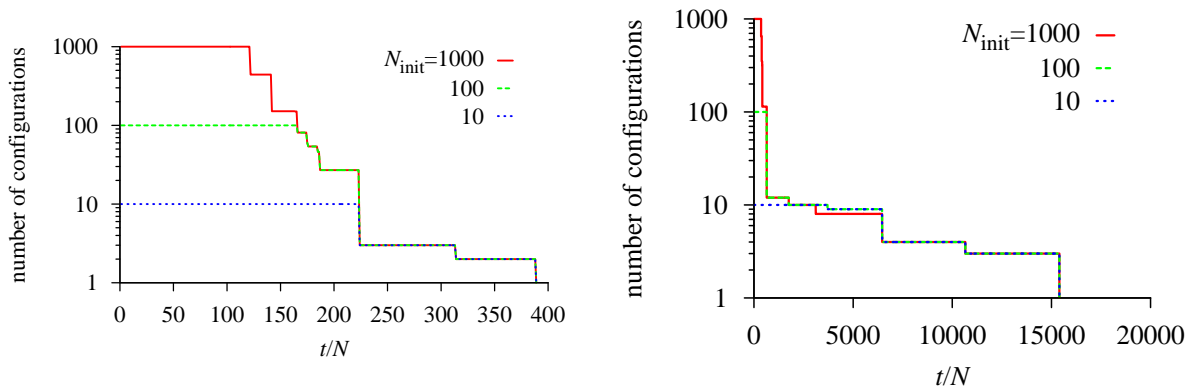


**Figure 6.1:** Independent partial survey with  $N_{\text{init}}$  initial configurations for the 2D Ising spin glass with  $64^2$  spins under heat-bath dynamics. *Left:*  $\beta = 0.5$ , the coupling time saturates at  $\tau_{\text{coup}} = 389$  (for this sample) even with  $N_{\text{init}} = 10$ . The patch algorithm gives the same value for the upper bound. *Right:*  $\beta = 0.6$ , the coupling time saturates at  $\tau_{\text{coup}} = 15402$ . Again, the patch algorithm gives the same value for the upper bound. (The strong increase of  $\tau_{\text{coup}}$  between the two densities hints the change of behavior at  $\beta \sim 0.6$ .)

initial configurations.

### 6.1.2 Random walks in high dimensions

Before analyzing 2D spin glasses and hard spheres, we illustrate the coupling and the damage spreading in a simple Markov-chain algorithm. This algorithm can be interpreted either as a random walk in an  $N$ -dimensional hypercubic lattice, as the dynamics of

$N$  distinguishable non-interacting particles in a 1D lattice of length  $L$ , or as  $N$  non-interacting Potts spins with  $L$  configurations. For the random walk (see Fig. 6.1), each  $N$ -dimensional lattice site  $i = \{i_0, \dots, i_{N-1}\}$  is described by integers  $i_k \in \{0, \dots, L-1\}$  with periodic boundary conditions. The particle can hop from site  $i$  to one of  $i$ 's nearest neighbors in direction  $k$ ,  $j = i \pm \delta_k$ , with  $\delta_k = \{0, \dots, 1, 0, \dots\}$  (periodic boundary conditions are again understood). The probability for moving from  $i$  to  $j$  is

$$P(i \rightarrow j) = \begin{cases} \frac{1}{3N} & \text{for } j = i \pm \delta_k \\ \frac{1}{3} & \text{for } j = i \\ 0 & \text{otherwise} \end{cases} . \quad (6.1)$$

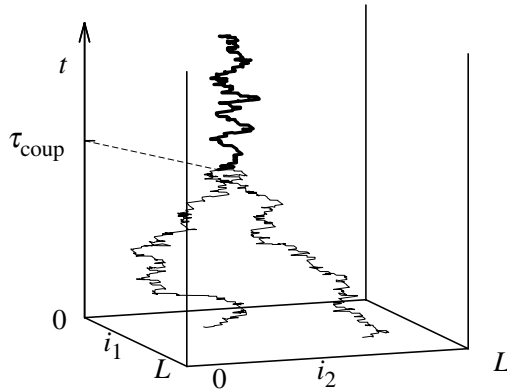


**Figure 6.2:** Coupling of two random walks in a periodic  $N$ -dimensional hypercubic lattice of length  $L$ . After the time  $\tau_{\text{coup}}$ , the two random walks evolve identically. The chaotic coupling of Eq. (6.2) is shown. For the regular coupling of Eq. (6.3), the displacement at time  $t$  is in the same dimension  $k$ , and it is a function of  $i_k$  only. (Ref [131]).

The simulation thus samples at each time step one dimension,  $k$ , among the  $N$  available ones (it moves in “ $x$ ”, or “ $y$ ” or “ $z$ ”, etc). In dimension  $k$ , it then hops with probability  $1/3$  each to the left or to the right, or remains on the same site. Eq. (6.1) also describes  $N$  distinguishable non-interacting particles on a 1D lattice of length  $L$ , again with periodic boundary conditions. At time  $t$ , a randomly chosen particle  $k$  hops to the left or to the right, or it remains on the same site, each with probability  $1/3$ , as above.

A two-configuration coupling is a random process  $\tilde{P}(i \rightarrow j, i' \rightarrow j')$  for the joint evolution of two random walks such that integrating over one of them yields the original random walk of Eq. (6.1) for the other. After they meet, the two configurations evolve in the same way. The simplest choice for a coupling is the product ansatz,

$$\tilde{P}(i \rightarrow j, i' \rightarrow j') = \begin{cases} P(i \rightarrow j)P(i' \rightarrow j') & \text{if } i \neq i' \\ P(i \rightarrow j) & \text{if } i = i', j = j' , \\ 0 & \text{otherwise} \end{cases} , \quad (6.2)$$

where the two random walks evolve independently from each other if they are on different sites  $i$  and  $i'$ , but stay together once they have met ( $j = j'$  if  $i = i'$ ). To implement this

coupling for any number of configurations, one samples at each time step independent random moves at each site, so that particles on the same site experience the same randomness. In the above-mentioned representation of particles on the 1D line, we consider the coupling of two  $N$ -particle systems, again described by Eq. (6.2), as the independent evolution, at time  $t$ , of the  $L^N$  possible configurations of the system. Naturally, the coupling time behaves as  $\tau_{\text{coup}} \propto L^N$  whereas the correlation time (in displacements per particle) behaves as  $\tau_{\text{corr}}/N \propto L^2$ .

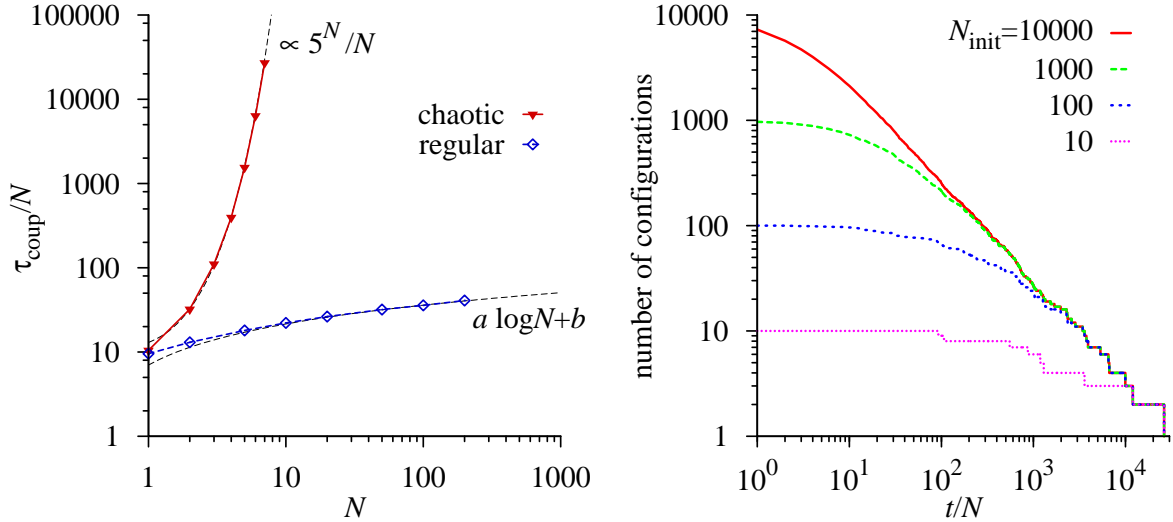


**Figure 6.3:** *Left:* Chaotic and regular couplings for the random walk in a  $N$ -dimensional hypercubic lattice of length  $L = 5$  (see Eq. (6.2) and Eq. (6.3), respectively). The random process for a single random walk is defined by Eq. (6.1) in both cases. (Ref [7], see Section 7.2). *Right:* Number of configurations *vs.* time as a function of the number  $N_{\text{init}}$  of initial configurations, for  $N = 7$ ,  $L = 5$ , with the chaotic coupling. The number of configurations slowly decays in a power-law function.

An alternative coupling consists in sampling, at time  $t$ , one dimension  $k$  common to all random walks. The two-configurations coupling scheme is then

$$\tilde{P}(i_k \rightarrow j_k, i'_k \rightarrow j'_k) = \begin{cases} P(i_k \rightarrow j_k)P(i'_k \rightarrow j'_k) & \text{if } i_k \neq i'_k \\ P(i_k \rightarrow j_k) & \text{if } i_k = i'_k, j_k = j'_k \\ 0 & \text{otherwise} \end{cases} \quad (6.3)$$

so that two configurations  $i$  and  $j$  with  $i_k = i'_k$  will preserve this common coordinate ( $j_k = j'_k$ ). In the representation of  $N$  particles on a 1D lattice, the same particle  $k$  is selected for each configuration, and for two different configurations, the particles labeled  $k$  stay together once they have met on the same site. The dynamics is then regular and the coupling time is  $\tau_{\text{coup}}/N \sim a \log N$  (see Fig. 6.2). The logarithmic behavior is explained by the fact that particles move independently from each other. The coupling time for the entire system is thus the maximum of the  $N$  coupling times for each particle.

In conclusion, we see that the same  $N$ -dimensional random walk of Eq. (6.1), with a correlation time of order  $L^2$ , allows for two very different couplings, one chaotic and the other regular. In spin glasses and hard spheres, these regimes are realized for the same coupling at different temperatures.

## 6.2 Spin glass

### 6.2.1 Heat-bath dynamics

The random walk considered previously can also be considered as an  $L$ -state Potts model at infinite temperature evolving under heat-bath dynamics. The product ansatz of Eq. (6.2) would correspond to the independent evolution of the spin configurations, and it is chaotic. With the coupling of Eq. (6.3), in contrast, all spins evolve and couple independently at  $\beta = 0$ , and the global coupling time is again the maximum of the coupling times of the individual spins. The Monte Carlo dynamics is thus regular, and the diagram of Fig. 6.2 carries over to the general case with  $L \geq 2$ . We first consider heat-bath dynamics, and the coupling is defined by the use of the same random numbers for each configuration (see Section 5.3.2).

As shown in Section 5.3.1, for the 2D ferromagnetic Ising model (all  $J_{ij} = 1, L = 2$ ), the dynamics remains regular at all temperatures. Below the Curie temperature,  $\tau_{\text{coup}}$  is very large, but so is the correlation time  $\tau_{\text{corr}}$ , and the partial order implies that the complexity of  $\tau_{\text{coup}}/\tau_{\text{corr}} \leq O(\log N)$  (see Section 5.3.1). The partial order is preserved in the disordered Ising model with ferromagnetic interactions  $J_{ij} = J_{ji} \geq 0$ , and in this model also, the theorem of Propp and Wilson guarantees that  $\tau_{\text{coup}}$  is, up to logarithms, of the same order as  $\tau_{\text{corr}}$ .

Frustrated models, for example spin glasses, do not exhibit partial order, and can thus undergo a damage-spreading transition. In the 2D  $\pm J$  Ising spin glass, the quenched random interactions satisfy  $J_{ij} = J_{ji} = \pm 1$  with equal probability. Although this model is paramagnetic for all finite temperatures, Campbell and de Arcangelis [145] found a damage-spreading transition for the heat-bath algorithm at  $\beta_{\text{ds}} \simeq 0.59$ .

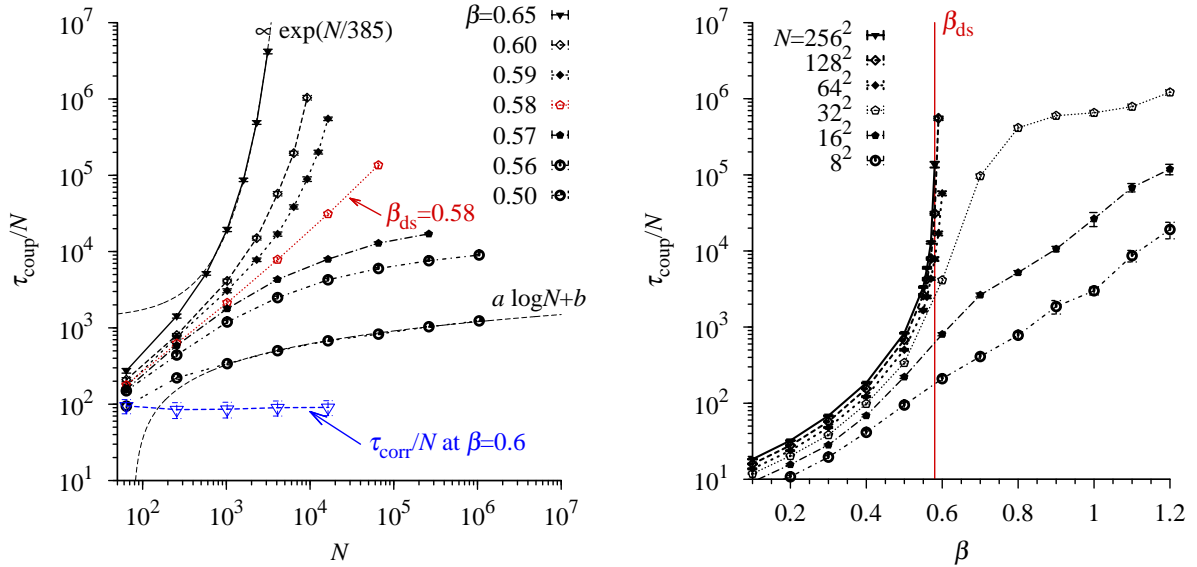


**Figure 6.4:** Disorder-averaged coupling time for the heat-bath algorithm of the 2D  $\pm J$  Ising spin glass. *Left:* Size dependence for different densities. A dynamical phase transition is seen at the damage-spreading temperature  $\beta_{\text{ds}} \simeq 0.58$ . (Ref [7], see Section 7.2). *Right:* Temperature dependence for different system sizes. The transition is seen for the largest systems.

In Fig. 6.3, we show the coupling time as a function of  $N$  and  $\beta$ . A dynamical phase

transition is seen at the damage-spreading temperature  $\beta_{\text{ds}} \simeq 0.58$ . In the chaotic phase,  $\tau_{\text{coup}}/N$  grows exponentially with  $N$ , but only logarithmically in the regular phase. The dynamical phase transition in this model (without a spin-glass phase at finite  $\beta$ ), although not mathematically proved, appears firmly established. It is without influence on single-particle properties. To illustrate this point, we verify that the correlation time  $\tau_{\text{corr}}/N$ , computed with the auto-correlation function

$$C(t) = \frac{1}{N} \sum_{i=0}^N \langle s_i(0)s_i(t) \rangle, \quad (6.4)$$

remains constant in the chaotic phase and only  $\tau_{\text{coup}}/\tau_{\text{corr}}$  diverges with  $N \rightarrow \infty$ .

## 6.2.2 Local Metropolis algorithm

After the heat-bath algorithm, we discuss the local Metropolis algorithm, where individual spins  $s_k$  are flipped with a probability depending on their local field. In the standard implementation, spin flips are accepted with a probability equal to 1 at infinite temperature, and this prevents the coupling from occurring. To allow coupling at any  $\beta$  we use

$$P(s_k \rightarrow -s_k) = \frac{2}{3} \min(1, \exp(-2\beta s_k h)). \quad (6.5)$$

At each step, the same spin  $k$  is updated for all copies of the system. For these dynamics, several coupling schemes can be set up. If the same random number  $\gamma$  is used for each configuration, the coupling does not take place, as two opposite configurations will always stay opposite. We adapt the regular coupling of Eq. (6.3) and use two independent random numbers,  $\gamma_1$  for “up” spins and  $\gamma_2$  for “down” spins. The coupling time is again logarithmic at high temperatures and exponential at low temperatures, with a critical temperature  $\beta_{\text{ds}} \simeq 0.33$  (see Fig. 6.4).

The Metropolis algorithm, with this coupling scheme, has thus a higher dynamical critical temperature than the heat-bath algorithm, with which it shares all the qualitative features. This confirms that the dynamic damage-spreading transition is algorithm dependent and can, in particular, not be explained by thermodynamic properties. One may also choose the random numbers in the Metropolis algorithm using  $\gamma$  for  $s_k = 1$  and  $1 - \gamma$  for  $s_k = -1$ . This scheme correlates opposite spins better and the critical temperature is found to be  $\beta_{\text{ds}} \simeq 0.52$  (see Fig. 6.4). This result shows that, like the previous random walk, the same Markov chain allows for qualitatively different couplings.

## 6.3 Hard spheres

After spin glasses, we consider the hard-sphere model (see Part I). In this section, three Monte Carlo algorithms for hard spheres are presented, which allow for coupling of the entire configuration space. Two of the algorithms remain regular below a finite critical packing fraction,  $\eta_{\text{ds}}$ , in the limit  $N \rightarrow \infty$ , while the latter is chaotic at all densities.



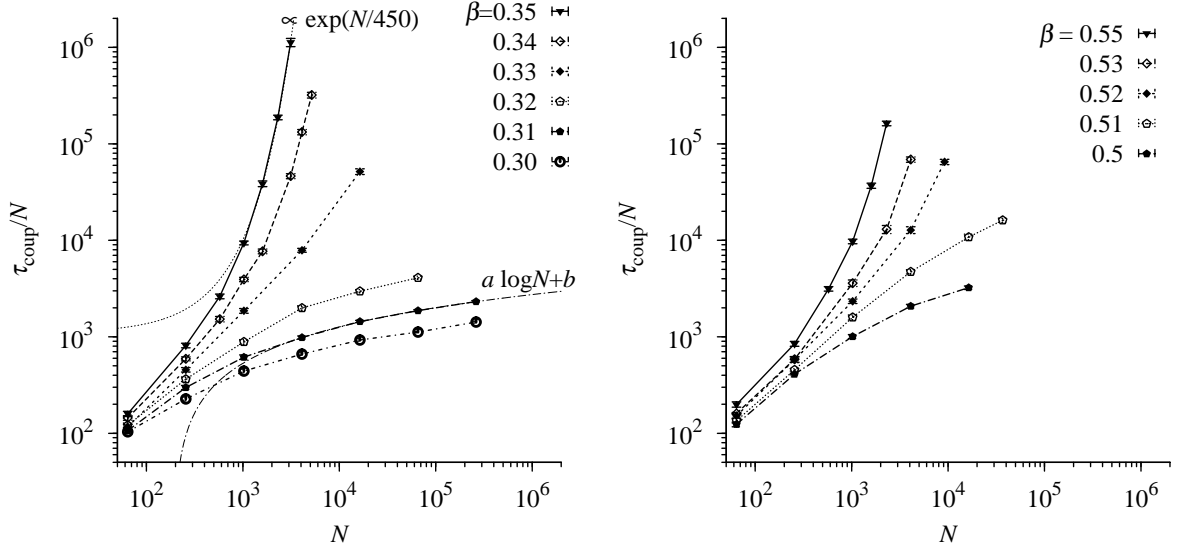


**Figure 6.5:** Size dependence of the coupling time for the Metropolis algorithm in the 2D  $\pm J$  Ising spin glass. Two different coupling schemes are used *Left*: The random numbers  $\gamma_1$  for “up” spins and  $\gamma_2$  for “down” spins are independent. The damage-spreading transition occurs at  $\beta_{\text{ds}} \simeq 0.33$ . *Right*: The random numbers are  $\gamma$  for  $s_k = 1$  and  $1 - \gamma$  for  $s_k = -1$ . The damage-spreading transition occurs at  $\beta_{\text{ds}} \simeq 0.52$ .

### 6.3.1 Birth-and-death and “Labeled displacement” algorithm

In the grand-canonical birth-and-death Monte Carlo algorithm [148, 149], particles are placed inside a box at random positions  $\vec{r} = (x_k, y_k)$  at rate  $\lambda$  if no overlaps with previously placed disks are generated. The life time of each disk is sampled from an exponential distribution with rate 1. One realization of the algorithm is represented in the diagram of Fig. 6.5. The mean number  $\langle N \rangle$  of particles in this system is controlled by the activity  $\lambda$ .

This model’s configuration space is infinite, but the survey of all possible initial conditions is nevertheless feasible [150, 151, 131]. For any realization of the algorithm, the possible configurations at time  $t$  are a subset of the finite set produced from a horizontal cut in the diagram of Fig. 6.5. The patch algorithm again yields sharp upper bounds for  $\tau_{\text{coup}}$  [131]. Surprisingly, this algorithm for hard disks remains regular below a finite density  $\eta_{\text{ds}}$  in the limit  $N \rightarrow \infty$  [151, 150].

We again study damage spreading in this model by applying the same Monte Carlo dynamics (same choice of  $\vec{r}_i, t_i, \tau_i$ ) to  $N_{\text{init}}$  random hard-sphere initial conditions at time  $t = 0$  with life times sampled from an exponential distribution. The data shown in Fig. 6.6 again indicate a dynamical phase transition between the regular regime at packing fractions  $\eta < \eta_{\text{ds}} \simeq 0.29$  and the chaotic regime above  $\eta_{\text{ds}}$ . This density corresponds to the limiting density found with the patch algorithm [131].

A canonical version of the birth-and-death algorithm is the “labeled displacement” algorithm where, at times  $t = 0, 1, 2, \dots$ , a randomly chosen particle  $k$  is moved to a random position  $\vec{r}_k$ , if this move creates no overlaps. We see clear evidence of a dynamical phase transition at a critical density  $\eta_{\text{ds}} \simeq 0.13$  (see Fig. 6.6), which is smaller than for the closely related birth-and-death algorithm.

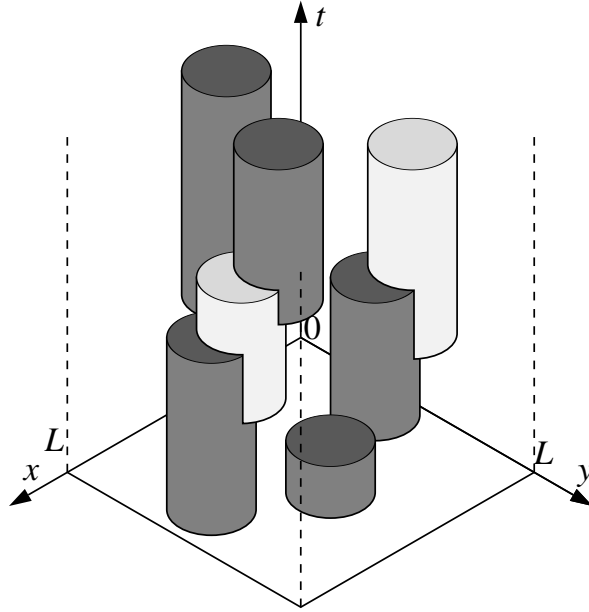


**Figure 6.6:** Grand-canonical birth-and-death algorithm for hard disks. Disk  $i$  appears at time  $t_i$ , at position  $\vec{r}_i = (x_i, y_i)$ , and it disappears at time  $t_i + \tau_i$ . In time, disk  $i$  describes a cylinder. Disks (cylinders) which are accepted, because they create no overlaps with earlier disks, are drawn in dark gray. The rejected disks are drawn in light gray. The configuration space of this system is infinite, yet the possible configurations at time  $t$  are a subset of the finite set (of dark and light cylinders) produced from a horizontal cut in this diagram. (Ref [7], see Section 7.2).

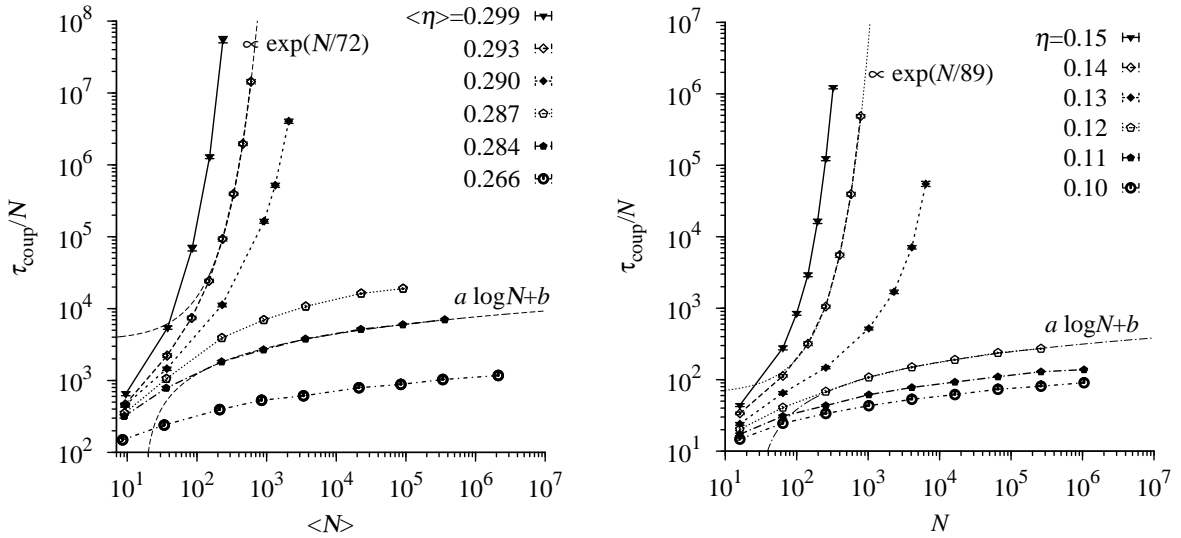


**Figure 6.7:** *Left:* Coupling time of the birth-and-death algorithm of Fig. 6.5 for 2D hard spheres. The damage spreading transition occurs at a packing fraction  $\eta_{\text{ds}} \simeq 0.29$ . *Right:* Coupling time for the labeled displacement algorithm. The dynamical transition to chaos occurs at a lower density ( $\eta_{\text{ds}} \simeq 0.13$ ) than for the birth-and-death algorithm. (Ref [7], see Section 7.2).

### 6.3.2 Spot algorithm

We finally study the coupling for a Markov chain similar to the Metropolis algorithm: the spot algorithm.

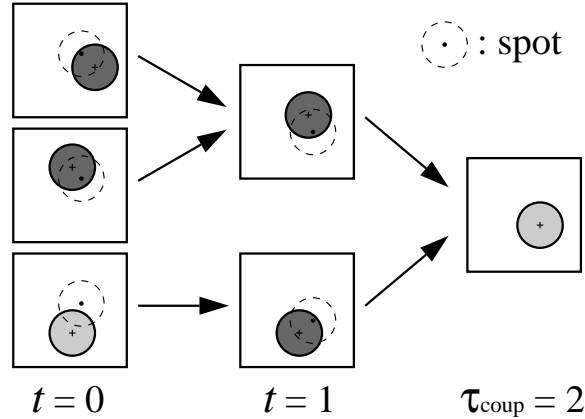


**Figure 6.8:** Spot algorithm for hard spheres: The randomly chosen spot position defines the attempted move of a disk inside the spot. The spot radius satisfies  $\sigma_{\text{spot}} \leq \sigma$ , and, at most, one disk is moved at time  $t$ . An example with  $N = 1$  and  $\sigma_{\text{spot}} = \sigma$  is shown. (Ref [7], see Section 7.2).

The Metropolis algorithm for  $N$  hard spheres consists of moving, at time  $t$ , a particle  $k$  by a random vector  $\vec{\delta} = (\delta_x, \delta_y)$ . As the configuration space is continuous, the coupling probability is zero if one uses a naive coupling scheme. The following spot algorithm is more successful (although its coupling is chaotic at all densities): at time  $t$ , it places a spot, a disk-shaped region with radius  $\sigma_{\text{spot}} \leq \sigma$ , at a random position  $\vec{r}_s$ .

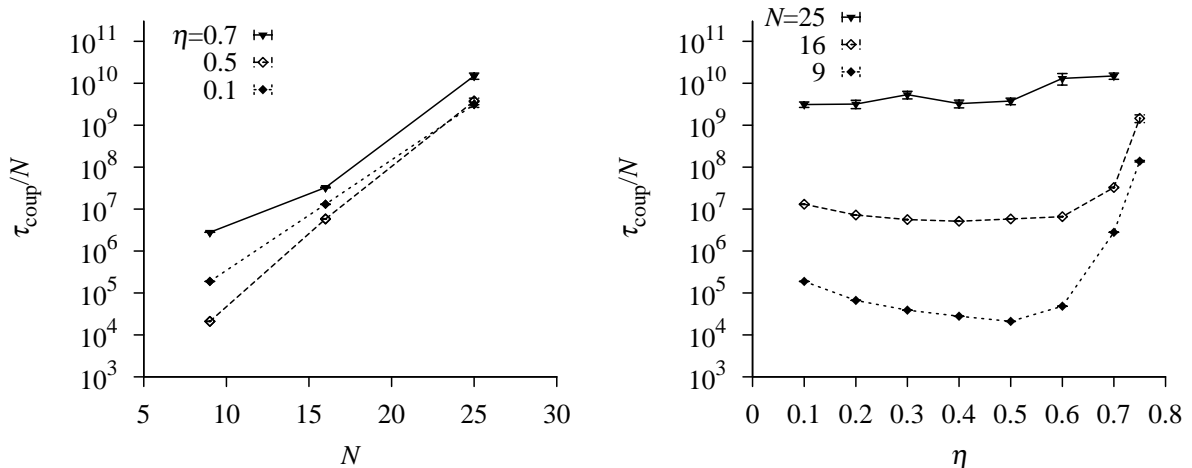


**Figure 6.9:** Coupling time  $\tau_{\text{coup}}$  of the spot algorithm *Left:* Size dependence of  $\tau_{\text{coup}}$  for different packing fraction  $\eta$ . For all  $\eta$ , the coupling time is exponential in  $N$ . *Right:* Packing fraction dependence for different system size. For  $N = 25$ , the coupling time is similar at all densities in the region  $\eta \in [0.1, 0.7]$ . (Ref [7], see Section 7.2).

The spot contains at most one disk center, and the move consists in placing this disk at  $\vec{r}_s$ , if this creates no overlap with other particles (see Fig. 6.7). The spot algorithm satisfies the detailed-balance condition, and it generates the same moves as the Metropolis algorithm. Moreover, as illustrated in Fig. 6.7, it succeeds in coupling. However, as shown in Fig. 6.8, the coupling time of the spot algorithm is an exponential function of  $N$  for all densities: the coupling is always chaotic.

## 6.4 Griffeath's coupling

As seen in this chapter, the coupling time depends on the coupling scheme. Griffeath [152] designed a coupling scheme which is always regular. We consider two Markov chains  $x$  and  $y$  under a coupling process. We define  $p_{xk}^{(n)}$  as the probability for the chains  $x$  to be at the configuration  $k$  after  $n$  steps, and  $p_{yk}^{(n)}$  the equivalent for the chain  $y$ . We also define  $P_{xy}(k, n)$  as the probability for the chains  $x$  and  $y$  to both be at the configuration  $k$  at the time  $n$  (and therefore to have coupled at  $\tau_{\text{coup}} \leq n$ ). For any coupling scheme,

$$P_{xy}(k, n) \leq \min(p_{xk}^{(n)}, p_{yk}^{(n)}). \quad (6.6)$$

The algorithm of Griffeath [152] is maximal, that is, it satisfies

$$P_{xy}(k, n) = \min(p_{xk}^{(n)}, p_{yk}^{(n)}). \quad (6.7)$$

Therefore, this coupling is always regular, and  $\tau_{\text{coup}} \sim \tau_{\text{corr}}$ . This scheme, which is designed for the coupling of two chains, can be extended to an arbitrary number of Markov chains [8]. However, Griffeath's coupling is non-Markovian: the transition probabilities of the chains depend on the previous configurations. As a consequence, this algorithm is difficult to implement in practice. Nevertheless, its existence shows that regular coupling do exist, and it could be an inspiration for the realization of better coupling scheme.

## Conclusion

In this chapter, we studied the relationship between the coupling of Markov chains, which is of critical importance for the subject of perfect sampling, and damage spreading.

For the 2D  $\pm J$  Ising spin glass, which lacks an equilibrium phase transition at finite temperatures, we found a dynamical phase transition at  $\beta_{\text{ds}} \simeq 0.58$  for the heat-bath algorithm, corresponding to the damage-spreading transition [145]. For lower temperatures the coupling time explodes. The Metropolis algorithm has the same damage-spreading behavior but with higher critical temperatures:  $\beta_{\text{ds}} \simeq 0.33$  or  $\beta_{\text{ds}} \simeq 0.52$  for two simple coupling schemes. All damage-spreading transitions for this system are deeply inside the paramagnetic phase.

For the hard-disk system, we analyzed three local Monte Carlo algorithms, the birth-and-death algorithm, inspired from Poisson point processes, its canonical version (the ‘‘labeled displacement’’ algorithm), and the spot algorithm, a straightforward adaptation of the Metropolis algorithm. The first algorithm shows a regular regime only for packing densities below  $\eta_{\text{ds}} \simeq 0.29$ , the coupling time was then of the same order of magnitude

as the correlation time. The canonical version of the birth-and-death algorithm had a critical density of  $\eta_{\text{ds}} \simeq 0.13$ . These transition densities are again deeply inside the liquid phase.

The application of perfect sampling methods to these challenging problems is therefore not so much limited by the survey problem, as the patch algorithm allows to track the evolution of the entire configuration space, but rather by damage spreading, the underlying chaotic nature of the Monte Carlo dynamics.



## Conclusion

The Monte Carlo method, with the use of Markov chains, has revolutionized the computation of high-dimensional integrals, and therefore the understanding of  $N$ -element systems. This widely used method encounters its limitation in the lack of rigorous method to ensure the convergence of Markov chains. The coupling-from-the-past method is designed to overcome this problem of convergence, and could provide a sampling method which combines the efficiency of Markov chains with the rigor of direct-sampling methods. Part II of this thesis showed that the limitation of this method was due to damage spreading, the underlying chaotic nature of the Markov chains. Moreover, this limitation depends on the coupling scheme. The application of coupling-from-the-past methods thus hinges on the design of coupling schemes which remain regular even for complicated many-body systems. Such scheme exist, as is shown by Griffeath's coupling [152], which is never chaotic although difficult to construct in practice. The discovery of efficient coupling schemes would have important consequences for the physics of disordered systems, and more generally for the countless applications of the Markov-chain Monte Carlo method.





## Bibliography

- [1] L. D. Landau, *Phys. Z. Sowjet.* **11**, 26 (1937).
- [2] K. G. Wilson, *Rev. Mod. Phys.* **47**, 773 (1975).
- [3] D. P. Landau and K. Binder, *A guide to Monte Carlo simulations in statistical physics* (Cambridge Univ Press, 2005).
- [4] W. Krauth, *Statistical mechanics: algorithms and computations* (Oxford University Press, 2006).
- [5] E. P. Bernard, W. Krauth, and D. B. Wilson, *Phys. Rev. E* **80**, 056704 (2009).
- [6] E. P. Bernard and W. Krauth, ArXiv e-prints (2011), [arXiv:1102.4094](https://arxiv.org/abs/1102.4094) .
- [7] E. P. Bernard, C. Chanal, and W. Krauth, *Europhys. Lett.* **92**, 60004 (2010).
- [8] E. P. Bernard, M. Michel, and W. Krauth, Manuscript in preparation .
- [9] B. J. Alder and T. E. Wainwright, *Phys. Rev.* **127**, 359 (1962).
- [10] J. G. Propp and D. B. Wilson, *Random Struct. Algorithms* **9**, 223 (1996).
- [11] B. J. Alder and T. E. Wainwright, *Phys. Rev. A* **1**, 18 (1970).
- [12] N. D. Mermin, *Phys. Rev.* **176**, 250 (1968).
- [13] J. M. Kosterlitz and D. J. Thouless, *J. Phys. C* **5**, L124 (1972).
- [14] J. M. Kosterlitz and D. J. Thouless, *J. Phys. C* **6**, 1181 (1973).
- [15] J. Kosterlitz and D. Thouless, *Two-dimensional physics* (North-Holland, Amsterdam, 1978).
- [16] J. Morán-López, *Physics of low dimensional systems* (Springer Us, 2001).
- [17] K. J. Strandburg, *Rev. Mod. Phys.* **60**, 161 (1988).

- [18] J. G. Dash, *Rev. Mod. Phys.* **71**, 1737 (1999).
- [19] T. Ando, A. B. Fowler, and F. Stern, *Rev. Mod. Phys.* **54**, 437 (1982).
- [20] E. Abrahams, S. V. Kravchenko, and M. P. Sarachik, *Rev. Mod. Phys.* **73**, 251 (2001).
- [21] Z. Hadzibabic and J. Dalibard, ArXiv e-prints (2009), [arXiv:0912.1490](https://arxiv.org/abs/0912.1490) .
- [22] D. Bensimon, L. P. Kadanoff, S. Liang, B. I. Shraiman, and C. Tang, *Rev. Mod. Phys.* **58**, 977 (1986).
- [23] E. Peierls, *Helvetica Physica Acta Suppl.* **7**, 81 (1934).
- [24] A. Jaster, *Phy. Rev. E* **59**, 2594 (1999).
- [25] C. H. Mak, *Phy. Rev. E* **73**, 065104 (2006).
- [26] L. D. Landau and E. M. Lifshitz, *Elasticity theory* (Pergamon Press, 1975).
- [27] N. W. Ashcroft and N. D. Mermin, Holt Rinehart and Winston, New York NY (1976).
- [28] R. Peierls, *Annales de l'IHP* (1935).
- [29] N. D. Mermin and H. Wagner, *Phys. Rev. Lett.* **17**, 1133 (1966).
- [30] C. C. Grimes and G. Adams, *Phys. Rev. Lett.* **42**, 795 (1979).
- [31] C. A. Murray and D. H. van Winkle, *Phys. Rev. Lett.* **58**, 1200 (1987).
- [32] B. I. Halperin and D. R. Nelson, *Phys. Rev. Lett.* **41**, 121 (1978).
- [33] B. Jancovici, *Phys. Rev. Lett.* **19**, 20 (1967).
- [34] Y. Imry and L. Gunther, *Phy. Rev. B* **3**, 3939 (1971).
- [35] B. Gavish and Y. Imry, *J. Chem. Phys.* **65**, 139 (1976).
- [36] J. Cardy, *Scaling and renormalization in statistical physics*, Vol. 5 (Cambridge Univ Pr, 1996).
- [37] K. S. Novoselov, A. K. Geim, S. V. Morozov, D. Jiang, Y. Zhang, S. V. Dubonos, I. V. Grigorieva, and A. A. Firsov, *Science* **306**, 666 (2004).
- [38] D. R. Nelson and L. Peliti, *Journal de Physique* **48**, 1085 (1987).
- [39] H. S. Seung and D. R. Nelson, *Phys. Rev. A* **38**, 1005 (1988).
- [40] D. R. Nelson, ArXiv e-prints (1995), [arXiv:9502114](https://arxiv.org/abs/9502114) .
- [41] J. C. Meyer, A. K. Geim, M. I. Katsnelson, K. S. Novoselov, T. J. Booth, and S. Roth, *Nature* **446**, 60 (2007).

- [42] E. Cadelano, P. L. Palla, S. Giordano, and L. Colombo, *Phys. Rev. Lett.* **102**, 235502 (2009).
- [43] C. Lee, X. Wei, J. W. Kysar, and J. Hone, *Science* **321**, 385 (2008).
- [44] J. D. van der Waals, Koninklijke Nederlandse Akademie van Wetenschappen Proceedings Series B Physical Sciences **1**, 138 (1898).
- [45] L. Boltzmann, Koninklijke Nederlandse Akademie van Wetenschappen Proceedings Series B Physical Sciences **1**, 398 (1898).
- [46] N. Metropolis, A. W. Rosenbluth, M. N. Rosenbluth, A. H. Teller, and E. Teller, *J. Chem. Phys.* **21**, 1087 (1953).
- [47] B. J. Alder and T. E. Wainwright, *J. Chem. Phys.* **27**, 1208 (1957).
- [48] J. P. Hansen and I. R. McDonald, *Theory of simple liquids* (Academic Press, 2006).
- [49] W. G. Hoover and F. H. Ree, *J. Chem. Phys.* **49**, 3609 (1968).
- [50] S. Asakura and F. Oosawa, *J. Chem. Phys.* **22**, 1255 (1954).
- [51] A. Patrascioiu and E. Seiler, *Phys. Rev. Lett.* **60**, 875 (1988).
- [52] R. Gupta, J. DeLapp, G. G. Batrouni, G. C. Fox, C. F. Baillie, and J. Apostolakis, *Phys. Rev. Lett.* **61**, 1996 (1988).
- [53] R. H. Swendsen and J.-S. Wang, *Phys. Rev. Lett.* **58**, 86 (1987).
- [54] U. Wolff, *Phys. Rev. Lett.* **62**, 361 (1989).
- [55] V. L. Berezinskiĭ, *Sov. Phys. - JETP* **32**, 493 (1971).
- [56] V. L. Berezinskiĭ, *Sov. Phys. - JETP* **34**, 610 (1972).
- [57] D. J. Bishop and J. D. Reppy, *Phys. Rev. Lett.* **40**, 1727 (1978).
- [58] D. R. Nelson and J. M. Kosterlitz, *Phys. Rev. Lett.* **39**, 1201 (1977).
- [59] W. Janke, *Phys. Rev. B* **55**, 3580 (1997).
- [60] Y. Han, N. Y. Ha, A. M. Alsayed, and A. G. Yodh, *Phys. Rev. E* **77**, 041406 (2008).
- [61] M. Hasenbusch, *J. Phys. A: Math. Gen.* **38**, 5869 (2005).
- [62] M. Hasenbusch and K. Pinn, *J. Phys. A: Math. Gen.* **30**, 63 (1997).
- [63] E. Domany, M. Schick, and R. H. Swendsen, *Phys. Rev. Lett.* **52**, 1535 (1984).
- [64] B. Nienhuis, A. N. Berker, E. K. Riedel, and M. Schick, *Phys. Rev. Lett.* **43**, 737 (1979).
- [65] H. W. Blöte, W. Guo, and H. J. Hilhorst, *Phys. Rev. Lett.* **88**, 047203 (2002).

- [66] A. C. van Enter and S. B. Shlosman, *Phys. Rev. Lett.* **89**, B5702 (2002).
- [67] J. E. Mayer and W. W. Wood, *J. Chem. Phys.* **42**, 4268 (1965).
- [68] D. R. Nelson and B. I. Halperin, *Phys. Rev. B* **19**, 2457 (1979).
- [69] A. P. Young, *Phys. Rev. B* **19**, 1855 (1979).
- [70] D. S. Fisher, B. I. Halperin, and R. Morf, *Phys. Rev. B* **20**, 4692 (1979).
- [71] S. T. Chui, *Phys. Rev. B* **28**, 178 (1983).
- [72] H. Kleinert, *Phys. Lett. A* **95**, 381 (1983).
- [73] T. V. Ramakrishnan, *Phys. Rev. Lett.* **48**, 541 (1982).
- [74] J. Friedel, *Dislocations* (Pergamon, Oxford, 1964).
- [75] D. R. Squire, A. C. Holt, and W. G. Hoover, *Physica* **42**, 388 (1969).
- [76] M. A. Bates and D. Frenkel, *Phys. Rev. E* **61**, 5223 (2000).
- [77] O. Farago and Y. Kantor, *Phys. Rev. E* **61**, 2478 (2000).
- [78] K. Bagchi, H. C. Andersen, and W. Swope, *Phys. Rev. Lett.* **76**, 255 (1996).
- [79] K. Zahn, R. Lenke, and G. Maret, *Phys. Rev. Lett.* **82**, 2721 (1999).
- [80] G. Aeppli and R. Bruinsma, *Phys. Rev. Lett.* **53**, 2133 (1984).
- [81] R. J. Birgeneau and P. M. Horn, *Science* **232**, 329 (1986).
- [82] R. Pindak, D. E. Moncton, S. C. Davey, and J. W. Goodby, *Phys. Rev. Lett.* **46**, 1135 (1981).
- [83] S. C. Davey, J. Budai, J. W. Goodby, R. Pindak, and D. E. Moncton, *Phys. Rev. Lett.* **53**, 2129 (1984).
- [84] Y. Peng, Z. Wang, A. M. Alsayed, A. G. Yodh, and Y. Han, *Phys. Rev. Lett.* **104**, 205703 (2010).
- [85] J. Q. Broughton, G. H. Gilmer, and J. D. Weeks, *Phys. Rev. B* **25**, 4651 (1982).
- [86] S. Prestipino, F. Saija, and P. V. Giaquinta, *Phys. Rev. Lett.* **106**, 235701 (2011).
- [87] S. Toxvaerd, *Phys. Rev. Lett.* **44**, 1002 (1980).
- [88] K. Chen, T. Kaplan, and M. Mostoller, *Phys. Rev. Lett.* **74**, 4019 (1995).
- [89] S. Muto and H. Aoki, *Phys. Rev. B* **59**, 14911 (1999).
- [90] B. K. Clark, M. Casula, and D. M. Ceperley, *Phys. Rev. Lett.* **103**, 055701 (2009).
- [91] J. Lee and K. J. Strandburg, *Phys. Rev. B* **46**, 11190 (1992).

- [92] J. A. Zollweg and G. V. Chester, *Phys. Rev. B* **46**, 11186 (1992).
- [93] H. Weber, D. Marx, and K. Binder, *Phys. Rev. B* **51**, 14636 (1995).
- [94] G. A. Chapela, L. E. Scriven, and H. T. Davis, *J. Chem. Phys.* **91**, 4307 (1989).
- [95] D. Jones, *Communications of the ACM* **29**, 300 (1986).
- [96] M. Marín, D. Risso, and P. Cordero, *J. Comput. Phys.* **109**, 306 (1993).
- [97] G. Paul, *J. Comput. Phys.* **221**, 615 (2007).
- [98] M. Isobe, *Int. J. Mod. Phys. C* **10**, 1281 (1999).
- [99] M. N. Bannerman, R. Sargant, and L. Lue, ArXiv e-prints (2010), [arXiv:1004.3501](https://arxiv.org/abs/1004.3501).
- [100] M. Marín, *Computer Physics Communications* **102**, 81 (1997).
- [101] S. Miller and S. Luding, *J. Comput. Phys.* **193**, 306 (2004).
- [102] Y. Sinai, *Russ. Math. Surv.* **25**, 137 (1970).
- [103] N. Simányi, *Invent. Math.* **154**, 123 (2003).
- [104] P. Diaconis, S. Holmes, and R. M. Neal, *The Ann. Appl. Proba.* **10**, 726 (2000).
- [105] K. S. Turitsyn, M. Chertkov, and M. Vucelja, *Physica D* **245 4-5**, 410 (2011).
- [106] H. C. M. Fernandes and M. Weigel, *Computer Physics Communications* **182**, 1856 (2011).
- [107] D. A. Levin, Y. Peres, and E. L. Wilmer, *Markov chains and mixing times* (Amer Mathematical Society, 2009).
- [108] J. K. G. Dhont, *An introduction to dynamics of colloids*, Vol. 2 (Elsevier Science, 1996).
- [109] J. P. Wittmer, H. Meyer, A. Johner, T. Kreer, and J. Baschnagel, *Phys. Rev. Lett.* **105**, 037802 (2010).
- [110] I. Lifshitz and V. Slyozov, *Journal of Physics and Chemistry of Solids* **19**, 35 (1961).
- [111] W. W. Wood, *J. Chem. Phys.* **48**, 415 (1968).
- [112] J. Lee and J. M. Kosterlitz, *Phys. Rev. B* **43**, 3265 (1991).
- [113] G. M. Torrie and J. P. Valleau, *J. Comput. Phys.* **23**, 187 (1977).
- [114] B. A. Berg and T. Neuhaus, *Phys. Lett. B* **267**, 249 (1991).
- [115] B. Delaunay, *Izvestia Akademii Nauk SSSR, Otdelenie Matematicheskikh i Estestvennykh Nauk* **7**, 793 (1934).

- [116] B. J. Alder and T. E. Wainwright, *J. Chem. Phys.* **33**, 1439 (1960).
- [117] B. Widom, *J. Chem. Phys.* **39**, 2808 (1963).
- [118] J. J. Alonso and J. F. Fernández, *Phy. Rev. E* **59**, 2659 (1999).
- [119] D. Nelson, T. Piran, and S. Weinberg, *Statistical mechanics of membranes and surfaces* (World Scientific Pub. Singapore, River Edge, NJ, 2004).
- [120] H. Furukawa and K. Binder, *Phys. Rev. A* **26**, 556 (1982).
- [121] M. Schrader, P. Virnau, and K. Binder, *Phy. Rev. E* **79**, 061104 (2009).
- [122] R. C. Tolman, *J. Chem. Phys.* **17**, 333 (1949).
- [123] A. Jaster, *Phys. Lett. A* **330**, 120 (2004).
- [124] A. Z. Panagiotopoulos, *Molecular Physics* **61**, 813 (1987).
- [125] I. R. McDonald, *Molecular Physics* **23**, 41 (1972).
- [126] N. G. Almarza, *J. Chem. Phys.* **130**, 184106 (2009).
- [127] S. Pronk and D. Frenkel, *Phys. Rev. E* **69**, 066123 (2004).
- [128] A. T. Ogielski and I. Morgenstern, *Phys. Rev. Lett.* **54**, 928 (1985).
- [129] C. Chanal and W. Krauth, *Phys. Rev. Lett.* **100**, 060601 (2008).
- [130] S. A. Kauffman, *J. Theor. Biol.* **22**, 437 (1969).
- [131] C. Chanal and W. Krauth, *Phy. Rev. E* **81**, 016705 (2010).
- [132] P. Diaconis, *Proc. Natl. Acad. Sci. USA* **93**, 1659 (1996).
- [133] K. Binder and A. P. Young, *Rev. Mod. Phys.* **58**, 801 (1986).
- [134] L. Saul and M. Kardar, *Phy. Rev. E* **48**, 3221 (1993).
- [135] C. K. Thomas and A. A. Middleton, *Phy. Rev. E* **80**, 046708 (2009).
- [136] M. Kac and J. C. Ward, *Phys. Rev.* **88**, 1332 (1952).
- [137] J. A. Fill and M. Huber, in *focs* (Published by the IEEE Computer Society, 2000) p. 503.
- [138] D. Aldous and P. Diaconis, *The American Mathematical Monthly* **93**, 333 (1986).
- [139] W. S. Kendall and E. Thonnes, *Pattern Recognition* **32**, 1569 (1999).
- [140] L. N. Vasershtein, *Problemy Peredachi Informatsii* **5**, 64 (1969).
- [141] M. Huber, in *Proceedings of the thirtieth annual ACM symposium on Theory of computing* (ACM, 1998) pp. 31–40.

- [142] M. Harvey and R. M. Neal, in *Proceedings of the 16th Conference on Uncertainty in Artificial Intelligence* (Citeseer, 2000) pp. 256–263.
- [143] A. M. Childs, R. B. Patterson, and D. J. Mackay, *Phy. Rev. E* **63**, 036113 (2001).
- [144] B. Derrida and G. Weisbuch, *Europhys. Lett.* **4**, 657 (1987).
- [145] I. A. Campbell and L. de Arcangelis, *Physica A* **178**, 29 (1991).
- [146] I. Morgenstern and K. Binder, *Phys. Rev. Lett.* **43**, 1615 (1979).
- [147] W. L. McMillan, *Phys. Rev. B* **28**, 5216 (1983).
- [148] O. Häggström, M. Van Lieshout, and J. Møller, *Bernoulli* , 641 (1999).
- [149] W. Kendall, *Probability towards* **218**, 234 (2000).
- [150] W. S. Kendall and J. Moller, *Adv. in Appl. Probab.* **32**, 844 (2000).
- [151] D. B. Wilson, *Random Struct. Algorithms* **16**, 85 (2000).
- [152] D. Griffeath, *Probab. Theory Relat. Field* **31**, 95 (1975).





## 7.1 Publication I

Etienne P. Bernard, Werner Krauth and David B. Wilson  
*Event-chain Monte Carlo algorithms for hard-sphere systems*  
*Physical Review E* **80** 056704 (2009)

This article presents the event-chain algorithm (see Chapter 2), which has been designed and used to study the melting transition. The article describes the different versions of the algorithm, and it analyzes their performances.

**Event-chain Monte Carlo algorithms for hard-sphere systems**Etienne P. Bernard,<sup>1,\*</sup> Werner Krauth,<sup>1,†</sup> and David B. Wilson<sup>2,‡</sup><sup>1</sup>*CNRS–Laboratoire de Physique Statistique, Ecole Normale Supérieure, 24 rue Lhomond, 75231 Paris Cedex 05, France*<sup>2</sup>*Microsoft Research, One Microsoft Way, Redmond, Washington 98052, USA*

(Received 19 March 2009; revised manuscript received 15 October 2009; published 18 November 2009)

In this paper we present the event-chain algorithms, which are fast Markov-chain Monte Carlo methods for hard spheres and related systems. In a single move of these rejection-free methods, an arbitrarily long chain of particles is displaced, and long-range coherent motion can be induced. Numerical simulations show that event-chain algorithms clearly outperform the conventional Metropolis method. Irreversible versions of the algorithms, which violate detailed balance, improve the speed of the method even further. We also compare our method with a recent implementations of the molecular-dynamics algorithm.

DOI: [10.1103/PhysRevE.80.056704](https://doi.org/10.1103/PhysRevE.80.056704)

PACS number(s): 05.10.Ln, 05.20.Jj

Hard spheres in three and in two dimensions (hard disks) occupy a special place in statistical mechanics. Indeed, many fundamental concepts, from the virial expansion (by van der Waals and Boltzmann), to two-dimensional melting [1], to long-time tails [2], were first discussed in these extraordinarily rich physical systems. These models have also played a crucial role in the history of computation: both the Metropolis algorithm [3] and molecular dynamics [4] were first implemented for monodisperse hard disks in a box. In contrast with the spectacular algorithmic developments for lattice spin models [5,6], Monte Carlo algorithms for hard spheres have changed little since the 1950s, especially for high densities. Recent sophisticated implementation have reduced the complexity of the molecular-dynamics algorithm to a value comparable to that of the Monte Carlo method. Nevertheless, one can today still not equilibrate sufficiently large systems [7] to clarify whether the melting transition in two-dimensional hard disks, at density (occupied volume fraction)  $\eta \approx 0.70$ , is weakly first order, or whether it is of the Kosterlitz-Thouless type [8], with a narrow hexatic phase in between the liquid and the solid.

In this paper, we propose a class of Monte Carlo algorithms for hard-sphere systems: the “event-chain” algorithms. In contrast to the Metropolis algorithm, these methods are rejection-free. In a single move, they displace an arbitrary long chain of spheres, each advancing until it strikes the next one. Event-chain algorithms are generically faster than other Markov-chain algorithms, in part because the mean-square displacements of individual particles are larger. In addition, one of the event-chain algorithms moves coherently over long distances. This further improves equilibration times. Finally, the absence of rejections allows us to consider irreversible versions, which violate detailed balance, but preserve the correct stationary distribution. These versions accelerate the algorithm even further. The event-chain algorithms clearly outperform the traditional Metropolis algorithm for hard-disk and hard-sphere systems.

In the local Metropolis algorithm, the move of a sphere is

accepted if it induces no overlaps, and is rejected otherwise (see Fig. 1). This algorithm is notoriously slow at high density because, although a particle can move back and forth in the “cage” formed by its neighbors, it cannot easily escape from it [9].

To overcome the limitations of the local Metropolis algorithm, coordinated particle moves have been considered: When the displacement of one sphere generates overlaps with other spheres, the latter are in turn moved out of the way. The rejection-free pivot cluster algorithm [10], for example, works extremely well for binary [11] or for polydisperse [12] mixtures, but it breaks down for the high densities of interest in two-dimensional melting. In Jaster’s algorithm [13], overlapping spheres forming a chain are displaced, all of them by a fixed vector, until a configuration without overlaps is obtained (see Fig. 1). If a sphere branches out to more than one other sphere during the chain construction, the move is rejected (see Fig. 1). This happens frequently, so the expected chain length is short and Jaster’s algorithm barely faster than the local Metropolis algorithm.

In the algorithms presented here, each move consists in a deterministic chain of “events:” a disk advances until it strikes another one, which then in turn is displaced. The move starts with a randomly chosen disk, and stops when the lengths of all displacements add up to a total-displacement parameter  $\ell$  (see Fig. 2). This parameter allows the move to be reversible without rejections. To satisfy detailed balance, the move must also conserve configuration-space volume. This implies that when a disk strikes a neighbor, the latter

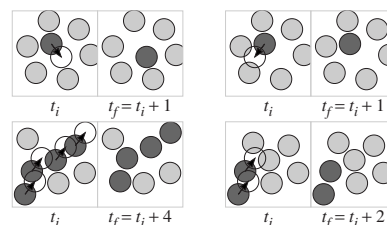


FIG. 1. *Upper panels:* Accepted (left) and rejected (right) local Metropolis moves of a disk in the cage formed by its neighbors. *Lower panels:* Accepted and rejected moves in Jaster’s chain algorithm.

\*etienne.bernard@ens.fr

†werner.krauth@ens.fr

‡http://dbwilson.com

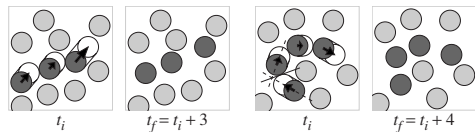


FIG. 2. *Left two panels*: Move of the straight event-chain (SEC) algorithm. The individual displacements add up to a distance  $\ell$ . *Right two panels*: Reflected event-chain (REC) move.

may be displaced either in the original direction [“straight event-chain” (SEC) algorithm] or in the direction reflected with respect to the symmetry axis of the collision [“reflected event-chain” (REC) algorithm] (see Fig. 2). In a periodic box, and with the initial direction  $\theta$  sampled uniformly in  $[0, 2\pi]$ , both versions, which we call “reversible,” preserve the uniform measure because of detailed balance.

The detailed balance condition is allowed to be broken in the SEC algorithm. Indeed, for a given direction  $\theta$ , a configuration  $\Gamma$  of  $N$  disks can reach  $N$  other configurations in one move. By applying to  $\Gamma$  the  $N$  possible moves in direction  $\theta$ , one finds the  $N$  configurations that reach  $\Gamma$ . Therefore, the SEC algorithm satisfies global balance for any distribution of  $\theta$ . Algorithms breaking detailed balance induce probability flows in the configuration space and potentially speed-up equilibration [18]. We study such an irreversible version of the SEC algorithm where  $\theta$  is uniformly distributed in  $[0, \pi]$ . To preserve ergodicity, at least two independent directions are needed. By far our fastest implementation (the “ $xy$  version” of the SEC algorithm) alternates moves in the positive  $x$  and  $y$  directions ( $\theta=0, \pi/2$ ). A version of the SEC algorithm, but with rejections and which cannot break detailed balance, was also mentioned in [13].

In Fig. 3 we show the integrated distribution of  $|\Psi|$  of Eq. (5),

$$\int_0^x \pi(|\Psi|) d|\Psi|, \quad (1)$$

for the  $xy$  version of the SEC algorithm, for the Metropolis algorithm, and for molecular dynamics in the same system. They are found to be equal. This demonstrates the correctness of our implementations.

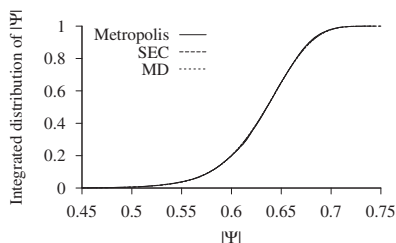


FIG. 3. Comparison of the integrated distribution of an observable [the absolute value of the order parameter  $\Psi$  of Eq. (5)] between the SEC algorithm which breaks detailed balance, molecular dynamics (MD) and the local Metropolis algorithm for 1024 disks at  $\eta=0.71$ .

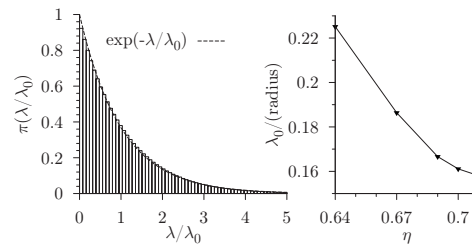


FIG. 4. *Left*: Histogram  $\pi(\lambda/\lambda_0)$  of the free path  $\lambda(\theta)$  for 1024 disks at density  $\eta=0.71$ . The distribution is close to exponential even in the solid phase. *Right*: Mean-free path  $\lambda_0$  in units of the disk radius as a function of  $\eta$ .

As a first step to analyze the performance of the event-chain algorithms, we consider the mean-square displacement  $\langle \Delta_x^2 \rangle$  of individual disks, both in the local Metropolis and in the event-chain algorithms. As mentioned, event-chain algorithms generically outperform the Metropolis algorithm in part because they take larger steps on average. In order to compare the two methods, we measure time in units of attempted one-particle displacements.

Let us define the “free path”  $\lambda=\lambda(\theta)$  of a disk as the distance it must move in direction  $\theta$  to strike another particle. The ensemble average of  $\lambda$  yields the mean-free path  $\lambda_0$ . The distribution of the free path  $\pi(\lambda/\lambda_0)$  is well approximated by an exponential

$$\pi(\lambda/\lambda_0) \simeq \exp(-\lambda/\lambda_0), \quad (2)$$

even in the solid phase (see Fig. 4). This exponential ansatz allows us to estimate the mean-square displacement for the local Metropolis algorithm, supposing, for simplicity, that the proposed moves have fixed step size  $\ell$  in random directions. The acceptance probability  $p_{\text{acc}}(\ell)=\exp(-\ell/\lambda_0)$  yields  $\langle \Delta_x^2(\ell) \rangle = \ell^2 \exp(-\ell/\lambda_0)$ , which is maximized when  $\ell=2\lambda_0$ ,

$$\max_{\ell} \langle \Delta_x^2(\ell) \rangle = \langle \Delta_x^2(2\lambda_0) \rangle = 4\lambda_0^2 e^{-2}. \quad (3)$$

To estimate the mean-square displacement for the event-chain algorithms, we suppose that the lengths of subsequent displacements in the chain are independent. In this case, the expected number of particles in the chain equals  $\ell/\lambda_0+1$ . We index the displacement during one event-chain move through a timelike variable  $s$  with  $0 \leq s \leq \ell$ . The mean-square displacement of an event-chain move (the expected sum of the squares of the individual displacements) can be expressed through the probability  $\pi(s, s')$  that two times  $s$  and  $s'$  belong to the same particle movement,

$$\langle \Delta_x^2(\ell) \rangle = \int_0^\ell \int_0^\ell ds ds' \pi(s, s').$$

With the ansatz of Eq. (2), we have  $\pi(s, s') = \exp(-|s-s'|/\lambda_0)$ . This yields the mean-square displacement per particle, which can be viewed as a short-time (local) diffusion coefficient,

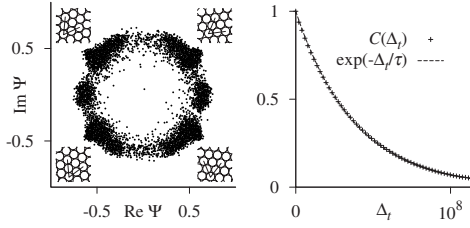


FIG. 5. *Left*: Order-parameter distribution for 256 disks in a periodic square box for  $\eta=0.71$ . *Right*: Correlation function  $C(\Delta_t)$  for this system. The correlation time is obtained from an exponential fit, as shown.

$$D_{\text{loc}}^{\infty}(\ell) = \frac{\langle \Delta_{\mathbf{x}}^2(\ell) \rangle}{\langle M(\ell) \rangle} = 2\lambda_0^2 \underbrace{\frac{\exp(-\ell/\lambda_0) + \ell/\lambda_0 - 1}{\ell/\lambda_0 + 1}}_{\rightarrow 1 \text{ for } \ell/\lambda_0 \rightarrow \infty} \quad (4)$$

This tends to  $2\lambda_0^2$  for large  $\ell/\lambda_0$ , that is, to a value  $e^2/2 \sim 4$  times larger than what we found in Eq. (3), for the local Metropolis algorithm. This factor corresponds to the efficiency gain we might expect for a generic event-chain algorithm with large  $\ell/\lambda_0$ , even though we will obtain considerably larger factors for the SEC algorithm.

In a finite system, the expressions in Eq. (4) must be corrected for the center-of-mass displacement. For the SEC algorithm, the corrected mean-square displacement per particle,  $D_{\text{loc}}^{\infty}(\ell)$ , drops to zero for  $\ell/\lambda_0 \rightarrow \infty$  because in that limit, for a finite box, all disks participate in the chain, and the system ends up moving as a solid block. The REC algorithm, in contrast, saturates to a constant mean-square displacement per particle for large chains.

To further analyze the event-chain algorithms, we determined the autocorrelation time of the orientational order parameter  $\Psi$  [14] for hard-disk systems at densities near the melting transition. The orientational order parameter  $\Psi$  averages the complex-valued local bond order  $\psi_j$  for each disk  $j$ , where

$$\Psi = 1/N \sum_j \psi_j \quad (5)$$

and

$$\psi_j = \frac{1}{n_j} \sum_{(k,j)} \exp(i6\varphi_{j,k}). \quad (6)$$

In Eq. (6), the sum is over the  $n_j$  neighbors of  $j$ , and  $\varphi_{j,k}$  is the angle of the shortest vector equivalent to  $\mathbf{x}_k - \mathbf{x}_j$  [14]. Probable values of  $\Psi$  form an irregular ring around the origin [see the scatter plot in Fig. 5; the  $\Psi \rightarrow \Psi + \pi$  symmetry in a square box imposes  $\langle \Psi(t) \rangle = 0$ ].

We suppose that the correlation time of this system is proportional to the time the order parameter takes to wander around the ring, that is, the autocorrelation time of  $\Psi$ . This global measure of the overall speed of a Monte Carlo simulation is more appropriate than, for example, single-particle diffusion constants. However  $\Psi$  is very long to decorrelate at the interesting densities (see Fig. 7), and we have to limit

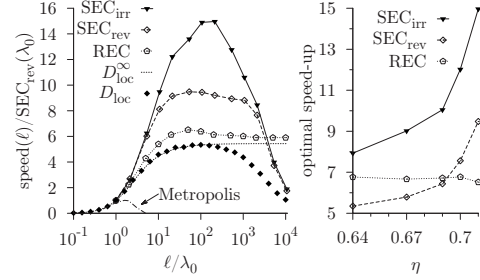


FIG. 6. *Left*: Efficiency of SEC and REC algorithms for 1024 disks at  $\eta=0.71$  (all speeds normalized by the speed of the reversible SEC algorithm at  $\ell/\lambda_0=1$ ). The speed of the local Metropolis algorithm and the mean-square displacement per particle from Eq. (4) are also shown. *Right*: Density dependence of the optimal speed-up factor.

ourselves to small systems. The autocorrelation function  $C(\Delta_t)$  of the orientational order parameter is defined by the ensemble average

$$C(\Delta_t) \propto \langle \Psi(t) \Psi^*(t + \Delta_t) \rangle,$$

normalized so that  $C(0)=1$ . In our square box, this function decays to zero exponentially for large  $\Delta_t$  (see Fig. 5), and the decay constant  $\tau$  and the speed  $1/\tau$  are obtained by a fit, for each value of the parameters ( $N, \eta, \ell$ ), from one single very long simulation (with  $t \gg \tau$ ). The local Metropolis algorithm, for its optimal step size, is as fast as the event-chain algorithms with  $\ell/\lambda_0 \approx 1$ . (Our implementation moves  $3 \times 10^{10}$  particles per hour on a 2.8 GHz single-processor workstation for  $N=4096$ .)

For small total displacements  $\ell/\lambda_0 \ll 1$ , the speed of all the algorithms (reversible and irreversible SEC, REC, and local Metropolis algorithm) is proportional to  $D_{\text{loc}}^{\infty}(\ell)$ , as given by Eq. (4), that is, they all follow the single-particle behavior (see Fig. 6). For larger  $\ell/\lambda_0$ , the event-chain algorithms realize a considerable speed-up compared to the local Metropolis algorithm (also in Fig. 6). Moreover, both versions of the SEC algorithm set up coherent motion across the system and are clearly better than the REC algorithm, whose particle chains meander through the system (as shown in Fig. 2), so that the disks move incoherently. For large  $\ell/\lambda_0$ , the irreversible SEC algorithm is faster than the reversible version: it is of advantage to break detailed balance. Figure 6 also illustrates that the SEC algorithm becomes more efficient (as compared to the local Metropolis algorithm) as one approaches the transition from the liquid phase (at density  $\eta \sim 0.708$ ). The optimal speed-up increases with the system size, as shown in Table I. This suggests that the speed-up of the SEC algorithm may well increase with the correlation length of the system, and may, in the transition region, have a more favorable scaling than the local Metropolis algorithm.

Let us finally discuss the relationship between the Monte Carlo method and the molecular-dynamics algorithm. All these approaches describe the same equilibrium state. Unlike the Monte Carlo method, the molecular dynamics follows the physical time-evolution of the system. The first implementa-

TABLE I. Optimal speed-up reached by the SEC algorithm (with respect to the reversible SEC algorithm for  $\ell/\lambda_0=1$ ) at density  $\eta=0.71$  as a function of particle number.

$N$	Optimal speed-up	
	Reversible	Irreversible
64	$\sim 6$	$\sim 8$
256	$\sim 8$	$\sim 11$
1024	$\sim 9$	$\sim 15$
4096	$\sim 10$	$\sim 20$

tions of the molecular-dynamics algorithm [4] were very time consuming, with a complexity of  $O(N)$  per event (collision), slower than the Metropolis algorithm [ $O(1)$  per move]. The complexity of modern implementations has improved to  $O(\log N)$  [15] per event and even  $O(1)$  [16]. A closer look is thus needed to choose between the two methods.

We used a simple version of the molecular dynamics to compute the decorrelation time of  $\Psi$  in the same way as in Fig. 5. In number of events, molecular dynamics is found to be about three times faster than the irreversible version of SEC for  $\eta \sim 0.7$  and  $N=64-1024$ . It is very interesting to notice that molecular dynamics shows, unlike REC, the same density dependence of its speed as SEC around the transition region. We then determined the CPU time per collision of one of the most rapid current implementations of the hard-disk molecular-dynamics algorithm [15]. For the  $32 \times 32$  system at  $\eta \sim 0.7$ , this implementation reaches about  $1.7 \times 10^9$  collisions per hour on a 2.6 GHz workstation [17]. Our  $xy$  implementation of the SEC algorithm reaches  $3 \times 10^{10}$  collisions per hour on similar hardware. Our implementation is thus about 5 times faster in CPU time to reach thermodynamic equilibrium than the best molecular-dynamics implementation. We should also note that SEC is much easier to implement. A synopsis of these relative and absolute timing issues is presented in Fig. 7. For clarity, we give times in terms of “equivalent Metropolis moves;” this means that one event of the molecular-dynamics algorithm corresponds to  $\sim 3$  SEC events and to  $\sim 60$  Metropolis moves. The horizontal lines indicate what can be achieved in approximately one hour with our implementation of the Metropolis algorithm, irreversible SEC, and the implementation of the molecular-dynamics algorithm of [15].

In conclusion, we have in this paper proposed a class of algorithms for hard spheres and related systems, which clearly outperform the local Metropolis algorithm. We discussed three aspects of our algorithms, which all contributed to improve their speed. First, we showed that event-chain algorithms have a larger effective step size than the local Metropolis algorithm, because spheres move until they strike one of their neighbors. We computed mean-square displacements per particle (local diffusion constants) to quantify this point. Nevertheless, local diffusion constants are not clearly related to the speed of the algorithm: they merely describe the short-time rattling of a particle in its cage (only for small

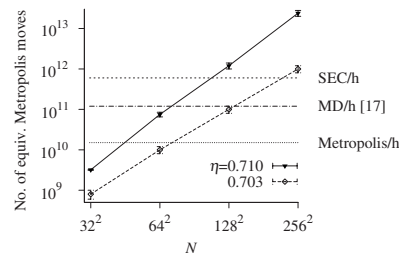


FIG. 7. System-size dependence of the correlation time of the orientational order parameter for two densities. What can be achieved in approximately one hour using the different algorithms discussed in this paper is indicated by horizontal lines.

$\ell/\lambda_0$  is the local diffusion constant directly proportional to the algorithm’s speed). Second, we performed numerical simulations of two variants of the method, and carefully analyzed the autocorrelation function of the orientational order parameter. One of them, the SEC algorithm, induces coherent motion of a long chain of spheres, and it allows the different parts of the system to communicate with each other. We witnessed considerable performance gains of this algorithm in the critical region, in the same way than the molecular dynamics. This suggests the exciting possibility that the speed-up of the event-chain algorithm grows with the correlation length of the system, and may have a more favorable scaling than the local Metropolis algorithm in the critical region. This speed-up, which is shared by both the molecular-dynamics algorithm and the SEC algorithm, is not understood and should be further investigated. Third, we noticed that the absence of rejections permitted to conceive an irreversible version of the SEC algorithm which improves the performances.

Our implementation of the SEC algorithm approaches equilibrium (for large systems at  $\eta \approx 0.70$ ) about 40 times faster than our local Metropolis algorithm, not only because of the speed-up evidenced in Fig. 6 but also because the  $xy$  version of the algorithm computes no scalar products and uses very few random numbers. It also equilibrates about five times faster than the best molecular-dynamics implementation and preserves certainly a large potential for improvement.

Nevertheless, CPU times needed for convergence remain extremely large, and even with our algorithm, full convergence of systems with  $10^6$  particles at high densities comes barely into reach. The irreversible SEC algorithm not only appears to be the fastest currently known simulation method for dense hard-disk and hard-sphere systems, but it also provides a telling example of the benefits of breaking detailed balance in Monte Carlo algorithms going beyond the “lifting” Markov chains [18].

This research was initiated at the Kavli Institute for Theoretical Physics at UCSB (URL: <http://www.kitp.ucsb.edu/>). We thank the NSF for partial support under Grant No. PHY05-51164. We are grateful to M. Isobe for helpful correspondence.

- [1] B. J. Alder and T. E. Wainwright, *Phys. Rev.* **127**, 359 (1962).
- [2] B. J. Alder and T. E. Wainwright, *Phys. Rev. A* **1**, 18 (1970).
- [3] N. Metropolis *et al.*, *J. Chem. Phys.* **21**, 1087 (1953).
- [4] B. J. Alder and T. E. Wainwright, *J. Chem. Phys.* **27**, 1208 (1957).
- [5] R. H. Swendsen and J. S. Wang, *Phys. Rev. Lett.* **58**, 86 (1987).
- [6] U. Wolff, *Phys. Rev. Lett.* **62**, 361 (1989).
- [7] C. Mak, *Phys. Rev. E* **73**, 065104 (2006).
- [8] B. I. Halperin and D. R. Nelson, *Phys. Rev. Lett.* **41**, 121 (1978); D. R. Nelson and B. I. Halperin, *Phys. Rev. B* **19**, 2457 (1979); A. P. Young, *ibid.* **19**, 1855 (1979).
- [9] W. Krauth, *Statistical Mechanics: Algorithms and Computations* (Oxford University Press, Oxford, U.K., 2006).
- [10] C. Dress and W. Krauth, *J. Phys. A* **28**, L597 (1995).
- [11] A. Buhot and W. Krauth, *Phys. Rev. Lett.* **80**, 3787 (1998).
- [12] L. Santen and W. Krauth, *Nature (London)* **405**, 550 (2000).
- [13] A. Jaster, *Physica A* **264**, 134 (1999); *Phys. Lett. A* **330**, 120 (2004).
- [14] K. J. Strandburg, *Rev. Mod. Phys.* **60**, 161 (1988).
- [15] M. Isobe, *Int. J. Mod. Phys. C* **10**, 1281 (1999); *Phys. Rev. E* **77**, 021201 (2008).
- [16] G. Paul, *J. Comput. Phys.* **221**, 615 (2007).
- [17] M. Isobe (private communications).
- [18] P. Diaconis, S. Holmes, and R. M. Neal, *Ann. Appl. Probab.* **10**, 726 (2000).

## 7.2 Publication II

Etienne P. Bernard, Cédric Chanal and Werner Krauth  
*Damage spreading and coupling in Markov chains*  
*Europhysics Letters* **92** 60004 (2010)

This article addresses the problem posed by damage-spreading transitions in the application of perfect-sampling methods (see Chapter 6). It shows, through the analysis of algorithms in hard disks and spin glasses, that this problem is the main obstacle to the realization of efficient perfect-sampling method.



## Damage spreading and coupling in Markov chains

ETIENNE P. BERNARD<sup>(a)</sup>, CÉDRIC CHANAL and WERNER KRAUTH<sup>(b)</sup>

*Laboratoire de Physique Statistique, CNRS, UPMC, Ecole Normale Supérieure - 24 rue Lhomond, 75231 Paris Cedex 05, France, EU*

received 8 October 2010; accepted in final form 2 December 2010

published online 18 January 2011

PACS 05.10.Ln – Monte Carlo methods

PACS 02.50.Ga – Markov processes

PACS 75.10.Nr – Spin-glass and other random models

**Abstract** – In this paper, we relate the coupling of Markov chains, at the basis of perfect sampling methods, with damage spreading, which captures the chaotic nature of stochastic dynamics. For two-dimensional spin glasses and hard spheres we point out that the obstacle to the application of perfect-sampling schemes is posed by damage spreading rather than by the survey problem of the entire configuration space. We find dynamical damage-spreading transitions deeply inside the paramagnetic and liquid phases, and we show that the critical values of the transition temperatures and densities depend on the coupling scheme. We discuss our findings in the light of a classic proof that for arbitrary Monte Carlo algorithms damage spreading can be avoided through non-Markovian coupling schemes.

Copyright © EPLA, 2010

**Introduction.** – Chaos manifests itself in Hamiltonian dynamical systems when any two nearby initial configurations drift apart with time. Chaos can also be defined for cellular automata and for Markov-chain algorithms. In these dynamical systems, following Kauffman [1], the drifting-apart of configurations is termed “damage spreading”. In contrast, for “regular” dynamics, two nearby initial configurations become identical after a finite time, and remain indistinguishable from then on. For Markov-chain Monte Carlo algorithms, the closely related case where the entire space of initial configurations becomes identical is termed “coupling”. Once it has coupled, the Markov chain has lost all correlations with the initial configuration. The coupling of Markov chains has risen to great prominence when Propp and Wilson used it for a perfect sampling method for Markov chains named “Coupling From The Past” (CFTP) [2]. When applicable, this method overcomes the problem of estimating the correlation time of a Monte Carlo calculation. In the present article, we shall discuss the fruitful connection between damage spreading and coupling [3].

In systems with  $N$  elements (spins, hard spheres, etc.), the configuration space generally grows exponentially with  $N$ , and CFTP thus faces two distinct challenges. First, it must *survey* the entire configuration space in order to

prove coupling. Second, it must avoid damage spreading which would cause the coupling time to *explode*: it would become much larger than the correlation time as any two configurations have a very small probability for finding each other in a large space.

The surveying problem is avoided in systems with a special property called “partial order”, as for example the ferromagnetic Ising model under heat-bath dynamics [2,4]. For more general systems (without partial order, but with local update algorithms), such as spin glasses and hard spheres, a recent “patch” algorithm inspired by numerical block scaling ideas [3,5] allows us to rigorously follow a superset of all initial conditions until it couples. This algorithm generates only modest overheads of memory and CPU time [3]. It was found that the coupling can be established after a time evolution very close to the coupling time.

The second problem, the explosion of the coupling time related to damage spreading, poses the veritable obstacle to the application of CFTP ideas. Damage spreading has been studied in many physical systems, in particular spin glasses [6]. In several spin glass models with heat-bath dynamics, it is now well established that a dynamical damage-spreading transition occurs at a critical temperature,  $\beta_{ds}$ , located in the paramagnetic phase [7]: the dynamic is regular at temperatures higher than  $1/\beta_{ds}$  and chaotic at lower temperatures. Even for the two-dimensional  $\pm J$  Ising spin glass, which has a

<sup>(a)</sup>E-mail: [etienne.bernard@ens.fr](mailto:etienne.bernard@ens.fr)

<sup>(b)</sup>E-mail: [werner.krauth@ens.fr](mailto:werner.krauth@ens.fr)

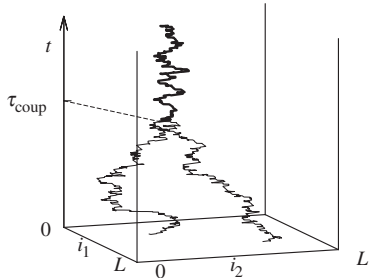


Fig. 1: Coupling of two random walks in a periodic  $N$ -dimensional hypercubic lattice of length  $L$ . After the time  $\tau_{\text{coup}}$ , the two random walks evolve identically. The chaotic coupling of eq. (2) is shown. For the regular coupling of eq. (3), the displacement at time  $t$  is in the same direction  $k$ , and it is a function of  $i_k$  only.

thermodynamic phase transition at  $T=0$  [8–11], the transition to chaos takes place at finite temperature [7]. We study in this paper the damage spreading of spin glasses and hard spheres, the divergence of the ratio of the coupling time and the correlation time, for different algorithms.

**Random walks in high dimensions.** – Before analyzing two-dimensional spin glasses and hard spheres, we illustrate coupling and damage spreading in a simple Markov-chain algorithm that can be interpreted either as a random walk in an  $N$ -dimensional hypercubic lattice, as the dynamics of  $N$  distinguishable non-interacting particles in a one-dimensional lattice of length  $L$ , or as  $N$  non-interacting Potts spins with  $L$  states. For the random walk (see fig. 1), each  $N$ -dimensional lattice site  $i = \{i_0, \dots, i_{N-1}\}$  is described by integers  $i_k \in \{0, \dots, L-1\}$  with periodic boundary conditions in the  $i_k$ . The particle can hop from site  $i$  to one of the  $i$ 's nearest neighbors in direction  $k$ ,  $j = i \pm \delta_k$ , with  $\delta_k = \{0, \dots, 1, 0, \dots\}$  (periodic boundary conditions are again understood). The probability for moving from  $i$  to  $j$  is

$$p(i \rightarrow j) = \begin{cases} \frac{1}{3N}, & \text{for } j = i \pm \delta_k, \\ \frac{1}{3}, & \text{for } j = i, \\ 0, & \text{otherwise.} \end{cases} \quad (1)$$

The simulation thus samples at each time step one dimension,  $k$ , among the  $N$  available ones (it moves in “ $x$ ”, or “ $y$ ” or “ $z$ ”, etc). In dimension  $k$ , it then hops with probabilities  $1/3$  each to the left or to the right, or remains on the same site. Equation (1) also describes  $N$  distinguishable non-interacting particles on a one-dimensional lattice of length  $L$ , again with periodic boundary conditions: At time  $t$ , a randomly chosen particle  $k$  hops to the left or to the right, or it remains on the same site, each with probability  $1/3$ , as above.

A two-configuration coupling is a random process  $\tilde{p}(i \rightarrow j, i' \rightarrow j')$  for the joint evolution of two random walks such that integrating over one of them yields the original random walk of eq. (1) for the other. After they meet, the two configurations evolve in the same way. The simplest choice for a coupling is the product ansatz,

$$\tilde{p}(i \rightarrow j, i' \rightarrow j') = \begin{cases} p(i \rightarrow j)p(i' \rightarrow j'), & \text{if } i \neq i', \\ p(i \rightarrow j), & \text{if } i = i', j = j', \\ 0, & \text{otherwise,} \end{cases} \quad (2)$$

where the two random walks evolve independently of each other if they are on different sites  $i$  and  $i'$ , but stay together once they have met ( $j = j'$  if  $i = i'$ ). To implement this coupling for any number of configurations, one samples at each time step independent random moves at each site, so that particles on the same site experience the same randomness. In the above-mentioned representation of particles on the one-dimensional line, we consider the coupling of two  $N$ -particle systems, again described by eq. (2), as the independent evolution, at time  $t$ , of the  $L^N$  possible configurations of the system. Naturally, the coupling time scales as  $L^N$  whereas the correlation time (in sweeps) behaves as  $L^2$ .

An alternative coupling consists in sampling, at time  $t$ , one dimension  $k$  common to all random walks. The two-configurations coupling scheme is then

$$\tilde{p}(i_k \rightarrow j_k, i'_k \rightarrow j'_k) = \begin{cases} p(i_k \rightarrow j_k)p(i'_k \rightarrow j'_k), & \text{if } i_k \neq i'_k, \\ p(i_k \rightarrow j_k), & \text{if } i_k = i'_k, j_k = j'_k, \\ 0, & \text{otherwise,} \end{cases} \quad (3)$$

so that two configurations  $i$  and  $j$  with  $i_k = i'_k$  will preserve this common coordinate ( $j_k = j'_k$ ). In the representation of  $N$  particles on a one-dimensional lattice, the same particle  $k$  is selected for each configuration, and for two different configurations, the particles labelled  $k$  stay together once they have met on the same site. The dynamics is then regular and the coupling time is  $\tau_{\text{coup}}/N \sim a \log N$  (see fig. 2). The logarithmic behaviour is explained by the fact that particles move independently of each other, the coupling time for the entire system is thus the maximum of the  $N$  coupling times for each particle.

In conclusion, we see that the same  $N$ -dimensional random walk of eq. (1), with a correlation time of order  $L^2$ , allows two very different coupling, chaotic and regular. In spin glasses and hard spheres, these regimes are realized for the same coupling at different temperatures.

**Spin glass.** – The random walk considered previously can also be considered as an  $L$ -state Potts model at infinite temperature evolving under heat-bath dynamics.

The product ansatz of eq. (2) would correspond to the independent evolution of the spin configurations, and it is clearly chaotic. With the coupling of eq. (3), in contrast, all spins evolve and couple independently at  $\beta = 0$ , and the

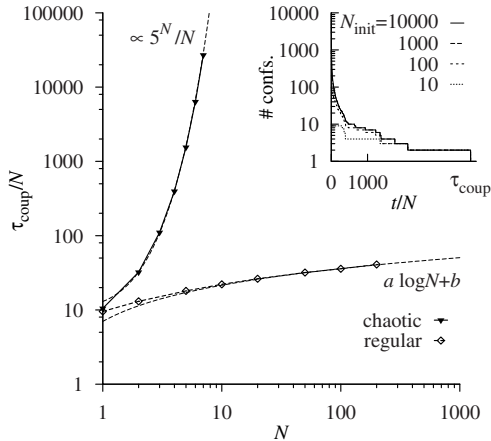


Fig. 2: Chaotic and regular couplings for the random walk in an  $N$ -dimensional hypercubic lattice of length  $L = 5$  (see eqs. (2) and (3), respectively). The random process for a single random walk is defined by eq. (1) in both cases. Inset: number of configurations *vs.* time as a function of the number  $N_{\text{init}}$  of initial configurations, for  $N = 6$ ,  $L = 5$  for the chaotic coupling. The same realization of the coupling of eq. (3) is used for all runs.

global coupling time is again the maximum of the coupling times of the individual spins. The Monte Carlo dynamics is thus regular, and the diagram of fig. 2 carries over to the general case with  $L \geq 2$ . At finite temperatures  $\beta$ , the energy of a spin configuration is given by

$$E = - \sum_{(i,j)} J_{ij} s_i s_j.$$

We first consider heat-bath dynamics, which consists in choosing one spin  $s_k$  and updating it with probabilities

$$\pi(s_k = \pm 1) = \frac{1}{1 + \exp(\mp 2h_k \beta)}, \quad (4)$$

where the field on site  $k$  is given by  $h_k = \sum_l J_{kl} s_l$ . The coupling is defined by the use of the same random numbers for each configuration.

For the two-dimensional ferromagnetic Ising model (all  $J_{ij} = 1$ ,  $L = 2$ ), the dynamics remains regular at all temperatures. Below the Curie temperature,  $\tau_{\text{coup}}$  is very large, but so is the correlation time  $\tau_{\text{corr}}$ , and the partial order implies that the complexity of  $\tau_{\text{coup}}/\tau_{\text{corr}} \leq O(\log N)$  [2]. The partial order is preserved in the disordered Ising model with ferromagnetic interactions  $J_{ij} = J_{ji} \geq 0$ , and in this model also, the theorem of Propp and Wilson guarantees that  $\tau_{\text{coup}}$  is, up to logarithms, of the same order as  $\tau_{\text{corr}}$ .

Frustrated models, as for example spin glasses, do not exhibit partial order, and can thus undergo a damage-spreading transition. In the two-dimensional  $\pm J$  Ising spin glass, the quenched random interactions

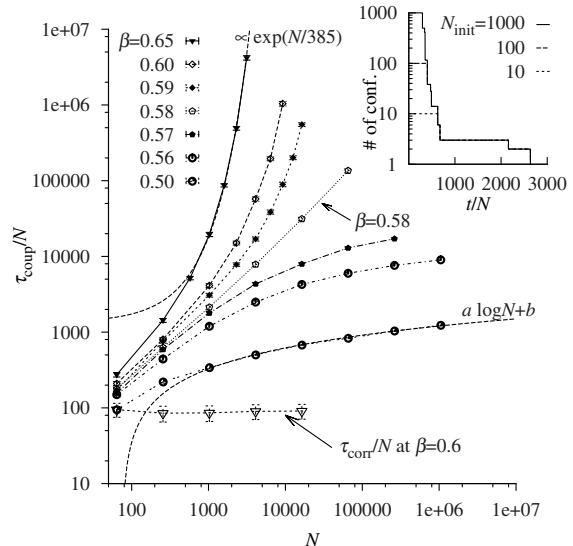


Fig. 3: Disorder-averaged coupling time for the heat-bath algorithm of the two-dimensional  $\pm J$  Ising spin glass. A dynamical phase transition is seen at the damage-spreading temperature  $\beta_{\text{ds}} \simeq 0.58$ . Inset: saturation phenomenon for  $N = 64^2$  spins at  $\beta = 0.56$ .

satisfy  $J_{ij} = J_{ji} = \pm 1$  with equal probability. Although this model is paramagnetic for all finite temperatures, Campbell and de Arcangelis [7] found a damage-spreading transition for the heat-bath algorithm at  $\beta_{\text{ds}} \simeq 0.59$ . In previous work [3,5], we succeeded in coupling large systems down to this temperature using the patch algorithm. We showed that the patch algorithm's upper bound on the coupling times agrees well with the lower bound obtained from a partial-coupling approach, where one checks coupling for a finite number  $N_{\text{init}}$  of random initial conditions rather than for the entire configuration space ( $N_{\text{init}} = 2^N$ ). As shown in the inset of fig. 3, for one realization of the random process, the coupling time does not vary if  $N_{\text{init}} \gtrsim 10$ , and for  $N_{\text{init}} = 1000$  it equals the coupling time for the entire configuration space.

In the main graph of fig. 3, we show the coupling time as a function of  $N$  at constant temperature. A dynamical phase transition is seen at the damage-spreading temperature  $\beta_{\text{ds}} \simeq 0.58$ . In the chaotic phase,  $\tau_{\text{coup}}/N$  grows exponentially with  $N$ , but only logarithmically in the regular phase. The dynamical phase transition in this model (without a spin glass phase at finite  $\beta$ ), although not mathematically proven, appears firmly established. It is without influence on single-particle properties. To illustrate this point, we verify that the correlation time  $\tau_{\text{corr}}/N$ , computed with the autocorrelation function

$$q(t) = \frac{1}{N} \sum_{i=0}^N \langle s_i(0) s_i(t) \rangle, \quad (5)$$

remains constant in the chaotic phase and only  $\tau_{\text{coup}}/\tau_{\text{corr}}$  diverges with  $N \rightarrow \infty$ .

After the heat-bath algorithm, we now discuss the Metropolis algorithm, where individual spins  $s_k$  are flipped with a probability depending on their local field. In the standard implementation, spin flips are accepted with a probability equal to 1 at infinite temperature. To allow coupling at any  $\beta$  we use

$$p(s_k \rightarrow -s_k) = \frac{2}{3} \min(1, \exp(-2\beta s_k h)). \quad (6)$$

At each step the same spin  $k$  is updated for all copies of the system. For this dynamics, several coupling schemes can be set up. If the same random number  $\gamma$  is used for each configuration, the coupling does not take place, as two opposite configurations will always stay opposite. We adapt the regular coupling of eq. (3) and use two independent random numbers,  $\gamma_1$  for “up” spins and  $\gamma_2$  for “down” spins. The coupling time has then the same qualitative behaviour as in fig. 3, logarithmic at high temperatures and exponential at low temperatures, but with a critical temperature  $\beta_{\text{ds}} \simeq 0.33$ . The Metropolis algorithm, with this coupling scheme, has thus a higher dynamical critical temperature than the heat-bath algorithm, with which it shares all the qualitative features. This confirms that the dynamic damage-spreading transition is algorithm dependent. One may also choose the random numbers in the Metropolis algorithm using  $\gamma$  for  $s_k = 1$  and  $1 - \gamma$  for  $s_k = -1$ . This scheme correlates opposite spins better and the critical temperature is found to be  $\beta_{\text{ds}} \simeq 0.52$ . This results shows that, like for the previous random walk, the same Markov-chain allows for qualitatively different coupling.

**Hard spheres.** – After spin glasses, we now consider another key model in statistical physics, namely hard spheres. This model’s Hamiltonian dynamics, realized in the event-driven molecular dynamics algorithm [4,12], is chaotic for all densities and for all  $N$  [4,13,14]. In this section, we will present several Monte Carlo algorithms for hard spheres, which allow for coupling of the entire configuration space. Two of the algorithms remain regular below a finite critical packing fraction,  $\eta_{\text{ds}}$ , in the limit  $N \rightarrow \infty$ . In the following discussion we are not concerned with algorithmic efficiency of the implementation, and only concentrate on the coupling properties.

*Birth-and-death algorithm.* In the grand-canonical birth-and-death Monte Carlo algorithm, particles are placed inside the box at random positions  $\mathbf{x} = (x_k, y_k)$  at rate  $\lambda$  if no overlaps with previously placed disks are generated. The life time of each disk is sampled from an exponential distribution with rate 1. One realization of the algorithm is represented in the diagram of fig. 4. The mean number  $\langle N \rangle$  of particles in this system is controlled by the activity  $\lambda$ .

This model’s state space is infinite, but the survey of all possible initial conditions is nevertheless feasible [5,15].

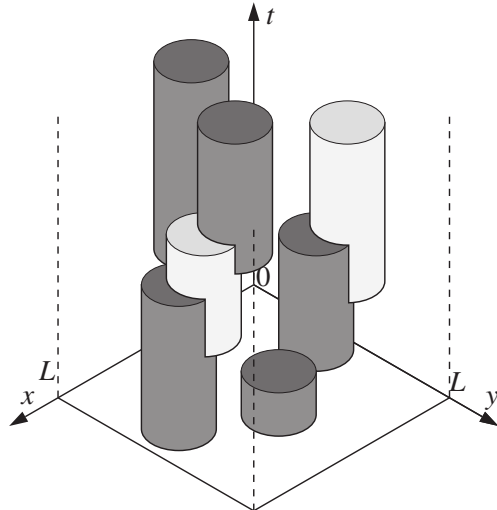


Fig. 4: Grand-canonical birth-and-death algorithm for hard disks. Disk  $i$  appears at time  $t_i$ , at position  $\mathbf{x}_i = (x_i, y_i)$ , and it disappears at time  $t_i + \tau_i$ . In time, disk  $i$  describes a cylinder. Disks (cylinders) which are accepted, because they create no overlaps with earlier disks, are drawn in dark gray, while rejected disks are drawn in light gray. The configuration space of this system is infinite, yet the possible configurations at time  $t$  are a subset of the finite set (of dark and light cylinders) produced from a horizontal cut in this diagram.

For any realization of the algorithm, the possible configurations at time  $t$  are a subset of the finite set produced from a horizontal cut in the diagram of fig. 4. The patch algorithm again yields sharp upper bounds for  $\tau_{\text{coup}}$  [5]. Surprisingly, this algorithm for hard disks remains regular below a finite density  $\eta_{\text{ds}}$  in the limit  $N \rightarrow \infty$  [15,16].

We again study damage spreading in this model by applying the same Monte Carlo dynamics (same choice of  $\mathbf{x}_i, t_i, \tau_i$ ) to  $N_{\text{init}}$  random hard-sphere initial conditions at time  $t = 0$  with life times sampled from an exponential distribution. The data shown in fig. 5 again indicate a dynamical phase transition between the regular regime at packing fractions  $\eta < \eta_{\text{ds}} \simeq 0.29$  and the chaotic regime above  $\eta_{\text{ds}}$ . This density corresponds to the limiting density found with the patch algorithm [5].

*“Labelled displacement” algorithm.* A canonical version of the birth-and-death algorithm is the “labelled displacement” algorithm where, at times  $t = 0, 1, 2, \dots$ , a randomly chosen particle  $k$  is moved to a random position  $\mathbf{x}_k$ , if this move creates no overlaps. We see clear evidence of a dynamical phase transition at a critical density  $\eta_{\text{ds}} \simeq 0.13$  (see fig. 6), which is smaller than for the closely related birth-and-death algorithm.

*Spot algorithm.* We finally study the coupling for a Markov chain similar to the Metropolis algorithm: the spot algorithm. The Metropolis algorithm for  $N$  hard

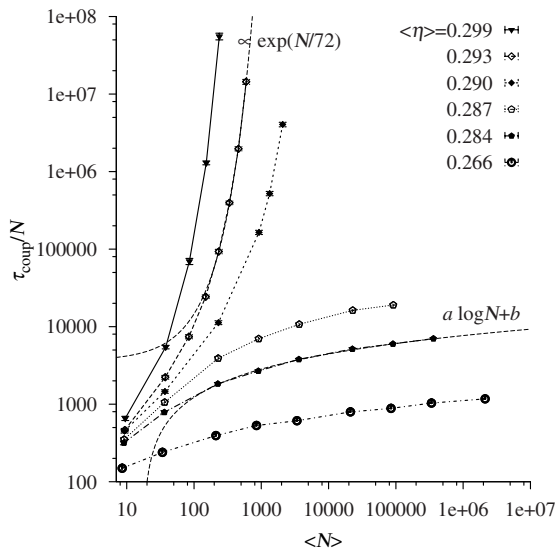


Fig. 5: Coupling time of the birth-and-death algorithm of fig. 4 for two-dimensional hard spheres (estimated with  $N_{\text{init}} = 100$ ). The damage spreading transition occurs at a packing fraction  $\eta_{\text{ds}} \simeq 0.29$ .

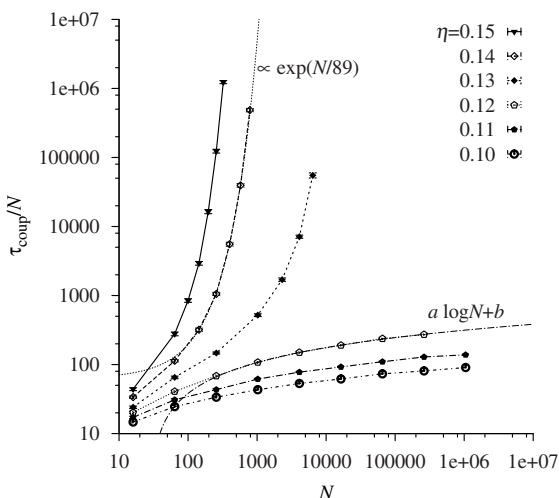


Fig. 6: Coupling time for the labelled displacement algorithm. The dynamical transition to chaos occurs at a lower density ( $\eta_{\text{ds}} \simeq 0.13$ ) than for the birth-and-death algorithm of fig. 5.

spheres consists in moving, at time  $t$ , a particle  $k$  by a random vector  $\delta = (\delta_x, \delta_y)$ . As the configuration space is continuous, the coupling probability is zero if one uses a naive coupling scheme. The following spot algorithm is more successful (although we will show its coupling is chaotic at all densities): at time  $t$ , it places a spot, a disk-shaped region with radius  $\sigma_{\text{spot}} \leq \sigma$ , at a random position  $\mathbf{x}_s$ . The spot contains at most one disk center,

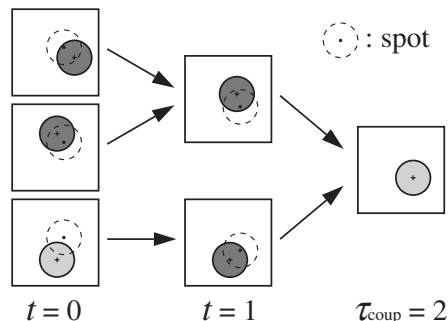


Fig. 7: Spot algorithm for hard spheres: The randomly chosen spot position defines the attempted move of a disk inside the spot. The spot radius satisfies  $\sigma_{\text{spot}} \leq \sigma$ , and at most one disk is moved at time  $t$ . An example with  $N = 1$  and  $\sigma_{\text{spot}} = \sigma$  is shown.

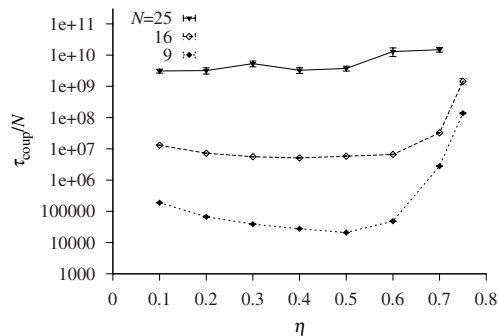


Fig. 8: Coupling time  $\tau_{\text{corr}}$  of the spot algorithm for  $N$  hard disks (estimated with  $N_{\text{init}} = 100$ ) as a function of packing fraction  $\eta$ . For all  $\eta$ , the coupling time is exponential in  $N$ , and we conjecture the coupling to be chaotic.

and the move consists in placing this disk at  $\mathbf{x}_s$ , if this creates no overlap with other particles (see fig. 7). The spot algorithm satisfies detailed balance, and it generates the same moves as the Metropolis algorithm. Moreover, as illustrated in fig. 7, it succeeds in coupling. However, as shown in fig. 8, the coupling time of the spot algorithm is an exponential function of  $N$  for all densities: the coupling is always chaotic.

**Conclusion.** – In conclusion, we have in this paper studied the relationship between the coupling of Markov chains, which is of critical importance for the subject of perfect sampling, and damage spreading, which exposes the chaotic nature of the Monte Carlo dynamics.

For the two-dimensional  $\pm J$  Ising spin glass, which lacks an equilibrium phase transition at finite temperatures, we confirm the existence of a dynamical phase transition at  $\beta_{\text{ds}} \simeq 0.58$  [7] for the heat-bath algorithm. For lower temperatures the coupling time explodes. The Metropolis algorithm has the same damage spreading behaviour but

with higher critical temperatures:  $\beta_{\text{ds}} \simeq 0.33$  or  $\beta_{\text{ds}} \simeq 0.52$  for two simple coupling schemes. All damage-spreading transitions for this system are deeply inside the paramagnetic phase.

For the two-dimensional hard-sphere system, we analyzed three local Monte Carlo algorithms, the birth-and-death algorithm, inspired from Poisson point processes, its canonical version (the “labelled displacement” algorithm), and the spot algorithm, a straightforward adaptation of the Metropolis algorithm. The first algorithm shows a regular regime only for packing densities below  $\eta_{\text{ds}} \simeq 0.29$ , the coupling time was then of the same order of magnitude as the correlation time. The canonical version of the birth-and-death algorithm had a critical density of  $\eta_{\text{ds}} \simeq 0.13$ . These transition densities are again deeply in the liquid phase.

Both for spin glasses and for hard spheres, the rigorous survey of the configuration space [3] remains feasible for all temperatures and densities. The application of perfect sampling methods to these challenging problems is thus not so much limited by the surveying problem, as the patch algorithm allows to track the evolution of the entire configuration space, but more by damage spreading, the underlying chaotic nature of the Monte Carlo dynamics.

In this context, it is of great interest that Griffeath [17] has constructed a coupling that always remains regular: It realizes the coupling at time  $t$  and at position  $X_t$  of two Markov chains that have started at time  $t=0$  at configurations  $X_0$  and  $X'_0$  with the minimum of the probabilities to go from  $X_0$  or from  $X'_t$  to  $X_t$ . Griffeath’s coupling is non-Markovian and very difficult to construct in practice, but it may point the way to couplings that remain regular at lower temperatures and higher densities than the naive couplings we discussed in this paper.

\*\*\*

We thank A. SINCLAIR for helpful correspondence.

#### REFERENCES

- [1] KAUFFMAN S., *J. Theor. Biol.*, **22** (1969) 437.
- [2] PROPP J. and WILSON D., *Random Struct. Algorithms*, **9** (1996) 223.
- [3] CHANAL C. and KRAUTH W., *Phys. Rev. Lett.*, **100** (2008) 060601.
- [4] KRAUTH W., *Statistical Mechanics: Algorithms and Computations* (Oxford University Press) 2006.
- [5] CHANAL C. and KRAUTH W., *Phys. Rev. E*, **81** (2010) 016705.
- [6] DERRIDA B. and WEISBUCH G., *Europhys. Lett.*, **4** (1987) 657.
- [7] CAMPBELL I. A. and DE ARCANGELIS L., *Physica A*, **178** (1991) 29.
- [8] MORGENSTERN I. and BINDER K., *Phys. Rev. Lett.*, **43** (1979) 1615.
- [9] MCMILLAN W. L., *Phys. Rev. B*, **28** (1983) 5216.
- [10] SINGH R. R. P. and CHAKRAVARTY S., *Phys. Rev. Lett.*, **57** (1986) 245.
- [11] BHATT R. N. and YOUNG A. P., *Phys. Rev. B*, **37** (1988) 5606.
- [12] ALDER B. J. and WAINWRIGHT T. E., *J. Chem. Phys.*, **27** (1957) 1208.
- [13] SINAI Y., *Russ. Math. Surv.*, **25** (1970) 137.
- [14] SIMÁNYI N., *Invent. Math.*, **154** (2003) 123.
- [15] WILSON D., *Random Struct. Algorithms*, **16** (2000) 85.
- [16] KENDALL W. and MOLLER J., *Adv. Appl. Probab.*, **32** (2000) 844.
- [17] GRIFFEATH D., *Probab. Theory Relat. Fields*, **31** (1975) 95.

## 7.3 Publication III

Phys. Rev. Lett. 107, 155704 (2011) Etienne P. Bernard and Werner Krauth  
*Two-step melting in two dimensions: First-order liquid-hexatic transition*  
*Physical Review Letters* **107** 155704 (2011)

This article studies the nature of the hard-disk melting transition (see Chapter 1, Chapter 3 and Chapter 4). The correlation functions, thermodynamic quantities, as well as direct visualization are computed for large-scale systems. The nature of the transition is found to be first order for the liquid-hexatic transition, and KT for the hexatic-solid transition.



## Two-step melting in two dimensions: First-order liquid-hexatic transition

Etienne P. Bernard\* and Werner Krauth†

*Laboratoire de Physique Statistique  
Ecole Normale Supérieure, UPMC, CNRS  
24 rue Lhomond, 75231 Paris Cedex 05, France  
(Dated:)*

Melting in two spatial dimensions, as realized in thin films or at interfaces, represents one of the most fascinating phase transitions in nature, but it remains poorly understood. Even for the fundamental hard-disk model, the melting mechanism has not been agreed on after fifty years of studies. A recent Monte Carlo algorithm allows us to thermalize systems large enough to access the thermodynamic regime. We show that melting in hard disks proceeds in two steps with a liquid phase, a hexatic phase, and a solid. The hexatic-solid transition is continuous while, surprisingly, the liquid-hexatic transition is of first-order. This melting scenario solves one of the fundamental statistical-physics models, which is at the root of a large body of theoretical, computational and experimental research.

Generic two-dimensional particle systems cannot crystallize at finite temperature[1–3] because of the importance of fluctuations, yet they may form solids[4]. This paradox has provided the motivation for elucidating the fundamental melting transition in two spatial dimensions. A crystal is characterized by particle positions which fluctuate about the sites of an infinite regular lattice. It has long-range *positional* order. Bond orientations are also the same throughout the lattice. A crystal thus possesses long-range *orientational* order. The positional correlations of a two-dimensional solid decay to zero as a power law at large distances. Because of the absence of a scale, one speaks of “quasi-long range” order. In a two-dimensional solid, the lattice distortions preserve long-range orientational order[5], while in a liquid, both the positional and the orientational correlations decay exponentially.

Besides the solid and the liquid, a third phase, called “hexatic”, has been discussed but never clearly identified in particle systems. The hexatic phase is characterized by exponential positional but quasi-long range orientational correlations. It has long been discussed whether the melting transition follows a one-step first-order scenario between the liquid and the solid (without the hexatic) as in three spatial dimensions[6], or whether it agrees with the celebrated Kosterlitz, Thouless[7], Halperin, Nelson[8] and Young[9] (KTHNY) two-step scenario with a hexatic phase separated by continuous transitions from the liquid and the solid[10–18].

Two-dimensional melting was discovered [4] in the simplest particle system, the hard-disk model. Hard disks (of radius  $\sigma$ ) are structureless and all configurations of non-overlapping disks have zero potential energy. Two isolated disks only feel the hard-core repulsion, but the other disks mediate an entropic “depletion” interaction (see, e.g., [19]). Phase transitions result from an “order from disorder” phenomenon: At high density, ordered configurations can allow for larger local fluctuations, thus higher entropy, than the disordered liquid. For hard disks, no

difference exists between the liquid and the gas. At fixed density  $\eta$ , the phase diagram is independent of temperature  $T = 1/k_B\beta$ , and the pressure is proportional to  $T$ , as discovered by D. Bernoulli in 1738. Even for this basic model, the nature of the melting transition has not been agreed on.

The hard-disk model has been simulated with the local Monte Carlo algorithm since the original work by Metropolis et al. [20]. A faster collective-move “event-chain” Monte Carlo algorithm was developed only recently[21] (see [22]). We will use it to show that the melting transition neither follows the one-step first-order nor the two-step continuous KTHNY scenario.

To quantify orientational order, we express the local orientation of disk  $k$  through the complex vector  $\Psi_k = \langle \exp(6i\phi_{kl}) \rangle$ , with  $\langle \rangle$  the average over all the neighbors  $l$  of  $k$ . The angle  $\phi_{kl}$  describes the orientation of the bond  $kl$  with respect to a fixed axis. The sample orientation is defined as  $\Psi = 1/N \sum_k \Psi_k$ . For a perfect triangular lattice, all the angles  $6\phi_{kl}$  are the same and  $|\Psi_k| = |\Psi| = 1$  (see [22]).

In Fig. 1, the local orientations of a configuration with  $N = 1024^2$  disks at density  $\eta = N\pi\sigma^2/V = 0.708$  in a square box of volume  $V$  are projected onto the sample orientation and represented using a color code (see [22]). Inside this configuration, a vertical stripe with density  $\sim 0.716$  preserving orientational order over long distances coexists with a stripe of disordered liquid of lower density  $\sim 0.700$ . Each stripe corresponds to a different phase. The two interfaces of length  $\simeq \sqrt{N}$  close on themselves *via* the periodic boundary conditions. Stripe-shaped phases as in Fig. 1a are found in the center of a coexistence interval  $\eta \in [0.700, 0.716]$ , whereas close to its endpoints, a “bubble” of the minority phase is present inside the majority phase for  $\eta \gtrsim 0.700$  and  $\eta \lesssim 0.716$  (see Fig. 2). This phase coexistence is the hallmark of a first-order transition.

The first-order transition shows up in the equilibrium equation of state  $P(V)$  (see Fig. 2). At finite  $N$ ,



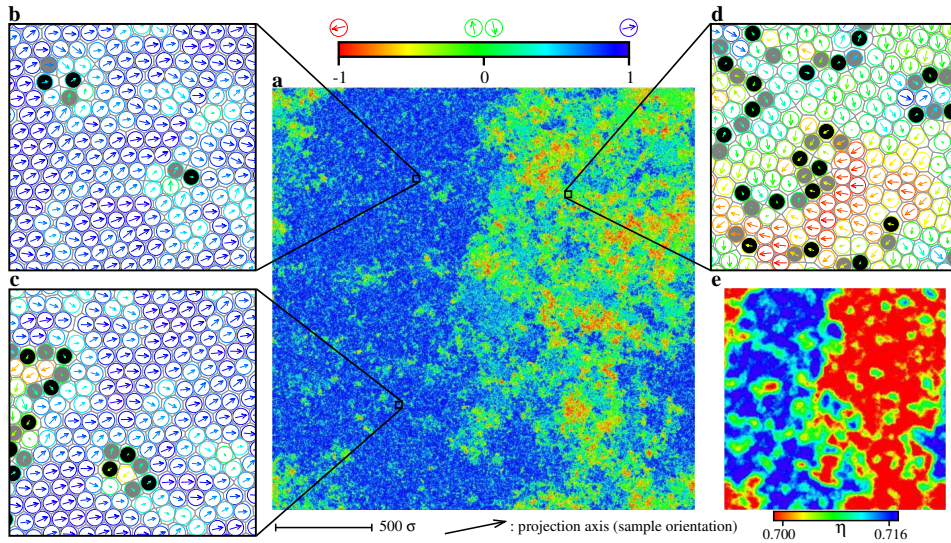


FIG. 1. Phase-coexistence for  $1024^2$  thermalized hard disks at density  $\eta = 0.708$ . **a**: Color-coded local orientations  $\Psi_k$  showing long orientational correlations (blue region, see **b,c**) coexisting with short-range correlations (see **d**). **e**: Local densities (averaged over a radius of  $50\sigma$ ), demonstrating the connection between density and local orientation (see [22]). In **b, c, d**, disks with five (seven) neighbors are colored in gray (black).

the free energy is not necessarily convex (as it would be in an infinite system) and the equilibrium pressure  $P(V) = -\partial F/\partial V$  can form a thermodynamically stable loop due to the interface free energy. The pressure loop in the coexistence window of a finite system is caused by the curved interface between a bubble of minority phase and the surrounding majority phase (see Fig. 2**b,d**). In a system with periodic boundary conditions, the pressure loop contains a horizontal piece corresponding to the “stripe” regime, where the interfaces are flat. This is visible near  $\eta \sim 0.708$  for the largest systems in Fig. 2. In a finite system, the Maxwell construction suppresses the interface effects. For the equation of state of Fig. 2**a**, this construction confirms the boundary densities  $\eta = 0.700$  and  $\eta = 0.716$  of Fig. 1 for the coexistence interval, with very small finite-size effects. The interface free energy per disk, the hatched area in Fig. 2, depends on the length  $\propto \sqrt{N}$  of the interface in the “stripe” regime so that  $\Delta f = \Delta F/N \propto 1/\sqrt{N}$  (see Fig. 2**f**).

The first-order nature of the transition involving the liquid is thus established by *i*): The visual evidence of phase coexistence in Fig. 1, *ii*): The  $\propto 1/\sqrt{N}$  scaling of the interface free energy per disk[23], and *iii*): The characteristic shape of the equation of state in a finite periodic system [24–26]. We stress that the system size is larger than the physical length scales so that the results hold in the thermodynamic limit (see [22]).

In the coexistence interval, the individual phases are difficult to analyze at large length scales because of the fluctuating interface, and only the low-density coexisting

phase is identified as a liquid with orientational correlations below a scale of  $\sim 100\sigma$  (see Fig. 1**a,d**). Unlike constant  $NV$  simulations, Gibbs ensemble simulations can have phase coexistence without interfaces, but these simulations are very slow at large  $N$  (see [22]). The single-phase system at density  $\eta = 0.718$ , is above the coexistence window for all  $N$  (see Fig. 2), and it allows us to characterize the high-density coexisting phase.

Positional order can be studied in the two-dimensional pair correlation  $g(\Delta\mathbf{r})$ , the high-resolution histogram of periodic pair distances  $\Delta\mathbf{r}_{ij} = \mathbf{r}_i - \mathbf{r}_j$  sampled from all  $N(N-1)/2$  pairs  $i, j$  of disks. To average this two-dimensional histogram over configurations (as in Fig. 3) the latter are oriented such that the  $\Delta x$  axis points in the direction of the sample orientation  $\Psi$ . At short distances, hexagonal order is evident at  $\eta = 0.718$  (see Fig. 3**a**). The excellent contrast between peaks and valleys of  $g(\Delta\mathbf{r})$  at small  $|\Delta\mathbf{r}| \gtrsim 2\sigma$  underlines the single-phase nature of the system at this density. The cut of the histogram along the positive  $\Delta x$  axis leaves no doubt that the system has exponentially decaying positional order on a length scale of  $\sim 100\sigma$  and cannot be a solid. The (one-dimensional) positional correlation function  $c_{\mathbf{k}}(r)$ , computed by Fourier transform of  $g(\Delta\mathbf{r})$ , fully confirms these statements (see [22]).

The orientational correlations at density  $\eta = 0.718$  decay extremely slowly and do not allow us to distinguish between quasi-long range and long-range order (see [22]). However, short-ranged positional correlation is inconsistent with long-ranged orientational order. It follows that

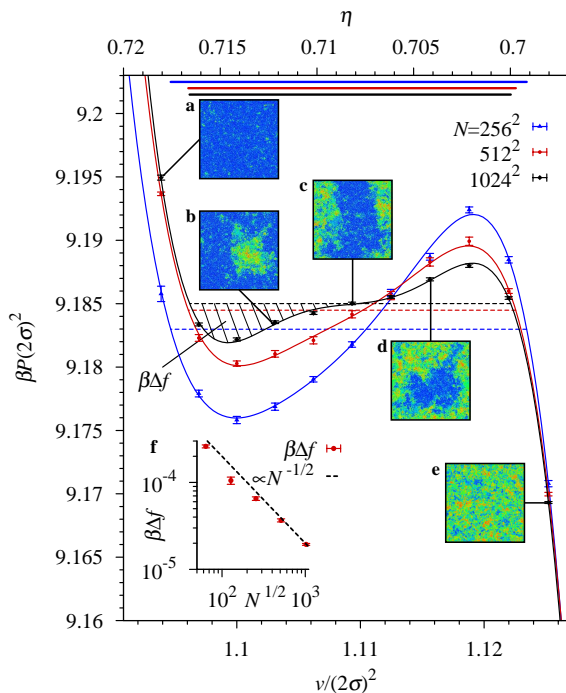


FIG. 2. Equilibrium equation of state for hard disks. The pressure is plotted *vs.* volume per particle ( $v = V/N$ ) (lower scale) and density  $\eta$  (upper scale). In the coexistence region, the strong system-size dependence stems from the interface free energy. The Maxwell constructions (horizontal lines) suppress the interface effects (with a convex free energy) for each  $N$ . “Stripe” (c, for  $N = 1024^2$ ) and “bubble” configurations (b,d) are shown in the coexistence region, together with two single-phase configurations (a,e). The interface free energy per disk  $\beta\Delta f$  (hatched area) scales as  $1/\sqrt{N}$  (f).

the orientation must be quasi-long ranged with a small exponent  $\lesssim 0$ , and that the system at  $\eta = 0.718$  and the high-density coexisting phase are both hexatic.

The two-dimensional pair correlation  $g(\Delta\mathbf{r}) - 1$  of Fig. 3b allows us to follow the transition from the hexatic to the solid: The positional order increases continuously with density and crosses over into power-law behavior at density  $\eta \sim 0.720$ , with an exponent  $\simeq -1/3$  which corresponds to the stability limit of the solid phase in the KTHNY scenario. The hexatic-solid transition thus takes place at  $\eta \gtrsim 0.720$ . At this density, the positional correlation function at large distances  $r$ , displays the finite-size effects characteristic of a continuous transition, but up to a few hundred  $\sigma$ ,  $c_k$  is well stabilized with system size (see [22]). Moreover, no pressure loop is observed in the equation of state, and the compressibility remains very small. The system is clearly in a single phase. Unlike the liquid-hexatic transition, the hexatic-solid transition therefore follows the KTHNY scenario, and is continu-

ous.

The single-phase hexatic regime is confined to a density interval  $\eta \in [0.716, 0.720]$ . Although narrow, it is an order of magnitude larger than the scale set by density fluctuations for our largest systems and can be easily resolved (see [22]). In the hexatic phase, the orientational correlations decay extremely slowly. The exponent of the orientational correlations is close to zero and negative. It remains far from the lower limit of  $-1/4$  at the continuous KTHNY transition, as this transition is preempted by a first-order instability.

The event-chain algorithm is about two orders of magnitude faster than the local Monte Carlo used up to now, allowing us to thermalize for the first time dense systems with up to  $1024^2$  disks. To illustrate convergence toward thermal equilibrium and to check that hard disks in the window of densities  $\eta \in [0.700, 0.716]$  are indeed phase-separated, we show in Fig. 4 two one-week simulations of our largest systems after quenches from radically different initial conditions, namely the (unstable) crystal, with  $|\Psi| = 1$ , and the liquid, for which  $|\Psi| \simeq 0$ . For both initial conditions, a slow process of coarsening takes place (see Fig. 4a,b). Phase separation is observed after  $\sim 10^6$  displacements per disk, and the sample orientation takes on similar absolute values (see Fig. 4c). Effective simulation times of many earlier calculations were much shorter[14, 15], and the simulations remained in an out-of-equilibrium state which is homogeneous on large length scales, whereas the thermalized system is phase-separated and therefore inhomogeneous. The production runs for  $N = 1024^2$  were obtained from Markov chains with running times of nine months, 30 times larger than those of Fig. 4a,b.

The solution of the melting problem presented in this work provides the starting point for the understanding of melting in films, suspensions, and other soft-condensed-matter systems. The insights obtained combine thermodynamic reasoning with powerful tools: advanced simulation algorithms, direct visualization, and a failsafe analysis of correlations. These tools will all be widely applicable, for example to study the cross-over from two to three-dimensional melting as it is realized experimentally with spheres under different confinement conditions[17].

In simple systems such as hard disks and spheres, entropic and elastic effects have the same origin: elastic forces are entropically induced. For general interaction potentials, entropy and elasticity are no longer strictly linked and order-disorder transitions, which can then take place as a function of temperature or of density, might realize other melting scenarios[27]. Theoretical, computational and experimental research on more complex microscopic models will build on the hard-disk solution obtained in this work.

We are indebted to K. Binder and D. R. Nelson for helpful discussions and correspondence. We thank J. Dalibard and G. Bastard for a critical reading of the

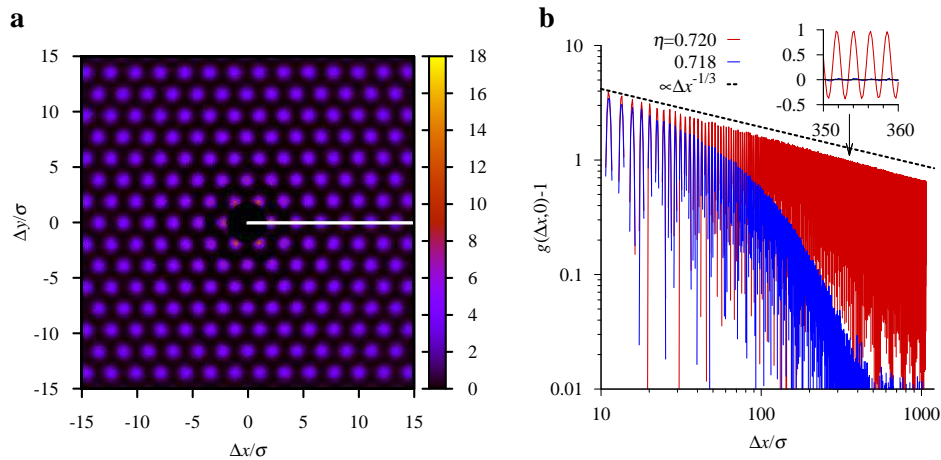


FIG. 3. Configuration-averaged two-dimensional pair correlation.  $g(\Delta\mathbf{r})$  is obtained from the two-dimensional histogram of periodic distances  $\Delta\mathbf{r}_{ij} = \mathbf{r}_i - \mathbf{r}_j$ . **a**: Pair correlation  $g(\Delta\mathbf{r})$  at density  $\eta = 0.718$  for small  $\Delta\mathbf{r} = (\Delta x, \Delta y)$ . Each disk configuration is oriented with respect to  $\Psi$ . The excellent contrast between the peak and the bottom values of  $g(\Delta\mathbf{r})$  at  $|\Delta\mathbf{r}| \gtrsim 2\sigma$ , of about (16 : 0.2), provides evidence for the single-phase nature of the system. **b**: Cut of the sample-averaged  $g(\Delta\mathbf{r}) - 1$  for  $\Delta\mathbf{r} = (\Delta x, 0)$ . Decay is exponential for  $\eta = 0.718$  and algebraic for  $\eta = 0.720$ . (See [22] for positional and orientational correlation functions.)

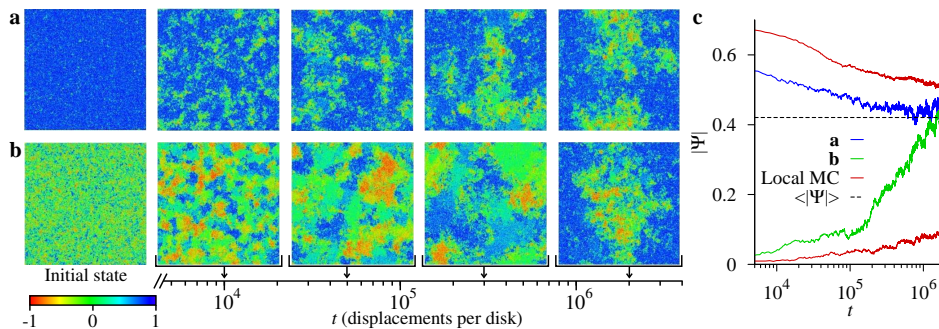


FIG. 4. Approach to thermal equilibrium from different initial conditions. **a,b**:  $1024^2$  hard disks at density  $\eta = 0.708$ , after a quench from a high-density crystal (**a**) and from a low-density liquid (**b**), showing coarsening leading to phase separation (Color code for  $\Psi_k$  as in Fig. 1b, see also [22]). Each of the runs takes about one week of CPU time. **c**: Absolute value of the sample orientation for the simulations in **a,b**, compared to runs with the local Monte Carlo algorithm from the same initial conditions (time in attempted displacements per disk). The correlation time of the event-chain algorithm, on the order of  $10^6$  displacements per disk, estimated from **c**, agrees with the correlation time estimated in our production runs with  $6 \times 10^7$  total displacements per disk.

manuscript.

\* etienne.bernard@lps.ens.fr

† werner.krauth@ens.fr

[1] R. Peierls, *Helv. Phys. Acta Suppl.* 7, 81 (1934)

[2] R. Peierls, *Annales de l'IHP* 5 177 (1935)

[3] N. D. Mermin, H. Wagner, *Phys. Rev. Lett.* 17, 1133 (1966).

[4] B. J. Alder, T. E. Wainwright, *Phys. Rev.* 127, 359 (1962)

[5] N. D. Mermin, *Phys. Rev.* 176, 250 (1968)

[6] W. G. Hoover, F. H. Ree, *J. Chem. Phys.* 49, 3609 (1968).

[7] J. M. Kosterlitz, D. J. Thouless, *J. Phys. C* 6, 1181 (1973).

[8] B. I. Halperin, D. R. Nelson, *Phys. Rev. Lett.* 41, 121 (1978).

[9] A. P. Young, *Phys. Rev. B* 19, 1855 (1979).

[10] K. J. Strandburg, *Rev. Mod. Phys.* 60, 161 (1988).

[11] J. Y. Lee, K. J. Strandburg, *Phys. Rev. B* 46, 11190 (1992).

[12] J. A. Zollweg, G. V. Chester, *Phys. Rev. B* 46, 11186 (1992).

- [13] H. Weber, D. Marx, K. Binder, *Phys. Rev. B* 51 14636 (1995).
- [14] A. Jaster, *Phys. Lett. A* 330, 120 (2004).
- [15] C. H. Mak, *Phys. Rev. E* 73, 065104(R) (2006).
- [16] K. Zahn, R. Lenke, G. Maret, *Phys. Rev. Lett.* 82, 2721 (1999).
- [17] Y. Peng, Z. Wang Z., A. M. Alsayed, A. G. Yodh., Y. Han, *Phys. Rev. Lett.* 104, 205703 (2010).
- [18] K. Bagchi, H. C. Andersen, W. Swope, *Phys. Rev. Lett.* 76 255 (1996).
- [19] W. Krauth, *Statistical Mechanics: Algorithms and Computations*. Oxford University Press (2006)
- [20] N. Metropolis, A. W. Rosenbluth, M. N. Rosenbluth, A. H. Teller, E. Teller, *J. Chem. Phys.* 21 1087 (1953).
- [21] E. P. Bernard, W. Krauth, D. B. Wilson, *Phys. Rev. E* 80 056704 (2009).
- [22] See Supplemental Material at [URL will be inserted by publisher].
- [23] J. Lee, J. M. Kosterlitz, *Phys. Rev. Lett.* 65, 137 (1990).
- [24] J. E. Mayer, W. W. Wood, *J. Chem. Phys.* 42, 4268 (1965)
- [25] H. Furukawa, K. Binder, *Phys. Rev A* 26, 556 (1982)
- [26] M. Schrader, P. Virnau, K. Binder, *Phys Rev E* 79, 061104 (2009)
- [27] A. C. D. van Enter, S. B. Shlosman, *Phys. Rev. Lett.* 89 285702 (2002).

# Résumé

Cette thèse porte sur la méthode de Monte-Carlo ainsi que sur des applications de cette méthode à la physique statistique.

La première partie concerne l'étude de la transition de phase liquide-solide à deux dimensions. La nature de cette transition est un problème de la physique statistique qui a longtemps été débattu, et en particulier pour le modèle fondamental des disques durs. Dans le but de traiter ce problème, nous avons développé l'algorithme de Monte-Carlo dit "event-chain". Notre analyse numérique montre que la transition se déroule en deux étapes: en augmentant la densité, le système passe de manière discontinue d'une phase liquide à une phase dite hexatique, puis de manière continue à une phase solide par une transition de type Kosterlitz-Thouless. Ces résultats posent une nouvelle base théorique aux expériences sur les solides bidimensionnels.

La deuxième partie concerne les algorithmes d'échantillonnage parfait utilisant la méthode "Coupling from the past". Ces algorithmes de Monte-Carlo permettent d'échantillonner des systèmes selon la distribution exacte désirée, ce qui supprime le problème de la connaissance du temps de thermalisation d'une chaîne de Markov. Cette méthode s'est avérée inefficace pour des systèmes physiques où elle serait utile: les verres de spins à basse température, ou les sphères dures à haute densité par exemple. Nous avons étudié différents algorithmes exacts pour ces systèmes. Les résultats obtenus montrent que cette limitation est due aux transitions vers le chaos des chaînes de Markov, ces transitions étant d'origine dynamique et non thermodynamique.

**Mots clés: algorithme de Monte-Carlo - systèmes à deux dimensions - sphères dures - transition de phase - chaîne de Markov - systèmes désordonnés.**

# Abstract

This thesis deals with the Monte Carlo method and some of its applications to statistical physics.

The first part concerns the study of the melting transition in two dimensions. The nature of this transition is an old problem of statistical physics, and especially for the fundamental model of hard disks. A Monte Carlo algorithm, called "event-chain", is developed for this model and is used to study the melting transition. The results show that the transition follows a two-step scenario with a hexatic phase between the liquid and the solid. The solid-hexatic transition is continuous of the Kosterlitz-Thouless type, and the hexatic-liquid transition is discontinuous. These results confirm the existence of the hexatic phase, and pose a new theoretical basis for experiments on two-dimensional melting transitions.

The second part concerns perfect sampling algorithms using the "coupling-from-the-past" approach. This paradigm of the Markov-chain Monte Carlo method allows to sample configurations from the exact desired distribution, and this suppresses the long-standing problem of accessing the mixing time of a Markov chain. This method is however difficult to apply to physical systems such as spin glasses at low temperature or hard spheres at high density. Perfect-sampling algorithms are studied for these systems. The results show that the limitation of this method is related to transitions toward chaos of Markov chains. These dynamical transitions are not caused by thermodynamical changes.

**Keywords: Monte Carlo algorithm - two-dimensional systems - hard spheres - melting transition - Markov chain - disordered systems.**